UNIVERSITÉ DE GENÈVE
Département de physique nucléaire et corpusculaire

FACULTÉ DES SCIENCES
Professeur Alain Blondel

Background and Instrumentation in MICE

the international Muon Ionization Cooling Experiment

THÈSE

présentée à la Faculté des sciences de l'Université de Genève
pour obtenir le grade de Docteur ès sciences, mention physique

par

Anton Rikard SANDSTRÖM

de Suède

Thèse N° 3922

GENÈVE
Atelier de reproduction de la Section de physique
2007

UNIVERSITÉ DE GENÈVE

FACULTÉ DES SCIENCES

Doctorat ès sciences mention physique

Thèse de *Monsieur Rikard SANDSTRÖM*

intitulée

" Background and Instrumentation in MICE "

La Faculté des sciences, sur le préavis de Messieurs A. BLONDEL, professeur ordinaire et directeur de thèse (Département de physique nucléaire et corpusculaire), D. RAPIN, professeur titulaire (Département de physique nucléaire et corpusculaire), P. JANOT, docteur (Conseil Européen pour la Recherche Nucléaire – Genève, Suisse), et A. BROSS, professeur (Fermi National Accelerator Laboratory – Batavia, U.S.A.), autorise l'impression de la présente thèse, sans exprimer d'opinion sur les propositions qui y sont énoncées.

Genève, le 1 décembre 2007

Thèse - 3922 -

Le Doyen, Jean-Marc TRISCONE

N.B. - La thèse doit porter la déclaration précédente et remplir les conditions énumérées dans les "Informations relatives aux thèses de doctorat à l'Université de Genève".

Nombre d'exemplaires à livrer par colis séparé à la Faculté : - 7

ABSTRACT

Experiments at the end of last century proved that the neutrinos had a small but nonzero mass in contrast with the Standard Model of particle physics. The light mass of the neutrinos and the experimental absence of right handed neutrinos can be explained through the See-Saw model, assuming the neutrino is a Majorana particle, with the right handed neutrino mass of the order of the GUT scale. $\mathcal{CP}$ violation in the heavy neutrino sector in the early Universe is the most natural explanation of the matter–antimatter asymmetry observed today.

Leptonic $\mathcal{CP}$ violation and the neutrino mixing angles are intimately linked. Should any mixing angle be zero, $\mathcal{CP}$ is conserved. Only one of the mixing angles, θ_{13}, is small. The current best fit to all neutrino oscillation data yields a value of zero for θ_{13}. In addition the mass hierarchy of the neutrino mass eigenstates is still unknown. The most powerful facility to measure the small mixing angle, $\mathcal{CP}$ violation and the mass hierarchy is the Neutrino Factory, which stores a low emittance muon beam in a storage ring. The muons decay into neutrinos which are detected in two detectors at distances of 1500–4000 km and 7000 km respectively.

Initially, the Neutrino Factory muon beam occupies a large volume in phase space, which must be reduced before the beam can be accelerated to desired energy. This will be accomplished by ionization cooling. The experimental demonstration will be supplied by the Muon Ionization Cooling Experiment built at Rutherford Appleton Laboratory outside Oxford, United Kingdom. The cooling channel consists of three liquid hydrogen absorbers, interspaced by two linacs of four RF cavities each. The emittance is measured before and after the cooling channel using scintillating fiber spectrometers and time of flight detectors. A Čerenkov detector and a calorimeter are ensuring high purity of the beam.

During operation of RF cavities in high electric and magnetic field, electrons are emitted from the cavity surfaces and accelerated in the beamline before they are stopped in the absorbers. This generates a substantial number of bremsstrahlung photons in the MeV range which exit the cooling channel. As the photons hit the spectrometers they form an important background to the spectrometers and time of flight detectors. This thesis presents the analysis of the data taken with an RF cavity in a Fermilab experiment. The results are applied to MICE, confirming that the problem will be serious.

Another source of experimental bias originates from muon decays. The electrons from the decay have a different single particle emittance than that of the muons, thus creating a systematic error on the emittance measurements. In this thesis effects creating systematic errors to the emittance measurements are studied in Monte Carlo simulations, the new design of calorimeter is compared to its predecessor and the transverse apertures of the experiment are redefined. It will be demonstrated that this effect can be reduced to an acceptable level.

Dedicated to Dick Sandström
$^{11}\!/_{11}$ 1951 – $^{5}\!/_{10}$ 2006

RÉSUMÉ EN FRANÇAIS

Des expériences à la fin du siècle dernier ont montré que les neutrinos avaient une masse faible mais non-nulle, en contradiction avec le Modèle Standard de la physique des particules. Ces petites masses de neutrinos et l'absence expérimentale de neutrinos droits peuvent être expliqués par l'intermédiaire du modèle de Grande Unification See-Saw, en supposant que le neutrino est une particule de Majorana, avec des masses des neutrinos droits de l'ordre de l'échelle de Grande Unification. La violation de $\mathcal{CP}$ par les désintégrations des neutrinos lourds dans l'univers primordial est l'explication la plus naturelle de l'asymétrie matière–antimatière observée aujourd'hui.

Violation leptonique de $\mathcal{CP}$ et les angles de mélange des neutrinos sont intimement liés. Si un angle de mélange est zero, $\mathcal{CP}$ est conservée. L'un des angles de mélange, θ_{13}, est petit et pourrait être nul. En outre, la hiérarchie des masses des états propres de masse des neutrinos n'est pas encore connue. La plus puissante machine permettant de mesurer à la fois cet angle de mélange, la violation de $\mathcal{CP}$ et la hiérarchie des masses est l'Usine à Neutrinos' (*Neutrino Factory*), qui stocke un faisceau de muons de faible émittance dans un anneau de stockage. Les muons se désintégrent en neutrinos qui sont détectés dans deux détecteurs à des distances de 1500–4000 km et 7000 km.

Initialement, le faisceau de muons de la Neutrino Factory occupe un grand volume d'espace des phases, qui doit être réduit avant que le faisceau puisse être accéléré à l'énergie souhaitée. Ce refroidissement ne peut être atteint par des méthodes classiques mais peut être obtenu à l'aide du refroidissement par ionisation, une technique qui n'a jamais été démontrée. La démonstration expérimentale sera fournie par la *Muon Ionisation Cooling Experiment* (MICE) qui est en cours de construction au Rutherford Appleton Laboratory près d'Oxford, Royaume-Uni. Le canal de refroidissement se compose de trois absorbeurs d'hydrogène liquide, encadrant deux linacs de quatre cavités RF chacun. L'émittance est mesurée particule par particule avant et après le canal de refroidissement à l'aide de spectromètres en fibres scintillantes et de détecteurs de temps de vol. Un détecteur Tcherenkov et un calorimètre assurent la pureté du faisceau.

Une des particularités du canal de refroidissement par ionisation est la nécessité de plonger les cavités accélératrices radiofréquence à l'intérieur du champ magnétique de guidage. Pendant le fonctionnement de ces cavités RF à haut champ, des électrons sont émis par les surfaces des cavités et accélérés dans la ligne de faisceau avant d'être arrêtés dans les absorbeurs. Cela génère l'émission d'un nombre substantiel de photons de Bremsstrahlung dans la gamme des MeV. Ces photons forment un bruit de fond important dans les spectromètres.

Une autre source de biais expérimentaux provient de la désintégration des muons. Les

électrons de désintégration ont des émittances individuelles différentes de celles des muons, créant ainsi un biais et une erreur systématique potentielle sur les mesures d'émittance. Afin de réduire la contamination, un calorimètre est placé à la fin de l'expérience. Dans cette thèse, les effets créant des erreurs systématiques à la mesure du refroidissement sont étudiés par une simulation Monte Carlo, et nous avons montré qu'il fallait redéfinir la conception du calorimètre par rapport à son prédécesseur. Le nouveau calorimètre est décrit en détail. Les dimensions transverses de l'expérience sont elles aussi redéfinies.

Finalement une analyse des données prises avec une cavité RF de test à Fermilab est présentée et les résultats appliqués au cas de MICE, confirmant que le problème sera sérieux.

CONTENTS

LIST OF FIGURES

LIST OF TABLES

PREFACE

"When you are about to begin, writing a thesis seems a long, difficult task. That is because it is a long, difficult task." Those words of advice were the first I encountered when I was searching for guidelines and rules regarding how a thesis should be written. And indeed, it is true. After a while the initial frustration over not knowing where to begin, gives way to enjoyment, because it is fun to sit down and write about your favorite scientific topic after all. Eventually all the easy and interesting parts are already written and, no matter how many times the thesis is read, grammar and spelling errors never stop showing up. At a certain point, just like a colleague of mine warned me, you no longer care if you get your degree as long as you get the beast off your hands.

Writing a thesis is a struggle everyone who aspires to achieve a doctoral degree must suffer through, and for a good reason. While assembling the work I have performed for my degree, I was also forced to assemble my thoughts and knowledge on the topics discussed. Filling in the bits and pieces missing between chapters, I have learned very much during a relatively short time. I think this is the great personal benefit of taking the time to summarize and structure the knowledge gained during the four years of graduate studies. Of equal importance is the benefit for an eventual successor, to have a single volume where all topics of interest are documented.

One of the hardest parts of writing a thesis is to choose a suitable level of detail. Topics which for the initiated seem trivial require more elaborate explanations for the casual reader. Since the set of readers of a thesis spans from family and friends to world leading experts, it is sometimes very hard to know for whom you are writing. A good lecture series, a wise man once told me starts with a lecture which everybody understands. The following lectures increase in complexity until the final lecture where no one, not even the lecturer, fully understands what is going on. I have taken this doctrine to heart when working on this thesis, something should be apparent if reading the first two chapters. The range of topics presented is rather wide, but always following a red thread, or sometimes connected through a mesh of relations. This work was fueled by approximately 3000 cups of coffee, thus there is a lot to present. Another reason for the vast scope of the thesis is, naturally, the many open questions of the field.

Neutrino physics is a topic which is very much alive today. A few months ago MiniBooNE disproved the LSND claims of light sterile neutrinos, several neutrinoless double beta decay experiments are either running or about to start up, and with T2K and Double Chooz starting in 2009, a realistic probability of measuring a nonzero θ_{13} will be provided. With the high energy physics program running in parallel with LHC starting up in less than a year from now, it is an exciting time to be a particle physicist. It remains to see whether the high energy landscape is rich with new particles or if it is void of new phenomena.

As the presence of neutrino masses proves, however, the Standard Model is not a complete picture of the laws of particles and forces. Furthermore the indirect observations of dark matter and dark energy from cosmology strongly suggests that we know very little of the nature of matter. How are these topics connected with each other? Did they influence the inflation of Universe? Are the neutrinos Majorana particles, and can they be the cause of the asymmetry observed in Universe between matter and antimatter? Is parity spontaneously broken at high energy through right handed weak bosons, and how does that relate to the baryon lepton symmetry? These questions are the important questions we should ask now that we enter a new era of particle physics exploration, and these questions are a guarantee that Nature has more surprises in store for us.

I would give my sincerest gratitude to Département d'Instruction Publique and Fonds National Suisse for their financial support, and to Département de Physique Nucléaire et Corpusculaire for accepting me as a Graduate Student for this project. And to the Reader, whoever you may be, I thank you for interest in this thesis, and I hope I do not disappoint you too much. It is with a warm hand, a genuine relief, and a good deal of pride I offer you this thesis.

Rikard Sandström, July 2007, Geneva

1. HISTORICAL BACKGROUND

It is sometimes said that physics is a vertical science. New results build upon old results, which in turn are founded on even earlier experiments and theories.

This chapter is a brief summary of how the understanding of the neutrinos has evolved since it was first proposed during the beginning of the last century. A more extensive description of the phenomena mentioned in this historical background can be found in later sections of this thesis.

1.1 Beta decay and the advent of the neutrino

Radioactivity was accidentally discovered in 1896 by Antoine Henri Becquerel when investigating phosphorescence in uranium salts. He discovered that the photographic plates he used for wrapping the radioactive salts were already fully exposed before the experiment requiring bright sunlight was performed. This led to the discovery of spontaneous emission of nuclear radiation, for which he shared the 1903 Nobel Prize in physics with Marie and Pierre Curie.

In 1911 it was discovered that the energy of the emitted electrons is distributed about a continuous spectrum. Since the energy levels of the nucleus are quantized, one would expect the expected the energy of the electron to be unique if the process is a two body decay, and hence the spectrum to be discrete. This led researchers to challenge beliefs of both energy and angular momentum conservation. To save the show, Wolfgang Pauli in 1930 proposed that an extremely light particle with no electric charge, which he named *neutron*, also was emitted in the decay process.

> Pauli's historical letter:
>
> *Dear Radioactive Ladies and Gentlemen, As the bearer of these lines, to whom I graciously ask you to listen, will explain to you in more detail, how because of the "wrong" statistics of the N and Li^6 nuclei and the continuous beta spectrum, I have hit upon a desperate remedy to save the "exchange theorem" of statistics and the law of conservation of energy. Namely, the possibility that there could exist in the nuclei electrically neutral particles, that I wish to call neutrons, which have spin 1/2 and obey the exclusion principle and which further differ from light quanta in that they do not travel with the velocity of light. The mass of the neutrons should be of the same order of magnitude as the electron mass and in any event not larger than 0.01 proton masses. The*

> *continuous beta spectrum would then become understandable by the assumption that in beta decay a neutron is emitted in addition to the electron such that the sum of the energies of the neutron and the electron is constant...*
>
> *I agree that my remedy could seem incredible because one should have seen those neutrons very earlier if they really exist. But only the one who dare can win and the difficult situation, due to the continuous structure of the beta spectrum, is lighted by a remark of my honored predecessor, Mr. Debye, who told me recently in Bruxelles: "Oh, It's well better not to think to this at all, like the new taxes". From now on, every solution to the issue must be discussed. Thus, dear radioactive people, look and judge. Unfortunately, I cannot appear in Tubingen personally since I am indispensable here in Zurich because of a ball on the night of 6/7 December.*
>
> *With my best regards to you, and also to Mr. Back.*

Enrico Fermi changed the name to *neutrino* in 1931, since another heavy neutral particle called neutron had been discovered shortly after Pauli's letter.

1.2 Theory of interactions

Enrico Fermi developed a theory of weak interactions, where four fermions interact directly with each other. This is a point like approximation of the interaction which does not use intermediary bosons to carry the forces. As such it is not renormalizable and fails at high energies, but works remarkably well for small momentum transfers.

Later, Hikeki Yukawa proposed that the nuclear forces can be explained by the exchange of a new particle between the nucleons, similar to the photon. Unlike the photon this new particle must be very heavy, since the range of the nuclear forces is very short and confined to the nucleus. The mass of this intermediary boson is often much higher than the energy exchanged in the process, which is still permitted under the Heisenberg uncertainty principle.

Fermi received the Nobel Prize in 1938, and Yukawa in 1949, for their work on radioactivity and nuclear forces. Today their significant contributions are evident in the naming of the Fermi and Yukawa couplings.

1.3 Direct observation of the neutrino

With the advent of fission reactors, physicists got new means of producing vast quantities of neutrinos in a controlled environment. Clyde L. Cowan and Frederick Reines published in 1956 the first evidence of the existence of neutrinos by detection of inverse beta decay ($\overline{\nu}_e + p \rightarrow n + e^+$) at a nuclear reactor.

At first they used the annihilation of the positron with an electron into two photons in a water tank to detect the neutrino induced reaction. Although the annihilation process gives a very clear signal, the experiment was not conclusive enough. They added cadmium chloride to the tank, which allowed them to also detect the neutron which is released in the reaction. When the cadmium absorbs the neutron, it produces another cadmium isotope in an exited state. After a few microseconds the isotope falls back to its ground state by emitting a photon with a well defined energy which is easy to detect. This way they could count about three neutrino interactions per hour in the detector. To be absolutely sure that they were seeing neutrinos from the nuclear reactor, they did the same counting with the reactor shut down. Their measured cross section for the neutrino interaction was $6 \times 10^{-44}\ cm^2$, a very small cross section indeed.

1.3.1 More generations of neutrinos

The first clear evidence for a difference between electron neutrinos and muon neutrinos came from an experiment in Brookhaven in 1962, which was also the first man made neutrino beam from an accelerator. If muon neutrinos and electron neutrinos were identical, the inverse beta decay would produce as many muons as electrons in the final state, for incident muon neutrinos produced in pion decay. But they found only muons in the sample. Hence there is a difference between the two generations of neutrinos, and lepton family number is a conserved quantity.

The tau lepton, a third generation of leptons was indirectly discovered by a series of experiments at SLAC, USA, between 1974 and 1977, which suggested the existence of tau neutrinos. The presence of tau neutrinos could later be observed as missing energy in $W \to \tau\nu$ decay at LEP at CERN. In 2000 the tau neutrino was directly discovered in the DONUT experiment, and a few years earlier LEP at CERN had concluded from the Z boson width that the number of light active neutrinos must be three.

1.4 Violations of symmetries

Physics is the study of the laws of nature in the sense that it is using conserved quantities to understand and predict physical phenomena. At its very heart is the theorem that tells us that a symmetry in nature creates a conserved quantity. However what is conserved under one force of nature is not necessarily conserved under another force of nature. The importance of symmetries and the way they are broken is ultimately the foundation of particle physics.

1.4.1 Parity violation

It has long been assumed that parity is universally conserved. In 1956-1957 Chien-Shiung Wu proved that not only was parity violated, but that it was maximally violated in the weak interactions. Cobalt-60 nuclei were aligned magnetically at a temperature of 10 mK in such a manner that all their spins were aligned in one direction. The cobalt isotope decays into another nucleus and an electron and an antielectron neutrino. Since the spin of the final state nucleus is still in the direction of the initial state spin, the electron and the neutrino have opposite spin directions. If parity was conserved, the probability of finding the electron spin aligned with the nucleus spin would be equal to finding the electron spin in the opposite direction. Experimentally this was determined by counting the electron rates emitted in parallel and antiparallel directions compared to the magnetic field. However, the experiment found that all electrons had spins in the opposite direction of the nuclei. The reason for this parity violation is that the bosons mediating the weak force only couple to left handed particles.

An experiment performed in 1957 by Goldhaber, Grodzins, and Sunyar showed that the neutrino is created with negative helicity. This provided conclusive evidence for the V-A (vector minus axial) theory of weak interactions that is an integral part of today's Standard Model. This led to the overthrow of parity conservation in the weak interactions.

1.4.2 $\mathcal{CP}$ violation of quarks

After the discovery of parity violation in weak interactions, the product of charge by parity, $\mathcal{CP}$, was still considered to be conserved. It was discovered in 1964 that the mass eigenstate K_L^0 of neutral kaons occasionally decays into only two and not three pions, as would be expected if $\mathcal{CP}$ was conserved since K_L^0 is $\mathcal{CP}$ odd. While the weak interactions which mediate the decay process violates $\mathcal{C}$ and $\mathcal{P}$ individually, $\mathcal{CP}$ should still be conserved if the weak eigenstates are identical to the mass eigenstates.

In 1955 Gell-Mann and Pais had already proposed oscillation based on mixing for neutral kaons. This indirect $\mathcal{CP}$ violation was later observed in the time dependence of the electron charge from decays of the hadronic eigenstates K^0 and $\bar{K}^0$. Time evolution of the quantum states depends on the Hamiltonian, which in the case of mixing is a matrix with mass dependency.

The $\mathcal{CP}$ violation showed the world of physics that the interaction eigenstates are not the same as the mass eigenstates of the quarks, but the sets of eigenstates are related through mixing. The mixing is necessarily unitary and it is therefore equally correct to say that the baryon eigenstates are superpositions of the mass eigenstates as the other way round. This discovery helped physicists to better understand mixing in the leptonic sector.

1.4.3 Lepton number violation

In 1957 Pontecorvo suggested that a neutrino can oscillate into its antiparticle, using the same mechanism as for kaons. The neutrino oscillation would hence violate lepton number conservation. The theory of neutrino mixing evolved to our present understanding in 1969, where neutrinos can oscillate if there is mixing and a mass difference between the neutrino flavors. If the masses of the neutrinos are smaller than approximately 1 eV, neutrino oscillation is the most practical way to be sensitive to the neutrino masses. Direct measurements from radioactive decays could not detect a nonzero neutrino mass, but only give upper limits, and the neutrino was, in general, assumed to be massless.

In the 1960's Davis and Bahcall measured a neutrino flux from the Sun which was significantly smaller than what the standard solar model was predicting. One possible solution to the so called Solar Neutrino Problem was lepton number violating neutrino mixing.

However, all efforts using neutrino beams to experimentally detect neutrino oscillation gave null results.

In the early 1980's huge underground Čerenkov detectors were built to discover proton decay, which many Grand Unifying Theories were predicting, but no proton decay was ever found. Instead a deficit of muon neutrinos compared to electron neutrinos was observed for neutrinos produced by cosmic ray interactions in Earth's atmosphere, which could be interpreted as neutrino oscillations. Despite initial doubts regarding neutrino oscillation as a possible explanation for the deficit, due to the required assumption of very large mixing angles, the idea prevailed.

In 1998, Super-Kamiokande in Japan conclusively showed neutrino oscillation between muon neutrinos and tau neutrinos with a mass difference of about $(0.05\ \mathrm{eV})^2$. Furthermore the experiment showed that the mixing is nearly maximal. The results of Super-Kamiokande were combined with the neutrino deuterium scattering experiment at Sudbury Neutrino Observatory in 2002, which finally confirmed the neutrino mixing hypothesis for the Solar Neutrino Problem.

1.5 Neutrino physics today

With the discovery of massive neutrinos follows a necessary modification to the Standard Model. Since the neutrinos are massive, there must be a mass term in the Lagrangian which involves right handed neutrinos. The inclusion of right handed neutrinos contradicts the Standard Model assumption that all neutrinos are left handed.

Another interesting question is why the neutrino masses are so small compared to all other massive fermions. This can be explained using the See-Saw mechanism, if the neutrinos are Majorana particles. For every light neutrino, there is also a very heavy neutrino with masses close to the GUT scale. If this theory is correct, physicists could have a window for examining nature at energies much too high to be reached with particle accelerator experiments. If the neutrinos are Majorana particles, it should in principle be possible to observe beta decay with no final neutrinos, so called neutrinoless double beta decay. Experiments are being performed for the discovery of this phenomenon.

Since neutrino oscillation violates lepton number conservation, it is possible that the mixing also violates charge parity invariance. Decay of the heavy Majorana neutrinos could also cause a $\mathcal{CP}$ violation, and thus explain the matter-antimatter asymmetry observed in the universe.

Neutrinos are of further interest for cosmologists because of their vital role in the early expansion of universe, the inflation and the freeze out, and because the neutrino mass significantly contributes to the total mass of the universe. Since neutrinos are WIMPs, Weakly Interacting Massive Particles, they are not only of interest to cosmologists. The lack of electric charge makes neutrinos very interesting for studying the weak interaction.

For astrophysicists neutrino telescopes allow studies of optically opaque objects, such as the core of stars, and provide information on other neutrino rich phenomena such as supernovas. It has also been found that for stars evolved beyond the helium burning stage, the cooling is dominated by emission of neutrinos, which controls the lifetime of such stars.

The elusive neutrinos have a history strongly linked with particle, nuclear and astrophysics, a history full of surprises. This field of research is open and leaves room for many theories and experiments of potential great importance for general science. Time will tell if our understanding of the neutrinos is correct, but it would be foolish to assume that the days of surprises are gone. If anything the history of the neutrinos has taught us that humility is a good strategy for scientific endeavors in the study of the constituents of the world.

2. NEUTRINO MASS

The observed violation of lepton flavor conservation in the neutrino sector has been interpreted as small but nonzero neutrino mass associated with substantial mixing. In the Standard Model neutrinos are massless, and only left handed neutrinos exist. This chapter is a summary of the experimental observations and the models attempting to incorporate neutrino masses into the Standard Model formalism.

2.1 Neutrino mass observations

The neutrinos were long thought to be massless particles. In this section the experimental evidence for small, yet nonzero, neutrino masses are presented.

2.1.1 Nuclear decay

Traditionally the neutrino has been assumed to be massless, and the upper limit on the neutrino mass given by the kinematic end point of the final state electron. The most sensitive source is tritium, which decays into ^{3}He, an electron and an antielectron neutrino. Tritium has a low end point energy of 18.6 keV and a short life time; which together with a very simple shell structure make it the preferred isotope for direct neutrino mass measurements. The upper mass limit thus far obtained is 2 eV for the electron neutrino [1]. For the other lepton eigenstates the mass limits are worse, since for ν_μ the experiment must stop a pion and let it decay at rest while measuring the muon energy. And the ν_τ mass measurement involves the decay products of tau leptons.

In the case of neutrino mixing, the result would give a discrete value of the end point for each mass eigenstate i with the probability $|U_{li}|^2$, where U is a unitary mixing matrix. Experimentally it is not possible to separate masses of the mass eigenstates, hence the experimentally observed neutrino mass is

$$m_{\nu_l}^2 = \sum_i |U_{li}|^2 m_{\nu_i}^2. \tag{2.1}$$

Should the mass differences between mass eigenstates be determined, using for example neutrino oscillations, the direct measurement of the neutrino mass would hence set the overall mass scale of the neutrinos. Some experiments are in preparation to increase the precision; one of them is KATRIN which aims to determine m_ν to the 0.2 eV level, hence the required precision on the measured m_ν^2 must be of the 0.04 eV^2 level. This will be

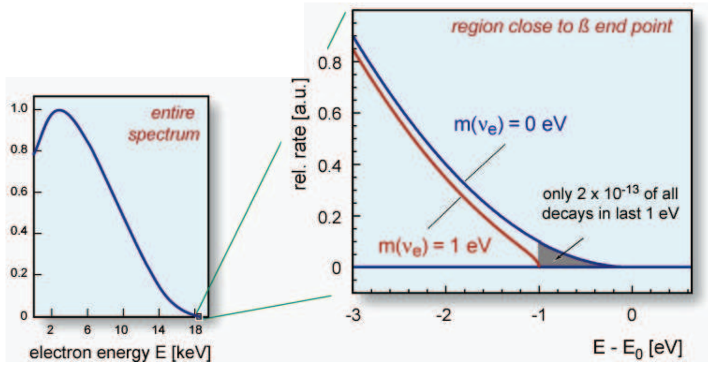

Fig. 2.1: The neutrino mass measured as the endpoint of the kinematic spectrum in β decay.

obtained with 90% confidence level after three years of data taking, and will also give a discovery potential of 5σ for neutrino masses larger than 0.35 eV [2].

2.1.2 Neutrino flavor transformation and interpretation

If neutrinos mix, lepton flavor numbers are not conserved separately within the standard electroweak theory. This would imply mixing of charged leptons. However any such mixing would necessarily involve the neutrino mass, which explains why charged lepton mixing is suppressed. For example the calculation of the neutrinoless charged lepton decay [3]

$$\Gamma(l_\alpha \to l_\beta \gamma) = \frac{1}{2}\alpha G_F^2 \left(\frac{1}{32\pi^2}\right)^2 m_{l_\alpha}^5 \left| \sum_i U_{\alpha i}^* U_{\beta i} \frac{m_{\nu_i}^2}{M_W^2} \right|^2 \qquad , \alpha \neq \beta \tag{2.2}$$

yields a branching ratio

$$B(l_\alpha \to l_\beta \gamma) \lesssim 2 \cdot 10^{-46} \qquad , \alpha \neq \beta \tag{2.3}$$

when the neutrino mass is chosen to be 2.5 eV. The best experimental value [1] is for muon decay

$$B(\mu \to e\gamma) \lesssim 1.2 \cdot 10^{-11} \tag{2.4}$$

so for all practical applications the charged leptons can safely be considered non-mixing. For interactions involving charged leptons, lepton numbers are hence conserved and the Standard Model agrees with experiments.

On the other hand, observing lepton number violation would mean that the neutrino lepton eigenstates are mixed, and the neutrinos thus have nonzero mass.

Mixing and neutrino oscillation

It has already been established that the interaction eigenstates of quarks are not identical to the mass eigenstates. The quarks are said to be mixed. The mixing between the lepton flavor eigenstates ν^α and mass neutrino eigenstates ν^i can be described as a rotation using a unitary $N \times N$ matrix

$$\nu^\alpha = U_{\alpha i}\nu'^i. \tag{2.5}$$

A convenient way of parameterizing this mixing matrix U for three generations is

$$U = \begin{pmatrix} c_{12}c_{13} & s_{12}c_{13} & s_{13}e^{-i\delta_{\mathcal{CP}}} \\ -s_{12}c_{23} - c_{12}s_{23}s_{13}e^{i\delta_{\mathcal{CP}}} & c_{12}c_{23} - s_{12}s_{23}s_{13}e^{i\delta_{\mathcal{CP}}} & s_{23}c_{13} \\ s_{12}s_{23} - c_{12}c_{23}s_{13}e^{i\delta_{\mathcal{CP}}} & -c_{12}s_{23} - s_{12}c_{23}s_{13}e^{i\delta_{\mathcal{CP}}} & c_{23}c_{13} \end{pmatrix} \tag{2.6}$$

where

$$c_{ij} \equiv \cos\theta_{ij} \tag{2.7}$$
$$s_{ij} \equiv \sin\theta_{ij} \tag{2.8}$$

and the non-vanishing phase has been chosen to be associated with mixing of the first and third generations.

An important characteristic of U is that if one of its elements is zero the phase δ can be rotated away by rephasing the fields. This is of course independent of the choice of parameterizing U (2.6). For example setting $s_{13} = 0$ making $U_{13} = 0$ removes all terms containing $e^{i\delta_{\mathcal{CP}}}$.[1] If any of the elements $U_{21}, U_{22}, U_{31}, U_{32}$ is zero the phase is already expressed in terms of the mixing angles. The phase can freely be multiplied to any of the mixing angles without changing the physical properties of U, but due to the smallness of θ_{13} it is most convenient to associate δ with θ_{13} when examining if any element of U is zero.

Using the Hamiltonian, ordinary quantum mechanics gives the time evolution of a quantum state as a super position of mass eigenstates

$$|\nu^\alpha\rangle_t = \sum_i U_{\alpha i}e^{-iE_it}\left|\nu'^i\right\rangle \tag{2.9}$$

where the ket on the right hand side can be substituted back into the flavor eigenstate basis

$$|\nu^\alpha\rangle_t = \sum_\beta\sum_i U_{\alpha i}e^{-iE_it}U^*_{i\beta}\left|\nu^\beta\right\rangle. \tag{2.10}$$

For relativistic neutrinos $p \gg m_i$, the energy can be expanded as

$$E_i \simeq p + \frac{m_i^2}{2E} \tag{2.11}$$

and in the two flavor case

$$U = \begin{pmatrix} \cos\theta & \sin\theta \\ -\sin\theta & \cos\theta \end{pmatrix} \tag{2.12}$$

[1] Often U_{1j} is denoted U_{ej}, $U_{2j} \to U_{\mu j}$ and $U_{3j} \to U_{\tau j}$.

which gives the oscillation probability

$$P_{\nu^\alpha \to \nu^\alpha} = |\langle \nu^\alpha | \nu^\alpha \rangle_t|^2 = 1 - \sin^2 2\theta \sin^2 \frac{m_i^2 - m_j^2}{4E} t \tag{2.13}$$

where unitarity of U and $\sin 2\theta = 2 \sin\theta \cos\theta$ was exploited. The notation

$$\Delta m_{ij}^2 \equiv m_i^2 - m_j^2 \tag{2.14}$$

is commonly used in literature. Using SI units, (2.13) can be written as

$$P_{\nu^\alpha \to \nu^\alpha} = 1 - \sin^2 2\theta \sin^2 \frac{1.267 \Delta m_{ij}^2 L}{E} \tag{2.15}$$

where Δm_{ij} is in eV, E in GeV and L in km.

Since neutrinos are highly relativistic, t is often substituted with the base line L, and the oscillation pattern is governed by the ratio L/E, which in accelerator experiments is controlled by experimental conditions.

Matter effects

As an electron neutrino traverses matter it can undergo *charged current* (CC) interactions, where the electron neutrino interacts with an electron or nucleon under the exchange of a W^- boson. If the final state also consists of an electron and an electron neutrino, the process can be mimicked by the exchange of a Z boson. This is called a *neutral current* (NC) event. The interactions $\nu_{\mu,\tau} + e^- \to \nu_{\mu,\tau} + e^-$ are limited to neutral current events and thus have smaller cross section than $\nu_e + e^- \to \nu_e + e^-$.

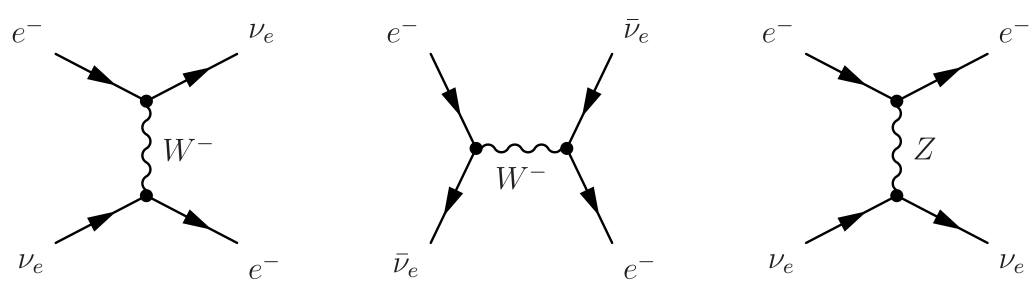

(a) CC, ν (b) CC, $\bar{\nu}$ (c) NC

Fig. 2.2: Feynman diagrams of charged current (CC) and neutral current (NC) neutrino interactions with electrons.

In the presence of the effective interaction Hamiltonian

$$\mathcal{H}_{eff} = \frac{G_F}{\sqrt{2}} \bar{\nu}_e \gamma_\mu (1 - \gamma_5) \nu_e \bar{e} \gamma_\mu (1 - \gamma_5) e \tag{2.16}$$

the electron neutrino receives an extra contribution $\sqrt{2}G_F n_e$ in the Schrödinger equation, where n_e is the electron number density in the media. Hence the angles in (2.12) are modified as [3]

$$\cos 2\tilde{\theta} = \frac{-2AE/\Delta m^2 + \cos 2\theta}{\sqrt{(2AE/\Delta m^2 - \cos 2\theta)^2 + \sin^2 2\theta}} \tag{2.17}$$

$$\sin 2\tilde{\theta} = \frac{\sin 2\theta}{\sqrt{(2AE/\Delta m^2 - \cos 2\theta)^2 + \sin^2 2\theta}} \tag{2.18}$$

where

$$A \equiv \sqrt{2}G_F n_e. \tag{2.19}$$

This creates a resonance at $2AE/\Delta m^2 = \cos 2\theta$ where the mixing is maximal and this resonance condition is usually expressed as a critical electron density

$$n_{e,critical} \equiv \frac{\Delta m^2}{2\sqrt{2}EG_F}\cos 2\theta. \tag{2.20}$$

If neutrinos are created in a very dense region where $n_e > n_{e,critical}$, and the density drops as the neutrino propagates though the matter, the neutrino can exit the region as a mass eigenstate if the density gradient is sufficiently small [3]

$$\frac{1}{n_e}\frac{\mathrm{d}n_e}{\mathrm{d}r} \ll \frac{\Delta m^2 \sin^2 2\theta}{2E\cos 2\theta} \tag{2.21}$$

to allow the neutrino conversion to be an adiabatic process [4]. Since the radial density profile of the sun is close to exponential and the electron density in the deep regions of the sun is very high, both the critical density and the adiabatic condition could be fulfilled in the sun, provided that the mass difference is small enough and the mixing angle is large. We will return to this phenomenon in section 2.1.2.

It is important to note that the matter effect gives fake $\mathcal{CP}$ violating effects for $\nu_\mu \to \nu_e$ oscillation compared to $\bar{\nu}_\mu \to \bar{\nu}_e$ oscillation as A changes sign for antiparticles. This can be understood in that the composition of matter in the universe is $\mathcal{CP}$ violated and the fake $\mathcal{CP}$ violation effect seen in matter is a trickle down effect of the matter–antimatter asymmetry. The two effects can however be separated since $2AE$ is proportional to the energy, but the eigenstate masses are constant with respect to energy, hence by comparing two similar experiments with different L/E base lines the problem can be untangled. This topic is discussed more extensively in chapter 3.

Atmospheric neutrinos

High energy particles are created in astrophysical processes, and when they enter Earth's atmosphere they often cause hadronic showers with pion and muon content. Those particles are unstable and will decay after some time, producing neutrinos. Such neutrinos are in the particle physics community referred to as *atmospheric neutrinos*.

The first atmospheric neutrinos were discovered in deep mines in 1965 in India and South Africa. The number of muons from cosmic rays were of the same order of magnitude as the number of muons produced in atmospheric neutrino interactions, but the experimenters noted a deficit in the muon neutrino flux. Reines was the first to suggest that neutrino oscillations caused the deficit, but the statistics were limited and large uncertainties in the calculated flux made the claims rather weak.

Many years later the same deficit was noted in other experiments, most notably the Kamiokande experiment, which found a zenith angle dependence in the ν_μ/ν_e ratio. This was followed up upon by the Super-Kamiokande experiment, which confirmed with compelling certainty that the muon neutrino flux is suppressed for particles going through the earth, while the electron neutrino flux is largely unchanged. A good fit using the neutrino oscillation hypothesis was achieved assuming maximal mixing and $\Delta m^2 \approx 2.2 \cdot 10^{-3}\ (\mathrm{eV})^2$, while the no oscillation hypothesis was inconsistent with their data [3]. This result was interpreted as $\nu_\mu \to \nu_\tau$ oscillation, since the data gave no indication of oscillation to ν_e. Furthermore the results favored matter effects as described in section 2.1.2 where ν_μ and ν_τ are equally affected. The sterile neutrino hypothesis was disfavored, and neutrino decay and neutrino decoherence theories were ruled out with 5.3σ and 4.8σ respectively [5].

Solar neutrinos

Neutrinos are continuously produced in the Sun in fusion processes. The Standard Solar Model is a very precise and accurate description of the Sun and similar stars, but the observed neutrino flux in the Davis chlorine tank experiment (1967–1994) was only about one third of what the Standard Solar Model had predicted. Thus the solar neutrino puzzle was born.

Despite many suggestions regarding systematical errors in the experiment, the problem persisted, and was later confirmed by Kamiokande. Most neutrinos are created through the *pp* chain, but these neutrinos typically have too low energy to be detected[2]. Instead much of the studies performed were focusing on neutrinos from the more energetic but also more rare ^{8}B neutrinos. The chlorine detector Davis used and also a later gallium detector, however, were in addition sensitive to low energy neutrinos. From these experiments, the flux suppression was found to vary with the neutrino energy in agreement with matter effects in the sun as described in section 2.1.2.

It was long thought that the lepton mixing angles would be small because the quark mixing angles were small, but the solar neutrinos supplied the researchers with a tool for testing the mixing angles. The suppression in $\nu_e \to \nu_e$ depends on the mixing angle and the energy, and from nuclear physics and the Standard Solar Model the neutrino energy spectrum is well known, thus the whole small mixing angle region was excluded to 95% confidence level in favor of nearly maximal mixing [3].

It is important to note that the flavor change occurring in the Sun is dominated by adiabatic matter effects, not neutrino oscillations. This makes the ^{8}B ν_e neutrinos radiated from the Sun 91% pure m_2 mass eigenstates [7], which naturally do not oscillate until they interact with matter again at Earth.

[2] The threshold is approximately 7 MeV in a Water Čerenkov detector.

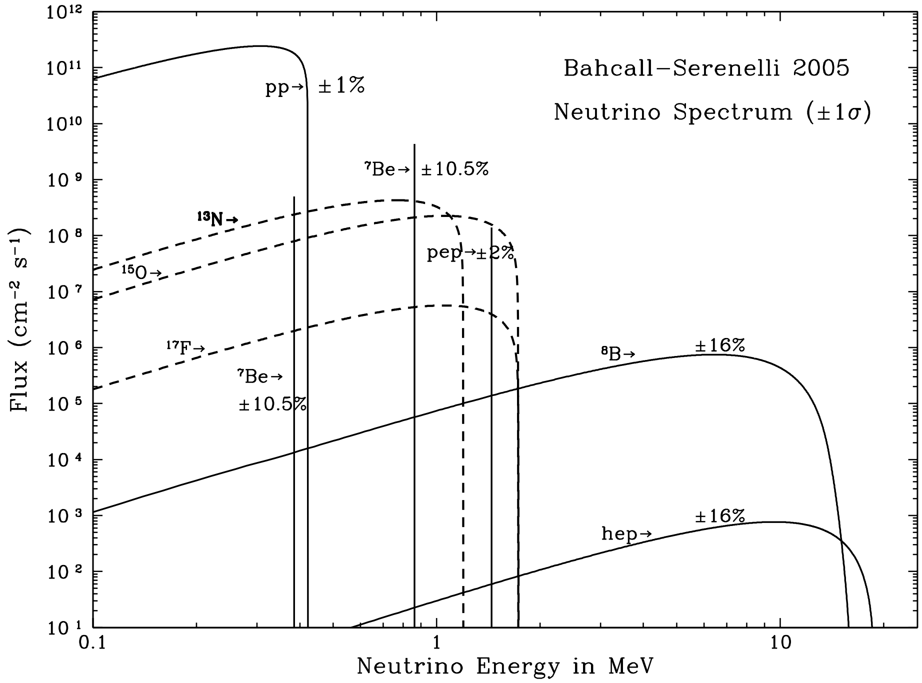

Fig. 2.3: The energy spectrum of solar neutrinos [6].

Reactor neutrinos

A tremendous amount of neutrinos, mainly $\bar{\nu}_e$, are produced in commercial nuclear reactors. Since these sources are both well measured and without cost to the particle physics community, they have been exploited to give powerful constraints on the solar neutrino mixing parameters, especially Δm^2_{21} and θ_{13}.

KamLAND was built to test LMA, *Large Mixing Angle*, solution in the solar neutrino sector. KamLAND uses a one kiloton liquid scintillator to detect antielectron neutrinos above 1.8 MeV [10], and is thus sensitive to neutrinos with too low an energy to be detected by Water Čerenkov detectors. It measures the neutrino rates from several nuclear reactors in Japan, and by taking full advantage of temporary shut downs of the reactors it provided a very precise measurement of Δ^2_{12} and θ_{12}. By observing the neutrino energy, it produced the worldâĂŹs first unambiguous evidence of the L/E dependence for positron appearance, thus confirming the neutrino oscillation hypothesis. See figure 2.4. The weighted average distance to the reactors is 180 km, so the experiment is sensitive to Δm^2 in the 10^{-5} eV^2 scale, hence oscillations between mass eigenstates 1 and 2. The SNO CC data strongly favored LMA, and KamLAND established LMA as a unique solution to the solar neutrino puzzle [11].

During 1998 and 1999 the CHOOZ experiment presented important reactor neutrino data. Similar to KamLAND the reactors deliver a flux of $\bar{\nu}_e$, but since the neutrino energy is approximately 3 MeV, and the distance is around 1 km, the experiment was sensitive

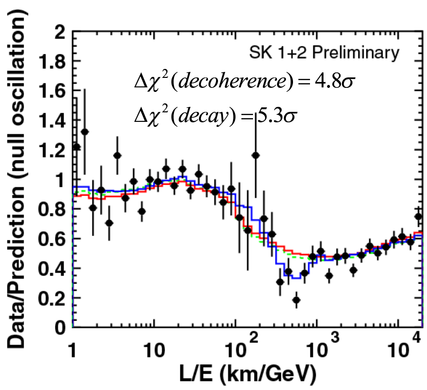

(a) SK

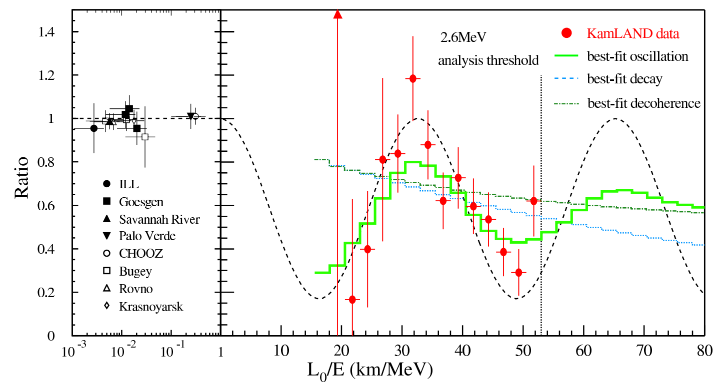

(b) KamLAND

Fig. 2.4: The ratio of the measured to the predicted neutrino flux is plotted as a function of $\frac{L}{E}$. In (a), the muon neutrino contribution to the atmospheric neutrino flux measured by the Super-Kamiokande collaboration [8] is shown. In (b), the antielectron neutrino contribution to the reactor neutrino flux measured by the KamLAND collaboration [9] is shown. At very short base lines, experimental errors obscure the neutrino oscillations. The neutrino-mixing model gives a good description of the data, while decoherence and neutrino decay hypothesis are inconsistent with the observations.

to Δm^2 of the order of 10^{-3} eV^2. Therefore CHOOZ was sensitive to oscillations between mass eigenstate 1 and a combination of eigenstates 2 and 3 [12]. The CHOOZ experiment did not find any evidence for $\bar{\nu}_e \longrightarrow \bar{\nu}_{\mu,\tau}$ oscillation, and the upper limit to the size of θ_{13} this implied still dominates the world average. Plans to measure θ_{13} in a future experiment named Double–Chooz exist. The experiment plans to take the first data in 2009 [13].

2.1.3 The open questions

Neutrino physics provides a rich field of studies with implications on the theory building of particle physics and our understanding of the Universe. There are many open questions

Tab. 2.1: Summary table of best fit values at 2σ, 3σ, and 4σ intervals (1 d.o.f.) for the three flavor neutrino oscillation parameters from global data including solar, atmospheric, reactor (KamLAND and CHOOZ) and accelerator (K2K and MINOS) experiments [5].

parameter	best fit	2σ	3σ	4σ
Δm^2_{21} [10^{-5} eV^2]	7.9	7.3–8.5	7.1–8.9	6.8–9.3
Δm^2_{31} [10^{-3} eV^2]	2.6	2.2–3.0	2.0–3.2	1.8–3.5
$\sin^2\theta_{12}$	0.30	0.26–0.36	0.24–0.40	0.22–0.44
$\sin^2\theta_{23}$	0.50	0.38–0.63	0.34–0.68	0.31–0.71
$\sin^2\theta_{13}$	0.000	≤ 0.025	≤ 0.040	≤ 0.058

that need to be answered, some of which we hope will be addressed by experiments in the near future.

Absolute mass scale

While neutrino oscillation have established that the neutrinos are massive and that the mass eigenstates have different masses, there is no theory or experiment which provides a good estimate of the absolute mass scale. Neutrino oscillation implies a minimum mass equal to the mass difference, but neutrino oscillation experiments are insensitive to the absolute value of the masses themselves. Direct mass measurements by the endpoint of the kinematic spectrum (as presented in section 2.1.1) give an upper bound which for now is too high to be of real value. Future experiments aimed to improve this upper bound, and experiments such as neutrinoless double beta experiments (see section 3.1), will push the upper limit closer to the measured mass differences.

Hierarchy

A second consideration is the so called mass hierarchy of the neutrino mass eigenstates. Most theories favor the *normal hierarchy* which assumes that the two lightest eigenstates are separated by a small mass difference and the third eigenstate is much heavier than the other two. In this case the "solar neutrinos" ν_1 and ν_2 are much lighter than ν_3 and the solar neutrinos are separated from ν_3 by the "atmospheric neutrino" mass difference. The other viable solution is the *inverted hierarchy* where instead ν_3 is much smaller than the solar neutrinos. See figure 2.5.

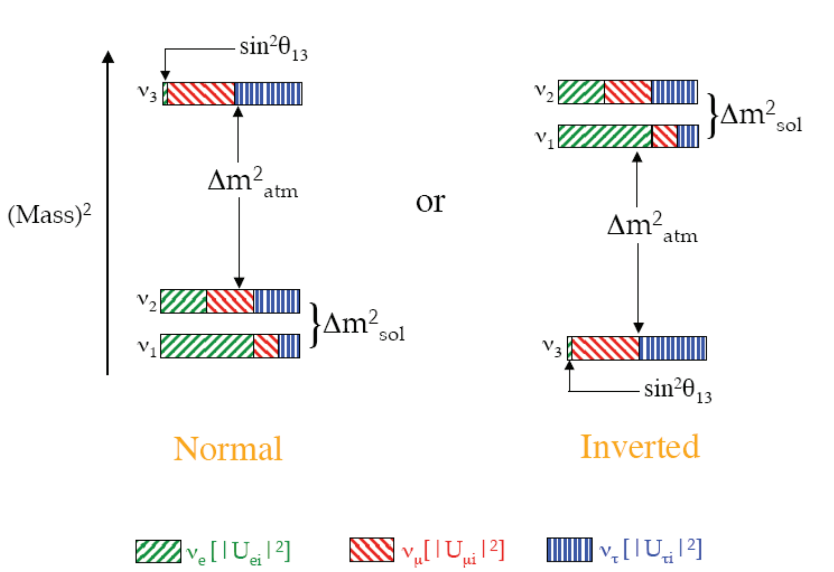

Fig. 2.5: The hierarchy of the neutrino mass eigenstates.

Majorana neutrinos

Are the neutrinos their own antiparticles? That would allow the See–Saw mechanism to explain the lightness of the neutrinos, but lepton number would no longer be conserved. Neutrino oscillations are independent of their Majorana nature, and the only way to determine whether the Majorana hypothesis is true is by a neutrinoless double beta experiment. This topic is discussed in section 2.2.2.

Charge parity violation

If θ_{13} is not zero, a complex phase factor would induce $\mathcal{CP}$ violations. This would be the first time $\mathcal{CP}$ is not conserved in the leptonic sector and would have implications for cosmology. The $\mathcal{CP}$ violations in neutrino oscillations is discussed in section 3.2, and later sections of the same chapter present possible experiments that could discover leptonic $\mathcal{CP}$ violation.

Leptogenesis

Originally the observed matter–antimatter asymmetry was explained by GUT baryogenesis, where heavy gauge bosons decayed while they decoupled from equilibrium in the early Universe. It was discovered that the masses of the gauge bosons were too small to satisfy the out-of-equilibrium condition. In the supersymmetric extension, however, large enough masses could be obtained, but were strictly constrained by the absence of observed proton decay.

Assuming that $B-L$ symmetry (section 2.2.2) is conserved at both the perturbative and non-perturbative level [5], a broken lepton number conservation would imply that baryon–antibaryon asymmetry would also be generated. However due to the sphaleron effect [3] above the electroweak scale, any baryon number generated while conserving $B - L$ is completely erased. In order to reproduce any matter–antimatter asymmetry, $B - L$ conservation must be violated. It is usually assumed that the asymmetry is a remnant of a leptonic $\mathcal{CP}$ violation, and the phenomenon is called *leptogenesis*.

If the See–Saw mechanism is correct, and the neutrino mixing matrix violates $\mathcal{CP}$, then the matter–antimatter asymmetry could be caused by $\mathcal{CP}$ violation in heavy right handed Majorana neutrino decays into charged Higgs bosons.

$\mathcal{CP}$ violation in the decay of heavy right handed Majorana neutrinos (see section 2.2.2)

$$B\left((\nu_L)^c \to \phi^+ l\right) \neq B\left((\nu_L)^c \to \phi^- \bar{l}\right) \tag{2.22}$$

where ϕ and l denote the Higgs boson and charged leptons respectively, can successfully reproduce the observed matter–antimatter asymmetry [5]. However, the theory requires a number of assumptions and depends on the so far not observed neutrino mass hierarchy.

Tab. 2.2: The families of fermions according to the Standard Model. The rows indicate the up-down like symmetry, while the columns indicate the generations and chirality. Since lepton numbers are conserved, all processes conserves the number of particles of a certain generation, for example a decaying muon produces one electron (charge conservation), one ν_μ and one $\bar{\nu}_e$ (lepton number conservation). Notice the absence of right handed neutrinos.

	1^{st} generation		2^{nd} generation		3^{rd} generation	
Lepton	$\nu_{e,L}$	-	$\nu_{\mu,L}$	-	$\nu_{\tau,L}$	-
	e_L	e_R	μ_L	μ_R	τ_L	τ_R
Quark	u_L	u_R	c_L	c_R	t_L	t_R
	d_L	d_R	s_L	s_R	b_L	b_R

Inflation

A problem in modern cosmology is that the cosmic microwave background from different regions of the Universe, which is a remnant of the very early Universe, is very uniform although these regions can never have been in touch with each other. Cosmologists usually assume that the initial Universe was pointlike, and there must have been a mechanism which inflated the Universe at some stage, thus allowing not causally connected regions to maintain a uniform temperature. It is widely believed that neutrinos played a leading role during the inflation, and there are theories [5] that require a gauge singlet with mass around 10^{13} GeV in order to obtain the observed density fluctuations, making a heavy right handed Majorana neutrino a natural candidate.

2.2 The origin of mass

The observation of a small but nonzero neutrino mass generated more questions than it answered. Among them, why have no right handed neutrinos been observed, why are the neutrino masses so small, what is the absolute mass scale of neutrinos, etc. These questions are only meaningful with a conceptual understanding of how particle masses are generated.

2.2.1 The Standard Model

In the Standard Model, the mass of a particle is the strength of its coupling between the fermion field and the Higgs field. Writing

$$\overline{\psi} = \psi^\dagger \gamma_0 \tag{2.23}$$

the mass term in the Lagrangian connects the left handed field with its right handed partner,

$$\mathcal{L}_D \sim m(\overline{\psi}_R \psi_L + h.c.) \tag{2.24}$$

where the two-component Weyl spinors are

$$\psi_L \equiv \frac{1-\gamma_5}{2}\psi = \begin{pmatrix} 0 \\ \eta \end{pmatrix} \tag{2.25}$$

and

$$\psi_R \equiv \frac{1+\gamma_5}{2}\psi = \begin{pmatrix} \chi \\ 0 \end{pmatrix} \tag{2.26}$$

so

$$\psi = \psi_L + \psi_R = \begin{pmatrix} \chi \\ \eta \end{pmatrix} \tag{2.27}$$

is the Dirac spinor. In the Standard Model there are no right handed neutrinos, so the neutrinos are necessarily massless. The experimental evidence of massive neutrinos cannot thus be included in the Standard Model.

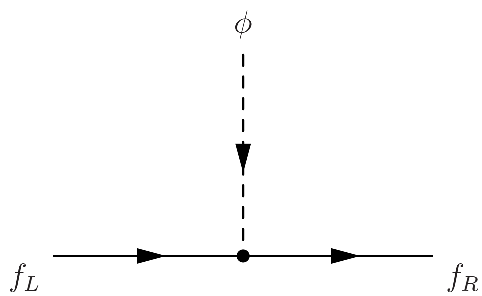

Fig. 2.6: Feynman diagram of a Higgs boson coupling to a fermion, thus giving the fermion mass. Note that the Higgs mechanism violates chirality symmetry, and that the Higgs boson has chirality -2.

The mass in equation (2.24) has its origin in the Higgs mechanism, which breaks the electroweak symmetry SU(2) × U(1). The simplest form of this theory is to take a Higgs field ϕ as a doublet,

$$\phi = \begin{pmatrix} \phi^+ \\ \phi^0 \end{pmatrix} \tag{2.28}$$

where ϕ^0 is a nonzero vacuum expectation value. Writing equation (2.24) with Yukawa couplings between leptons and the Higgs field

$$\mathcal{L}_Y = -f_e\overline{(\nu_e, e^-)_L}\begin{pmatrix} \phi^+ \\ \phi^0 \end{pmatrix} e_R^- + h.c. \tag{2.29}$$

gives the electron a mass

$$m_e = f_e\left\langle \phi^0 \right\rangle = f_e\frac{v}{\sqrt{2}} \tag{2.30}$$

where v is the vacuum expectation value given by the Fermi coupling constant G_F determined by measurements of muon decay [3],

$$v = (\sqrt{2}G_F)^{-1/2} \approx 246\ GeV. \tag{2.31}$$

Tab. 2.3: The families of fermions in the See-Saw model. The rows indicate the up-down like symmetry, while the columns indicate the mass eigenstates and chirality. The lepton and baryon eigenstates (generations) are superpositions of mass eigenstates. The right handed neutrinos have a very high mass which explains the small mass of the left handed neutrinos.

	1^{st} mass eigenstate		2^{nd} mass eigenstate		3^{rd} mass eigenstate	
Lepton	$\nu_{1,L}$	$\nu_{1,R} = (\nu_{1,L})^c$	$\nu_{2,L}$	$\nu_{2,R} = (\nu_{2,L})^c$	$\nu_{3,L}$	$\nu_{3,R} = (\nu_{3,L})^c$
	e_L	e_R	μ_L	μ_R	τ_L	τ_R
Quark	$u_{1,L}$	$u_{1,R}$	$u_{2,L}$	$u_{2,R}$	$u_{3,L}$	$u_{3,R}$
	$d_{1,L}$	$d_{1,R}$	$d_{2,L}$	$d_{2,R}$	$d_{3,L}$	$d_{3,R}$

2.2.2 Beyond the Standard Model

As (2.24) shows, the field only obtains a mass term if there exists both left handed and right handed particles. Since no right handed neutrinos have ever been observed, while the neutrino masses have been discovered, there is an anomaly in the Standard Model which requires special attention. This is in fact the only evidence of physics beyond the Standard Model. A very popular theory to explain this discrepancy is the assumption that the neutrinos are Majorana particles.

Majorana particles

In 1937 Majorana proposed that the neutrino is a self conjugate $\nu = \bar{\nu}$, except for helicity. The helicity flip is caused by a mass term that violates the lepton number conservation. This is very different from the Dirac neutrino which conserves the lepton number while flipping the helicity.

Using the notation

$$\psi^c = \mathcal{C}^\dagger \psi \mathcal{C} = \mathcal{C}\overline{\psi}^T \tag{2.32}$$

where $\mathcal{C}$ is the charge–conjugation operator and ψ^c is the charge–conjugate field, a relation between the left and right handed fields can be found (here explicitly derived)

$$\begin{aligned}
((\psi^c)_L)^c &= (\mathcal{C}\overline{\psi}_L^T)^c \\
&= ((i\gamma^0\gamma^2\gamma^0\psi^*)_L)^c \\
&= (\frac{1}{2}(1+\gamma^5)i\gamma^0\gamma^2\gamma^0\psi^*)^c \\
&= i\gamma^0\gamma^2(-i\frac{1}{2}(1+\gamma^5)\gamma^2\psi^*)^\dagger\gamma^0)^T \\
&= -\gamma^0\gamma^2\gamma^0\frac{1}{2}(1+\gamma^5)\gamma^{2*}\psi \\
&= \gamma^0\gamma^0\gamma^2\gamma^{2*}\frac{1}{2}(1-\gamma^5)\psi \\
&= \frac{1}{2}(1-\gamma^5)\psi = \psi_R,
\end{aligned} \tag{2.33}$$

where symmetry and commutation rules of the gamma matrices were used. Both Majorana and Dirac particles fulfill the Dirac equation

$$(i\gamma^{\mu}\partial_{\mu} - m)\psi(x) = 0 \tag{2.34}$$

but the Majorana particles also satisfies the Majorana condition

$$\psi = \psi^{c}. \tag{2.35}$$

For any fermion field the relation (2.33) is valid but here is a crucial difference between the Dirac fields and Majorana fields; the Dirac field does not satisfy (2.35), hence the left–handed component is independent of the right–handed component, while for a Majorana field

$$\psi_R = (\psi_L)^c \tag{2.36}$$

which can easily be proven using the equations above. The Majorana spinor only contains two independent fields. In other words a Majorana neutrino is its own antiparticle. This causes lepton number violation, and thus processes like neutrinoless double beta decay should be possible. The Lagrangian in this case would then be [3]

$$\mathcal{L}_M = i\overline{\psi}_L \not{\partial} \psi_L - \frac{M}{2}\overline{\psi}^c_L \psi_L + h.c. \tag{2.37}$$

where also the kinetic part is included. The mass term violates the lepton number conservation of the field, and the mass, M, is complex. However the phase of M can be absorbed into the phase of ψ_L.

In the Dirac case the neutrino mass is generated by the Higgs mechanism. The mass term in the Lagrangian is given by

$$\mathcal{L}_D = -\sum_{l,l'} \overline{\nu_{lR}} M^{D}_{ll'} \nu_{l'L} + h.c. \qquad (l = e, \mu, \tau) \tag{2.38}$$

where M^D is the complex 3×3 Dirac mass matrix.

This matrix can be diagonalized using unitary matrices V, U

$$M_D = V\hat{m}U^{\dagger} \tag{2.39}$$

defining the rotated states as

$$\nu_{lL} \equiv \sum_{k} U_{lk}\nu_{kL} \tag{2.40}$$

$$\nu_{lR} \equiv \sum_{k} V_{lk}\nu_{kR}. \tag{2.41}$$

Rewriting (2.38) using the mass eigenstates (2.40, 2.41) this give a diagonal mass term

$$\begin{aligned}
\mathcal{L}_D &= -\sum_{l,l'} \overline{\nu_{lR}} V \hat{m} U^\dagger \nu_{l'L} + h.c. \\
&= -\sum_{l,l'} \Big(\sum_k V_{lk} \nu_{kR} \Big)^\dagger \gamma^0 V \hat{m} U^\dagger \Big(\sum_k U_{l'k} \nu_{kL} \Big) \\
&= -\sum_k m_k \overline{\nu_{kR}} \nu_{kL}. \qquad (2.42)
\end{aligned}$$

From this result it is obvious that Dirac neutrinos can only have mass if both a left– and a right–handed field is present. The main difficulty in the Dirac neutrino hypothesis is the existence of the extremely small couplings m_k.

For neutral current interactions, the Noether current is

$$\begin{aligned}
j_\rho^{NC} &= \sum_{l=e,\mu,\tau} \overline{\nu_{lL}} \gamma_\rho \nu_{lL} + \ldots \\
&= \sum_{l=e,\mu,\tau} \sum_{k=1,2,3} \overline{\nu_{kL}} U_{lk}^\dagger \gamma_\rho U_{lk} \nu_{kL} + \ldots \\
&= \sum_{k=1,2,3} \overline{\nu_{kL}} \gamma_\rho \nu_{kL} + \ldots \qquad (2.43)
\end{aligned}$$

so no mixing occurs. Looking at the charged current

$$\begin{aligned}
j_\rho^{CC} &= 2 \sum_{l=e,\mu,\tau} \overline{l_{lL}} \gamma_\rho \nu_{lL} + \ldots \\
&= 2 \sum_{l=e,\mu,\tau} \sum_{k=1,2,3} \overline{l_{kL}} U_{lk}^{(l)\dagger} \gamma_\rho U_{lk}^{(\nu_l)} \nu_{kL} + \ldots \qquad (2.44)
\end{aligned}$$

where

$$U^{(l)\dagger} U^{(\nu_l)} \neq 1. \qquad (2.45)$$

Allowing the theory to extend beyond the Standard Model, Majorana particles are allowed to give contributions to the mass term. The Dirac-Majorana mass term is defined as

$$\mathcal{L}^{D+M} \equiv \mathcal{L}^D + \mathcal{L}_L^M + \mathcal{L}_R^M \qquad (2.46)$$

where

$$\begin{aligned}
\mathcal{L}^D &= -\sum_{r,l} \overline{\nu_{rR}} M_{rl}^D \nu_{lL} + h.c. \qquad (2.47) \\
\mathcal{L}_L^M &= -\frac{1}{2} \sum_{l,l'} \overline{(\nu_{lL})^c} M_{ll'}^L \nu_{l'L} + h.c. \qquad (2.48) \\
\mathcal{L}_R^M &= -\frac{1}{2} \sum_{r,r'} \overline{\nu_{rR}} M_{rr'}^R (\nu_{r'R})^c + h.c. \qquad (2.49)
\end{aligned}$$

Here l, l' run over left–hand flavor fields ($l = e, \mu, \tau$), and r, r' run over right–hand flavor fields.

By introducing the vector

$$n_L \equiv \begin{pmatrix} \nu_L \\ (\nu_R)^c \end{pmatrix} \tag{2.50}$$

where ν_L is the lepton eigenstates, (2.46) can be expressed in a more compact form:

$$\mathcal{L}^{D+M} = -\frac{1}{2}\overline{(n_L)^c} M^{M+D} n_L + h.c. \tag{2.51}$$

with the combined mass matrix

$$M^{M+D} = \begin{pmatrix} M^L & (M^D)^T \\ M^D & M^R \end{pmatrix}. \tag{2.52}$$

Similarly to the Dirac case, this matrix can be diagonalized using unitary operators. This transforms the flavor eigenstates (2.50) to the corresponding mass eigenstates ν_k. These fields all satisfy the Majorana condition (2.35), so a Lagrangian containing both Dirac and Majorana mass terms infers that all neutrinos are Majorana neutrinos.

In the case where the neutrinos are Majorana particles, two additional phases are should be added to the unitary matrix (2.6)

$$U_M = U_D \begin{pmatrix} e^{i\alpha_1/2} & 0 & 0 \\ 0 & e^{i\alpha_2/2} & 0 \\ 0 & 0 & 1 \end{pmatrix} \tag{2.53}$$

but since the Majorana phases are situated on the diagonal they do not give rise to any $\mathcal{CP}$ violation during neutrino oscillation.

The see-saw mechanism

To illustrate how neutrino masses are generated through the see-saw mechanism in an easily understandable manner, only one generation is considered. The field and the mass matrix are written as

$$n_L \equiv \begin{pmatrix} \nu_L \\ (\nu_R)^c \end{pmatrix}, \qquad M \equiv \begin{pmatrix} m_L & m_D \\ m_D & m_R \end{pmatrix} \tag{2.54}$$

where m_L, m_D and m_R are scalars. To simplify even more we assume $\mathcal{CP}$ invariance in the lepton sector in which case we get m_L, m_D and m_R are real parameters. The mass matrix M can be diagonalized and the diagonal matrix will then have the eigenvalues of M on the diagonal. The eigenvalues are

$$eig(M) = \frac{m_L + m_R}{2} \mp \frac{1}{2}\sqrt{(m_R + m_L)^2 + 4m_D^2} \tag{2.55}$$

and in if $m_R \gg m_L$ one can use the Taylor expansion

$$\sqrt{x+1} = 1 + \frac{x}{2} + \mathcal{O}(2) \tag{2.56}$$

which gives the eigenvalues

$$eig(M) \doteq \begin{cases} m_\nu & \approx & -\frac{m_D^2}{m_R} \\ m_N & \approx & m_R \end{cases} \tag{2.57}$$

where the minus sign can be removed by choosing the phase factor appropriately. The name See-Saw mechanism follows from the fact that if m_R is much larger than the other elements in the mass matrix, one mass eigenstate has a very large mass, while the other is very small; the larger one neutrino mass is, the smaller the other neutrino mass is. This model is attractive since it explains the small neutrino masses of the observed left handed neutrinos in a natural way, but this mechanism requires the neutrinos to be Majorana particles which is not yet confirmed experimentally.

If one assumes that the Dirac mass m_D is the similar to the mass of the top quark, and that the light neutrino mass m_ν is approximately 0.05 eV, then equation (2.57) gives a mass for the right handed neutrino of about 10^{15} GeV, which is very close to where physicists expect the GUT scale to reside. Should the See-Saw model be correct this allows indirect exploration of the Grand Unification by associating the left handed neutrinos with their right handed counterparts.

The Lagrangian for the See-Saw mechanism presented here[3] is expressed as follows once the heavy field has been integrated out

$$\mathcal{L}_{eff} = \frac{f^2}{2M}\phi^0\phi^0\overline{\nu_L^c}\nu_L \tag{2.58}$$

where f is the Yukawa couplings and ϕ^0 is the Higgs field.

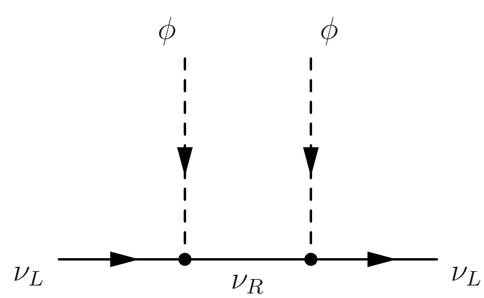

Fig. 2.7: Feynman diagram of type I see-saw mechanism.

[3] Most often called type I see-saw mechanism.

The Grand Unification

Physicists commonly believe that the electromagnetic, the weak and the strong forces unite at very high energies, and that the three gauge groups are merely low energy manifestations of a more fundamental symmetry. This idea is called the Grand Unification Theory, GUT.

The minimal GUT group that can contain the three gauge groups SU(3)×SU(2)×U(1) is SU(5), and it gives relations between the masses of leptons and quarks such that the down-like quarks have similar masses to charged leptons. However SU(5) theories predict that the proton is unstable, but the measured life time of the proton rules out SU(5) GUT. In order to solve the problem with the missing proton decays, one can either extend the theory to SO(10) which allows longer proton lifetime, or impose supersymmetry, SUSY, in SU(5).

Supersymmetric GUT shows good agreement [4] between the theoretical and experimental weak mixing angle θ_W [3],

$$\sin^2\theta_W = \begin{cases} 0.2312 \pm 0.0002 & (experiment) \\ 0.2273 \pm 0.0006 & (SU(5)SUSY) \end{cases} \tag{2.59}$$

and, in addition, the Higgs masses remain stable to radiative corrections. However the experimental limits on the proton lifetime leads to the fact that the colored Higgs mass $m_{H_c} > 2 \times 10^{17}$ GeV if the SUSY scale is < 1 TeV, which is required for making the Higgs mass stable. This is a problem since SUSY grand unification can only occur at $3.5 \times 10^{14} < m_{H_c} < 3.6 \times 10^{15}$ GeV [3].

Most GUT theories postulate that the baryon number minus the lepton number, $B-L$, is a conserved quantity. In order to limit the proton decay rate given by supersymmetric couplings, the so called *R-parity* is introduced, under which all Standard Model particles are even and all supersymmetric partners are odd. The scalar component of any chiral supermultiplet has the R-parity number

$$R = (-1)^{B-L} \tag{2.60}$$

while the fermions have the same number multiplied by -1. As a side effect, R-parity conservation implies that any couplings between light fermions and heavy fields which would violate $B-L$ are forbidden. Since the fermionic content of SUSY SU(5) is the same as the one in the Standard Model, $B-L$ asymmetry cannot be generated [14]. As previously mentioned, $B-L$ conservation must be violated in order to obtain baryogenesis [3], which rules out SUSY SU(5) as a GUT candidate. In SO(10) however, it is possible to include heavy right handed Majorana neutrinos, which could cause a $B-L$ asymmetry through decay of the heavy neutrinos.

In order to introduce massive neutrinos it is required to introduce an extra U(1) symmetry. SU(5)×U(1) is a subgroup of SO(10), and SU(5)×U(1) breaks into

$$\mathrm{SU(3)} \times \mathrm{SU(2)} \times \mathrm{U(1)_Y} \times \mathrm{U(1)_{B-L}} \tag{2.61}$$

[4] Qouting Fukugita&Yanagida [3] *"This weak mixing angle shows very good agreement with experiment, and this is taken as evidence supporting the presence of supersymmetry."* While the values are close, the standard deviations de facto suggest that the agreement is rather bad.

where $\mathrm{U(1)_Y}$ is the normal hyper charge and $\mathrm{U(1)_{B-L}}$ is a new symmetry between baryons and lepton numbers.

A more elegant theory uses

$$\mathrm{SU(3)} \times \mathrm{SU(2)_L} \times \mathrm{SU(2)_R} \times \mathrm{U(1)_{B-L}} \tag{2.62}$$

which breaks down at some high energy to the Standard Model where $\mathrm{SU(2)_R}$ disappears and the baryon–lepton symmetry is replaced by the hypercharge. The electric charge is here [15, 16]

$$Q = T_{3L} + T_{3R} + \frac{B-L}{2}. \tag{2.63}$$

The left–right symmetry model, also known as the chiral symmetry model, assumes that the neutrinos are Majorana particles and the leptons

$$\psi_L = \begin{pmatrix} \nu_L \\ e_L \end{pmatrix}, \qquad \psi_R = \begin{pmatrix} \nu_R \\ e_R \end{pmatrix} \tag{2.64}$$

have the $\mathrm{SU(2)_L} \times \mathrm{SU(2)_R} \times \mathrm{U(1)_{B-L}}$ representation numbers $(1/2, 0, -1)$ and $(0, 1/2, -1)$ respectively [17].

In this left–right symmetric model the parity violation is thus only a low energy phenomenon caused by the suppression of right handed weak currents. This model predicts right handed weak bosons whose masses are related to the masses of the neutrinos [16, 17].

$$m_{\nu_l} = \frac{m_l^2}{g m_{W_R}} \qquad , \; l = (e, \mu, \tau) \tag{2.65}$$

Equation (2.65) can be used to predict the mass of the right handed weak bosons; choosing $m_{\nu_e} \leq 1.5$ eV, gives $m_{W_R} \geq 300$ GeV, while using the assumption $m_{\nu_e} \approx 0.05$ eV of page 23 gives an upper limit of $m_{W_R} \approx 9$ TeV. If the spontaneous parity breaking of the left–right model is due to a pair of bidoublet Higgs fields $(0, 1, 2)$ and $(1, 0, 2)$, in addition to the Standard model doublet Higgs field $(1/2, 1/2, 0)$, there are two very massive weak bosons, the previously mentioned W_R and the neutral Z_R, where $m_{Z_R} \approx m_{W_R}$ [15]. The large mass of the right handed weak bosons is a natural explanation for the $V + A$ suppression compared to $V - A$. Hopefully these new bosons are not too heavy for LHC and future high energy physics experiments, and that their signals are not masked by background or misinterpreted as super symmetry.

Since the quarks

$$q_L = \begin{pmatrix} u_L \\ d_L \end{pmatrix} \qquad , \; q_R = \begin{pmatrix} u_R \\ d_R \end{pmatrix} \tag{2.66}$$

have representation numbers $(1/2, 0, 1/3)$ and $(0, 1/2, 1/3)$, respectively [17], the non-integer $B-L$ property ensures that the parity violating Higgs bidoublets do not couple to quarks. Since the mass generating neutral Higgs field carries no $B - L$ charge, the quarks can still couple to it, allowing quarks to be massive.

3. NEUTRINO BEAMS AND DETECTORS

As chapter 2 showed, several important fundamental questions regarding neutrinos remain to be answered. One of the most important outcomes are the predictions and suggestions for experiments which can prove or disprove the theoretical concepts. The most important physical processes which such particle physics experiments rely on for detection and characterization are presented in chapter 5. This chapter presents some of the neutrino experiments which have been proposed for the next decades, with the focus on future neutrino beams and associated detectors.

3.1 Lepton number violating beta decays

The neutrinoless double β decay experiments provide vital information on the Majorana nature of the neutrinos. For some isotopes where single β decay

$$(A, Z) \rightarrow (A, Z+1) + e^- + \bar{\nu}_e \quad \text{single } \beta \text{ decay} \tag{3.1}$$

is forbidden, the nucleus can decay by emitting two electrons at once, and hence also two antineutrinos.

$$(A, Z) \rightarrow (A, Z+2) + 2e^- + 2\bar{\nu}_e \quad \text{double } \beta \text{ decay} \tag{3.2}$$

This process is shown in figure 3.1(a). For double β decay to be possible the mass of the (A, Z) must be larger than $(A, Z+2)$. There are only 35 $2\beta^-$ isotopes known in nature, though $2\beta^+$ isotopes also exists.

If the neutrinos are Majorana particles, a related yet different process can occur called *neutrinoless double beta decay ($0\nu2\beta$)*. Since a Majorana neutrino is its own antiparticle the neutrinos can form a lepton number violating current between the two vertices, acting as an intermediary force carrier. The total energy of the two electrons would hence be exactly the energy released from the binding energy of the nuclei, forming a sharp energy spectrum which could be detected in an experiment. The rare nature of these events however — the half life is larger than 10^{20} years — makes the experiments very sensitive to background and difficult to conduct.

Super Symmetry and other new physics could also produce neutrinoless double beta decay, suggesting that it would not be possible to tell what process caused the suppression of the two neutrinos. In 1982 the Schechter-Valle theorem [18] (also known as the "Black Box Theorem") was published which states that independent of the mechanism which caused the $0\nu2\beta$ reaction, Majorana neutrino mass will appear in a higher order. Thus should $0\nu2\beta$ be observed, the Majorana property of the neutrinos would be proven. To

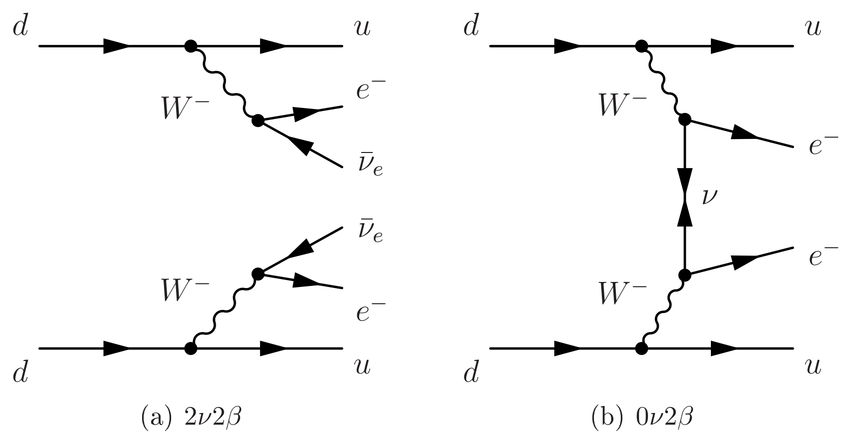

Fig. 3.1: Feynman diagrams (a) double beta decay, and (b) neutrino less double beta decay. While (a) conserves lepton number, (b) violates lepton number conservation by 2 through the exchange of a Majorana neutrino.

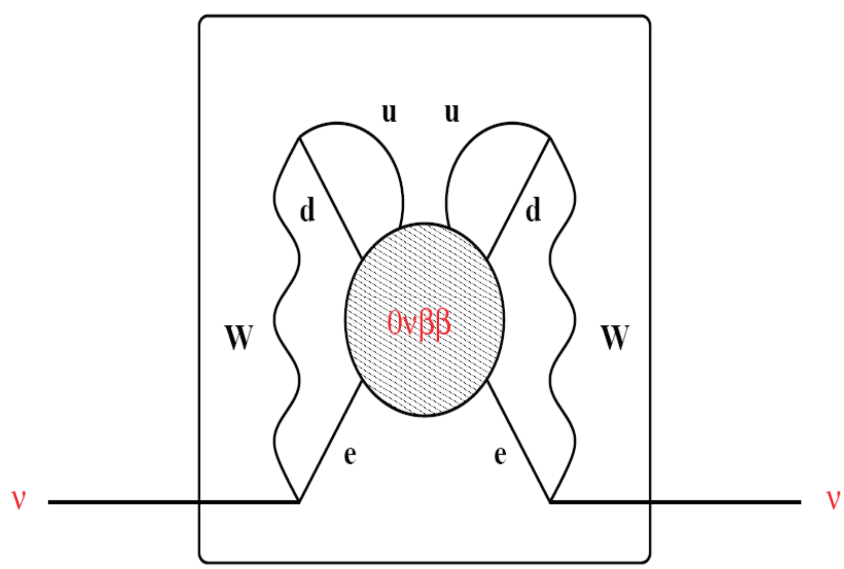

Fig. 3.2: The "Black Box Theorem" states that neutrinoless double beta decay implies a nonvanishing Majorana neutrino mass term, independent of the exact process causing the lepton number violating decay.

prove this [19] one uses the fact that u, d, e are massive particles and that there exists a weak interaction Lagrangian

$$\mathcal{L} = \frac{g}{\sqrt{2}} \left(\bar{\nu}_L \gamma^\mu (1-\gamma_5) e_L + \bar{u}_L \gamma^\mu (1-\gamma_5) d_L\right) W_\mu^+ + h.c. \tag{3.3}$$

Also note that the fundamental process for neutrinoless double beta decay is

$$d + d \rightarrow u + u + e + e \tag{3.4}$$

with the exact process which produces the neutrinoless double beta decay unknown. Since (3.3) allows $d \rightarrow u$ and $e \rightarrow \nu_e$ through the exchange of a W boson, processes like the one shown in figure 3.2 are allowed. This generates a Majorana neutrino mass proportional to $\bar{\nu^c_{eL}} \nu_{eL}$ just like in the previous chapter. However the neutrino mass could be cancelled by other processes while maintaining the possibility of neutrinoless double beta decay. A cancellation to all orders would require a discrete symmetry, which can be described as

$$\nu_{eL} \rightarrow \eta_\nu \nu_{eL} \tag{3.5}$$
$$q_L \rightarrow \eta_q q_L \tag{3.6}$$
$$e_L \rightarrow \eta_e e_L \tag{3.7}$$
$$W_L^+ \rightarrow \eta_W W_L^+ \tag{3.8}$$

where η_i are phase factors. If (3.4) is allowed,

$$\eta_u^2 \eta_d^{*2} \eta_e^2 = 1 \tag{3.9}$$

and (3.3) implies

$$\eta_d \eta_u^* = \eta_W = \eta_e \eta_\nu^* \tag{3.10}$$

while preventing the existence of a Majorana mass term would require

$$\eta_\nu^2 \neq 1. \tag{3.11}$$

However, using the conditions (3.9) and (3.10) it follows that

$$\eta_\nu^2 = 1 \tag{3.12}$$

which proves that

- if there is no Majorana neutrino mass term, neutrinoless double beta decay cannot occur
- if neutrinoless double beta decay occur, the neutrinos are Majorana particles

regardless of the exact process in the "black box". While this proof was only considering electron neutrinos, Hirsch et al [20] have extended the proof of the "Black Box Theorem" to incorporate mixing between neutrino flavors.

Since experiments like KATRIN are measuring the neutrino mass directly from β decay, neutrinoless double beta decay experiments can also supply information on the neutrino masses. Using (2.1) with the parameterization from (2.6), KATRIN measures

$$m_{\bar{\nu}_e} = \left(\sum_i |U_{ei}|^2 m_i^2 \right)^{1/2} = \left(\cos^2\theta_{13} \left(m_1^2 \cos^2\theta_{12} + m_2^2 \sin^2\theta_{12} \right) + m_3^2 \sin^2\theta_{13} \right)^{1/2} \quad (3.13)$$

while neutrinoless double beta experiments measure a coherent sum over all the different Majorana neutrino masses m_i weighted by their mixings with the electron flavor eigenstate. Using the notation from (2.53)

$$\left| m_{(0\nu 2\beta)} \right| = \left| \sum_i U_{ei}^{*2} m_i \right| = \left| \cos^2\theta_{13} \left(m_1 e^{i\alpha_1} \cos^2\theta_{12} + m_2 e^{i\alpha_2} \sin^2\theta_{12} \right) + m_3 \sin^2\theta_{13} \right| \quad (3.14)$$

it is clear that the neutrinoless double beta experiments are sensitive to the complex Majorana phases. However as the equation is underdetermined by the experiments, the two phases cannot be disentangled. It is possible that the effective neutrino mass is zero due to a resonance between the terms in (3.14), induced by nonzero Majorana phases.

The effective Majorana neutrino mass $\langle m_{(0\nu 2\beta)} \rangle$ is estimated by using the half life as observable,

$$\frac{1}{T_{1/2}} = P N^2 \left(\frac{\langle m_{(0\nu 2\beta)} \rangle}{m_e} \right)^2 \quad (3.15)$$

where P is a calculable phase space integral and N are nuclear transition matrix elements.

Several $0\nu 2\beta$ experiments are either running or in development at the moment. One experiment claims to have seen lepton number violating double beta decay with a confidence level of 4.2σ [21]. The same experiment gives

$$0.1 \text{ eV} < \langle m_{(0\nu 2\beta)} \rangle < 0.9 \text{ eV} \quad (3.16)$$

at 99.73% confidence level by analysis of the half life of ^{76}Ge [21]. Future experiments will investigate the claims further.

3.2 $\mathcal{CP}$ violation in neutrino oscillation

In the previous chapter evidence of nonzero neutrino mass based on the observation of neutrino mixing was presented. In addition the mixing angles were determined or confined to small parameter regions through neutrino oscillation or matter effects in the Sun. The phase δ present in the mixing matrix does not affect the mass of the neutrinos, but will imply that $\mathcal{CP}$ is not conserved, provided that all elements of the mixing matrix are nonzero. The $\mathcal{CP}$ asymmetry

$$A_{\mathcal{CP}} = \frac{P(\nu_\alpha \to \nu_\beta) - P(\bar{\nu}_\alpha \to \bar{\nu}_\beta)}{P(\nu_\alpha \to \nu_\beta) + P(\bar{\nu}_\alpha \to \bar{\nu}_\beta)} \quad (3.17)$$

is often used as the $\mathcal{CP}$ violation observable. The most common experiments would have $(\alpha = \mu, \beta = e)$ (Super beam) or $(\alpha = e, \beta = \mu)$ (Beta beam or Neutrino Factory) or $(\alpha = \mu, \beta = \tau)$ (Neutrino Factory).

As discussed in section 2.1.2, the presence of matter creates a fake $\mathcal{CP}$ violation due to the $\mathcal{CP}$ asymmetry of the medium. Using the parameterization

$$\begin{aligned}
X_\mu^\pm &= \sin^2\theta_{23}\left(\frac{\Delta_{23}}{B^\mp}\right)^2 \sin^2\left(\frac{B^\mp L}{2}\right) && (3.18)\\
Y_c^\pm &= \sin(2\theta_{23})\sin(2\theta_{12})\frac{\Delta_{12}}{A}\frac{\Delta_{23}}{B^\mp}\sin\left(\frac{AL}{2}\right)\sin\left(\frac{B^\mp L}{2}\right)\cos\frac{\Delta_{23}L}{2} && (3.19)\\
Y_s^\pm &= \sin(2\theta_{23})\sin(2\theta_{12})\frac{\Delta_{12}}{A}\frac{\Delta_{23}}{B^\mp}\sin\left(\frac{AL}{2}\right)\sin\left(\frac{B^\mp L}{2}\right)\sin\frac{\Delta_{23}L}{2} && (3.20)\\
Z_\mu &= \cos^2\theta_{23}\sin^2(2\theta_{12})\left(\frac{\Delta_{12}}{A}\right)^2 \sin^2\left(\frac{AL}{2}\right) && (3.21)
\end{aligned}$$

where X is the atmospheric term, Y is the interference term and Z is the solar term, and where

$$\begin{aligned}
\Delta_{ij} &\equiv \frac{\Delta m_{ij}^2}{2E} && (3.22)\\
B^\mp &\equiv |A \mp \Delta_{23}| && (3.23)
\end{aligned}$$

and A is defined in (2.19), the probability of $\nu_e \to \nu_\mu$ oscillation is

$$P_{e\mu}^\pm = X_\mu^\pm \sin^2(2\theta_{13}) + (Y_c^\pm \cos\delta \mp Y_s^\pm \sin\delta)\sin(2\theta_{13}) + Z_\mu \qquad (3.24)$$

under the assumptions

$$\begin{aligned}
\frac{\Delta_{12}}{\Delta_{13}} &\ll 1 && (3.25)\\
\sin\theta_{13} &\ll 1 && (3.26)
\end{aligned}$$

where $\mp$ refers to neutrinos and antineutrinos respectively [22]. This oscillation channel is obviously very sensitive to θ_{13}, and in addition it is sensitive to the $\mathcal{CP}$ violating phase δ. The presence of Δ_{23} in $Y^\pm$ infers that the channel is in addition sensitive to the sign of the atmospheric mass splitting. While $X_\mu^\pm$ contains a $\sin^2\theta_{23}$ term, Z_μ is proportional to $\cos^2\theta_{23}$, which means that this oscillation channel should be able to determine in what octant θ_{23} resides.

With the same notation, the only term in the numerator of (3.17) which does not cancel when $A \to 0$ (vacuum limit) is the Y_s term. The strongest term in the denominator is the X_μ term, giving the approximation

$$\begin{aligned}
A_{\mathcal{CP}} &\approx \frac{1}{2}\frac{Y_s\sin(2\theta_{13})\sin\delta_{\mathcal{CP}}}{X_\mu\sin^2(2\theta_{13}) + Y_c\sin(2\theta_{13})\cos\delta_{\mathcal{CP}} + Z_\mu} \approx \\
&\approx \frac{1}{2}\frac{\sin(2\theta_{12})\sin(2\theta_{23})\sin(2\theta_{13})\sin(\frac{\Delta_{12}L}{2})\sin(\frac{\Delta_{23}L}{2})\sin(\frac{\Delta_{13}L}{2})\sin\delta_{\mathcal{CP}}}{\sin^2(2\theta_{13})\sin^2(\theta_{23})\sin^2(\frac{\Delta_{23}L}{2}) + \sin^2(2\theta_{12})\cos^2(\theta_{23})\sin^2(\frac{\Delta_{12}L}{2}) + \mathcal{O}} && (3.27)
\end{aligned}$$

which shows that should any of the mixing angles or the mass differences be zero, the $\mathcal{CP}$ violation would vanish.

Due to its many virtues, the $\nu_e \to \nu_\mu$ oscillation channel is often called the *golden channel*. However, the ability to measure all these unknown parameters comes at a price of degeneracies. To solve the degeneracies of the golden channel one can either improve the detector or use an additional oscillation channel. A third alternative, the magic baseline, will be discussed in section 3.2.1.

With the notation

$$X_\tau^\pm = \cos^2\theta_{23}\left(\frac{\Delta_{23}}{B^\mp}\right)^2 \sin^2\left(\frac{B^\mp L}{2}\right) = \frac{\cos^2\theta_{23}}{\sin^2\theta_{23}} X_\mu^\pm \tag{3.28}$$

$$Z_\tau = \cos^2\theta_{23}\sin^2(2\theta_{12})\left(\frac{\Delta_{12}}{A}\right)^2 \sin^2\left(\frac{AL}{2}\right) = \frac{\sin^2\theta_{23}}{\cos^2\theta_{23}} Z_\mu \tag{3.29}$$

$$\tag{3.30}$$

the oscillation $\nu_e \to \nu_\tau$ can be written [22]

$$P_{e\tau}^\pm = X_\tau^\pm \sin^2(2\theta_{13}) - (Y_c^\pm \cos\delta \mp Y_s^\pm \sin\delta)\sin(2\theta_{13}) + Z_\tau. \tag{3.31}$$

This channel has the same sensitivities as the golden channel, but the minus sign in front of the parenthesis gives a different correlation between δ and θ_{13}. The disadvantage of this channel is that the tau lepton must be detected before it decays into a muon, which adds to the difficulty of designing the detector. It is thus named the *silver channel*. A channel similar to the silver channel is the "*forgotten channel*", which is the oscillation $\nu_\mu \to \nu_\tau$. If the neutrinos were created by a muon beam, the final state muon in the silver channel has a charge which is the opposite sign of the muon beam, while the "forgotten channel" will have a final state muon with the same sign as the particles in the muon beam. The *platinum channel* is the oscillation $\nu_\mu \to \nu_e$, which also has a different δ to θ_{13} correlation, but the electron neutrino content of a neutrino beam created from muon decay infers that the charge sign of the final state electron must be determined, which is experimentally challenging.

3.2.1 Combinations of baselines

As (2.6) shows the elements of the mixing matrix are combinations of several parameters, the most notorious is the $U_{e3} = \sin\theta_{13} e^{-i\delta_{CP}}$ element. This leads to degeneracies when measuring a parameter which must be solved by performing multiple oscillation experiments. One option is to measure several different oscillation channels with the same facility, but any charge determination requires magnetic fields, and electrons are particularly difficult since they induce electromagnetic showers. For tau lepton identification the short lifetime requires dedicated fine grained vertex detectors. The neutrino detectors are discussed in section 3.6.

By using the same facility but with different baselines, the integrated electron density between the neutrino production and the detectors is different, hence the matter effects

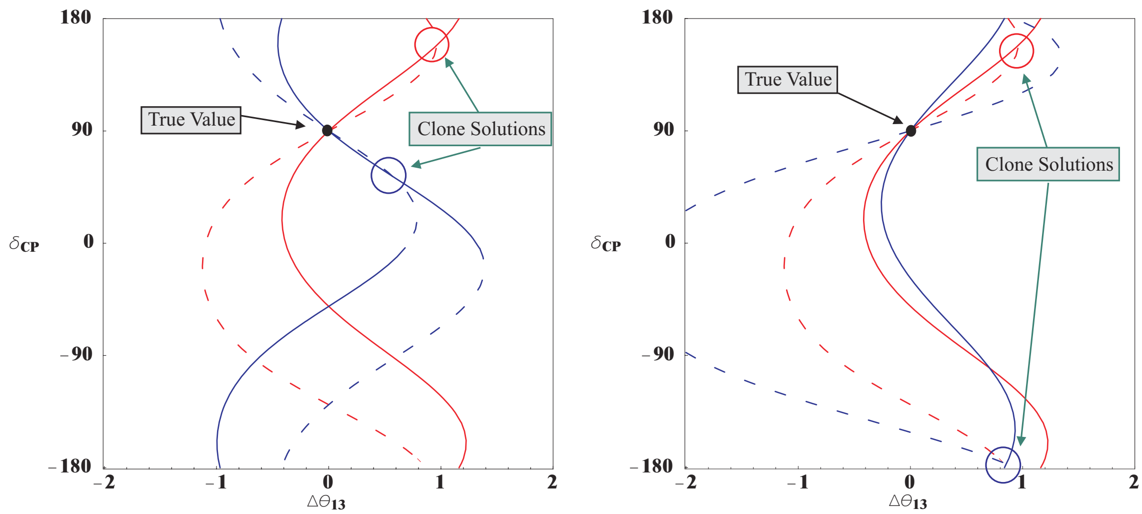

(a) Different channels (b) Different baselines

Fig. 3.3: Solving the intrinsic degeneracy using: (a) same L/E, but two different oscillation channels (i.e., golden and silver); (b) same oscillation channel, but two different baselines. From reference [23].

(see section 2.1.2) for the two neutrino beams are different. This is illustrated in figure 3.3. By choosing the neutrino oscillation baseline to be [5]

$$L_{magic} \simeq \frac{32726}{\rho[\mathrm{g/cm^3}]} \simeq 7250 \text{ km} \tag{3.32}$$

a resonance effect similar to (2.19) occurs where the $\mathcal{CP}$ violating phase δ_{CP} is cancelled by matter effects. This baseline is henceforth named *the magic baseline*, and is very useful for measuring θ_{13} and the mass hierarchy through $sign(\Delta m^2_{31})$ as the experiment is completely insensitive to $\mathcal{CP}$ violation. A second detector at approximately 3000 km (1500–5000 km), where the sensitivity to U_{e3} is large, will provide a good measurement of the $\mathcal{CP}$ violating phase since θ_{13} is already constrained by the magic baseline data.

3.3 Conventional neutrino beams

Neutrinos from conventional neutrino beams are created in the decay of charged pions, which in turn are produced by proton interaction with a target and are charge selected using one or more magnetic horns [24]. An additional contribution is given by decays of charged kaons, but since both π^+ and K^+ predominately decay into μ^+ and ν_μ, the neutrino beam is dominated by ν_μ. The main ν_e contamination comes from $K^+ \rightarrow \pi^0 e^+ \nu_e$, $K^0_L \rightarrow \pi^+ e^- \bar{\nu}_e$ or $\pi^- e^+ \nu_e$, and at low energies μ^+ decays. The contributions from $\pi^+ \rightarrow e^+ \nu_e$ are negligible [3]. Since the kaon production increases with energy, conventional neutrino beams have a problem with electron neutrino contamination which becomes worse with increased primary proton energy.

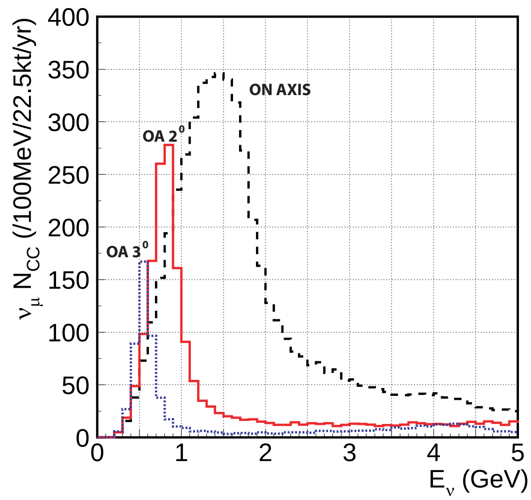

Fig. 3.4: T2K neutrino beam energy spectrum for different off-axis angle θ.

When running the experiment with π^+ the neutrino beam will primarily consist of ν_μ contaminated by $\bar{\nu}_\mu$, ν_e and $\bar{\nu}_e$. This contamination limits the detection power of the $\nu_\mu \rightarrow \nu_e$ oscillation, and the background becomes worse with higher energy as ν_e production increases with energy, mainly due to kaon production in the target.[1] As figure 3.4 shows, the neutrino beam has a more narrow energy width at large angles from the beam axis, which can be used to deal with the ν_e contamination and tune the beam to the oscillation maximum.

3.3.1 Super beam

Super beam experiments are a natural development of the existing neutrino beam experiments. One of the problems conventional neutrino beams are suffering from is the irreducible content of several neutrino flavors in the beam, due to the decay channels of pions. As described in section 3.3, a cleaner separation between neutrino flavors can be obtained by running the beam slightly off axis. The main problem with an off axis beams is that the flux at the detector is severely reduced. Super beam experiments counter this draw back by increasing the intensity of the beam. To achieve this proton drivers in the range of 2-5 MW will be utilized [5].

3.3.2 T2K

The next generation neutrino beam experiment with many features of the future Super beams experiments is the T2K experiment in Japan, which under construction. Neutrinos are created from decaying pions at J-PARC in Tokai, and are detected using the 50 kton SuperKamiokande detector in Kamioka as the far detector. The distance between the pion production and SuperKamiokande is 285 km. Pions are created using a 30 GeV proton

[1] The ν_e content is $\approx 0.1\%$ at low energy but $\approx 3\%$ at higher energies [3].

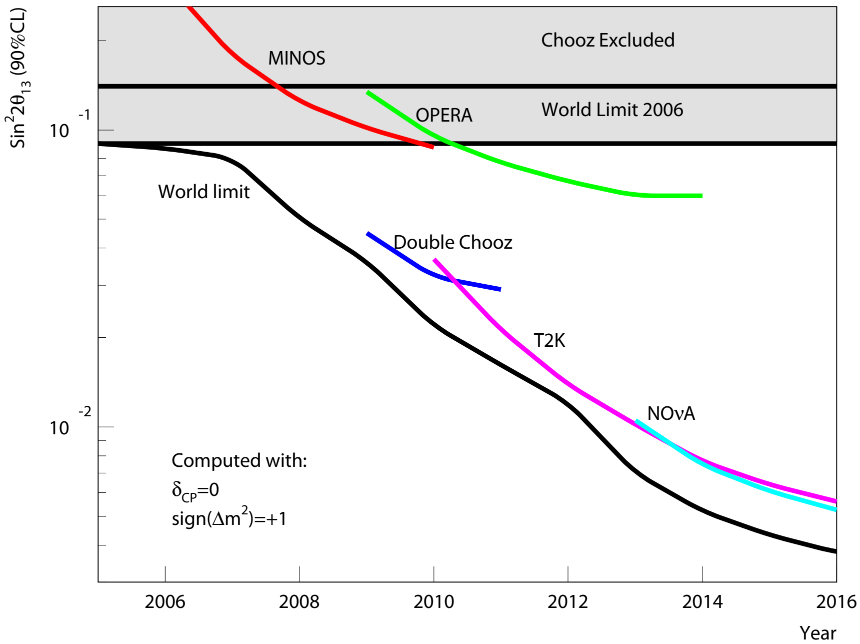

Fig. 3.5: Projected evolution of the world limit on $sin^2 2\theta_{13}$ at 90% CL for near future neutrino experiments [5].

beam whose power is expected to reach 0.75 MW in a first phase. The experiment could be upgraded at a later stage[2] with increased power of 4 MW, 50 GeV proton energy and a megaton detector (Hyper-Kamiokande).

The main physics goals of T2K are to

- improve the accuracy on the θ_{23} and Δm^2_{23} measurements
- search for the $\nu_\mu \rightarrow \nu_e$ appearance, and thus improve the sensitivity of θ_{13} by an order of magnitude compared to existing results.

The first of these points will rely on ν_μ disappearance due to oscillations, while θ_{13} will rely on ν_e appearance. The latter suffers from the ν_e background in the beam and π^0 production in neutral current interactions. The experiment will for these reasons run 2.5° off axis in order to obtain a more narrow energy spread, and the electron like events will be required to correspond to the neutrino oscillation maximum $0.35 < E_\nu^{rec} < 0.85$ GeV. Since the expected neutrino rates in the far detector is model dependent, a near detector is placed 280 m downstream of the proton target. In addition to the off axis near detector ND280, an on axis beam monitoring detector called INGRID will be installed in the same pit. While INGRID will monitor the intensity, direction and mean energy, ND280 will measure the ν_μ and ν_e spectra and study the neutrino cross sections to predict the response of the far detector.

[2] This Phase II could start at 2015 [25].

T2K Phase I will start operating in 2009 [25], and since it has the potential to measure a nonzero θ_{13}, its findings will heavily influence the choice of futures neutrino beams.[3]

ND280

The ND280 detector consists of three TPC trackers, a dedicated π^0 detector and two *Fine Grained Detectors* (FGD), surrounded by an electromagnetic calorimeter, which in turn is encased in a 0.2 T magnet.

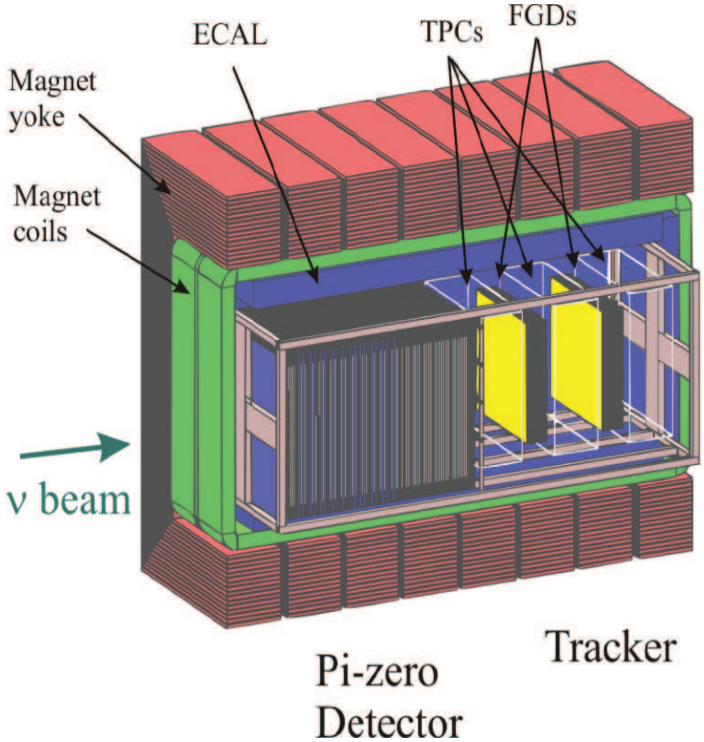

Fig. 3.6: The ND280 off axis near detector in the T2K experiment.

The π^0 detector consists of triangular extruded scintillator bars, interleaved with 0.6 mm lead sheets for photo conversion. The upstream section of the detector has in addition layers of water, which provides a total water target of 1700 kg. The gives an expected 17000 π^0 events produced in the water during one year of operation.

Tracking in ND280 is performed by the three TPCs and the two FGDs. The TPCs are 2.5×2.5 m transversally and 1.0 m along the beam direction. The ionization electrons are drifted to the sides using 200 V/cm, and a central cathode will divide the drift space in two halves in order to limit the maximum drift length to approximately one meter. Based on studies performed for the MICE TPG (section 6.3.1) the gas was chosen to be 95% Ar, 2% CF_4, 3%iC_4H_{10}, which has a transverse diffusion of 280 $\mu\text{m}\sqrt{\text{cm}}$ at 0.2 T. The drift electrons are amplified by *micromegas*, which is a mesh positioned 100 μm above the pad

[3] Another experiment, *NOνA*, will have similar experimental strengths and a similar run plan.

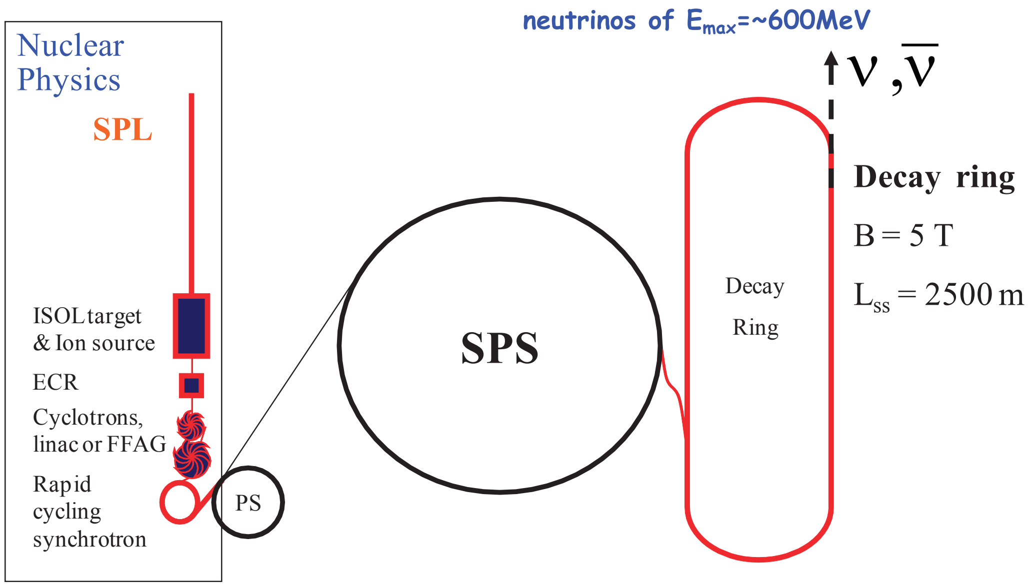

Fig. 3.7: The general layout of a Beta beam. The left section is similar to the EURISOL project [26], while the central part is already existing at CERN. A very high γ Beta beam would need to replace the central section. The decay ring would have to be built.

plane. The small distance allows very strong fields (40 to 70 kV/cm) to be used while keeping the voltage low. The 124000 pads are square and read out individually.

The FGDs use $0.96\times0.96\times184.3$ cm extruded scintillator bars, and provides the target mass for neutrino interactions as well as tracking of charged particles. Each scintillator bar is equipped with a wave length shifting fiber going through its center, and the 30 layers of bars are oriented perpendicular to the neighboring layers. The second FGD has 3 cm of (passive) water between each layer of scintillators.

The surrounding calorimeter is primarily used for measuring photons from π^0 decay, but is also used for $\mu - e$ separation. It is a lead-scintillator sandwich sampling calorimeter, with 32 layers of 4 cm wide and 1 cm thick plastic scintillators, separated by 31 layers of 1.75 mm thick lead sheets.

3.4 Beta beam

Another potential high performance beam for neutrino oscillation is the Beta beam. A Beta beam uses light radioactive isotopes which produce either ν_e or $\bar{\nu}_e$ depending on whether the decay is a β^+ or β^- decay. This has the big advantage compared to Super beams of producing a very pure neutrino beam, with well measured cross sections from β decay at rest.

The isotopes should have large enough life time to allow the beam to be accelerated without excessive decay losses, while at the same time have a short enough life time to allow decay in the storage ring. For this reason a life time around one second is desired.

In addition to the life time, a high production yield is desired for obtaining high beam intensity. For ν_e production ^6He has been chosen as a prime candidate, and for $\bar{\nu}_e$ ^{18}Ne has been selected, though ^8Li and ^8B also show promising properties with the additional virtue of three to four times higher neutrino energy [5], but with a loss of flux due to the higher decay angle.

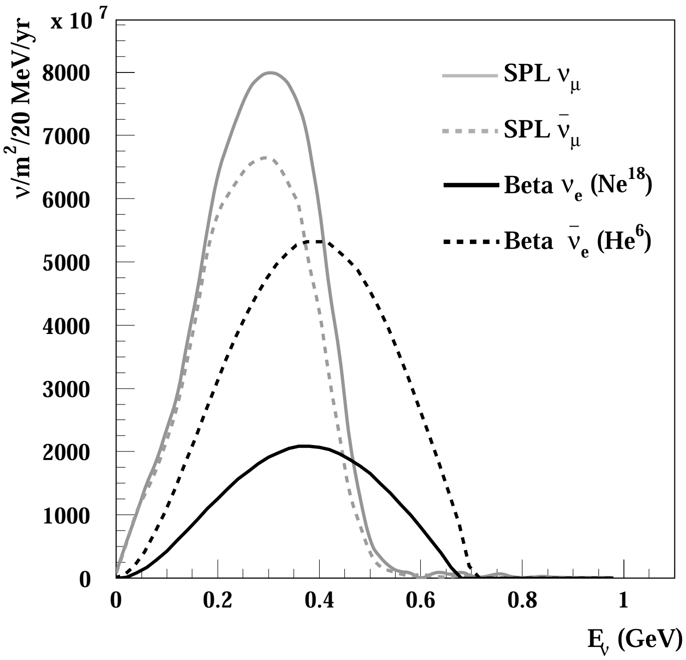

Fig. 3.8: Neutrino flux of Beta beam ($\gamma = 100$) and CERN-SPL Super beam, 3.5 GeV, at 130 Km of distance.

For several reasons, such as that the neutrino energy must be above the muon production threshold, and increased neutrino cross sections with increased energy, the Beta beam performs better with a more energetic ion beam. Figure 3.8 shows a comparison of the expected energy spectrum from a Beta beam, using ^{1}8He and ^{6}He, compared with a Super beam. For all useful beams $\gamma_{\rm He} \geq 100$. For $\gamma_{\rm He} = 150$, which can be obtained in the CERN-SPS, with 5 T bending magnets and 36% useful decay length, the decay ring length is approximately 6880 meters [5]. If the field strengths are unchanged, higher energy thus forces the length of the decay ring to scale up accordingly, which in practice prohibits too large an energy for economical reasons.

The neutrino oscillation discovery potential in a Beta beam facility is mainly based on the so called *golden channel*, which is the oscillation from a ν_e to a ν_μ.[4] Since the beam is free of antineutrinos, it is not necessary to magnetize the far detector, hence huge Megaton Water Čerenkov detectors can be used. There is no benefit to go above $\gamma = 400$ with such detectors since the events are likely to produce more than one Čerenkov ring and thus not be selected [5]. The Beta beam outlined here is not sensitive to τ appearance from $\nu_e \rightarrow \nu_\tau$

[4] Oscillation $\bar{\nu}_e \rightarrow \bar{\nu}_\mu$ for β^- decay.

oscillations, the so called *silver channel*, and its capability of resolving degeneracies in the (θ_{13}, δ) plane is therefore limited.

At the present, the largest technical obstacle to Beta beams is the production of the nuclei and their injection into the accelerator, while avoiding excessive activation of the accelerators by removing unwanted radioactive nuclei from the beam.

3.5 Neutrino Factory

The third high performing neutrino beam concept proposed is the Neutrino Factory, which relies on muon decay for production of neutrinos. The Neutrino Factory benefits from that all processes involved are well measured and understood, and that the muon decay produces very clean beams of $\mu^- \rightarrow \nu_\mu + \bar{\nu}_e$, or $\mu^+ \rightarrow \nu_e + \bar{\nu}_\mu$ beams. Another advantage of the Neutrino Factory compared to Beta beam is that the posterior probability density function of ν_μ produced in muon decay has a maximum located at the muon beam energy (figure 5.4), whereas the neutrino energy modes for Beta beams and Super beams are located significantly below the beam energy (figure 3.8). The Neutrino Factory can be run with either muon sign at the same facility, thus allowing comparisons in cross sections. With a magnetized far detector, appearance of "wrong sign" muons (the golden channel) is a very striking signal of leptonic $\mathcal{CP}$ violation and shows great sensitivity to θ_{13}.

Another potential neutrino oscillation channel is the silver channel, where a ν_e oscillates to a ν_τ. Since the energy to produce a final state τ through charged current interaction is too high even for the highest energy Beta beams, the silver channel is a unique feature of the Neutrino Factories [5]. In order to separate the silver channel oscillation from the golden channel, adequate vertex reconstruction must be achieved in addition to determining the muon sign.

3.5.1 General design

High intensity protons are fired on a mercury jet target to produce pions. The high intensity of the Neutrino Factory calls for high beam power on to the target. A 4 MW proton driver has been proposed [27, 28, 29] which should be compared with present devices of approximately 0.5 MW. The need for new proton drivers is shared with a potential LHC upgrade and could therefore already be in place at CERN by the time the Neutrino Factory is constructed. The best pion yields are obtained for 10-30 GeV protons, but 5-10 GeV is favored since the subsequent muons from decaying pions are more easily captured [30]. There are presently some disagreements between Monte Carlo implementations in the low energy range, but the HARP experiment points to the 10 GeV range as being optimal [31].

Studies have shown that a solid target would melt or explode under the intense proton beam. Instead a scheme using a liquid mercury jet has been devised, where ripples and distortions are dampened by a strong magnetic field applied to the conducting liquid. The pions produced by interaction with the target are captured by the magnetic field. The MERIT experiment [32], which examines possible target designs, uses a 24 GeV/c proton beam with a 1-2 mm spot size together with a 15 T field.

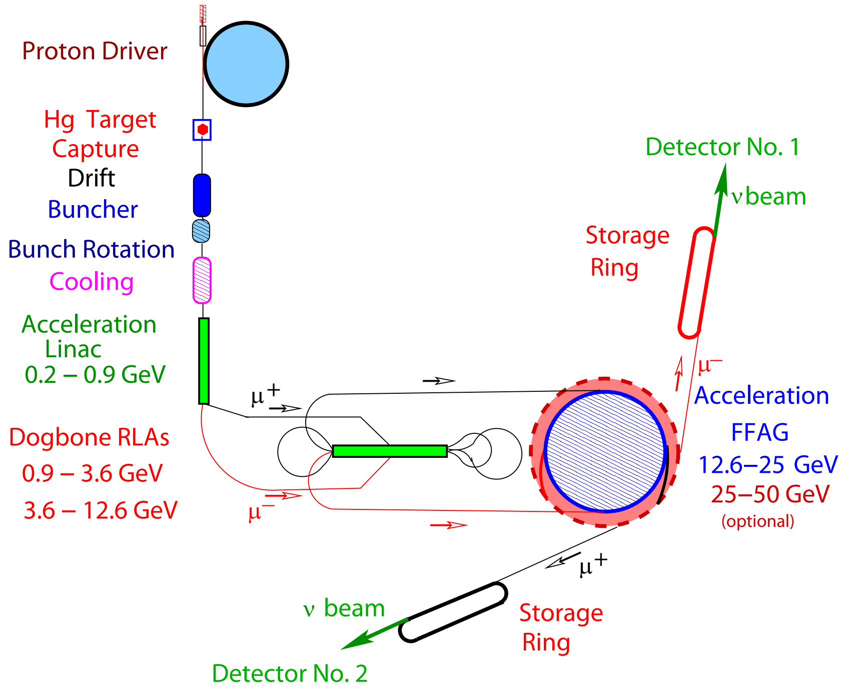

Fig. 3.9: The ISS Neutrino Factory concept.

Pions, and hence also muons, are generated with large angular and energy spread. The pions decay into muons in an empty magnetic lattice (the *decay channel*) of 90 meters where an energy–time correlation arises through drift. The beam is bunched in 0.5 ns micro bunches by applying high frequency RF cavities. The beam is phase rotated to convert the energy spread into large time spread on the macro structure, while the micro bunches are kept small. This allows high frequency RF cavities to be efficiently used in the subsequent cooling linac.

The muon beam created in this manner has a large emittance, and a cooling channel based on the ionization cooling mechanism (section 3.5.2) reduces the emittance to match the acceptance of the subsequent apertures. Previous studies have assumed an accelerator acceptance limit at 30π mm rad. Later studies assumed that 45π mm rad was possible [33]. However the FFAGs (see below) have problems to cope with transverse emittance larger than 30π mm rad [29].

After having passed through the cooling section, the beam of energy 138 MeV [29] is reaccelerated in a linear accelerator to 0.9 GeV [29], after which a "dog bone" accelerator takes the muons to 3.6 GeV, followed by a second "dog bone" accelerator which accelerates the muons to 12.6 GeV [29]. The dog bone accelerator is a kind of *recirculating linear accelerator* (RLA), which uses the same straight accelerating section for different energies, but the field at the turning points does not vary with energy like in a synchrotron accelerator. Instead high aperture dipoles guide the beam to and from the straight sections. A *fixed field alternating gradient* (FFAG) accelerator, accelerates the beam to the desired 25 GeV, optionally followed by a second FFAG which would give a final muon energy of

50 GeV. The FFAG accelerators use a higher bending field for particles at large radii, thus allowing a wide momentum range without changing the accelerating gradient.

The last component of a Neutrino Factory is the muon storage ring. Muons are circulated in either a racetrack shaped or triangular "ring" with long straight sections where the muons will decay and a low angular divergence neutrino beam is thus produced in the direction of the straight section. In order to maximize the neutrino flux, the angular opening of the muon beam must be negligible with respect to the opening angle of neutrinos in muon decay, i.e., [34]

$$\sigma_\theta \lesssim \frac{0.1}{\gamma}. \tag{3.33}$$

No acceleration is applied to the muons at this stage, only soft focusing with large apertures are utilized to control the beam.

3.5.2 Ionization cooling

In the ionization cooling scheme emittance reduction is obtained by energy loss in absorbers and reacceleration in linacs. The energy loss of the beam is dominated by ionization (section 5.1.2).

By sending the particle through a massive object, energy is lost through ionization and the momentum is reduced in all directions. This breaks the emittance conservation, and if the effect of multiple scattering (section 5.5) is smaller than the energy loss, the emittance is reduced. After this momentum reduction, the particle is reaccelerated with a series of radio frequency (RF) cavities such that the energy of the particle is identical to the energy before the particle entered the absorber. A Neutrino Factory will use 201 MHz cavities operating at 16 MV/m [29]. However the RF cavities boost the particle only in the longitudinal direction, and the net effect is that the particle track is more focused in the forward direction after passing through the cooling element. In a full scale Neutrino Factory, the cooling section would consist of many such cooling elements, reducing the emittance in steps until the beam is sufficiently cool to be accelerated to the desired energy.

The transverse emittance is given by (A.29)

$$\epsilon^4 \equiv \frac{\sqrt[4]{|\mathbf{V}_\perp|}}{m} \tag{3.34}$$

where for a cylindrically symmetric beam [35]

$$\begin{aligned} \sqrt{|\mathbf{V}_\perp|} &= <x^2><p_x^2> - <xp_x>^2 - <xp_y>^2 \\ &\approx p_z^2\left(<x^2><\theta_x^2> - <x\theta_x>^2 - <x\theta_y>^2\right). \end{aligned} \tag{3.35}$$

The change in emittance after going through a thin absorber is

$$\frac{\mathrm{d}\epsilon}{\mathrm{d}z} = \frac{1}{2m^2\epsilon}\frac{\mathrm{d}\sqrt[2]{|\mathbf{V}_\perp|}}{\mathrm{d}z}. \tag{3.36}$$

If second order effects like energy straggling are ignored, only p_z and θ^2 depends on z, thus

$$\begin{aligned}\frac{\mathrm{d}\epsilon}{\mathrm{d}z} &\approx \frac{1}{2m^2\epsilon}\left(\frac{1}{p_z}\sqrt{|\mathbf{V}_\perp|}\frac{\mathrm{d}p_z}{\mathrm{d}z} + p_z^2 < x^2 > \frac{\mathrm{d} < \theta^2 >}{\mathrm{d}z}\right) \\ &= \epsilon\frac{1}{p_z}\frac{\mathrm{d}p_z}{\mathrm{d}z} + \frac{p_z^2}{2m^2\epsilon} < x^2 > \frac{\mathrm{d} < \theta^2 >}{\mathrm{d}z} \end{aligned} \quad (3.37)$$

and using $p_z dp_z \approx EdE$ and the betatron function

$$\beta_\perp = \frac{< x^2 > p}{m\epsilon} \quad (3.38)$$

the emittance change can be expressed as

$$\frac{\mathrm{d}\epsilon}{\mathrm{d}z} \approx \frac{\epsilon}{E\beta^2}\frac{\mathrm{d}E}{\mathrm{d}z} + \frac{p_z\beta_\perp}{2m}\frac{\mathrm{d} < \theta^2 >}{\mathrm{d}z}. \quad (3.39)$$

Substituting the mean-square scattering angle in the last term for (5.61) the expression becomes

$$\frac{\mathrm{d}\epsilon}{\mathrm{d}z} \approx \frac{\epsilon}{E\beta^2}\frac{\mathrm{d}E}{\mathrm{d}z} + \frac{\beta_\perp p_{MS}^2}{2m\beta^3 EX_0} \quad (3.40)$$

where E is the energy and $p_{MS} = 13.6$ MeV/c. This expression was first derived by Neuffer [36].

The first term is a cooling term since dE/dz is always negative in the absorber, while the second term is a heating term due to multiple scattering. Equation (5.18) shows that the cooling term is proportional to the atomic number, Z, while the heating term is inversely proportional to the radiation length. Using (5.33), the heating term is thus proportional to $Z(Z+1)\ln(287/\sqrt{Z})$, which shows that optimal cooling performance is obtained with as low Z material as possible. The obvious candidate material for an ionization cooling absorber is thus hydrogen. Following the same line of reasoning, any components in the beamline should be made of low Z material.

Multiple scattering makes ionization cooling ineffective for very small emittances, as the cooling term is proportional to the emittance while the heating term is inversely proportional to the emittance[5]. The point where the ionization cooling mechanism is no longer cooling the beam is known as *equilibrium emittance*, and is given by (3.40) with the left hand side set to zero,

$$\epsilon_{eq} = \frac{\beta_\perp p_{MS}^2}{2m\beta X_0 \frac{\mathrm{d}E}{\mathrm{d}z}}. \quad (3.41)$$

An 80 m long cooling channel with 1 cm thick LiH absorbers would reduce the initial 17 π mm rad to 7.4 π mm rad [27]. The LiH absorbers are also used as windows to the RF cavities, and are coated with beryllium, which in turn is coated with thin layers of TiN to prevent electron emission [29]. This design has however an equilibrium emittance, 5.5 π

[5] Through the betatron function.

mm rad [29], which is approximately twice that of a design based on liquid hydrogen. This cooling channel increases the number of muons accepted in the subsequent accelerating devices by about a factor of 1.6 [29] compared to no cooling.

While the arguments outlined here are based on the thin absorber assumption, Fernow, Gallardo and Palmer [37] showed that the ionization cooling principle is still valid for thick absorbers, provided that the beam is strongly focused as to keep the transverse size of the beam small.

3.5.3 Muon collider

LEP, the electron–positron collider at CERN had a rich physical program and was a huge success. Synchrotron radiation made it practically impossible to achieve much higher center of mass energies than 200 GeV. Instead a new era of hadron colliders was born with the Tevatron at Fermilab and the Large Hadron Collider, LHC, at CERN. Hadrons however, are "dirty" and generate large amounts of hadronic jet events which form background to interesting events such as Higgs boson production. A number of linear electron–positron colliders have therefore been proposed, but their center of mass energy is limited to 500 GeV and they require very large accelerators.

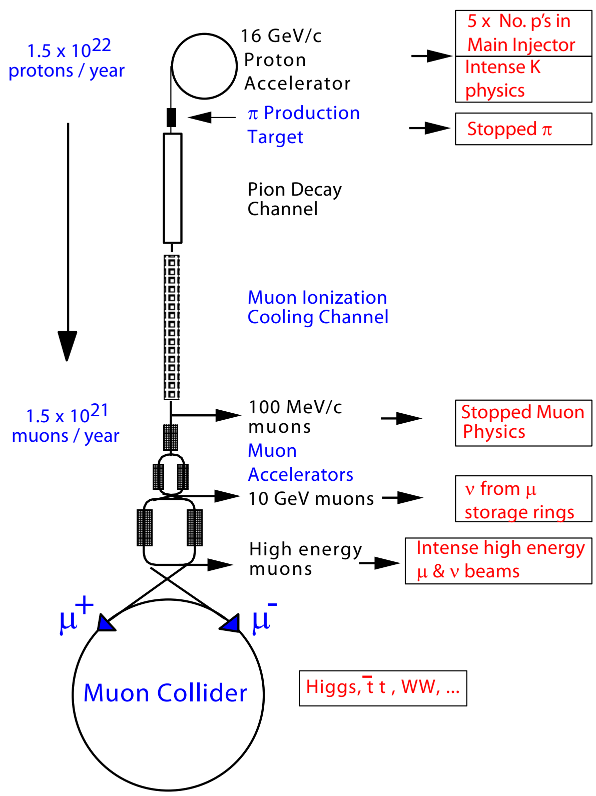

Fig. 3.10: The Muon collider concept.

Since the synchrotron radiation scales as

$$\Delta E_{synchrotron} \propto \left(\frac{E}{m}\right)^4 \tag{3.42}$$

and

$$\frac{m_\mu}{m_e} \approx 206 \tag{3.43}$$

Muon Colliders could reach much higher energies than electron colliders [6], while maintaining a purely leptonic beam. Another advantage a muon accelerator has compared to an electron accelerator is that the muons can still have a small energy spread at energies over 3 TeV, which allows precise energy scans ($\Delta E/E \approx 0.01\%$) at very high energies. In addition the energy calibration can be obtained from spin precession of polarized muons with very high precision ($\sim 10^{-6}$ or better) [40]. This would allow direct measurement of the Higgs mass and determination of degenerate Higgs, something an electron–positron collider could not do since its energy resolution would be $\Delta E/E \approx 1\%$ [41]. For instance a light Higgs boson ($m_H < 2m_W$) could be measured to fractions of one MeV [40].

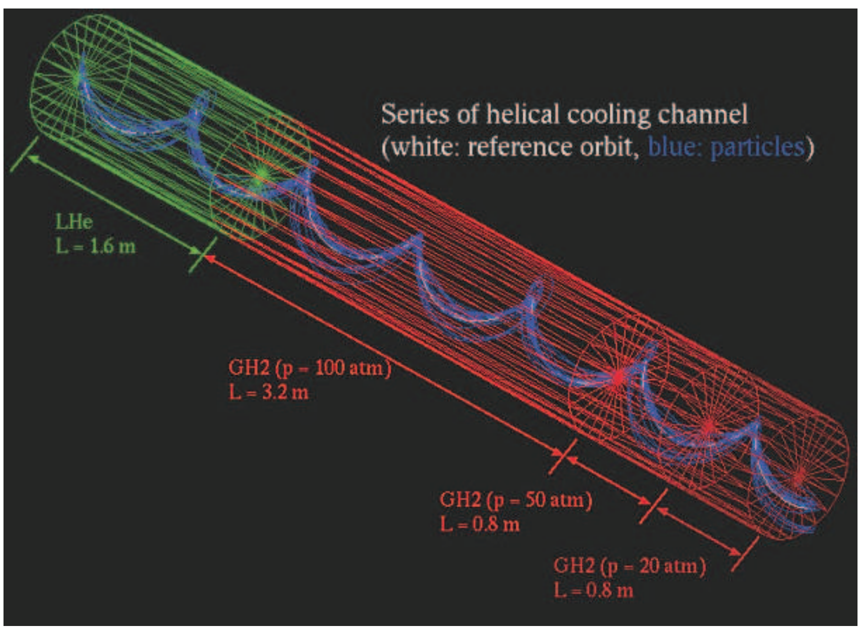

Fig. 3.11: A helical cooling channel, simulated in G4MICE.

The principle behind a Neutrino Factory and a Muon collider are the same [42] up to the point of the muon storage ring. While the Neutrino Factory is content with no additional acceleration, a Muon collider will accelerate the beam to a center of mass energy of approximately 4 TeV, and force interactions at the bunch crossings. Since the Muon

[6] 3 to 4 TeV [38], possibly up to 8 TeV [39], compared to 500 GeV of the ILC.

collider requires [39]

$$\epsilon_\perp \approx 0.025\,\pi \text{ mm rad} \tag{3.44}$$
$$\epsilon_\parallel \approx 72\,\pi \text{ mm rad} \tag{3.45}$$

it also needs much stronger cooling than the Neutrino Factories, about three orders of magnitude of transverse cooling and one order of magnitude of longitudinal cooling. For this reason it is a challenging task to make Ionization Cooling perform sufficiently for a Muon collider, though novel ideas such as Helical Cooling channels look promising [43].

A problem with the Muon collider is intense neutrino radiation. Muons are the secondary tracks in neutrino interactions with the longest range, a 5 TeV muon is stopped after 10 km of earth. This is easily achieved by placing the collider at a moderate depth. Even though the cross section for neutrino interactions is very small[7], the divergence of the beam is inversely proportional to the energy, and the dose conversion coefficients scale as the square of the energy, thus the neutrino dose equivalent scales with E^3. The low cross section further implies that the neutrino flux is not noticeably attenuated with distance. For a collider with a center of mass energy of 3 TeV, this infers that the distance along the acceleration plane between the accelerator and residential housing must be at least 30 to 40 km, in order to have a radiation lower than 0.3 mSv [44]. This can be achieved by placing the collider at a depth similar to the LHC.

3.6 Detectors for neutrino beams

A neutrino oscillation experiment is only as good as the detectors allow, and much effort of the neutrino beam facility R&D is to determine the performance of the associated far detectors. Since the neutrino beams presented here differ in content and energy spectrum, the detectors must be optimized for each type of beam facility individually. This work is underway and all results presented in this section should be considered preliminary.

3.6.1 Water Čerenkov

As a charged particle passes through a material the local electromagnetic field is disrupted. Photons are released as the material goes back to the equilibrium state. Normally the photons interfere destructively and no light can be observed, but at speeds exceeding the speed of light in the material the interference is constructive and radiation can be observed as rings of light.[8] Water Čerenkov detectors can thus be used to detect charged particles produced in neutrino interactions in the detector. Water Čerenkov detectors are mostly useful for detecting charged current events.

It is very hard to correctly identify neutrino events with electrons in the final state due to the small neutrino cross section and the presence of background events. If the energy is high enough π^0 events are produced which decay into two high energy photons, and

[7] Of the order of 10^{-35} cm^2 at a neutrino energy of 1 TeV [44].

[8] This is similar to the bow wave of boats which builds up as the boat picks up speed.

it is difficult to determine whether such an event has one or two Čerenkov rings. It is therefore better to use *quasi elastic* (QE) charged current events, where the low energy of the incoming neutrino leaves the struck quark in the same hadron it initially was residing in. However the quasi elastic interactions depend on the structure of the nucleus which adds a significant level of complexity to the cross sections. Neutral current events with charged pion production are a background to quasi elastic charged current detection, but since the pions are absorbed before decaying, time information on the Čerenkov rings can reduce the effective background level.

Alternatively instead of water one can use a scintillating liquid, such as in NOνA, with the much better energy reconstruction for neutrino events above the quasi elastic region. However it is not feasible to construct this type of Čerenkov detector as large as the water based counterparts, and 50 kiloton is often used as a realistic upper size limit [5].

The main advantages of large water Čerenkov detectors are that there is considerable experience and knowledge in the particle physics community on how to build and operate the detectors, and that it seems possible to build huge detectors in the megaton scale. The synergy between the search for proton decay which is predicted by many GUT theories, and detection of neutrinos produced in supernovae, constitutes a large scientific program for water Čerenkov detectors. However due to cosmic rays this type of detector must be built deep underground, limiting access to the site and complicating the experiment construction. Background from atmospheric neutrino flux cannot so easily be reduced and must be rejected by cuts on reconstructed energy and directionality. Furthermore excavating caves of the scale needed for this size of detectors is a difficult technical challenge, and the hundreds of thousands of hand blown photomultiplier tubes[9] is a cost hard to cover.

3.6.2 Magnetized scintillation detectors

In a Neutrino Factory running with μ^+ the neutrinos produced in the decay ring are ν_e and $\bar{\nu}_\mu$. If there is no oscillation, the neutrino interactions in the far detector should hence generate e^- and μ^+. Should muons with "wrong sign" be detected, a clear signal for $\nu_e \to \nu_\mu$ oscillation would be proven. This so called golden channel requires separating μ^+ from μ^-, hence a magnetized detector is required.

A magnetized detector in a Neutrino Factory could also look for the disappearance of $\nu_\mu \to \nu_\mu$, providing a good measurement on the atmospheric parameters θ_{23} and Δm^2_{31}, which will help solve the degeneracies. Observing the appearance of $\nu_\mu \to \nu_e$ oscillation (platinum channel) is much more challenging due to the electron in the final state.

Cervera et al proposed in 2000 [46, 47] a magnetized detector named MIND[10], a 10 m radius 20 m long cylinder consisting of 6 cm wide iron rods interspaced with 2 cm scintillator rods positioned at the corners of the iron rods, such that a neutrino traversing the detector would see a sandwich of iron and scintillator. The scintillators are read out in both ends to determine the spatial coordinates along the scintillators. A super conducting coil generates

[9] Hyper–Kamiokande plans to use 200'000 20 inch custom made PMT's, placed in twin 500 kiloton volumes [45].

[10] Magnetized Iron Neutrino Detector, previously called LMD, or MID.

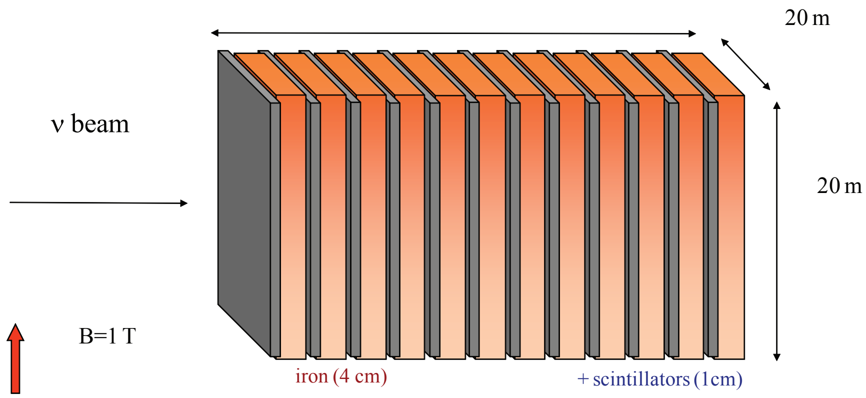

Fig. 3.12: The Magnetized Iron Neutrino Detector, MIND, is capable of measuring the charge of muons produced in neutrino interactions and is the baseline detector for a Neutrino Factory.

a 1 T dipole field inside the iron. The main backgrounds to a "wrong sign" μ^- signal event is

- $\bar{\nu}_\mu$ CC event where the μ^+ is not detected, and subsequent meson decay produces a μ^-.
- ν_e CC events where the primary electron is not detected, and the hadronic jet contains π^- which decays into μ^-.
- $\bar{\nu}_\mu$ and ν_e NC events where the deep inelastic scattering produces hadronic jets containing π^-.

The hadron induced backgrounds to the wrong sign muon signal is rejected in MIND by range. The average muon at 3 GeV/c travels 3 meters in the detector, while more than 99.9% of all hadrons have a shorter range than that [48]. Fortunately genuine wrong sign muons will have larger energy than the fake wrong sign muons from the hadronic jet. This type of background can hence be rejected by cuts on reconstructed muon momentum and angle with respect to the hadronic jet. For a baseline of 3500 km, the optimal cuts are $p > 5$ GeV/c and $p \sin 2\theta > 0.7$ GeV/c, which give a total background rate of $8 \cdot 10^{-6}$ for 45% signal efficiency [48].

A problem with the MIND design is that the low energy neutrinos are important for measuring θ_{13} and δ_{CP}. However at approximately 3 GeV the sensitivities saturate, and improvements below this energy do not enhance the θ_{13} and δ_{CP} measurements. MIND thus aims to keep the impurities below 0.1% at a signal efficiency of 80% for energies above 2 GeV, which preliminary studies suggest is possible. However it will require a magnetic field of 1.5 to 1.7 T [49]. Furthermore, the presence of iron eliminates the charge determination performance for electrons, thus MIND is not suitable for the platinum channel.

The simulation studies performed for MIND are rather primitive Geant3 simulations and the detector needs more detailed simulations in order to optimize the scintillator to lead ratio. It would also greatly benefit from a more sophisticated analysis, but it remains the baseline detector for the Neutrino Factory. As shown in figure 3.12, the present design uses large sheets of iron instead of iron rods.

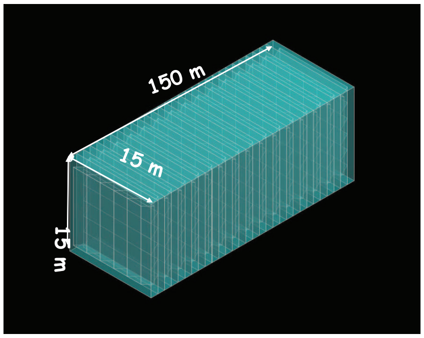

(a) TASD modeled in G4MICE [50].

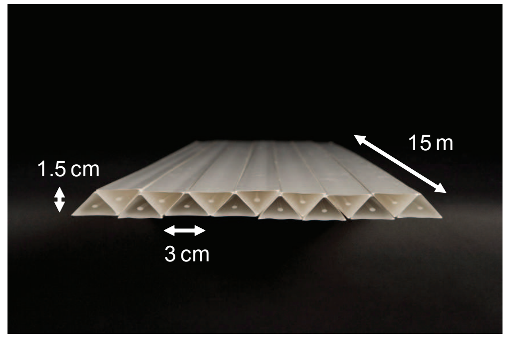

(b) TASD scintillators (photograph).

Fig. 3.13: The Totally Active Scintillator Detector, a magnetized neutrino detector for the golden channel.

An alternative is to make the detector totally active, using triangular scintillator bars running along the x and y coordinates with a 0.5 T solenoidal field [51]. This *totally active scintillator detector*, TASD, is essentially a magnetized version of the NOνA detector used in the NuMI beam at Fermilab [52]. The scintillators are triangular with a base of 3 cm, a height of 1.5 cm and are 15 cm long [51]. The total mass is 22.5 kilotons [51], of which approximately 84% is active scintillator and the rest is PVC [45]. See figure 3.13. The lower mass compared to MIND is compensated by better energy resolution[11] and four times as many hits per track length which helps π^0 to e separation. The low density combined with fine granularity give efficient muon charge measurement at low momentum. The fraction of muons with mis-identified charge is below 10^{-4} for $p \gtrsim 300$ MeV/c [51].

While it is possible to magnetize a volume of this size using a number of different techniques, the cost is usually the prohibiting factor. Although very expensive compared to normal superconducting coils, the rapid developement of high Tc solutions makes it an option [51]. Another option is based on the superconducting transmission line, STL, developed for the VLHC superferric magnets. The solenoid windings consist of a superconducting cable inside its own coaxial helium cryostat. This design eliminates the need for a large and bulky cryostat. By adding plates of 1 m thick iron at the two ends, simulations have achieved an average field in the detector of 0.58 T at 50 kA excitation current[12] [51]. These options are interesting, but require R&D, so magnetizing TASD will not be as straightforward as magnetizing MIND.

A 50 kg near detector prototype called NOMAD-STAR has been built and studied in the NOMAD neutrino oscillation experiment [53]. It used five layers of active scintillating micro strips interspaced with four layers of boron carbide, and an external magnetic field

[11] $\Delta E/E \lesssim 10\%/\sqrt{E[GeV]}$ [51] compared to $\Delta E/E \sim 15\%/\sqrt{E[GeV]}$ [45].

[12] The STL for VLHC is designed for 1 T at 100 kA [51].

was applied for charge determination of muons and electrons. It was concluded that the very limited number of planes and the passive target reduced the performance of the detector, but with a larger number of active layers the vertex reconstruction performance could be greatly improved.

3.6.3 Liquid Argon TPC

Another interesting detector concept is the *Liquid Argon Time Projection Chamber*, LAr-TPC, which is based on the fact that the ionization tracks in liquid argon of high purity can be drifted over several meters. At the end of the drift path, the charge is read out using position segmented electrodes. By applying a magnetic field, golden channel oscillations can be detected from sign determination of the muons, making the detector useful not only for Super beams and Beta beams but also for Neutrino Factories. It is estimated that a field strength of 0.1 T is sufficient to determine the muon charge, while electron–muon separation requires 1 T [54]. This would allow detection of $\nu_\mu \to \nu_e$ oscillations, called the *platinum channel*, which is the $\mathcal{T}$ conjugate of the golden channel. The lower energy threshold for the platinum channel in a liquid argon TPC is assumed to be 0.5 GeV/c [5]. Since high energy electrons tend to create electromagnetic showers early, the platinum channel has reduced efficiency at high energy.

The fiducial mass of LArTPC's is somewhere between 10 and 100 kilotons, where a 10 kiloton detector at 200 meters depth would have the same astrophysical physics reach equal to Super–Kamiokande [54]. The large volume containers already exist in industrial applications, but the areas where more investigations are required are the high voltage of large drift lengths, readout and embedding in a magnetic field.

3.6.4 Magnetized Emulsion Cloud Chamber

An alternative detector concept with much the same possibilities as a LArTPC to detect golden, silver and platinum channels is a *magnetized emulsion cloud chamber*, MECC, which uses thin nuclear emulsion films sandwiched between lead layers. A unmagnetized nuclear emulsion cloud chamber has been built and operated in the OPERA detector in the CNGS experiment, which is used to study the $\nu_\mu \to \nu_\tau$ oscillation channel. OPERA has excellent track separation precision, but can determine the charge only for muons [54]. With a magnetized detector also electron charge could be adequately measured.

3.7 Comparison of performance

A high performance neutrino facility will require substantial resources in both manpower and funds, and it is likely that the particle physics community can only afford to build one of the proposed accelerators. The International Scoping Study Physics group [5] has performed studies on the prospective physics reach for the proposed designs. Since the R&D on the facilities is still in progress two sets of parameters for each facility was used for the evaluation; the first set used conservative assumptions while the second set used more optimized parameters.

- Second generation Super beams: Three Super beam facilities were considered, the SPL, T2HK, and the wide-band beam experiment. The optimized parameter set corresponds to the assumption of a total systematic uncertainty of 2%. The conservative parameter set assumes a total systematic uncertainty of 5%;

- Beta beam facilities: The conservative option is taken to be the CERN baseline scenario with stored ^{6}He and ^{18}Ne beams at $\gamma = 100$ serving a 500 kiloton water Čerenkov detector at a baseline of 130 km. The optimized parameter set assumes stored ^{6}He and ^{18}Ne beams at $\gamma = 350$ illuminating a 500 kiloton water Čerenkov at a baseline of 730 km.

- The Neutrino Factory: The conservative setup assumes 10^{21} muon decays per year and a stored muon-beam energy of 50 GeV. Neutrino events are recorded in the golden detector at a baseline of 4000 km. A setup corresponding to a more recent Neutrino Factory design assumes a 20 GeV stored muon beam delivering 10^{21} muon decays per year. Neutrino interactions are recorded in two golden detectors, one placed at a baseline of 4000 km, the second at a baseline of 7500 km.

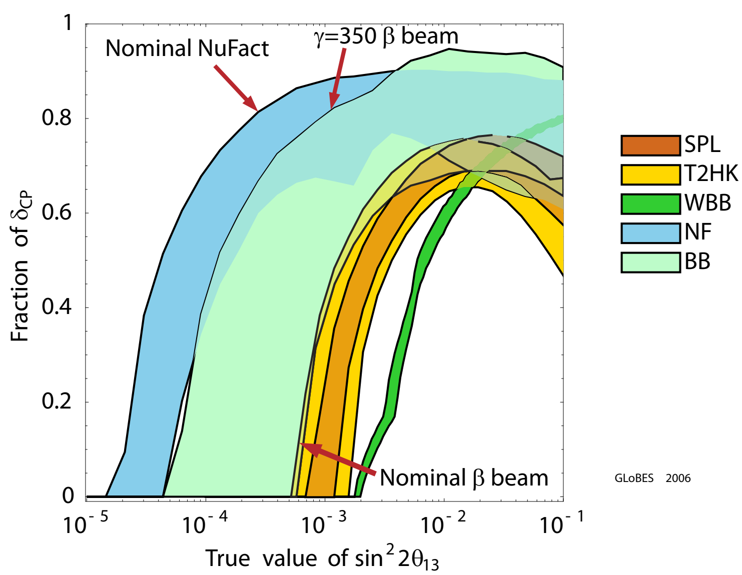

Fig. 3.14: The $\mathcal{CP}$ violation discovery potential for possible values of δ and θ_{13}. To the right of the lines the $\mathcal{CP}$ conserving solutions $\delta = 0$ and $\delta = \pm\pi$ are excluded to 3σ confidence level. The right hand edges of each band correspond to conservative experimental setups, while the left hand edge is the solution for optimized experiments [5].

As figures 3.14, 3.15 and 3.16 show, the uniformly most powerful facility is the Neutrino Factory which outperforms all other neutrino beams. Should the true value of $\sin^2 2\theta_{13}$ be

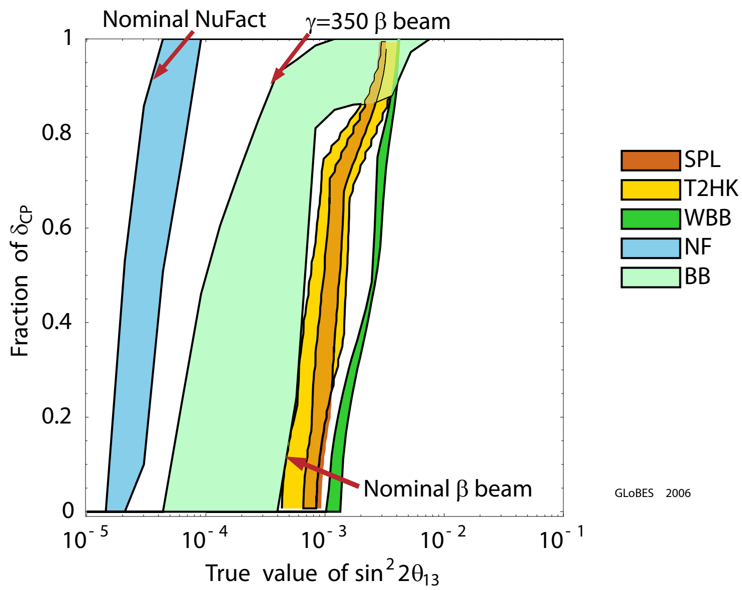

Fig. 3.15: The discovery potential of nonzero mixing angle θ_{13} for possible values of δ and θ_{13}. To the right of the lines the $\mathcal{CP}$ conserving solution $\sin^2 2\theta_{13} = 0$ is excluded to 3σ confidence level. The right hand edges of each band correspond to conservative experimental setups, while the left hand edge is the solution for optimized experiments [5].

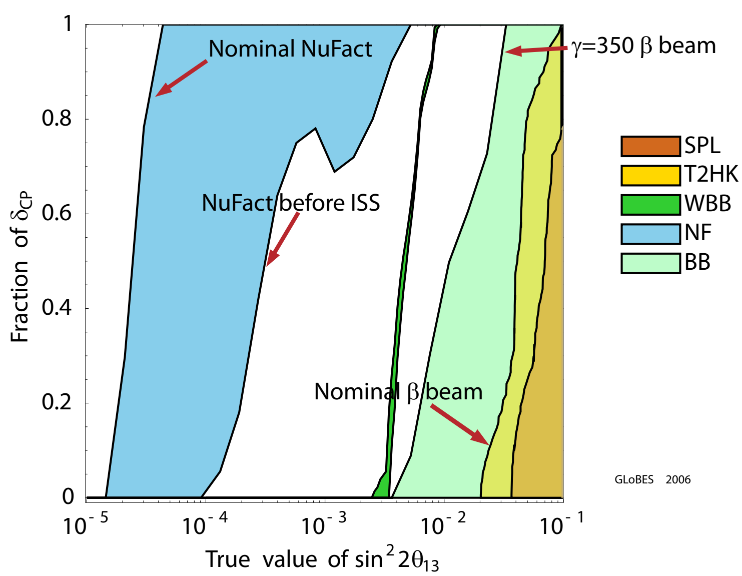

Fig. 3.16: The discovery potential of the neutrino mass hierarchy for possible values of δ and θ_{13}. To the right of the lines the signΔm^2_{31} is determined to 3σ confidence level. The right hand edges of each band correspond to conservative experimental setups, while the left hand edge is the solution for optimized experiments [5].

within the region $5 \times 10^{-4} \lesssim \sin^2 2\theta_{13} \lesssim 10^{-2}$ a Beta beam experiment would perform as well as a Neutrino Factory for discovering $\mathcal{CP}$ violation and non-zero θ_{13}. At even higher values of the mixing angle all three types of experiments would give comparable results. However, as figure 3.16 shows, only at very large θ_{13} are the Beta beam and Super beams sensitive to the mass hierarchy.

4. INTRODUCTION TO MICE

The second part of this thesis is dedicated to the Muon Ionization Cooling Experiment [55], MICE. This chapter presents an overview of the experiment, while subsequent chapters deal with special topics of the experiment the author has been working on.

4.1 Purpose of MICE

The objective of MICE is to demonstrate ionization cooling as outlined in section 3.5.2, and is therefore considered as the first step towards neutrino factories and Muon colliders.

The muons in MICE are produced from pion decay. Pions in turn are produced from proton interaction with a target. Since muons are short lived particles standard methods of cooling, such as stochastic and electron cooling used for electrons and protons, are not applicable to a muon beam. In order to avoid decay losses, the emittance reduction must be quick, and preferably while the particles are relativistic.

The full scale MICE experiment (MICE Stage 6) will have two physical cooling elements, corresponding to one period of an SFOFO lattice as outlined in section 3.5.2, plus one additional absorber to enclose the cooling section with absorbers so RF induced electrons are not accelerated down the beamline.

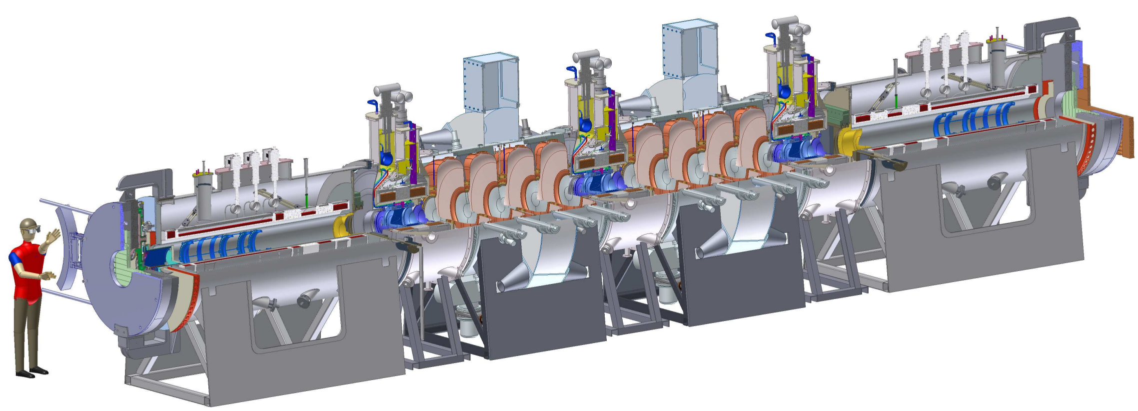

Fig. 4.1: The MICE cooling channel, Stage 6, complete with spectrometers [56].

Figure 5.7 shows the dependency of the energy loss of a particle per unit length as a function of its momentum. Ideally the working energy for an ionization cooling channel would be in the high energy regime where the slope is rather flat, providing rebunching of the beam. Since the gyroradius in a magnetic field increases linearly with momentum, the transverse size of the experiment would have to scale accordingly. For MICE, the choice was thus made to operate the experiment around minimum ionization energy.

The nominal beam is a minimum ionizing muon beam of 6 π mm radian, but different beams with central momenta from 140 to 240 MeV/c and emittances up to 10 π mm radian will also be studied. The expected cooling that can be achieved for the nominal beam using this setup is 10%. The MICE objective is to measure this cooling with 1% accuracy, and as a consequence the emittance upstream and downstream must be measured to 0.1% accuracy or better. MICE will have the ability to distinguish individual particles, thus associating single particle emittance measured downstream of the cooling channel, with the corresponding quantity measured at the upstream end. This imposes additional requirements for the detectors. In order to obtain sufficient statistics the experiment is designed to handle 600 good muons per 1 ms spill, with a spill rate of 1 Hz.

4.2 General design

MICE is being built at Rutherford–Appleton laboratories (RAL) where protons from the ISIS ring are used in parasitic mode to produce pions, which in turn decay into muons. The cooling channel consists of two RF linacs, made of four 201.25 MHz cavities each, and three liquid hydrogen absorbers. The muon tracks are measured upstream as well as downstream of the cooling channel, using two identical spectrometers installed in 4 T solenoids. Together with a pair of time of flight detectors, they provide all parameters for six dimensional emittance measurement. A third time of flight detector is placed further upstream, which together with a Čerenkov detector, provides particle identification and characterization of the beam content. A calorimeter at the end of the experiment is used to detect electrons from muon decay, which otherwise would bias the emittance measurement.

4.2.1 Target

MICE produces pions by dipping a titanium target into the halo of the ISIS proton beam. Since ISIS is primarily designed as a neutron spallation source, it is required that MICE does not disturb the normal operation of ISIS and its associated experiments. For this reason the MICE target is only injected into the proton beam once per ISIS cycle, just before the beam extraction. Since the beam radius shrinks with time, the target must move 43 mm and return during a period of 30 ms [57], in order to stay clear of the subsequent pulse. The necessary acceleration of $80g$ is provided by linear magnetic drive. Due to a small amount of dust produced by wear at the bearing surfaces, a diamond-like carbon (DLC) coated shaft and DLC coated upper bearing have been tested. The DLC coating was 3.5 μm thick. This target system has performed 1.25 million actuations over a period of two weeks without any visible dust produced.

Inside every ISIS cycle is a micro structure with 100 ns bunches of protons, each separated 224 ns apart, as shown in figure 4.2. Ideally for MICE only one good muon per burst is created for easier identification of muon tracks in the various detectors. If MICE

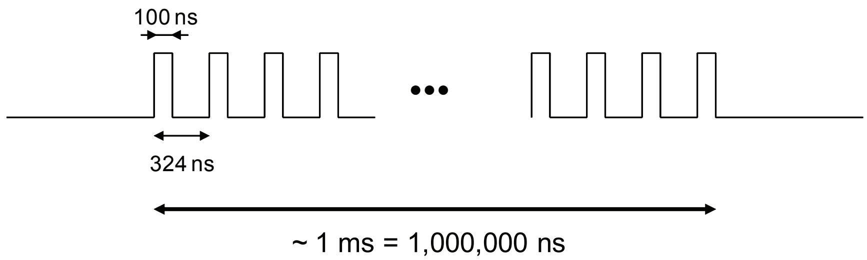

Fig. 4.2: The ISIS beam structure. The 1 ms long cycle contains a micro structure of 100 ns long bursts.

is to have 500 good muons per spill in the cooling channel, the required number of protons incident on the target is estimated to be $1.4 \cdot 10^{12}$, which results in 1.9 J deposited in the target. Most of this heat must be dissipated by radiation. Assuming the target is the only radiator and a rate of 1 Hz, the equilibrium temperature is 600°C [58]. For this reason the target is designed so the radiating area is increased for maximal radiative heat loss. Since the production rate of μ^- is only one third of the rate of μ^+, it is not clear that the desired beam intensity can be reached, if operating the experiment on μ^-. Studies regarding the production of muons have been performed using MARS [59], LAHET [60] and Geant4 [61], and their responses compared with experimental data [30].

4.2.2 Beam optics

The pions produced by proton interactions in the target are captured by a triplet of quadrupoles. A dipole magnet bends the beam toward the MICE hall and selects pions of high momentum. The pions then decay in a 5 m long, 12 cm bore, superconducting 5 T solenoid, which penetrates the wall between the ISIS ring and the MICE experimental hall. The decay solenoid was contributed by the Paul Scherrer Institute, Switzerland. After the decay solenoid a thin polyethylene absorber is installed in the beamline to remove any remaining protons, followed by a second dipole magnet which selects muons from backward decaying pions, and thus ensures a large reduction in the pion content of the beam. Muons are selected at central momenta between 140 MeV/c and 240 MeV/c, with a spread of 10%.

After the second dipole magnet, two quadrupole triplets transfer the beam to the entrance of the cooling channel. Two thin solenoids serve to match the beam between the 4 T tracker solenoids and the cooling channel, while focus coils for every absorber reduce $\beta_\perp$. Together with a coupling coil at each of the two linacs, the cooling channel constitutes one period of an SFOFO lattice.

By flipping the field in the focus coil pair, build up of canonical angular momentum, L^c, given by [35]

$$L^c = xp^c_y - yp^c_x \approx x(p_y + \frac{xB_0}{2}) - y(p_x - \frac{yB_0}{2}) = xp_y - yp_x + \frac{\rho^2 B_0}{2} \tag{4.1}$$

is cancelled. When the focus coils are set up to create field flips in every absorber the experiment is said to be operating in *flip mode*, while *non–flip mode* refers to focusing

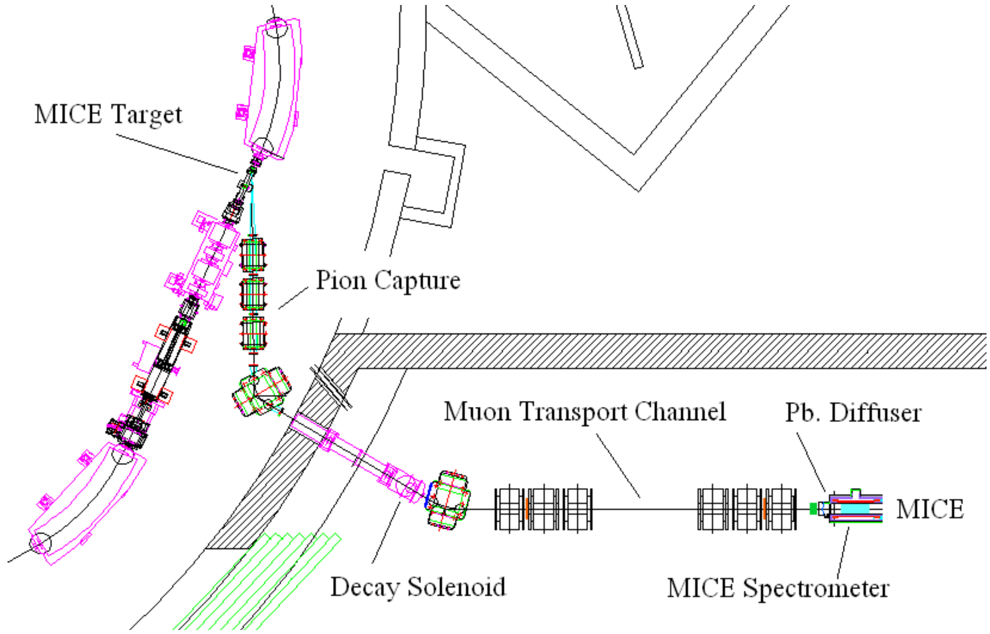

Fig. 4.3: The ISIS ring, target station and beamline into the MICE hall.

without flipping the fields. The buildup of canonical angular momentum could cause a mismatch of the longitudinal momentum in the RF cavities. By flipping the field any canonical angular momentum which is built up in the first half of the absorber is cancelled by the opposite sign of the field in the second half of the absorber. In addition to this desirable quantity, the diverging field lines force electrons to defocus and thus the effective background rate in the experiment due to muon decay is decreased.

The goal of the beamline design is to give a matched beam of the desired momentum to the lead diffuser at a good muon rate of 600 particles per millisecond spill, while maintaining a very high purity. Table 7.1 summarizes the expected beam content at the target and TOF1.

The main tools used for optimizing the beamline are the Geant4 [61] based G4BeamLine [62], and TURTLE [63]. While TURTLE is a beam optics tool, G4BeamLine can study particle physics related issues such as secondary particle production, and it also contains time information which TURTLE lacks.

Diffuser

MICE will investigate the cooling performance as a function of the beam momentum and the beam emittance. While the momentum is determined by the dipole and collimator settings, the emittance is in addition controlled by passing the beam through a lead diffuser. For this reason the diffuser is often considered an integral part of the beamline. The diffuser is a circular lead disk with a radius of 15 cm and a thickness specified by the desired emittance[1]. Since the diffuser thickness is changed numerous times during operation of the experiment, a design has been developed where lead disks of various thicknesses are arranged in a circle, and the chosen diffuser is rotated into position by a remote controlled motor. This allows changing the beam emittance of the experiment without any personnel entering the experimental hall.

As a side effect, the diffuser will also work as a radiation shield for TOF1 against RF induced background. In addition, positrons still left in the beamline after the dipole momentum selection lose more energy than the muons in the diffuser and might be absorbed or defocused enough such that they are scraped in the cooling channel. For some runs however, the experiment will not use any diffuser at all.

4.2.3 Time of flight detectors

A set of detectors, of varying size and segmentation, is used to measure the time of flight in the experiment. Each detector is made of two perpendicular layers, of 2.5 cm thick scintillating plastic slabs. Each scintillating slab is read out at both ends by fast photo multipliers tubes coupled to straight light guides. TOF0 is the most upstream detector and is placed after the first triplet of quadrupoles in the MICE hall. Due to the small size of the beam at this stage combined with the high rate of particles, it is made of ten 4 cm wide slabs per layer, making its full size 40 by 40 cm. It is used together with TOF1, which is placed in front of the lead diffuser. TOF1 consists of seven 6 cm wide slabs per layer. Since TOF1 is situated in a high magnetic field area, the photo multiplier tubes (PMT) are shielded by heavy iron shields. There is a 10 cm thick shield located just downstream of TOF1, and a thinner 5 cm shield is located at the upstream end. The shields are linked at the outer radius by iron, of radial thickness and longitudinal thickness of 10 cm, as shown in figure 10.11. The time of flight measured between TOF0 and TOF1 is primarily used for separating pions from muons, and if there are still proton remnants or electrons in the beam, it will reject those as well.

A third time of flight detector, called TOF2, is stationed between the downstream tracker and the calorimeter. Originally TOF2 was designed as an identical mirror image of TOF1, but as presented in chapter 10 the author of this thesis showed that it must be larger. Therefore it is chosen to consist of ten 6 cm wide slabs per layer. Likewise the associated iron shield configuration has larger aperture. The times measured at TOF1 and TOF2 are primarily used for six dimensional emittance measurements, but are also used for estimating the RF phase at which a particle is entering the cooling channel. The absolute error on the time of flight measurement should not be larger than 70 ps, which in addition makes it useful for particle identification. The resolution can be achieved if each layer has 70 ps resolution, since the double layer improvement is cancelled by the two individual time measurements at TOF1 and TOF2 respectively.

The signal triggering the digitization of the analog signal in the front end electronics associated with the detectors, is formed from the time of flight station. Several logical

[1] For the nominal beam of 200 MeV/c and 6π mm rad, the thickness is 7.6 mm.

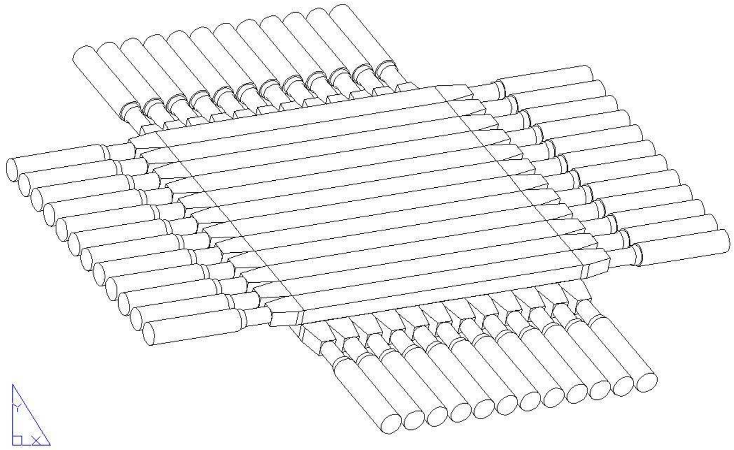

Fig. 4.4: The most upstream time of flight detector in MICE, TOF0. The other time of flight detectors have similar designs, only the number of channels per layer and the width of the slabs differ.

combinations are foreseen from triggering on every single burst to only coincidence of TOF0, TOF1 and TOF2. In the simulations presented in this thesis, the author always triggered the data taking of the calorimeter by hits in TOF2, as presented in section 6.3.2.

4.2.4 Čerenkov system

Due to the impurities of the beam at TOF1 presented in table 7.1, it is necessary to identify the particles which are passing through TOF1 and into the cooling section. Virtually all protons still present will range out in TOF1, and of the remaining polluters only pions, and to a lesser extent positrons, constitute beam contamination to the experiment. The time of flight between TOF0 and TOF1 already gives very useful information on the velocity of the particle and could in principle be used in conjunction with the momentum measured in the upstream tracker. However the particles are subjected to heavy energy loss in the diffuser and the two detectors themselves, which limits the particle identification capability of this approach. A Čerenkov detector is installed just downstream of TOF0 which is able to correctly tag pions and muons through a threshold.

Due to the large range of beam momentum used in MICE, there is no single material with a refractive index that could make a device sensitive to muons yet blind to pions. Therefore two different aerogels are used, with $n = 1.07$ and $n = 1.12$ respectively. As shown in figure 4.5, the refractive indexes have been chosen such that the threshold for muons in the first aerogel is at the same momentum as the threshold for pions in the second aerogel. This affordable solution gives net purities from pion contamination of 99.983% for {I on & II off} and 99.683% for {I on & II on} [58], given pion and muon distributions from a G4BeamLine simulation [64] of MICE Stage 6. For the same scenario, at low momentum where the Čerenkov detector is blind to both pions and muons, the purity is

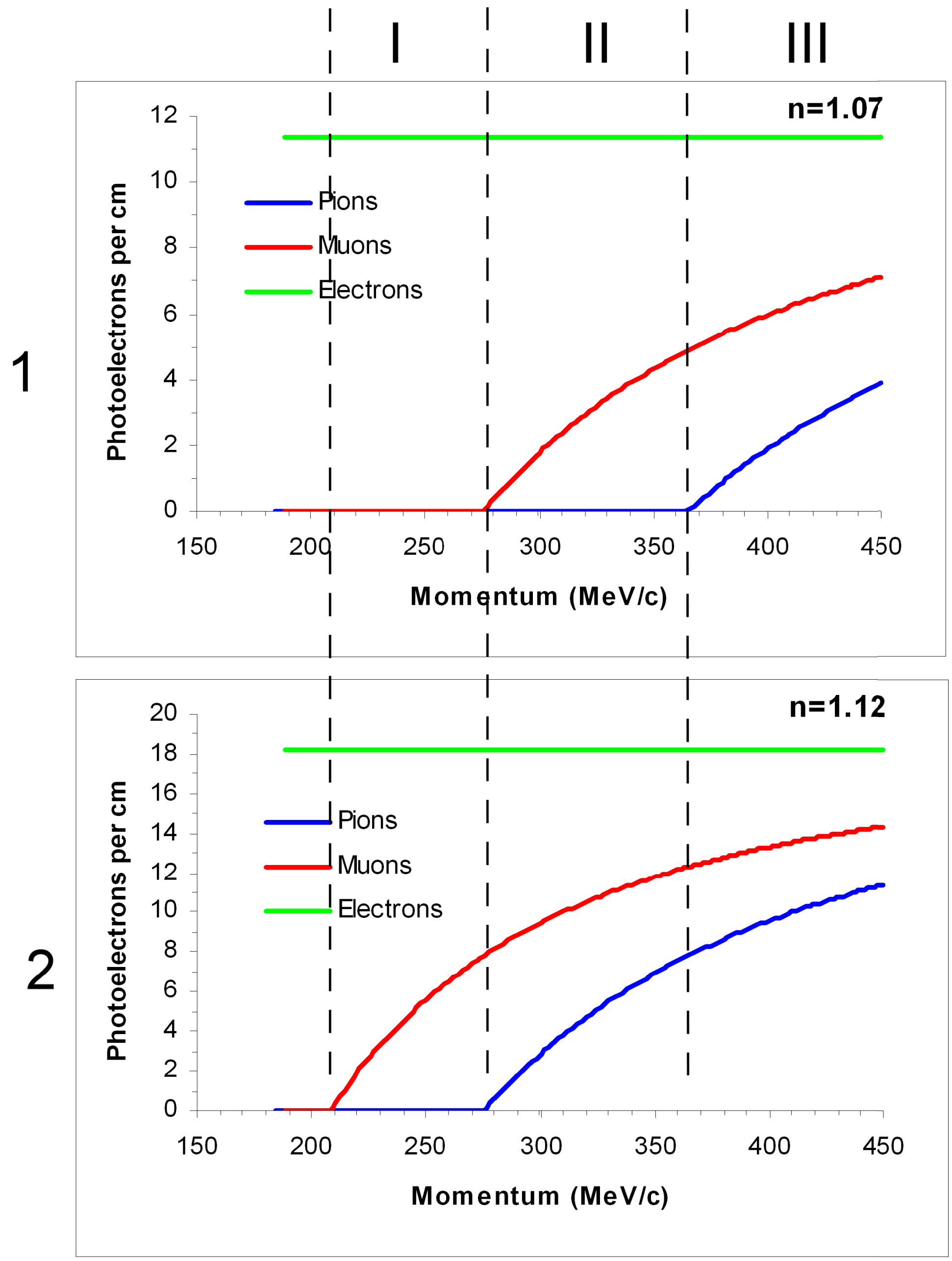

Fig. 4.5: The two aerogels in the Čerenkov detector are chosen such that the aerogel which gives signal for muons (red, middle) but not pions (blue, lowest) is dependent on whether the momentum is below or above 275 MeV/c. Positrons (green, highest) are always above threshold. At very high momentum (365 MeV/c, above the MICE range) all three particles are above threshold, and at low momentum (210 MeV/c) only the positrons can be separated from $\{\mu, \pi\}$.

only 87.819%. The conclusion is that the Čerenkov system provides good pion rejection between 210 MeV/c and 365 MeV/c (before energy loss in TOF1 and diffuser). At lower momentum, the Čerenkov system is blind to both pions and muons, hence time of flight is used for pion discrimination.

4.2.5 Spectrometers

The MICE experiment will measure the emittance of muons with a very high precision before and after the cooling channel. This requires a pair of high performance spectrometers, since the systematic errors on the measurement are dominated by the tracker resolution. Two conceptually different designs have emerged, each with its own advantages and short comings. Eventually the SciFi tracker was chosen as the base line of the experiment, with the TPG option as a fallback solution and potential upgrade.

In both designs the surrounding solenoids are the same. The solenoids have a four tesla magnetic field with 1% field uniformity with an inner bore of 40 cm diameter. The active area of the spectrometers is 30 cm in diameter. The dimensions and positions of the solenoid relative to other experiment components are indicated in figure 4.6.

SciFi

The Scintillating fiber tracker, *SciFi*, consists of five planar stations, each made of three doublet[2] layers of scintillating fibers arranged at 120° with respect to the neighboring layers. The five stations are not equidistantly spaced in order to avoid resonances for certain beam momenta. The separations range between 10 and 45 cm, with the largest separation for the stations closest to the cooling channel. The fibers are double clad polystyrene fibers with a diameter of 0.350 mm, and the fiber pitch is 0.427 mm. The fibers must be as thin as possible to minimize multiple scattering and energy loss in the spectrometer, while still giving a sufficient number of photons to allow for event reconstruction. Fibers are ganged together in groups of seven fibers to optimize the resolution to cost ratio. The width of a channel is thus 1.63 mm, allowing a spatial resolution of 0.44 mm [58].

The concentrations of the dopants in the fibers have been chosen to maximize light output while minimize optical cross talk between neighboring fibers. The primary dopant has been chosen to be para-terphenyl, which gives scintillation light with a maximum at the wavelength 3500 Ångström. The secondary dopant, 3-hydroxflavone (3HF), absorbs this light and re-emits it at a wavelength of 5250 Ångström. Outside the 150 mm active radius the light will be piped by 1.05 mm clear fibers of a maximal length of 3 m to the readout system. Since the attenuation length of the clear fibers is 7.6 m this corresponds to 40% of the attenuation length, which is acceptable [58].

The SciFi trackers will use Visible Light Photon Counters, *VLPC*, on loan from the D0 experiment at Fermilab [65]. The VLPC is a low band-gap light-sensitive diode that is operated at 9 K to reduce thermal excitation and is ideal for use in MICE because

[2] A doublet layer consists of two singlet layers of fibers, arranged parallel but offset with respect to the other singlet layer, such that a pattern of equilateral triangles are formed.

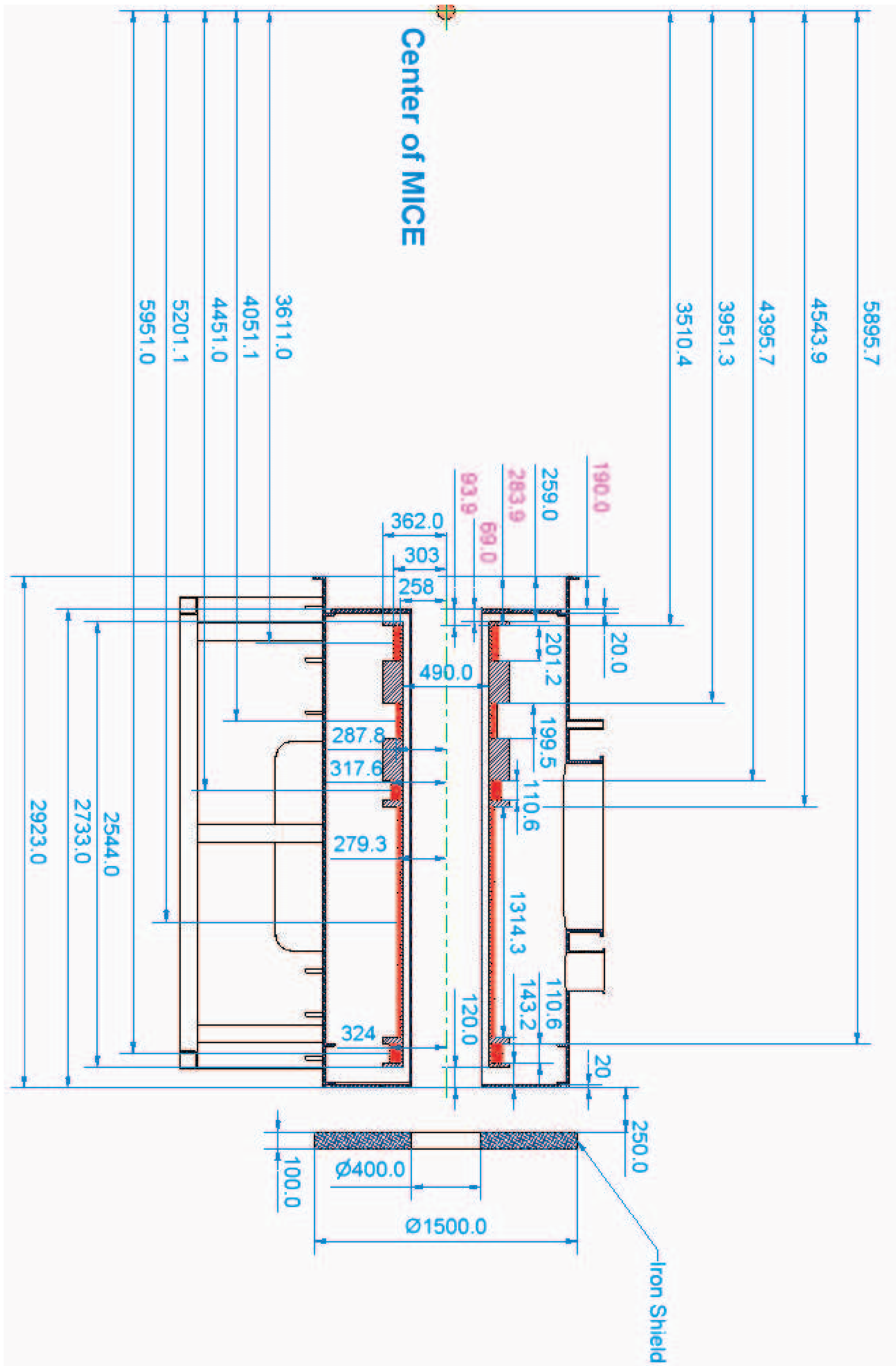

Fig. 4.6: A technical drawing of the spectrometer solenoid. This drawing was used by the author to define the positions of the iron shields, TOF1, TOF2 and the calorimeter. This was used for studies presented in chapter 10, where the iron shield geometry was redefined.

of its large quantum efficiency (85%) and relatively high gain (50,000). The VLPCs are also insensitive to the strong magnetic fields in the spectrometer regions, and have been successfully operated in the vicinity of an RF power source at D0. The expected light yield of a muon hit in this configuration is 8 photoelectrons per fiber singlet [58].

TPG

The second tracker design is a Time Projection Chamber, *TPC*, with GEM readout, named TPG. *GEM* stands for Gas Electron Multiplier. It is a 50 μm thick polymer foil with 5 μm copper coating on both sides, pierced by 60 μm diameter holes forming a hexagonal pattern with a pitch of 150 μm. The MICE TPG uses three GEM foils, separated by 2 mm gaps, with a high potential difference across the foils creating a high field region inside the holes. This allows efficient collection and amplification of drift electrons, while ion feedback into the active region is suppressed by the GEM structure itself.

The active volume is filled with gas at atmospheric pressure which is ionized along the track of a charge particle. The electrons are drifted toward the GEMs by an intense electric field. The charge is multiplied by the GEMs before it is picked up and digitized by the readout electronics. Initially the active volume was designed as 100 cm long and filled with Helium gas with ten percent of CO_2, which gave approximately 40 samplings of a track with 500 ns sampling period for the Flash ADCs. The large number of sampling points gave a superior momentum resolution of the reconstruction compared to the SciFi trackers, but this configuration has a number of problems.

- The vicinity of radio frequency cavities would produce a substantial background rate of RF induced electrons which create bremsstrahlung photons in the absorbers with the potential to generate low energy photoelectrons in the spectrometers.
- The transverse diffusion of the drift electrons was too wide at the end of the one meter drift, worsening the cluster position resolution.
- The low sampling frequency of the Flash ADCs, and the low drift velocity, together with the 600 good muon tracks per millisecond meant that on average a new muon track would be entering the spectrometer every three samplings, leading to multiple tracks in the tracker at any given time to disentangle.

The first potential problem was studied by the author and the results are presented in section 7.3. The second and third problems were solved by using a neon based gas mixture with much lower transverse diffusion over the drift length, and at the same time shortening the tracker active volume to 18 cm, while making the sampling time of the Flash ADC channels 100 ns. Furthermore the neon mixture has a faster drift velocity than its helium based counterpart, which reduces the occupancy in the spectrometer. Since the track is measured at so many points a full helix is not necessary, and an arc suffices. This also reduces the pile up of events and reduces the effective exposure to RF induced background.

The single problem which was not solved was the manufacturing process of the readout *hexaboard*, which consisted of three layers of strips at 120° angles with 0.5 mm pitch. The

Tab. 4.1: The two gas mixture candidates for the TPG tracker at 4 T.The drift field is 520 V/cm for $HeCO_2$ and 300 V/cm for $NeCO_2$ [66]. The lower diffusion together with faster drift velocity makes the neon based gas mixture a better candidate. Its increased sensitivity to RF induced background on form of bremsstrahlung photons can be negated by shortening the active region.

Parameter	$HeCO_2$	$NeCO_2$
Drift velocity [cm/μs]	1.68	3.0
Transversal diffusion [mm/$\sqrt{z[\mathrm{cm}]}$]	1.08	0.08
Longitudinal diffusion [mm/$\sqrt{z[\mathrm{cm}]}$]	1.64	0.2
Radiation length [cm]	151000	33000
Photo absorption factor at 100 keV [cm^{-1}]	$2.5 \cdot 10^{-5}$	$1.3 \cdot 10^{-4}$

amount of cross talk between individual strips was significant and occasionally shorts were found. Although later iterations of the hexaboard prototype showed better quality, it was decided by the review committee to keep the SciFi tracker design as the base line of the experiment. However the TPG shows better performance[3] and is the more economical option. Another argument for the short TPG was that the spectrometer solenoid could be much shorter, thus substantially reducing the cost of the experiment. The TPG design remains not part of the run plan of MICE but is considered a potential upgrade solution.

4.2.6 Absorber modules

A cooling cell consists of two linacs and two Absorber Focus Coil modules (AFC), shown in figures 4.7 and 4.8. An AFC module contains an absorber and a pair of focus coils, and is designed so the absorber is essentially independent of the surrounding volume for easy mounting and extraction during operation of the experiment.

As motivated in section 3.5.2, the optimal material for ionization cooling is hydrogen. The hydrogen is contained inside an aluminum vessel with thin aluminum windows, called *absorber windows*. In order to maintain a high ionization to multiple scattering ratio, the amount of hydrogen should be as large as possible for a given window thickness. However the change in emittance (3.40) also depends on the betatron function $\beta_\perp$ (3.38), which increases with the thickness of the absorber. The optimal cooling is obtained with 35 cm of liquid hydrogen. For safety reasons a vacuum region of longitudinal thickness 133 mm surrounds the hydrogen vessel, and an extra pair of aluminum windows, the *vacuum windows*, ensures the integrity of the vacuum.

Since the amount of passive material in the beamline must be kept at a minimum while supporting the differential pressure of the liquid hydrogen and the surrounding vac-

[3] The transverse momentum resolution obtained during tests with radioactive sources was 0.1 MeV/c [67], which is an order of magnitude better than the SciFi detector, and simulations using muons show twice as good resolution, even with the most recent SciFi tracker reconstruction software [66, 68].

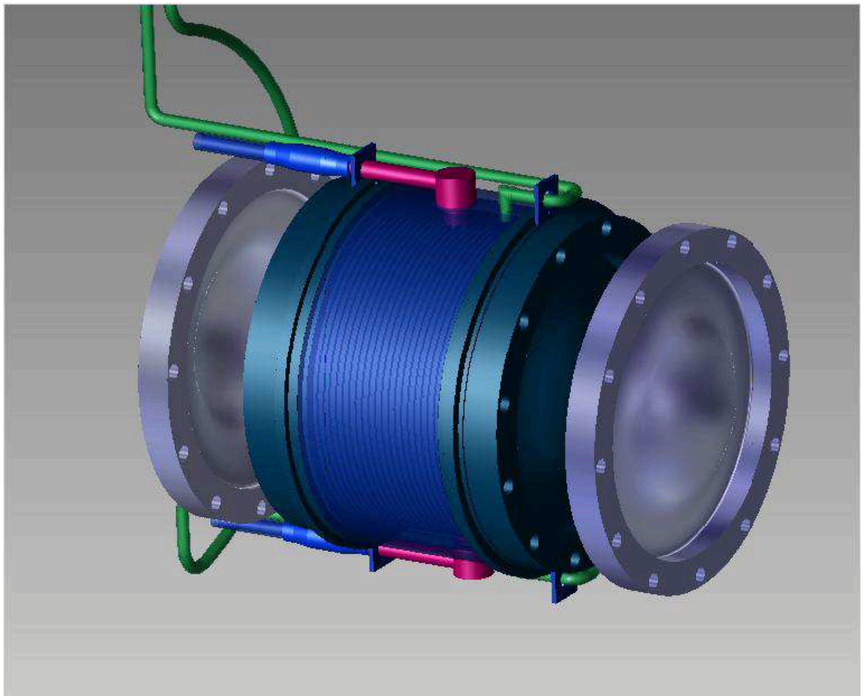

Fig. 4.7: A 3D rendering of an absorber generated from drawings stored in the MICE design office [56]. The absorber vessel containing liquid hydrogen is shown, together with its windows and the vacuum windows.

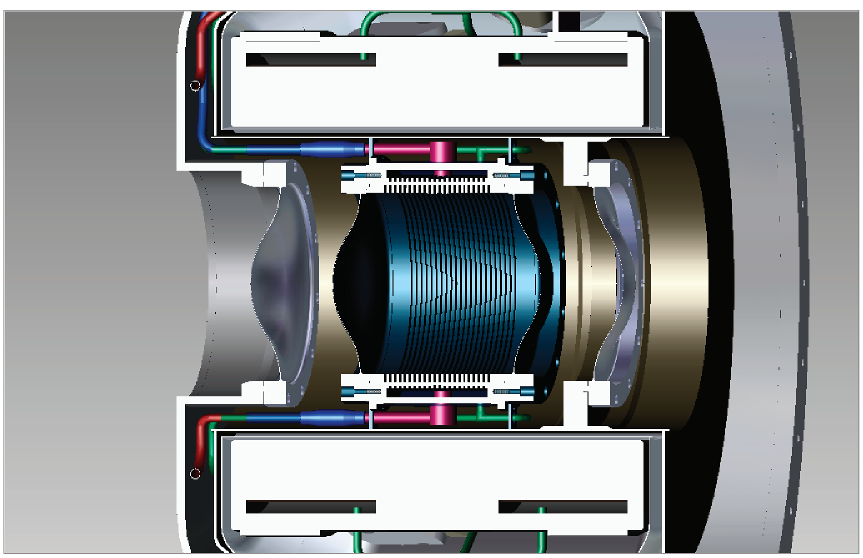

Fig. 4.8: A cut view of an absorber installed in an AFC module, generated from drawings stored in the MICE design office [56]. A pair of coils provides focusing.

uum, inflected tapered windows have been developed.[4] This window design incorporates a spherical cap joined to the mounting flange via an inflected, tapered toroidal section. This design is used for both absorber and vacuum windows.

Due to the convex shape, the liquid hydrogen in an absorber is 350 mm thick on the beam axis, and thinner further from the axis. The vessels have an inner diameter of 300 mm to accommodate the muon beam, while the vacuum windows have a diameter of 320 mm [56]. The absorber windows are 0.18 mm thick in the center, and the thickness increases with radius. With this thickness the bellow shaped windows support a burst pressure exceeding 6.4 bar, the minimum required for safe operation [58]. Should the pressure gradually increase beyond the breakpoint, the windows begin to leak before a breakdown occurs.

Hydrogen is maintained in liquid state by a cryocooler and natural convection. The absorber vessel has a heat-exchanging surface in the form of fins that extend into the hydrogen volume inside and into a channel outside of the cylinder. During operation the absorber is precooled by liquid nitrogen, and optionally liquid helium, before the nitrogen is pumped out and replaced by hydrogen. The vacuum space uses the warm bore tube of the focusing coil cryostat as its outer wall. The maximum heat removal capacity is 15 W, while the expected heat load for MICE is approximately 1 W [58].

4.2.7 RF cavities

After a particle has passed through an absorber and lost a fraction of its kinetic energy, it is reaccelerated in a linac consisting of four RF cavities for a total length of 1.87 m. The linac is designed to restore the same amount of energy to the muon as the energy loss in the absorber. The RF gradient available to the experiment is limited to 8 MV/m. The RF frequency is 201.25 MHz, and the linac is operated on crest.

Due to the large transverse size of the beam, the irises of the RF cavities must be large. To overcome the problem of low shunt impedance associated with large-iris open-cell cavities, the cavities are terminated electromagnetically by 0.38 mm thick beryllium windows. By making the windows thin and of a low Z material, the emittance heating effects due to multiple scattering can be kept to a minimum. It has been found that the thinnest window design for a given tensile stress is obtained for precurved windows. As the window temperature increases above 35°C, the windows start to flex in a gentle shape. By using precurved shapes (see figure 4.9(c)), the two windows of a cavity flex in the same direction thus keeping the cavity frequency shift to a minimum and well within the tuner's range [58].

For MICE, the available peak RF power is limited to 1 MW per cavity, and the duty factor is limited to one per mil. This is compatible with a 1 ms long spills at a repetition rate of 1 Hz, which brings the average power down to 1 kW per cavity. Nevertheless, the cavity bodies need direct cooling to handle the 1 kW average power losses and thus stabilize

[4] The designs of both absorber and vacuum windows have evolved from flat, via spherical and torispherical windows, to the present design which is also known as "bellow" shaped windows.

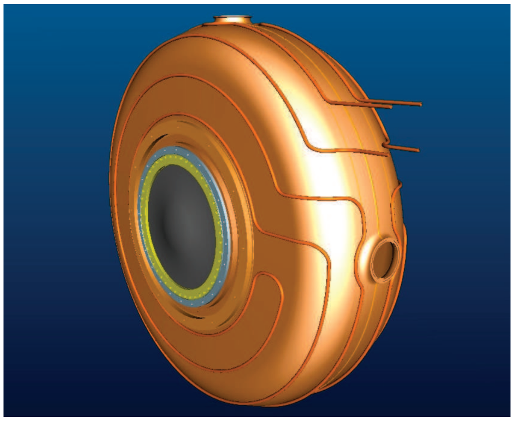

(a) MICE RF cavity

(b) Prototype cavity

(c) Cavity window

Fig. 4.9: MICE uses eight 201.25 MHz RF cavities for reaccelerating the beam in the cooling channel. (a) A 3D rendering of a MICE RF cavity with cooling pipes attached to the outer surfaces. (b) The 201.25 MHz prototype cavity. (c) A beryllium window used to close a MICE RF cavity.

the cavity frequency. A scheme using external water cooling tubes at room temperature will give sufficient cooling for the MICE cavities.

4.2.8 Downstream PID detectors

Originally the last time of flight detector should be followed by a Čerenkov detector, *CKOV2*, and a lead and scintillation fiber calorimeter at the very end for identification and classification of particles. However, work by the author of this thesis led to an improved calorimeter design which made CKOV2 redundant and a decision was taken to remove it from the experimental design. This work and the design of the calorimeter is presented extensively and discussed in chapter 8.

4.3 Run plan

The MICE experiment will be run in six well defined Stages, evolving from a very simple setup to a complete experiment with a full cooling channel. The six Stages are illustrated in figure 4.10 with their prospective dates.

The first step, Stage 1, is designed to characterize the beamline and estimate the beam content and calibrate detectors. For this purpose two time of flight stations, TOF0 and TOF1 will be installed together with the Čerenkov detector and the calorimeter. Since a full calorimeter cannot be constructed at this time, MICE will use a partial calorimeter.

In Stage 2, the first spectrometer will be installed in a spectrometer solenoid and positioned downstream of TOF1. The third time of flight detector, TOF2, will be placed between the spectrometer and the calorimeter. A few months later the second spectrometer

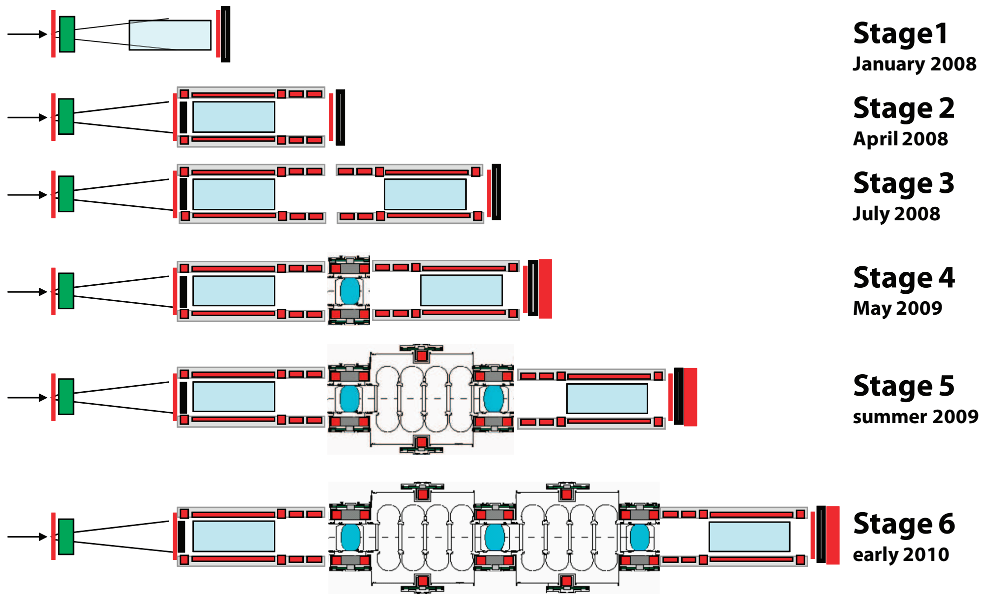

Fig. 4.10: The MICE Stages, with dates given October 2007.

with solenoid will be installed in Stage 3. Since there is no other material in the beam than what the spectrometers themselves introduce, the beam properties should be identical in both spectrometers. This will allow the spectrometers to be calibrated against each other, which will be important for accurate cooling measurements. Stage 3 concludes the first experimental phase, since all experimental factors should be well calibrated and understood by then.

With Stage 4, the experiment enters its second phase as the first absorber is installed between the two spectrometers. This allows measurements of the energy loss and multiple scattering in liquid hydrogen under a variety of focusing conditions. These parameters are the basis for the ionization cooling principle.

Acceleration is introduced in Stage 5, as a first cooling cell is installed which will allow the first experimental measurements of ionization cooling. In addition it will be the first time the experiment is exposed to RF induced background. In the sixth and final Stage of MICE, a second cooling cell is installed, which will provide the experiment with 10% cooling for a nominal 6π mm 200 MeV/c beam. In this phase, the experiment will run with several different beam settings to explore the emittance region between equilibrium emittance and 10π mm, for central momenta of 140, 170, 200 and 240 MeV/c respectively. The goal of the MICE collaboration is to complete the experiment by 2010, two years before the anticipated completion of the NF-IDS (http://www.hep.ph.ic.ac.uk/ids/) Conceptual Design Report.

5. INTERACTIONS AND PROCESSES

In this chapter particle physics processes and interactions which are of importance for later chapters are presented. The focus has been set on the implementation of these phenomena in Monte Carlo simulations, and special attention has been put on how the Geant4 software [61] models the processes.

As the primary scope of this thesis is neutrinos and muons, it is natural that greatest care has been taken for muonic processes. However, at the energies given for muon based neutrino experiments, radiative corrections and similar high energy physics phenomena do not occur. At theses energies muons are only semi relativistic, and a substantial number of electrons are thus generated through muon decay. Since electrons will mimic muon signals in the detectors, they are treated as background and must be correctly identified. For this reason it is important to understand, model and simulate both muonic and electronic processes accurately. Essentially all chapters in the second half of this thesis depend on the Monte Carlo implementations presented here.

For photons the most significant processes are the photoelectric effect, Compton scattering and electron positron pair production. There are other quantum mechanical processes for photons such as muon pair production, but due to the energy of the scenarios presented here, these three processes are sufficient. Figure 5.1 illustrates the absorption coefficient as a function of energy, and at very low energy the photoelectric effect dominates while the other processes make a significant contribution at the MeV scale.

At low energy the atomic shell structure becomes important. The default Geant4 process models are optimized for high energy physics and are using parameterization of atomic shell data. Geant4 provides low energy extensions to processes of photons and negative electrons using shell cross section directly, and in all simulations presented in this thesis, low energy extensions are used when available. For electrons, see figure 5.2 for an overview of the relative importance of the interactions as a function of energy.

5.1 Muonic processes

5.1.1 Muon decay

Muons are essentially heavy electrons and will decay into lighter particles while conserving the lepton number and other conserved quantities. The muon couples to a W boson and a muon neutrino in the first vertex. If the muon energy is low, the boson produces an electron and an antielectron neutrino in the second vertex.

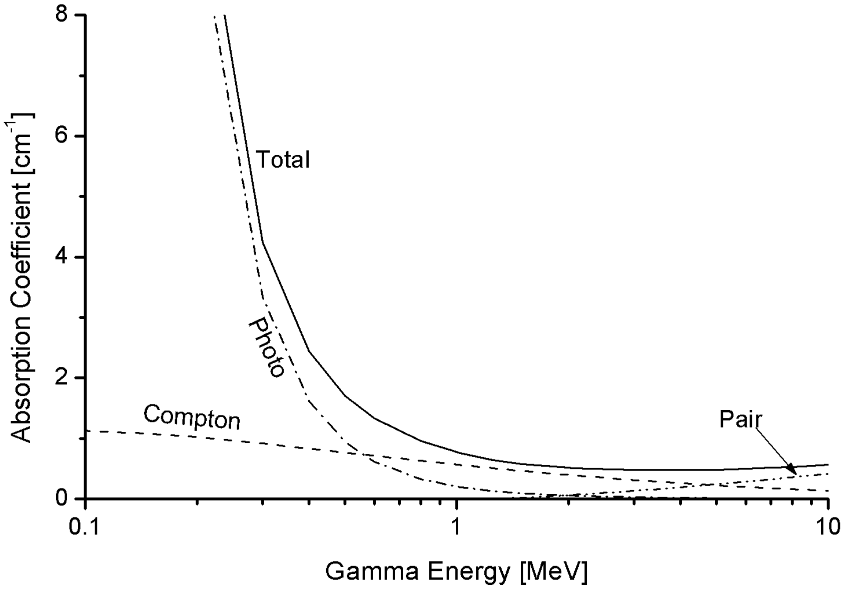

Fig. 5.1: The total absorption coefficient for gamma rays in lead, showing the contributions of photo electric effect, Compton scattering and pair production [69].

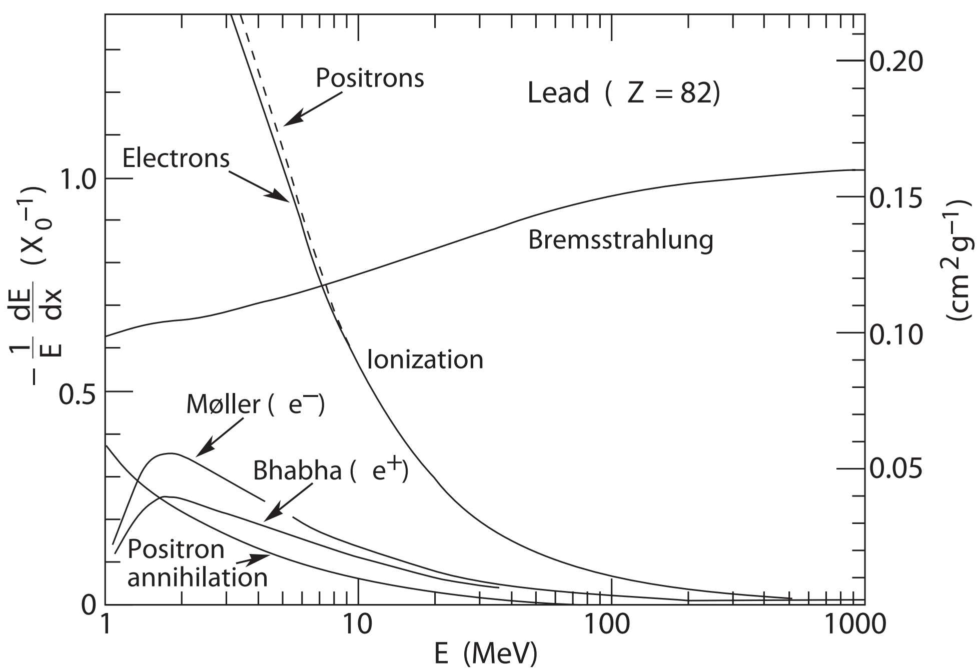

Fig. 5.2: Fractional energy loss per radiation length in lead as a function of electron or positron energy [1].

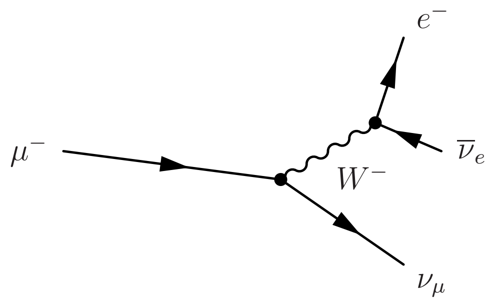

Fig. 5.3: Feynman diagram of a muon decay.

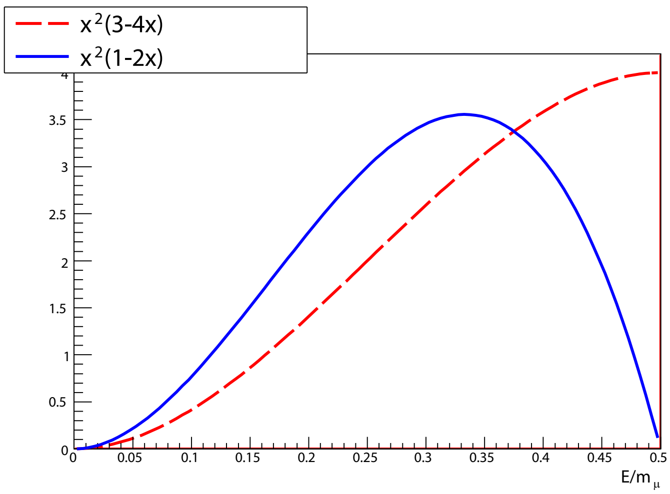

Fig. 5.4: The energy distributions in the rest frame of muon decay products, corresponding to (5.3) and (5.4).

In quantum field theory, the process can be expressed as

$$H_W^{eff} = \frac{G_F}{\sqrt{2}} \overline{\nu}_\mu \gamma_\mu (1-\gamma_5) \mu \overline{e} \gamma_\mu (1-\gamma_5) \nu_e \tag{5.1}$$

which after some algebra gives the differential decay rate, expressed as a function of electron energy in the center of mass frame,

$$\frac{\mathrm{d}\Gamma}{\mathrm{d}E_e} = \frac{G_F^2 m_\mu^2}{12\pi^3} E_e^2 \left(3 - 4\frac{E_e}{m_\mu}\right) \tag{5.2}$$

if the electron mass is neglected.

Fierz invariance allows the substitution of the electron by the muon neutrino,

$$\frac{\mathrm{d}\Gamma}{\mathrm{d}E_{\nu_\mu}} = \frac{G_F^2 m_\mu^2}{12\pi^3} E_{\nu_\mu}^2 \left(3 - 4\frac{E_{\nu_\mu}}{m_\mu}\right), \tag{5.3}$$

but for the antielectron neutrino one must instead of integrating over the electron and muon neutrino momenta, integrate over the two neutrino momenta, which gives

$$\frac{\mathrm{d}\Gamma}{\mathrm{d}E_{\overline{\nu}_e}} = \frac{G_F^2 m_\mu^2}{12\pi^3} E_{\overline{\nu}_e}^2 \left(1 - 2\frac{E_{\overline{\nu}_e}}{m_\mu}\right). \tag{5.4}$$

The two neutrino spectra are different, as shown in figure 5.4. The expectation value of the muon neutrino energy in the center of mass system is 37.0 MeV, while the antielectron neutrino has an expectation value of 31.7 MeV [3].

The decay rate can be calculated from equation (5.2) by integration over the possible electron energies,

$$\Gamma = \int_0^{m_\mu/2} \frac{\mathrm{d}\Gamma}{\mathrm{d}E_e} \mathrm{d}E_e = \frac{G_F^2 m_\mu^5}{192\pi^3}, \tag{5.5}$$

and with values for the Fermi constant $G_F = 1.166 \times 10^{-5}\ GeV^{-2}$ and muon mass $m_\mu = 0.1056\ GeV$ one arrives at the life time

$$t_\mu = \Gamma^{-1} = 2.1948\ \mu s \tag{5.6}$$

where $\hbar = 6.582 \times 10^-25\ GeVs$ was used to go from natural units to laboratory units. The experimental value is 2.1970 μs [3], hence the Standard Model theory of weak interactions agrees well with experiments. Even better agreement is found if the electron mass correction and the fine structure constant is included in the calculation.

Since the muon decay process does not involve any hadrons it is a very clean and simple weak interaction process which is used for determining the strength of the weak interactions. It is therefore of great importance to measure experimentally the decay rate of the muon with high accuracy. One such experiment is FAST [70], in which Geneva University is involved.

Kinematics of muon decay

The lab frame velocity of electrons resulting from muon decay is

$$\beta_e = \frac{\acute{\beta}_e + \beta_\mu}{1 + \acute{\beta}_e \beta_\mu}. \tag{5.7}$$

where $\acute{\beta}_e$ where is the electron velocity in the muon decay center of mass and β_μ is the muon velocity in the lab frame. Using natural units, $c = 1$,

$$\beta = \frac{p}{E} \tag{5.8}$$
$$E^2 = p^2 + m^2 \tag{5.9}$$

equation (5.7) can be expressed as

$$\frac{p_e}{E_e} = \frac{\acute{p}_e E_\mu + \acute{E}_e p_\mu}{\acute{p}_e p_\mu + \acute{E}_e E_\mu}. \tag{5.10}$$

Using conservation of energy and momentum in the center of mass frame, while neglecting polarization effects, one can conclude that the maximum center of mass energy the electron can obtain in the decay is

$$\acute{E}_e = \frac{m_\mu^2 + m_e^2}{2m_\mu} \approx \frac{m_\mu}{2} \tag{5.11}$$

which together with the relations above give the allowed range of electron momenta in the lab frame, illustrated in figure 5.5. As a rule of thumb the electron can have a maximum momentum in the forward direction equal to the momentum of the muon, and a minimum momentum of zero for backward decay. This holds for values of $p_\mu \gtrsim E_\mu$, until

$$p_\mu \geq \frac{m_\mu}{m_e} p_e \approx 10.9 \text{ GeV/c} \tag{5.12}$$

when the muon is as relativistic in the lab frame as the electron is in the muon rest frame.

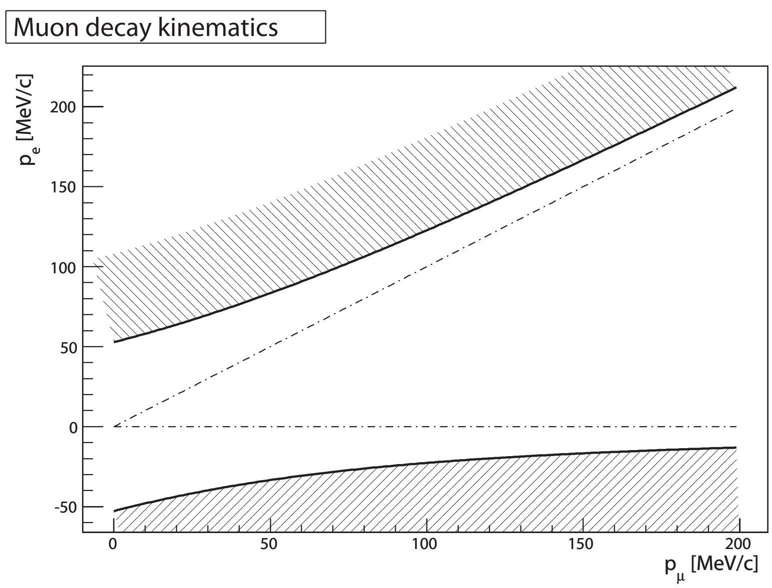

Fig. 5.5: The kinematically allowed longitudinal momentum of the electron coming from muon decay as a function of the longitudinal momentum of the muon. At rest, the maximum electron momentum is $m_\mu/2$. As the muon becomes more relativistic the electron tends to have a lab frame momentum in the forward direction. The dashed lines are given by $p_e = p_\mu$ and $p_e = 0$.

The reason for this rather lengthy exercise is to conclude some very important properties of the muon decay electrons:

- The electrons and muons fill up the same momentum space.
- The momentum spread of the electrons is very large.

The first of these properties is the reason why the MICE experiment is keeping close attention to this type of background. The second point indicates why a simple time of flight comparison between muons and electrons might not be enough for particle identification. Chapters 7 and 9 are dedicated to this issue.

Muon decay in Geant4

The muon decay process is handled in Geant4 using the G4MuonDecayChannel class. G4MuonDecayChannel simulates muon decay according to $V-A$ theory. Neglecting the electron mass, the electron energy is sampled from

$$\frac{\mathrm{d}\Gamma}{\mathrm{d}\epsilon} = \frac{{G_F}^2 {m_\mu}^5}{192\pi^3} 2\epsilon^2(3-2\epsilon) \tag{5.13}$$

where Γ is the decay rate, $\epsilon = E_e/E_{max}$, E_e is the electron energy and E_{max} is the maximum allowed electron energy. This is the same equation as (5.2), expressed in ϵ. Geant4 neglects the electron mass so $E_{max} \doteq m_\mu/2$.

The neutrino energy is not correctly modeled in Geant4, since it does not take the $V-A$ distributions into account. Instead they are generated back-to-back and isotropically in the neutrinos' center-of-mass frame, with the magnitude of the neutrino momentum chosen to conserve energy in the decay. The two neutrinos are then boosted opposite to the momentum of the decay electron. In all simulations presented in this thesis, the neutrinos are killed after generation and this simplification does not affect the results. However for a future study of a neutrino detector this could be a problem that must be solved. Neither the polarization of the muon nor the electron is considered in the implementation of the decay process.

If the particle energy changes during the step due to energy loss or electromagnetic fields, its lifetime in the laboratory frame changes. This update is performed after the step and is given by

$$\Delta t_{lab} = \frac{\Delta x}{0.5(v_0 + v)} \tag{5.14}$$

where Δx is the step length travelled by the particle velocity during the step. This expression is a good approximation if the velocity is not allowed to change too much during the step.

5.1.2 Muon ionization

When a muon passes through the electromagnetic field of an atom it can interact with its electrons and thus transfer energy to the atom. If the energy transfer is high enough, the atom is left ionized. If the muon traverses a dense material, several such interactions take place. Such a continuous energy loss is described by the Bethe-Block formula,

$$\frac{dE}{dx} = 2\pi r_e^2 mc^2 n_{el} \frac{z_p^2}{\beta^2}\left[\log\frac{2mc^2\beta^2\gamma^2 T_{up}}{I^2} - \beta^2\left(1+\frac{T_{up}}{T_{max}}\right) - \delta - \frac{2C_e}{Z}\right] \tag{5.15}$$

where r_e is the classical electron radius, mc^2 is the mass energy of the electron, n_{el} is the electron density of the material, I is the mean excitation of the material and T_{up} is the minimum of the maximum transferable energy T_{max}

$$T_{max} = \frac{2m_e c^2 \left(\gamma^2 - 1\right)}{1 + 2\gamma\frac{m_e}{m_\mu} + \left(\frac{m_e}{m_\mu}\right)^2} \tag{5.16}$$

and an energy cut $T_{cut} = 1$ keV [71].

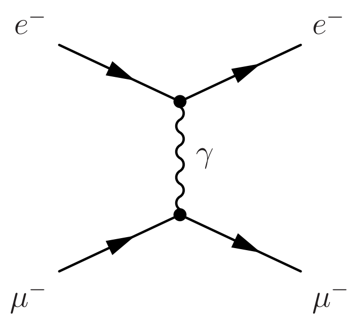

Fig. 5.6: Feynman diagram of a muon ionization. Energy is transferred from the incoming muon to the bound electron, ionizing the material.

The number of electrons can be expressed as

$$n_{el} = Zn_{atoms} = \frac{Z}{A}\mathcal{N}\rho \tag{5.17}$$

where $\mathcal{N}$ is the Avogadro number, A is the mass of a mole, and ρ is the density. A first order approximation is given by (5.15) and (5.17)

$$\frac{1}{\rho}\frac{dE}{dx} \propto \frac{Z}{A} \tag{5.18}$$

which decreases with increasing Z due to the increased neutron content in the nuclei. Thus hydrogen has the highest energy loss per density, a property which will be used extensively later.

At high particle energies the muon becomes more relativistic and the electromagnetic field of the muon flattens and extends. This causes the effective charge density of the medium to increase, which explains the logarithmic term in (5.15). However at these energies, the medium becomes polarized which truncates the field extension, and this correction is summarized as δ. At very high energies, radiative effects dominate the energy loss of muons. The Bethe-Block curve has a minimum where the negative slope makes the contribution at larger energies small, while the logarithmic rise is not yet dominant. The momentum where this occurs is called *minimum ionization* momentum, and a particle at this point is referred to as *minimum ionizing particle*, or *mip*.

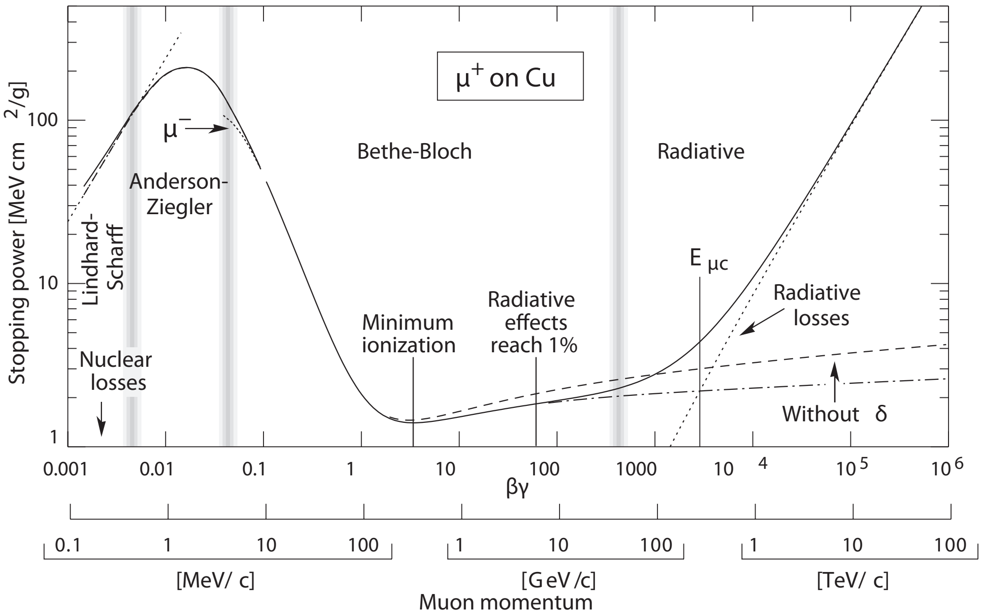

Fig. 5.7: Stopping power for positive muons in copper as a function of $\beta\gamma = p/m$. Solid curves indicate the total stopping power. Vertical bands indicate boundaries between different approximations. The short dotted lines labeled μ^- illustrate the "Barkas effect", the dependence of stopping power on projectile charge at very low energies. This figure was taken from [1].

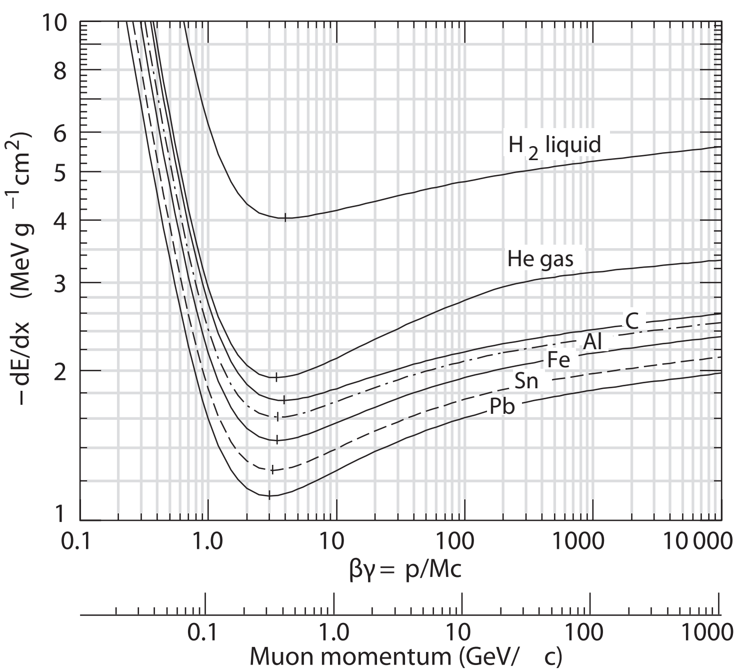

Fig. 5.8: Stopping power of various materials for muons as a function of momentum [1]. Radiative effects are not included, which become significant at $\beta\gamma \gtrsim 1000$. Notice the dependence on Z.

The last term in (5.15), $2C/Z$, is a function which corrects for the binding energy of the atoms. This is important for low energy, but there are few good models which describe all materials satisfactorily, and instead the Barkas [72] method is used which parameterizes C as

$$C(I, \beta\gamma) = \frac{a(I)}{(\beta\gamma)^2} + \frac{b(I)}{(\beta\gamma)^4} + \frac{c(I)}{(\beta\gamma)^6} \tag{5.19}$$

where a, b, and c are tabulated. At even lower energies

$$T < 2\frac{m_\mu}{m_{proton}} \approx 0.2 \text{ MeV} \tag{5.20}$$

the Bethe-Block formula (5.15) can no longer be used, and Geant4 instead uses a special model for the Bragg region.

Delta ray production in Geant4

Geant4 uses a cut in energy for the production of secondary particles. This production threshold is denoted T_{cut}, and was mentioned in the explanation of (5.15). Below the cut the ionization of the muons is modeled as a continuous energy loss, with no secondary particles created. For energies above the cut, secondary particles are explicitly generated, and in the case of muon ionization this is usually in the form of delta electrons. The mean rate of energy loss is given by:

$$\frac{\mathrm{d}E_{soft}(E, T_{cut})}{\mathrm{d}x} = n \int_0^{T_{cut}} \frac{\mathrm{d}\sigma(Z, E, T)}{\mathrm{d}T} T \; \mathrm{d}T \tag{5.21}$$

where n is the number of atoms per volume in the material. At energies above the delta electron production cut, the cross section for producing a secondary is

$$\sigma(Z, E, T_{cut}) = \int_{T_{cut}}^{T_{max}} \frac{\mathrm{d}\sigma(Z, E, T)}{\mathrm{d}T} \; \mathrm{d}T \tag{5.22}$$

where T_{max} (5.16) is the maximum energy transferable to the secondary particle. The cross section can be factorized as

$$\frac{\mathrm{d}\sigma}{\mathrm{d}T} = k f(T) g(T) \tag{5.23}$$

where

$$f(T) = \frac{1}{T^2}\left(\frac{1}{T_{cut}} - \frac{1}{T_{max}}\right) \tag{5.24}$$

$$g(T) = 1 - \beta^2 \frac{T}{T_{max}} + \frac{T^2}{2E^2} \tag{5.25}$$

and k is a Z dependent normalization constant [71].

Using these two functions, Geant4 performs a two dimensional rejection Monte Carlo integration of the differential cross section by sampling $f(T)$, and using a sampling on $g(T)$ as a rejection function[1].

The angle of the delta electron is given by energy momentum conservation, and is chosen with respect to the direction if the incident muon. The azimuthal angle is randomly chosen with a flat distribution. The method of secondary track generation outlined in this section is also used in Geant4 for other processes which produce secondaries.

5.2 Electronic processes

5.2.1 Electron ionization

Electron ionization is very similar to muon ionization. Ionization with an incoming positron is however slightly different than the corresponding phenomenon for negative electrons. Historically the e^-e^- scattering is called Møller scattering and the e^+e^- scattering Bhabha scattering. In addition to exchange of a virtual photon, an intermediary Z-boson also contributes to the total cross section, which causes parity violation. The parity violation is not modeled in the software used in this thesis.

The maximum energy transferable to a free electron is

$$T_{max} = \begin{cases} E - mc^2 & \text{for } e^+ \\ \frac{1}{2}\left(E - mc^2\right) & \text{for } e^- \end{cases} \tag{5.26}$$

where the factor of two comes from interchangeability of the two electrons.

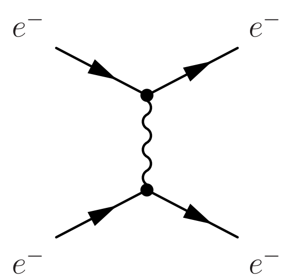

(a) t-channel

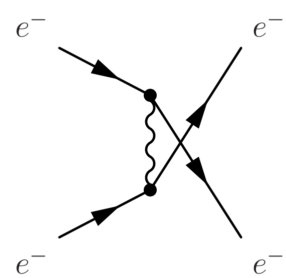

(b) u-channel

Fig. 5.9: Feynman diagrams of Møller scattering.

For negative electron ionization the work performed in this thesis uses the Geant4 low energy extension, where the energy loss of the incident electron expresses as a sum over all

[1] This method would give an error equal to $\sqrt{2var(g)/N}$ when applied to a two dimensional triangle, while a folding Monte Carlo would only have an error equal to $\sqrt{var(g)/N}$. Depending on the weighting function used, a weighting Monte Carlo method could be even more efficient by using a nonuniform sampling which is then weighted with the inverse of the distribution density [73].

atomic shells s

$$\frac{\mathrm{d}E}{\mathrm{d}x} = \sum_s \left(\sigma_s \frac{\int_{0.1eV}^{T_{cut}} t \frac{\mathrm{d}\sigma}{\mathrm{d}t} \mathrm{d}t}{\int_{0.1eV}^{T_{max}} \frac{\mathrm{d}\sigma}{\mathrm{d}t} \mathrm{d}t} \right) \tag{5.27}$$

where T_{cut} is the delta electron production threshold of the material and t is the energy of the δ-electron. The emission probability of a δ-electron is

$$\frac{\mathrm{d}\sigma}{\mathrm{d}t} = \frac{P(x)}{x^2} \quad \text{with } x = \frac{t + B_s}{T + B_s} \tag{5.28}$$

where B_s is the binding energy of atom s. The function $P(x)$ contains fits on EEDL data which for high energy ($x \gg 1$) transforms into Møller scattering.

The sampling of the final state proceeds in three steps. First a shell is randomly selected, then the energy of the delta-electron is sampled, finally the angle of emission of the scattered electron and of the δ-electron is determined from energy-momentum conservation, which also takes into account the electron movement in its bound state.

Note that a corresponding low energy extension for positrons does not exist in Geant4.

5.2.2 Bremsstrahlung

When a charged particle enters a region of electromagnetic field, it can be decelerated and the energy is lost as a photon. The phenomenon called synchrotron radiation is thus a special case of bremsstrahlung, although the latter term is usually reserved for the interaction with atoms in matter.

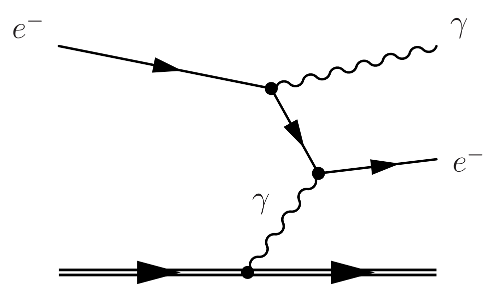

Fig. 5.10: Feynman diagram of a bremsstrahlung interaction for an electron.

At energies above minimum ionization, the ionization energy loss increases logarithmically, while the energy loss due to bremsstrahlung radiation rises almost linearly. *The critical energy*, E_c, is the energy where the energy loss contribution from bremsstrahlung equals the contribution from ionization. A simple estimate is [1]

$$E_c \approx \frac{800 \text{ MeV}}{Z + 1.2} \tag{5.29}$$

hence the energy loss for electrons are dominated by bremsstrahlung at energies above 7.8 MeV in lead, or 82 MeV in carbon. This feature plays a major role in the chapter of the calorimeter design (chapter 8).

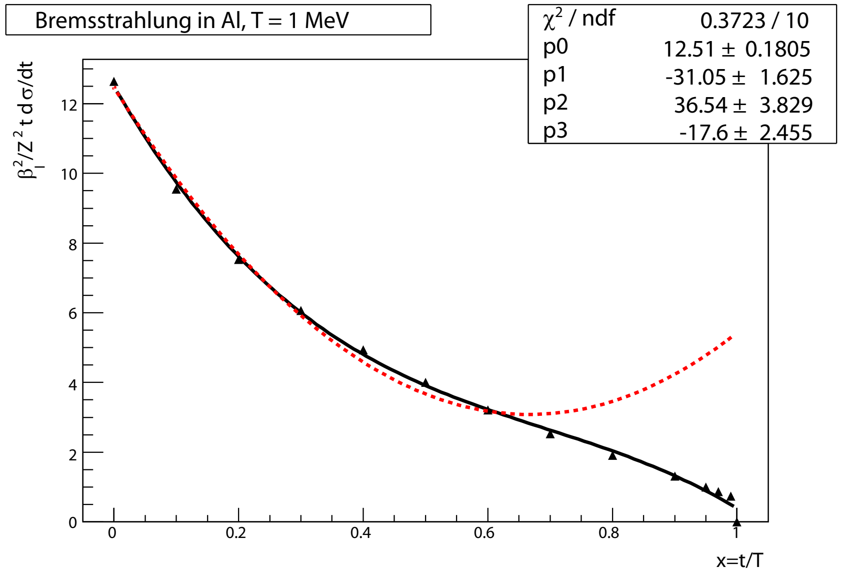

Fig. 5.11: The differential cross section for bremsstrahlung. The markers are values tabulated by Seltzer & Berger [74], and the dashed line is a fit using (5.31), while the solid line is a polynomial of the third degree. Close to the cutoff, the model described by (5.31) fails.

Other charged particles also have a "critical energy", but it is much higher than for electrons. No simple mass scaling law exists, but for muons in solids [1]

$$E_c^\mu \approx \frac{5.7 \text{ TeV}}{(Z+1.47)^{0.838}} \tag{5.30}$$

gives the energy where the radiative energy loss is equal to the energy loss due to ionization.

Throughout this thesis, the term bremsstrahlung is implicitly understood as bremsstrahlung for electrons and positrons, but it also applies to other particles as muons and protons. However, since the cross section for bremsstrahlung is inversely proportional to the square of the particle mass, the critical energy for muonic bremsstrahlung is found at several hundred GeV, and does not contribute to the energy loss in MICE. The low cross section for muonic bremsstrahlung is the main reason for the high penetration power of muons compared to electrons.

To the first order, the cross section for emitting a bremsstrahlung photon of energy t is given by

$$\frac{\mathrm{d}\sigma}{\mathrm{d}t} \approx \frac{4}{3}\frac{A}{X_0 \mathcal{N} t}\left(1 - x + 0.75x^2\right) \tag{5.31}$$

where $\mathcal{N}$ is the Avogadro number, A the atomic mass, X_0 the radiation length of the absorber, and

$$x = \frac{t}{T}\ ,\ 0 \leq x \leq 1 \tag{5.32}$$

is the fraction of energy transferred to the photon from an electron with initial kinetic energy T.

The radiation length is both the mean distance over which a high-energy electron loses all but $1/e$ of its energy by bremsstrahlung, and 7/9 of the mean free path for pair production by a high-energy photon. A good fit to the data is [1]

$$X_0 = \frac{716.4A \text{ g cm}^{-2}}{Z(Z+1)\ln(287/\sqrt{Z})} \tag{5.33}$$

and for a mixture or compound the radiation length can be calculated by

$$\frac{1}{X_0} = \sum_i \frac{w_i}{X_{0,i}} \tag{5.34}$$

where w_i is the fraction by weight.

As $t \to 0$, (5.31) diverges, and the formula is no longer applicable. This infrared divergence does however not appear in Nature due to the LPM effect (see below), and dielectric suppression. A more complete calculation of the cross section can be found in Seltzer & Berger [74], which uses the screened Bohr approximation with Coulomb corrections. The Coulomb corrections become significant for low energies and high Z[2]. Furthermore, close to the high energy cutoff

$$\frac{\mathrm{d}}{\mathrm{d}x}\left(t\frac{\mathrm{d}\sigma}{\mathrm{d}t}\right) > 0 \ , \text{ for } x \to 1, \tag{5.35}$$

which does not agree with experimental data or Seltzer Berger [74]. Therefore (5.31) is only a good description of the bremsstrahlung cross section for the midrange of x. Effects like electron–electron bremsstrahlung, multiple photon emission etc, appear in higher order corrections.

Bremsstrahlung in Geant4

To first order Geant4 uses the parameterization

$$\sigma(Z,T,k_c) = Z(Z+\xi_\sigma)(1-c_{sigh}Z^{1/4})\left(\frac{T}{k_c}\right)^\alpha \frac{f_s}{\mathcal{N}} \tag{5.36}$$

for electron kinetic energy $T > 10$ MeV, where ξ_σ, c_{sigh} and α are constants and f_s is a Z dependent polynomial. The energy cut off, k_c, is the point below which photons are treated as continuous energy loss without production of secondary particles. The user controls the value of k_c by giving an estimated minimum range for the secondaries, and is thus material dependent. This model gives a relative error on the energy loss of $\sim 5-6\%$ at energies above 1 MeV [71]. Positron cross section follows the same curve as electrons but with a different scaling. To first order this only depends on the energy and the Z of the material. At 1.35 MeV in lead, the energy loss of positrons due to radiation is half of the radiative energy loss of electrons, and the difference becomes larger for lower energies [71]. However

[2] 2-3% in aluminum for an outgoing electron with kinetic energy 1 MeV.

with decreased energy, the cross section for other processes like ionization increases and in practice the energy loss observed is rather similar for the two particles.

In the low energy extension, which only exists for e^-,

$$\frac{dE}{dx} = \sigma(T)\frac{\int_{0.1\ \mathrm{eV}}^{T_{cut}} t\frac{d\sigma}{dt}dt}{\int_{0.1\ \mathrm{eV}}^{T_{max}} \frac{d\sigma}{dt}dt} \tag{5.37}$$

where $\sigma(T)$ is the total cross section for a given T. At energies above the cut, T_{cut}, the emission probability of a photon with energy t is

$$\frac{d\sigma}{dt} = \frac{P(x)}{x} \quad \text{with } x = \frac{t}{T} \tag{5.38}$$

where $P(x)$ is a function which describes the energy spectra of outgoing photons and is taken from the EEDL data library. For high energies the function is close to

$$P(x) \propto 1 - x + 0.75x^2. \tag{5.39}$$

Figure 7.12(a) shows the distribution obtained when (5.39) is applied on (5.38).

Geant4 also implements the *Landau Pomeranchuk Migdal* (LPM) effect, which is the destructive interference due to multiple scattering in the formation zone. This effect becomes significant at

$$\frac{t}{T} \lesssim \frac{T}{E_{LPM}} \tag{5.40}$$

where E_{LPM} is a material constant given by

$$E_{LPM} = \frac{\alpha m^2 X_0}{2hc} \tag{5.41}$$

where α is the fine structure constant and h is the Planck constant. The LPM effect suppresses the infrared divergence which otherwise would occur as $t \to 0$.

5.2.3 Annihilation

Free positrons are rarely observed in nature. That is because they quickly interact with electrons in their vicinity and annihilate. Contrary to the literal translation of annihilation into English from Latin, "to make into nothing", the energy released by the annihilation mechanism is carried by new particles produced in the process. At low energy, electron positron annihilation can only produce a photon pair, since other channels are not kinematically allowed. Due to conservation of momentum and energy, a single photon cannot be produced by annihilation in vacuum.

In Geant4, the simulation of annihilation assumes that the electron is free and at rest. Furthermore the simulation model treats only two photon production, since formation of positronium is not implemented. The fraction of energy transferred to a photon a is

$$\epsilon = \frac{E_a}{E_{tot}} \equiv \frac{E_a}{T + 2mc^2} \tag{5.42}$$

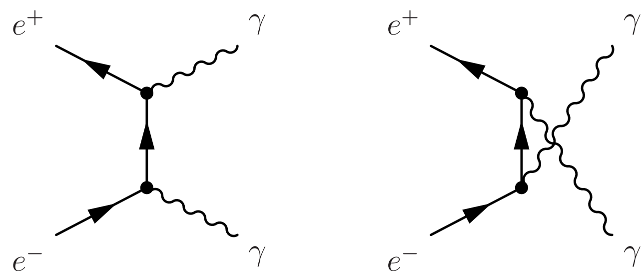

Fig. 5.12: Annihilation of an electron and a positron pair into photons.

where $T = (\gamma - 1)\, mc^2$ is the kinetic energy of the positron. The kinematics of the process gives that ϵ can only take values

$$\frac{1}{2}\left[1 - \sqrt{\frac{\gamma-1}{\gamma+1}}\right] \;\leq\; \epsilon \;\leq\; \frac{1}{2}\left[1 + \sqrt{\frac{\gamma-1}{\gamma+1}}\right]. \tag{5.43}$$

The value of ϵ is chosen randomly and can be used in the formula for the cross section [75]

$$\frac{d\sigma(Z,\epsilon)}{d\epsilon} = \frac{Z\pi r_e^2}{\epsilon\,(\gamma-1)}\left[1 + \frac{2\gamma}{(\gamma+1)^2} - \epsilon - \frac{1}{(\gamma+1)^2}\frac{1}{\epsilon}\right] \tag{5.44}$$

to calculate the probability of the process occurring. The angle between the incident positron and the photon a is given by conservation of momentum,

$$\cos\theta = \frac{\gamma + 1 - \epsilon^{-1}}{\sqrt{\gamma^2 - 1}} \tag{5.45}$$

while the angle ϕ is randomly chosen isotropically.

5.3 Photonic processes

5.3.1 Photoelectric effect

The photoelectric effect is the ejection of an electron from a material after a photon has been absorbed by that material, as shown in figure 5.13. Beer-Lambert's law gives the transmittance of photons through an absorber,

$$I = I_0 e^{-\mu x} \tag{5.46}$$

where μ is the absorption coefficient and x is the thickness of the absorber.

The photoelectric cross section depends very strongly on Z and E_γ,

$$\sigma_{p.e.} \propto \mu_{p.e.} \propto \frac{Z^n}{E_\gamma^3} \tag{5.47}$$

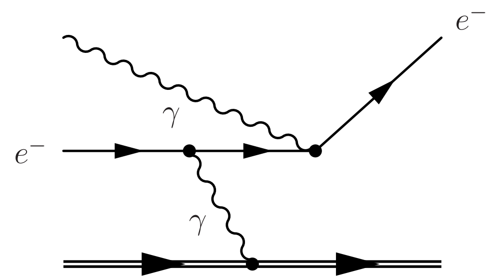

Fig. 5.13: Feynman diagram of photoelectric effect.

where $\mu_{p.e.}$ is the absorption coefficient due to photoelectric effect. The exponent n is close to 5 for materials with low Z, and decreasing to around 4 for high Z materials. For this reason, the photoelectric effect dominates the energy loss and attenuation of photons in dense materials and for low energy x-rays. Furthermore, the absorption coefficient contains sharp peaks at low energies, since the binding energy of high energy atomic shells exceeds the energy of the incoming photon. The energies of the photopeaks are material dependent.

The Geant4 implementation of the phenomenon uses least square fits on experimental data for the cross section calculation. In a given material the mean free path, λ, for a photon to interact via the photoelectric effect is given by :

$$\lambda(E_\gamma) = \left(\sum_i n_{ati} \cdot \sigma(Z_i, E_\gamma)\right)^{-1} \tag{5.48}$$

where n_{ati} is the number of atoms per volume of the i^{th} element of the material. A photon can be absorbed if $E_\gamma > B_{shell}$, where the shell energies in Geant4 are taken from experimental data. The photoelectron is emitted with kinetic energy :

$$T_{photoelectron} = E_\gamma - B_{shell}(Z_i). \tag{5.49}$$

A related process is called the Auger effect. It occurs when the photoelectric effect causes a higher energy level electron to fall into the hole created by the photoelectron, and the resulting energy release is carried away by a second emitted electron instead of the usual photo emission.

5.3.2 Compton scattering

Compton scattering, or the Compton effect, is the interaction between an incoming photon and the electron of a material which results in a decreased energy and change in direction of the photon. Compton scattering is a quantum mechanical effect which in the classical limit is called Thomson scattering.

The absorption coefficient is linearly proportional to Z and inversely proportional to the photon energy,

$$\mu_C \propto \frac{Z}{E_\gamma} \tag{5.50}$$

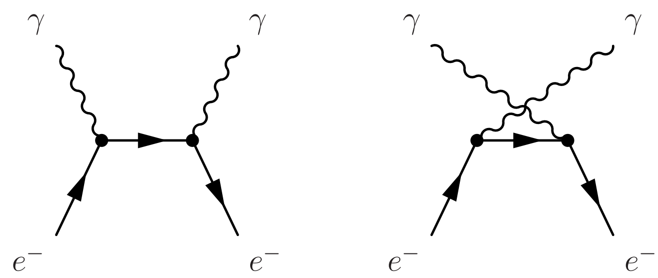

(a) s-channel (b) u-channel

Fig. 5.14: Feynman diagrams of Compton scattering.

and the weaker dependence on Z and E_γ compared to the photoelectric effect, entails that Compton scattering dominates over the latter when the Z of the material is low, or when the energy is large. At high energy, pair production dominates over both of these two effects, but as a rule of thumb Compton scattering always dominates the photonic interactions for $E_\gamma \approx 1$ MeV.

The quantum mechanical Klein-Nishina differential cross section per atom is

$$\frac{d\sigma}{d\epsilon} = \pi r_e^2 \, \frac{m_e c^2}{E_0} Z \left[\frac{1}{\epsilon} + \epsilon\right] \left[1 - \frac{\epsilon \sin^2\theta}{1+\epsilon^2}\right] \tag{5.51}$$

where r_e is the classical electron radius, $m_e c^2$ is the electron mass, E_0 is the energy of the incident photon, E_1 is the energy of the scattered photon and $\epsilon = E_1/E_0$. Assuming an elastic collision, the scattering angle θ is defined by the Compton formula for the wavelength shift

$$\Delta\lambda = \frac{h}{m_e c}\,(1 - \cos\theta) \tag{5.52}$$

which expressed in energy becomes

$$E_1 = E_0 \, \frac{m_\mathrm{e} c^2}{m_\mathrm{e} c^2 + E_0(1-\cos\theta)}. \tag{5.53}$$

Notice that this assumes that the electron is free. If the electron is bound to an atom, the expression would be a bit more complicated as the nucleus would also take part in the process. In the low energy extension, Geant4 uses Hubbel's atomic form factor to calculate the energy and angular distributions as a product of the Klein-Nishina formula and a material dependent scattering function. Since the incoherent scattering occurs mostly in the outermost atomic subshells, the binding energy of the atom can be neglected [71].

5.3.3 Gamma conversion into an electron-positron pair

When a photon passes through the electromagnetic field of an atom it can produce an electron–positron pair without violating momentum or energy conservation. In vacuum this would not be kinematically possible. Energy in excess of the equivalent rest mass of the two particles (1.02 MeV) appears as the kinetic energy of the pair and the recoil nucleus.

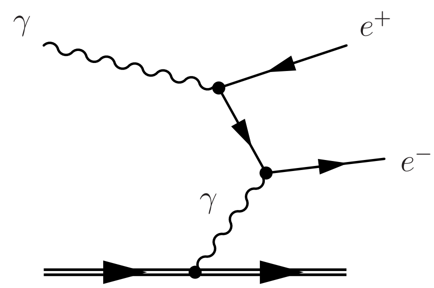

Fig. 5.15: Feynman diagram of electron–positron pair production.

Well above the threshold, the absorption coefficient for pair production is independent of the energy and depends only on the radiation length X_0 (5.33) of the material.

$$\mu_{pair} = \frac{7}{9} X_0^{-1} \tag{5.54}$$

Since the absorption coefficient does not decrease with increased energy, as in the case of the other photonic processes, pair production is the dominating process for photons of energies higher than a few MeV.

The total cross section in Geant4 is parameterized as

$$\sigma(Z, E_\gamma) = Z(Z+1)\left(F_1(x) + F_2(x)Z + \frac{F_3(x)}{Z}\right) \tag{5.55}$$

where

$$x = \ln \frac{E_\gamma}{m_e c^2} \tag{5.56}$$

and $F_1,\ F_2,\ F_3$ are polynomials of the 5^{th} degree whose parameters are determined from least square fits from data. The fit gives an estimated relative error on σ which is approximately 2.2%, averaged over all materials [71].

The low energy implementation of this process in Geant4 uses a Coulomb corrected Bethe-Heitler cross section which also takes screening into account. For details of the Geant4 model, see the Geant4 Physics Reference Manual [71].

5.4 Electromagnetic showers

If a charged particle hits a material and the energy is above the critical energy[3] (5.29), or a high energy photon produces an energetic e^+e^- pair, the hard bremsstrahlung causes multiple photons, which in turn produce more electrons through the processes outlined in this

[3] Since the critical energy for muons and other heavy particles is very large, only electrons and photons induce electromagnetic showers, unless extreme conditions apply. (Muon critical energy in lead is 141 GeV.)

chapter. The energy of the primary track is broken up in a high number of electromagnetic tracks. Eventually the energy of the particles falls below the critical energy and they start losing energy primarily through ionization. Due to the different cross sections of electrons and photons, the electron number falls off faster with increasing shower depth than the number of photons. The longitudinal shower profile is thus increasing until a maximum is obtained after which a long tail develops as the shower is increasingly dominated by photons.

A useful description of the electromagnetic showers uses

$$t = \frac{x}{X_0} \tag{5.57}$$

$$y = \frac{E}{E_c} \tag{5.58}$$

where X_0 is the radiation length (5.33) and E_c is the critical energy. The shower maximum is found at

$$t_{max} = \begin{cases} \ln y - 0.5 & \text{for incident } e^{\pm} \\ \ln y + 0.5 & \text{for incident } \gamma \end{cases} \tag{5.59}$$

so for a 100 MeV positron in lead, the shower maximum would be found at 11.5 mm.[4]

The Moliere radius, R_M, is a good first approximation to the transverse size of electromagnetic showers. It is a characteristic constant of a material and is related to the radiation length and the critical energy by

$$R_M = 0.0265 X_0 (Z + 1.2) \approx (21 \text{ MeV}) \frac{X_0}{E_c} \tag{5.60}$$

where X_0 is the radiation length and Z is the atomic number. The Moliere radius is the 90% confidence interval for the energy contained in the shower, and approximately 99% of the energy in the electromagnetic shower is contained within $3.5R_M$. At large radii the Moliere theory fails to accurately describe the transverse size of the shower. The Moliere radius of lead is 1.53 cm.

5.5 Multiple scattering

Multiple scattering is the phenomenon where the scatterers are densely distributed, and instead of a single scattering, the particle undergoes several scattering processes along its path. This is a stochastic process closely related to diffusion.

Traditionally the multiple scattering has been modeled using the Moliere formalism, which approximates the projected scattering angle of multiple scattering by a Gaussian with a width [1]

$$\theta_M = \frac{13.6 \text{ MeV}}{\beta c p} q \sqrt{\frac{x}{X_0}} \left(1 + 0.038 \ln \frac{x}{X_0} \right) \tag{5.61}$$

[4] This back of the envelope calculation is a used for the general design of the calorimeter presented in chapter 8.

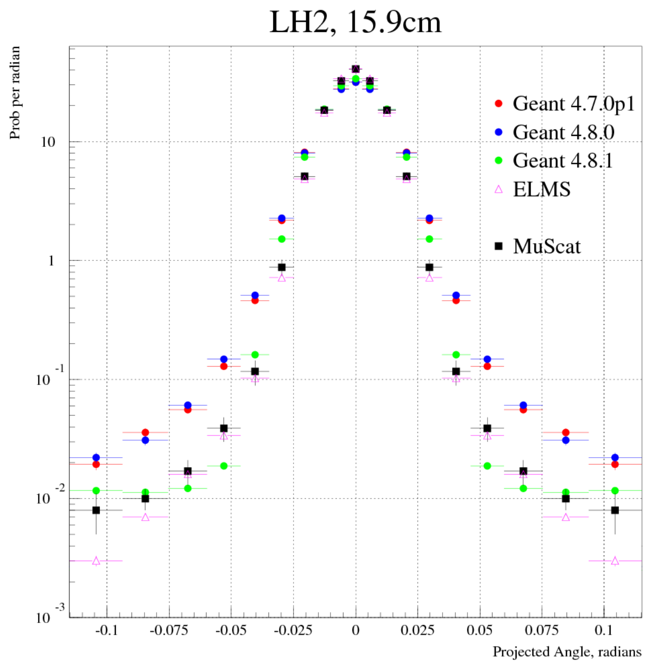

Fig. 5.16: Multiple scattering of muons in liquid hydrogen. Various versions of Geant4 are compared with MuScat experimental data [76] (black) and ELMS simulations (triangles). The version of Geant4 used in G4MICE is Geant4.8.1 (green), which shows good agreement with MuScat data.

where β is the particle velocity, p the momentum , q is the charge of the particle, x is the thickness of the material traversed, and X_0 is the radiation length of the material. The Gaussian approximation fails to describe the tails towards large scattering angles however. While the Moliere theory only calculates the angular dispersion of the trajectory after each step, the slightly more complex Lewis theory also calculates the lateral displacement due to intermediary scattering between the end points of the step. Both models are very dependent on the step length which is one of their major drawbacks. An alternative method is to calculate every single scattering process in the event, which would give a correct result, but for most applications this is not feasible even with modern computers.

In recent years more sophisticated models have been developed called *mixed models* which better reproduce experimental data [77]. These models simulate hard collisions one by one, while treating the soft interactions with traditional multiple scattering models. This gives better agreement with data while the number of operations is still kept at a reasonable level. In addition the algorithm is not as dependent on the step length, making simulations based on mixed models more robust than the traditional models for multiple scattering.

In Geant4, the model used for multiple scattering has evolved with time following these developments. Figure 5.16 compares the results of the MuScat experiment [76] with simulations, using ELMS [78] and different versions of Geant4.

Since Geant4 is a step based Monte Carlo, the probability for a particle to undergo a process is dependent on the path length or time spent on a step. Multiple scattering not only displaces a particle from its original path, but it also adds additional path length and time due to the scattering between the two end points, thus affecting the effective probability density functions of others physical processes. For this reason multiple scattering must always be invoked before any other physical process.

6. THE G4MICE SOFTWARE

The main software used for a multitude of tasks in MICE is the program package G4MICE [50]. The simulation part of the software is based on Geant4 [61], the new standard simulation program for high energy physics, which is developed at CERN and written in the C++ programming language. G4MICE has the capability to simulate the beamline and the detectors, and is widely used by the collaboration to study the general experimental design as well as optimization of individual detectors. To achieve this, a custom tailored simulation of the electronics and the detector responses has been created, which is entirely decoupled from Geant4.

In addition to its simulation capabilities, G4MICE contains tools to calculate accelerator physics quantities such as emittance, and it contains tracker, time of flight and calorimeter reconstruction. The reconstruction will be used both for simulated as well as real data taking of the experiment. This has already successfully been performed during test beams at KEK, Japan, and its functionality is being extended to encompass all MICE operational stages. The G4MICE software has been successful in detecting potential problems with the experimental design and has pointed to new solutions that could be implemented in the design before funds and manpower had been committed. It has thus been a cost effective tool, and it will help with understanding the systematics during experimental operation.

6.1 Programs in G4MICE

G4MICE allows the user to create their own programs in a very flexible manner, by simply adding the program name and path to a file which lists all applications and their corresponding dependencies. During compilation, makefiles for each program are automatically generated, with the desired package dependencies. For this reason, it is not feasible to list all G4MICE programs in this thesis, but only those which are of interest for the generic user, or those of importance for the scope of the following chapters. The relevant components of G4MICE are described in this section.

6.1.1 Simulation

Simulation is the first and foremost application, both in the sense that it is widely used and that many other applications depend on its results. It is usually the first application any user will run. The application has also the unfortunate property of being the most

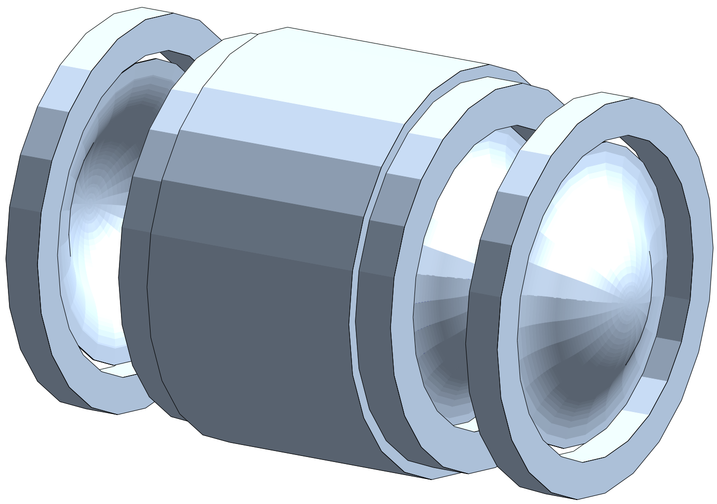

Fig. 6.1: An absorber as modeled in G4MICE. Like the its real counterpart, the modeled absorber consists of a aluminum vessel with corresponding polycone windows, also of aluminum. The absorber vessel is filled with liquid hydrogen. Outside the absorber windows are vacuum windows, which are modeled in a similar way as the absorber windows. All windows have aluminum flanges for mechanical mounting. Compare with figure 4.7.

processor time demanding of all G4MICE applications. Simulation is based on Geant4 [61], and the exact version which is used depends on the release version of G4MICE.[1]

Simulation shoots a user defined number of particles per event through the experiment. The particles can interact with materials and electromagnetic fields in a full scale particle physics simulation. The geometry can be freely chosen through user friendly text files which require no programming knowledge, and all MICE steps and stages, including past test beams, are predefined as configurations for easy access. Since every aspect of the beam can be arbitrarily chosen, Simulation has been used for everything from beamline studies using muons to RF background studies with low energy electrons. The default values of every input parameter have been chosen such that they correspond to normal running conditions, while still maintaining flexibility, so the user can, for example, switch off physical processes.

6.1.2 Digitization

Digitization is an application which uses the results of Simulation (section 6.1.1) to produce the response of the detectors in the form of digits. The implementation of every such

[1] At this writing the supported Geant4 version is v4.8.1.p01, but results in this thesis used Geant4 versions as far back as v4.5.2.p02.

mapping from Monte Carlo hits to digits is dependent on the detector in question, but most handle effects like noise in PMTs, conversion of charge to ADC counts, et cetera.

6.1.3 Reconstruction

This application uses the information from the detectors to reconstruct the event. The Reconstruction application takes data from either Monte Carlo simulation which has gone through the Simulation-Digitization chain, or it works with real experimental data. The SciFi tracker reconstruction uses the Kalman package for track fitting and returns the reconstructed momenta and positions at the *tracker reference planes*, which are located at the cooling channel side of the spectrometers. The time of flight reconstruction reconstructs the time of flight between the three time of flight detectors, while the calorimeter reconstruction summarizes important information of the event, such as the trajectory range in the detector, with minimal loss of information. See section 9.3.4 for a description of the reconstructed calorimeter event properties.

6.1.4 RootEvent

When the individual detectors have been simulated and reconstructed as outlined above, this application is used to evaluate cross detector properties of the event and make a ROOT [79] tree of the information for easy analysis in interactive or batch mode. The RootEvent application creates ROOT trees regardless of whether the full chain from simulation to reconstruction has been performed; this is useful for debugging the Monte Carlo or investigating accelerator physics phenomenon when one is not interested in the response of individual detectors. The ROOT trees created in this way, can be used for particle identification using ROOT macros. In addition they can be used as input to the application PidAnalysis which calculates the beam emittance and single particle emittance as a function of the weight assigned by the particle identification. The author of this thesis is the creator and maintainer of RootEvent, and is one of two programmers of the PidAnalysis application. Later chapters use the results given by these applications.

6.2 Components and packages

G4MICE is organized in an object oriented architecture where classes are collected in packages. To as large extent as possible the packages are independent both of other G4MICE packages, as well as external packages such as Geant4, ROOT, GNU Scientific Library and CLHEP.

6.2.1 MiceModules

The MiceModules package is an interface between the various other packages and applications, and a set of text files stored in a separate area. The text files control the configuration of the experiment and do not require any knowledge of programming language, nor do they

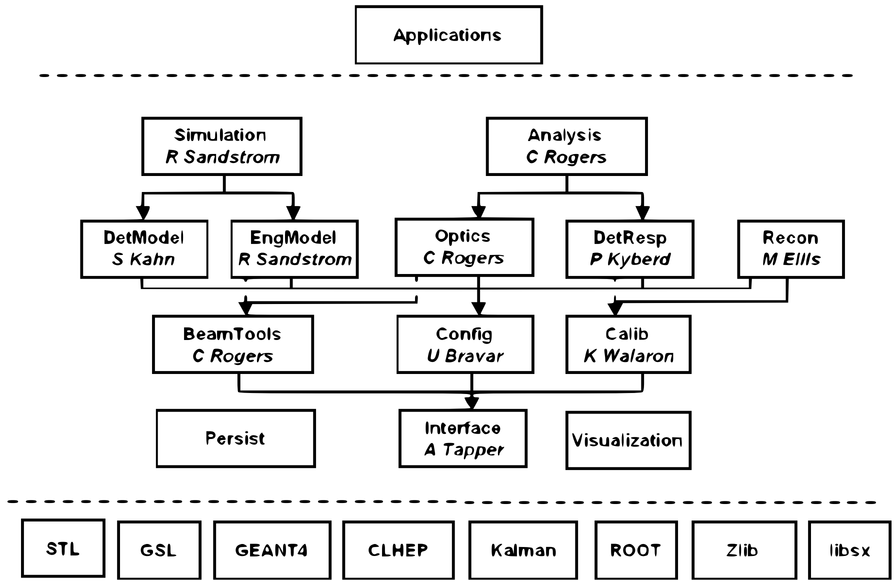

Fig. 6.2: The architecture of G4MICE. Packages can use other packages if they are connected, or if they can trace a connection through other packages in the direction of the arrows. Included are the package managers, who are responsible for maintaining the code and its documentation.

need to be compiled. Almost all aspects of the physical objects and the electromagnetic fields present in the experiment, are controlled this way. For easy setup of the different MICE Stages and test beams, every such scenario can be loaded as a configuration. Since this package is decoupled from Geant4, it can be visualized using HepRep without ever running the Simulation application.

Since MiceModules are independent of Geant4, a class called MiceMaterials has been developed which contains pointers to G4Material objects, referenced by a string which is the name of the material. This allows G4MICE to access all NIST database materials, as well as any user defined materials which are added to the MiceMaterials class.

Another useful class is the MiceUnits, which provides an interface to the CLHEP system of units definitions. This allows the text files used to control the MiceModules to use lines like "`Dimensions 19.0 100.0 cm`".

6.2.2 DetModel

This package is responsible for creating Geant4 volumes which are used during the simulation. Most volumes are created and controlled by the more user friendly MiceModules, however certain special volumes of high complexity must still be created using DetModel. An example of such a volume is the fiber–glue–lead geometry of the preshower layer of the calorimeter, which is very rich in complexity, and where only the fibers are active volumes (sensitive detectors) while the rest of the volume is passive material.

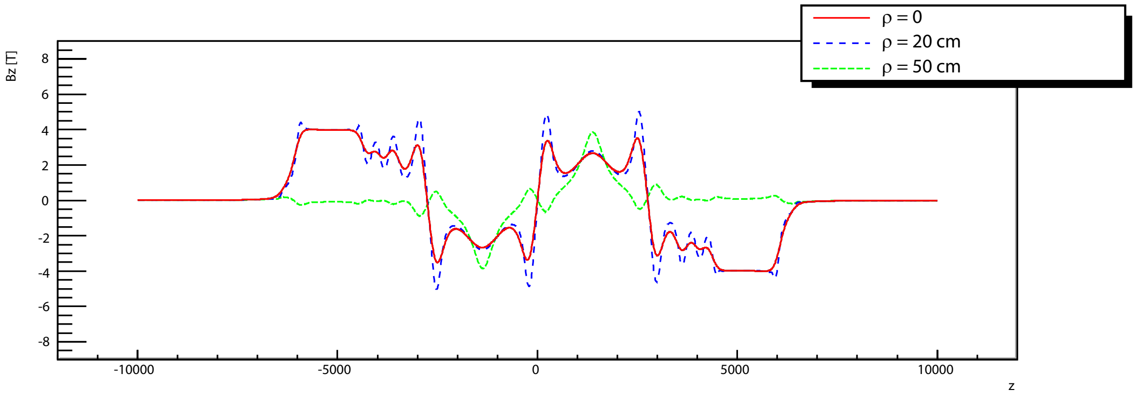

Fig. 6.3: The longitudinal component of the magnetic field as a function of longitudinal position. Three different transverse positions are indicated. This field map was generated externally by Holger Witte, Oxford, and used by G4MICE applications.

6.2.3 EngModel

EngModel is similar to DetModel in the respect that is creating physical volumes for Geant4 simulation, but while DetModel is intended for detector construction, EngModel is used to create engineering objects such as coils. The author is the package manager of this package.

6.2.4 Simulation

The Simulation package has dependencies on Geant4 libraries and is the G4MICE interface to Geant4. The Simulation package implements typical Geant4 classes such as the step manager and the physics list in a fairly conventional manner, though the G4MICE Simulation package contains a number of unique features. Due to the nature of the research the author has performed using this software, this package is of special interest. The author is the package manager of the Simulation package.

For debugging purposes the user can set a switch which creates a table of particle types and processes, and counts the number of occurrences per event during the simulation. This can be set to a specific physical volume of the experiment, or be used globally. Another special feature is the possibility to read in particles of any specification using a text file and start them at a user defined position during the same event as the primary particle (usually a muon). This was used extensively for the RF background simulation (see section 7.3). A similar feature is the option to read in a previous simulation, and start the particles with exactly the same properties at the boundaries of a given detector. This was also used for the RF background simulation, since the spectrum given by the bremsstrahlung photons created in the absorbers was decoupled from the detector configuration outside the cooling channel, allowing use of the same background spectrum for different configurations.

The policy of the physics model used for the G4MICE simulations has been to prevent the user from making something unphysical, while at the same time not wasting resources by simulating processes which are irrelevant to the experiment. For this reason, the author has opted for allowing all particles which Geant4 wants to produce to be generated, but particles which are of no interest to the experiment, such as ions and π^0, can only undergo the following processes

- ionization (if charged)
- decay (if unstable).

in addition to

- transportation
- step limiter
- user special cuts

which all particles in G4MICE are subject to. Should the particle not be created, the recoil of the primary particle would not necessarily be correct, which would bias the simulation. Should the particle not have any means of being destroyed, it would be stuck in an infinite loop bringing the simulation to a halt. Since neutrinos are both stable and neutral, they are allowed to be created but are explicitly killed after their first step.[2]

For particles of moderate interest, such as neutrons, charged pions and kaons, the default allowed processes are

- multiple scattering
- hadron ionization (for charged hadrons)
- low energy elastic scattering
- low energy inelastic scattering
- decay (if unstable)

where the inelastic scattering models are unique for the particle type and charge. For π^- there is an additional process, capture at rest, which the other particles are not subject to.

For e^- the processes are

- multiple scattering
- low energy ionization
- low energy bremsstrahlung

[2] This causes a great improvement in the simulation performance since for every muon there are two neutrinos produced, usually in the boundary rich calorimeter volume.

while for e^+

- multiple scattering
- electron ionization
- electron bremsstrahlung
- electron annihilation
- annihilation to muon pair.

Notice that the models for the ionization and bremsstrahlung are different for e^- and e^+. That is because the low energy models used for e^- are not applicable to e^+, and must not be used.

For muons of both signs the corresponding list of processes is

- multiple scattering
- muon ionization
- muon bremsstrahlung
- muon pair production
- decay

where the user has the option to set the life time of the muon manually. Crucially for the muon decay background studies presented in this thesis, the muons can decay in flight as well as at rest. The μ^- has an additional process, capture at rest.

Photons are the only bosons which are simulated in G4MICE, and their physics list is therefore somewhat different from the fermions. In addition to the common processes (transportation etc), photons are subject to

- low energy photoelectric effect
- low energy Compton scattering
- low energy gamma conversion
- low energy Rayleigh scattering.

For all processes listed above, the low energy models use the low energy package with associated experimental data included as an add-on to Geant4.

Energy loss

To cross check G4MICE results, an extrapolation from simulations with the ELMS [78] program was performed. The ELMS program generates a database of energy loss and momentum transfer for thin absorbers using modern data on photoabsorption spectra of molecular and atomic hydrogen. In a second step, ELMS gives the energy loss for finite absorbers. In Allison [78] energy loss over density is reported as

$$\left\langle \frac{dE}{\rho dx} \right\rangle = 4.64\ MeV g^{-1} cm^2 \tag{6.1}$$

with and RMS of

$$R\left(\frac{dE}{\rho dx} \right) = 0.65\ MeV g^{-1} cm^2 \tag{6.2}$$

after 10 cm of liquid hydrogen for 180 MeV/c muons.

With $\rho = 0.0708\, g\ cm^{-3}$ this can be expressed as

$$\left\langle \frac{dE}{dx} \right\rangle = 3.285\ MeV cm^{-1} \tag{6.3}$$

$$R\left(\frac{dE}{dx} \right) = 0.4602\ MeV cm^{-1}. \tag{6.4}$$

Assuming a Poisson distribution for the number of interactions and a constant energy loss per interaction, it is possible to extrapolate to 35 cm of material. Using the Poisson characteristic that the mean is equal to the variance, the RMS of the number of interactions is the square root of the mean number of interactions. We make the Ansatz

$$an = k_1 \tag{6.5}$$

$$a\sqrt{n} = k_2 \tag{6.6}$$

where k_1 and k_2 are the ELMS values, a is the energy loss per interaction and n is the mean number of interactions per decimeter. Solving the set of equations gives

$$a = 0.09106\ MeV \tag{6.7}$$

$$n = 50.96\ dm^{-1} \tag{6.8}$$

which was used to extrapolate to the MICE situation by multiplying n by 3.5. For one MICE absorber, neglecting windows, the mean energy loss is thus

$$< \Delta E >= 11.50\ MeV \tag{6.9}$$

with an RMS of

$$R(\Delta E) = 0.86\ MeV. \tag{6.10}$$

Tab. 6.1: Energy loss of a pencil beam. Energy differences as 200 MeV/c muons traverse the cooling channel on axis.

After location	$\Delta E[MeV]$
1^{st} vacuum window	-0.1±0.153
1^{st} absorber window	-0.2±0.188
1^{st} absorber	-11.3±1.045
1^{st} RF linac	-1.3±1.118
all cooling channel	-13.4±1.983
2^{nd} tracker	-15.7±2.052

The results above should be compared with G4MICE results. Close to 2000 monochromatic muons at $p_z = 200$ MeV/c and $p_t = 0$ starting on the z-axis where fired onto the upstream absorber. Only muons hitting the TOF2 reference plane where used for the analysis. Table 6.1 gives the energy loss as the particles go through the cooling section.

Note that both the mean and the RMS after one absorber are similar to the result of the previous section, although the windows were not included in the extrapolation from the ELMS result. However, since the energy loss for a fixed initial energy is distributed according to a Landau distribution, the energy loss spectrum has a long tail toward high loss, and the RMS is not a good quantity for comparing the two distributions.

The Landau nature of the energy loss is also a problem since there is no such thing as a mean value of a Landau distribution, unless one imposes a cut–off somewhere. In reality the energy loss cannot exceed the initial kinetic energy, but this property of ionization makes the average energy loss in an absorber ill defined and hard to predict accurately. Since the phases of the MICE RF cavities are set to restore the average energy loss of a muon going through an absorber, the problem with the Landau distribution extends to the phasing of the cavities. For the cavity phasing, it might be more useful to use other quantities of the distribution, such as the mode, median or truncated mean, which are defined for Landau distributions.

6.2.5 DetResp

The DetResp package simulates the electronics response of the MICE detectors. It is used by the Digitization application (see section 6.1.2) and creates digits from the Monte Carlo data given by Simulation. It is fully independent of Geant4. Section 6.3 contains detailed examples of the implementation of the DetResp package and the Digitization application.

6.2.6 Recon

The Recon package contains classes used for event reconstruction on a detector basis using the Reconstruction program (section 6.1.3).

6.2.7 Analysis

This package contains tools for emittance calculations and other beam related analysis topics. It can read in Virtual Planes, Special Virtual Planes, reconstructed tracks and RootEvent (section 6.1.4) TTrees [79].

6.2.8 Config

The Config package contains the setup of geometry materials and physical data. It handles the information in the MiceModules (section 6.2.1), and contains the fits presented in chapter 9 used in the particle identification analysis.

6.2.9 Calib

The Calib package is similar to the Config package, but handles detector calibration data including pedestals, electronics noise and dead channels.

6.2.10 Optics

The Optics package contains tools for calculating betatron functions, periodic lattices etc. For the results presented in this thesis, it was only used to generate matched beams given an external field map.

6.2.11 BeamTools

BeamTools contains tools for implementing cooling channel elements (coils, cavities, absorbers). This is a Fermilab package that has been modified for use in G4MICE.

6.2.12 Interface

The Interface package contains classes used for input and output of information to compressed text files. It also contains classes which are used for persistency purposes, such as *EmCalDigit* which is created by Digitization and can be read in by any subsequent application, for example Reconstruction.

6.3 Example of implementations

In this section some of the various implementations that the author has created in G4MICE are presented. For descriptions of the problems studied using the code presented here, see chapter 7.

6.3.1 Implementation of the TPG

A detailed simulation of the TPG trackers was programmed and performed by the author in order to investigate the momentum resolution of the detector and its sensitivity to RF induced background (see section 7.3). Since then G4MICE has undergone many iterations and as the TPG code could not be updated due to lack of manpower, it was removed from the CVS repository. It is still possible for the interested user to retrieve an older version of G4MICE with the TPG fully functional. Since the TPG tracker shows better performance than its SciFi counterpart, this might be of interest for future studies of a possible upgrade of MICE. This section presents the code as it is when it was still part of the official G4MICE distribution, and does not necessarily reflect the status of G4MICE today.

Detector construction

The TPG tracking detector is modeled in G4MICE by using a series of geometrical objects and materials. First there is a cylindrical mother volume which contains air. Its sole purpose is to be a container of all objects stored inside the TPG. One of the objects is a kapton tube, which fills the mother volume radially and along the beam line. Inside the kapton tube are two cylinder shaped gas volumes; one of them is the active gas volume, and the other is the gas on the high voltage (HV) side of the detector.

The HV gas volume is by default filled with helium at atmospheric pressure, while the default for the active gas is 10% carbon dioxide and 90% helium at 1 atmosphere. The only object which is (logically) placed inside the HV gas is a thin disk of kapton which separates the two gas volumes. The gas mixtures can be defined by the user and support exist for using helium and air as components of the HV gas, while He, Ne, CH_4, C_4H_{10} and CO_2 are available for the active region.

Inside the active gas volume there are three GEMs, the hexaboard support disk, the hexaboard readout, the sensitive detectors and the high voltage plane. The hexaboard support disk is made out of kapton, whereas the hexaboard readout is a modeled as a copper disk. The three GEMs are kapton disks coated on both faces with thin layers of copper. The model does not contain the holes which are present in the real GEMs. The HV plane is modeled as a copper coated kapton disk.

The sensitive detectors are modeled as a number of slices of the same gas as the gas volume they are placed in, but they do not fill up the gas volume radially all the way to the inside of the surrounding kapton cylinder. Their purpose is to supply the simulation with information on the particles traversing this region of interest.

Simulation

The class that holds the physical and logical volumes of the TPG is called TpgTracker. The class TpgSensitiveDetector inherits from G4VSensitiveDetector, and is therefore a sensitive detector class with some special code for the TPG. This class is responsible for collecting information of the particle track. A class called TpgHit is a container for the track information that will be written to the output file.

The number of sensitive detectors, or gas slices as they also are called, can be set using an input parameter to G4MICE. The cluster assignment precision (page 102) increases with the number of slices, but so does the time needed to run both Simulation and Digitization. By default the active gas volume is divided in 600 slices, and it is not recommended to use fewer slices than three or four times the number of samplings for one muon track.

Digitization

Creating hits Event.cc is a class shared by all detectors in G4MICE. It creates an empty TpgEvent as a member of Event. Thereafter, Event.cc fills the TpgEvent with a vector of TpgMCHits which contains the hit information stored in the output file of Simulation. The creation of TpgMCHits belonging to a TpgEvent is performed in the method TpgEvent::newHits, called from Event.

Creating clusters of electrons Immediately after the creation of hits, the method createClusters of the hit is called. This method creates a number of clusters of electrons, associated with the hit, depending on whether the hit generating particle is a μ^+ or another charged particle. If the hit generating particle is a positive muon, a random Poisson distributed number of clusters are created, using the mean as an input parameter. The default value of this mean is given by Garfield [80] simulations. If the hit generating particle is not a positive muon, the number of clusters created is derived from the simulated energy loss in that hit divided by the average energy needed to create an ionization electron. The electron clusters are stored in a vector of pointers, belonging to the hit which created the cluster.

Next Event calls the method *Process* in its TpgEvent. The end result of this method is that all digits have been created and have reached a status that is ready to be written to the output file. This is accomplished by utilizing many intermediate methods and objects which are called on or created from within the scope of *Process*. The first of these intermediate procedures is to put all clusters in their correct spatial positions. This is performed by taking the hit position and approximating a straight track from that point in a direction parallel to the momentum vector of the hit. The cluster is positioned a distance equal to a random number (flat distribution) multiplied by the step length of the hit generating particle at this particular step. Hence, if the step length is too long the approximated track will be unrealistic. A step length in the same order of magnitude as the pitch of strips on the hexaboard is recommended (~ 1 mm). The same method also sets the time of the cluster equal to the time of the hit. This should not make any difference in performance since the ionizing particle is very fast compared to the drift velocity.

Creating drift electrons In order to fill the electron cluster with drift electrons the method *createElectrons* is called for every cluster. This creates new TpgDriftElectron objects according to two different models.

For positive muons support exists for using a special input file for the distribution of the number of drift electrons per cluster. By default this is a file generated using Garfield [80], but if no file is found or the user chooses not to use the input file, a probability density function with $1/n^2$ behavior is used. For other ionizing particles, only one electron is assigned to the cluster. This is due to the way the number of clusters was created.

Once the drift electrons of a cluster have been created, the electrons are drifted toward the readout system. This is done by calling *driftToGEM* in TpgDriftElectron from the method *driftElectrons* for each cluster. The method driftToGEM first calculates the distance the particle has to drift (in the direction parallel to the beam axis). This distance is computed by taking the number of the sensitive detector which spawned the hit in the simulation, and multiplying that with the length along the beam axis one such gas slice corresponds to. This is then corrected by adding the difference in positions of the cluster and its corresponding hit. This procedure takes the orientation (up- or downstream of the cooling channel) of the TPG into account.

The drift distance is used to calculate the transverse and longitudinal drift according to equation 6.11.

$$\sigma_{\perp}^{Drifted} = \sigma_{\perp}\sqrt{z_{drift}/\mathrm{cm}} \tag{6.11}$$

Here $\sigma_{\perp}$ is given as an input parameter, with the default given by Garfield [80] after 100 cm drift. The formula for the longitudinal drift is identical to (6.11). The standard deviation as computed by (6.11) is used to position the drift electrons on the readout, in terms and x and y. The longitudinal diffusion is in a similar way used to set the time of arrival at the readout in global time, and it uses the drift velocity of the TPG gas as a parameter to do this. Both diffusion effects assume that the distributions are Gaussian, with means depending on the cluster time and position.

Creating digits After the drift electrons have arrived at the GEMs, the method *createDigits* of the TpgDriftElectron class is called. First this method calculates a region of interest on the hexaboard. This is defined as all hexaboard strips that are within a radius equal to $5\sigma_T^{Drifted}$, the drift spread as defined in (6.11). This cut is rounded upward to the nearest integer number of strips. For every strip in the three layers that are inside the region of the five sigma cut of a particular drift electron, a TpgDigit is created. The method *Process* in TpgDigit calculates how many electrons end up on the strip after amplification in the GEMs. The additional transverse spread due to the GEMs is assumed to be Gaussian, so the charge distribution of amplified electrons is given by incomplete gamma functions:

$$P(x_1 < X < x_2) = \frac{1}{2}\left(1 + erf\left(\frac{x_2 - X}{\sqrt{2}\sigma}\right)\right) - \frac{1}{2}\left(1 + erf\left(\frac{x_1 - X}{\sqrt{2}\sigma}\right)\right) \tag{6.12}$$

where X is the position of the drifted electron and x_1 and x_2 are the boundaries of the strips' effective region. It is assumed that these boundaries are exactly between the strips on the hexaboard, so there is no "dead" space between strips. Equation (6.12) is for a one dimensional distribution, but since the different layers are rotated with 120 degrees with respect to each other, they are considered as independent projections. In order to get the number of electrons that arrive at a hexaboard strip, the probability is multiplied by the GEM amplification factor, which in turn is a Gaussian with a fixed mean. These two parameters can both be user specified in the dataCards.

Dead strips The user can specify that a certain fraction of strips on the hexaboard shall be dead, meaning that they never return any signal. If this fraction is set to non-zero, a corresponding number of random strips will be considered dead and they are written to a file. This allows Reconstruction to use the same map of dead strips as Digitization. The user can also write such an input file by hand using the real characteristics of the hexaboard. The dead strip map only supports binary quality, i.e., good–bad.

Electronics response So far the digits have all information of the strips, layers etc, as well as the number of electrons that hit it. The next step is to take into account how the signal shape of a charge deposited on a read out strip behaves. To get the signal, the drift electron class calls TpgDigit::Get1eAmplitude together with the offset in sampling numbers as a parameter. This offset is defined as zero for the first sampling after the drift electron arrived at the strip, and every consequent sampling increments this number by 1. The global time of arrival at the hexaboard is then used to compute the time elapsed since sampling number n, which is here called t. Unless $t < 0$, the amplitude is given as

$$a = N \left(\frac{t}{\tau}\right)^2 \exp\left(-\frac{t}{\tau}\right) \tag{6.13}$$

where N is a normalizing constant between charge and ADC counts and τ is the electronics decay time. Both are given as input parameters. After this amplitude has been computed, random noise is added to the final amplitude. The noise level can be specified by the user in units of ADC counts.

In order to speed up this process of creating a set of digits that span time, a cut at one tenth of the threshold has been introduced. This means that unless the signal shape has an amplitude of at least the threshold divided by ten, or that the signal is increasing, the algorithm considers this signal finished/uninteresting, and looks at next strip instead. The reason why we do not simply take the threshold immediately is that several smaller magnitude digits can combine, and the sum of the individual amplitudes can reach the threshold. The downside of this is that it prevents a completely empty strip, or a strip with very low charge, to give a signal above threshold due to a pure electronic noise effect.

Combining the digits Next TpgEvent combines the digits occupying the same strip in the same sampling slot. This is performed in the method *combineDigits*. It uses a templated helper class called C4DVector which resides in the header file. The C4DVector object stores pointers to TpgDigits and the indexes of the object correspond to the positional identifiers of the digits (strip number, layer number, detector number and sampling number).[3]

The combination of two digits is performed by first looking if its corresponding element of the C4DVector object is a null pointer, in which case the pointer to the digit is assigned that element. In case the element already contains a pointer to another digit the method *mergeWithOther* of TpgDigit is called. This ensures that the amplitudes of the two digits are summed up, and that their associated drift electron is added to the list of drift electrons which spawned the digit. One of the two digits is hence not used any longer and is consequently deleted from memory, and the set of digits in this event is updated to reflect the changes. Once this has been done for all digits belonging to the event, every strip at a given sampling contains none or one digit. This reduces the amount of memory consumed considerably.

Checking against threshold The very last method call from the *Process* method of TpgEvent is *checkAgainstThreshold*. This method goes through all digits in the event, and if it finds a digit with an amplitude which does not reach the threshold, the digit is deleted and the vector of digits is updated.

Printing digitization output Inside the method *Print*, Event fetches all digits from the TpgEvent and calls the *WriteDigit* method for each of them. This method is inherited from the TpgHitBank which handles all input and output.

The cluster and hit information only refer to one object respectively, whereas in the digitization a digit may have several hits and clusters associated to it. In the present version of G4MICE this has been solved by persistency, and should one choose to rerun the TPG simulation with the present G4MICE release, one of the first things to do would be to change the TPG output from text file to persistent classes. There is also an option available to write the output to a special output file used by the HARP reconstruction framework.

Reconstruction

The track reconstruction was developed and its performance evaluated by Olena Voloshyn at Geneva University. The goal of the reconstruction is to extract the physical information contained in the strip signals, to build a complete three dimensional picture of the event, and reconstruct the transverse and longitudinal momentum of the track.

The reconstruction of the TPG events consists of three steps:

1. Cluster reconstruction: digitized hits with neighboring strip numbers at the same sampling are grouped into clusters.

[3] This avoids using a nested loop which would typically take three orders of magnitude more computing time to step through.

2. Space point definition: space points are reconstructed as a crossing of three associated clusters from different layers.

3. Track fitting: track parameters and momentum of the particle are reconstructed.

The center position of the cluster is obtained using a weighted average,

$$n_w = \frac{\sum_i n_i a_i}{\sum_i a_i} \tag{6.14}$$

where a_i is the ADC amplitude, and n_i is the strip number, of digit i.

The strip crossings of clusters in combinations of two of the projections are used to form two dimensional spatial points. The clusters in the third projection are added to form a triplet, which excludes fake space points where the χ^2 is larger than a threshold. The longitudinal coordinate, z, of the space point is reconstructed using

$$z = t_s(n_s - 0.5)v \tag{6.15}$$

where t_s is the sampling period, n_s is the sampling number and v is the drift velocity in the gas.

The track fitting starts by extrapolating a straight line from the first two neighboring space points. A window in the transverse plane defines the area where candidate track members can be found, and if no suitable space point is found in the window the search proceeds to the next sampling number, thus leaving a hole in the track. A charged particle moving parallel with a homogeneous magnetic field forms a helix. The track fit first fits the helix projected on the transverse plane as a circle, then a fit in the $xy - z$ plane gives the dip angle of the track. The track radius given by the first of these two fits is proportional to the transverse momentum, while the longitudinal momentum is extracted from the second fit.

Performance

Using the methods described above, the TPG was evaluated using

- helium based gas mixture, 100 cm drift length
- neon based gas mixture, 100 cm drift length
- neon based gas mixture, 18 cm drift length

where the sampling period for the helium option was 500 ns. The neon based gas option used different electronics with a sampling period of 100 ns. The resulting resolutions are summarized in table 6.2. Since the track fitting principle is the same as for the SciFi tracker, σ_{p_t} is expected to be independent of the momentum, while σ_{p_z} should diverge for straight tracks (small p_t). No such study has been performed for the TPG, however, (9.8) is likely also valid for the TPG[4].

[4] Values quoted in table 6.2 agrees well with this statement.

Tab. 6.2: The resolutions of the TPG tracker [66]. The values are for a 200 MeV/c, 6π mm emittance beam.

	long $HeCO_2$ TPG	short $NeCO_2$ TPG	long $NeCO_2$ TPG
σ_x [mm]	3.82	0.41	0.31
σ_y [mm]	3.74	0.40	0.30
σ_{p_t} [MeV/c]	3.59	0.53	0.37
σ_{p_z} [MeV/c]	12.89	1.63	1.27

These results are superior to the resolutions obtained by the SciFi tracker [81], and even better results were obtained with a prototype using radioactive sources [67]. Unfortunately the performance has never been evaluated in the presence of event pile up, nor in the presence of RF induced background.

T2K TPC

Although the TPG was not built for MICE, the lessons learned during the R&D of the device has been to a great help for the design of the T2K near detector TPC. See section 3.3.2. The TPC used in ND280 is based on argon as a primary gas instead of neon. The main reason for this choice was lower cost, and the reasonable number of primary ionization electrons per track length. The simulation of the T2K TPC is similar to the simulations performed for the TPG, however the T2K TPC does not rely on electron production tables given by Garfield [80], but is calculated by the simple formula

$$n_e = \frac{\Delta E}{W_I} \tag{6.16}$$

where ΔE is the energy loss and W_I is 26 eV [82]. Another simplification compared to the TPG simulations is that the drift velocity is assumed to be constant at 6.5 cm/μs[5] with no spread. The T2K TPC will operate at lower drift field voltage, 200 V/cm, which together with the lower magnetic field strength and different gas will give the diffusion parameters [82]

$$\begin{cases} \sigma_{\perp}^{T2K} = & 240\ \mu\text{m} \\ \sigma_{\parallel}^{T2K} = & 290\ \mu\text{m} \end{cases} \tag{6.17}$$

for use in (6.11). The corresponding values for MICE TPG at four tesla are shown in table 4.1 and since the drift lengths are comparable for the long neon based TPG and the T2K TPC, one should expect the latter to show a slightly worse resolution than the results for the neon based gas mixture with the long drift length presented in table 6.2. However the particle momentum and magnetic field strengths are different between the two experiments. Results using the full ND280 reconstruction software have not yet been published.

[5] The TPG helium gas mixture has a drift velocity of 1.68 cm/μs, while the neon based mixture was 3 cm/μs [66].

6.3.2 Implementation of the calorimeter

The simulation of calorimeter is vital for the studies presented in this thesis, and the choice of geometry is presented and motivated in chapter 8 and 10. The analysis is dependent on the simulation results and is presented in chapter 9.

Detector construction and Simulation

The calorimeter is constructed using *MICEModules* (section 6.2.1), configured by conventional text files. The "spaghetti layers" (the preshower layer in case of a Sandwich design, or all four layers in case of a KLOE light design) contain a complicated geometry of scintillating fibers, glue and grooved lead foils. Due to this complexity, the lead is created as standard MICEModules, and the glue and fibers use the property string *G4Detector* and modeled as *G4AssemblyVolume*'s[6] placed in the *DetModel* area of G4MICE.

The fibers and plastic bars are made sensitive, using the same sensitive detector implementation *EmCalSD*. Once the choice of material, shape and electronics have been finalized, it would be wise to separate the different active regions by individual sensitive detector models.

If a particle loses energy in a sensitive volume, the energy loss is recorded together with other hit information, such as volume number, position and time, track number and particle identification number. This information is used to digitize the data, and to cross check the reconstruction and particle identification performance.

Digitization

The purpose of digitization is to simulate the detector response. It relies on Monte Carlo hits as input, stored as EmCalHits. Later, the digits generated by Digitization are used for event reconstruction and pattern recognition.

The hits in the calorimeter are converted into digits containing ADC and TDC information. The average energy required to produce a scintillation photon is assumed to be 125 eV. This value is used together with the energy deposited in the hit to pull a Poisson distributed number of scintillation photons out of the hat. However, only 3.1% of the photons are captured in a fiber. This value for the light collection comes from a datasheet for the fibers. The same value was used for larger scintillator slabs, which should be be looked at more carefully in the next iteration of this study.

The photons are attenuated by an experimental formula from the KLOE collaboration;

$$a = 0.655e^{-\frac{l}{2400}} + 0.345e^{-\frac{l}{200}}. \tag{6.18}$$

where l is the distance in millimeters. Also here, the attenuation of the fibers and slabs are treated alike.

[6] The calorimeter would probably consume less memory should the volumes instead use parameterized volumes, but the final simulation result would still be the same.

The light guide efficiency is assumed to be 85%, and the quantum efficiency 18%. The number of electrons this results in is amplified by a Gaussian factor 10^6 with a standard deviation of 1000. The charge as a function of time is given by

$$q(t) = \left(\frac{t}{\tau}\right)^2 e^{-\frac{t}{\tau}} n_e q_e \tag{6.19}$$

where τ is 8 ns, n_e is number of electrons after amplification, and q_e is the electron charge constant. For ADC counts, this value is integrated using incomplete gamma functions (9.22), while for TDC counts the value is given by the equation directly. The integration limit is given by a 100 ns gate, which is opened by a trigger. For all results presented in this thesis, the trigger was defined as a hit in TOF2, apart from the Stage 1 simulations which does not have a TOF2 detector. One ADC count corresponds to 0.25 pC, which is also the threshold for the TDC. A digit not reaching at least 2 ADC counts will be rejected. The TDC is assumed to have 12 bits, and one channel is 25 ps.

The number of ADC counts for a given PMT is written to file together with a vector of TDC information, where every entry contains the channel when the signal first went over threshold and for how long it stayed over threshold. A TDC signal spanning to the end of the 12 bits is truncated.

Technical details of Digitization

The digitization of the calorimeter hits is started by a call from Event in the Applications/Digitization folder. For every event, it calls the *EmCalDigitisation::Process* method. It is from this method that the calorimeter digitization is managed.

Process creates one digit per side (PMT) of a cell for every hit in the event. A digit corresponds to one PMT, and by default every cell is read out at two ends, thus every hit creates a pair of digits. The program thus calls the constructor of the *EmCalDigit*, which adds the hit which caused the creation of the digit, to the list of hit mothers. Since this list is initially empty, the added hit will, at this stage, be the only element in the list.

Next the constructor of the digit calls *GetDistanceToReadout*, which returns the distance between the hit and the readout. The distance is used to call *CalcTimeAfterTrigger*, which returns the arrival time of photons with respect to the time of the trigger. The photons are assumed to travel at a fixed velocity; smearing could be applied if a higher level of detail would be desired.

After this, the constructor calls *CalculatePEAtPMT* to get the number of photoelectrons at the readout. This method returns the number of photoelectrons (unamplified) at the PMT. It takes energy deposition, light collection efficiency, attenuation, light guide efficiency and quantum efficiency into account. The photoelectrons are then amplified with a Gaussian smeared factor, whose mean and variance are given by the PMT characteristics.

The arrival time and number of electrons at readout are added to a class member vector, if

a) there are electrons in the PMT

b) the signal starts during or before sampling.

Digits not fulfilling these requirements will be removed by the same code that created it. If the digit survived this check, it is assigned to the hit by *EmCalHit::AssignDigit*. That is the end of the digit constructor, which takes the program back to the *Process* method of *EmCalDigitization*, where digits which are out of the time scope are removed.

The CombineDigits method is called, in order to merge digits which belong to the same PMT. In case two digits belong to the same PMT in the same time window, *EmCalDigit::MergeWithOther* is called. *MergeWithOther* adds the hit mothers of the digit to be removed, to the hit mothers of the digit that will remain. In the end, the method deletes the digit it took as argument. The end result of this method is that for a given time window, every digit corresponds to a unique PMT. Typically there is no longer a 1 to 2 relation between hits and digits, but rather every digit is associated with many hits, since there is more than one energy depositing hit per cell.

The program is now ready to calculate how the charge of a channel changes over time. This is performed by a call from *Process* to *EmCalDigit::CalculateAmplitudes*, which creates an ADC amplitude and a vector of TDC information. In order to do so, it uses a temporary vector to store amplitudes, in a toy Flash ADC style, where each bin is the size of the TDC binning. The contribution from multiple hits is summed up, so the vector is equivalent to amplitude as a function of time. For this TDC information, and possibly later Flash ADC implementation, the amplitude in a bin is calculated in the private method *CalcFlashCharge*. This method returns the unintegrated amplitude at a given time, for a given number of amplified electrons, according to (6.19). In the case of ADC counts, the amplitude is proportional to the integrated charge, and this calculation is performed in the private method *CalcIntegratedCharge*. That method returns the integrated amplitude at a given time for a given number of amplified electrons, a time window, and a function parameter which gives the signal width. To perform the integration it uses incomplete gamma functions (9.22) from GSL, GNU Scientific Library.

By this stage, all digits are associated with an amplitude in ADC counts. The Process method now calls *CheckAgainstThreshold*, which removes low level digits against a user defined threshold. The digitization is completed after all surviving digits are added back to the same *MICEEvent* from which the *EmCalHits* was read.

Reconstruction

The reconstruction of the calorimeter assumes that the event contains only one primary particle track, which is modeled in the interface class *EmCalTrack*. Should effects of event pileup be studied, this assumption would hence no longer hold.

The calorimeter reconstruction interprets the set of digits as observables in the calorimeter such as to energy loss, range etc. This often involves a parameterization given by a fit, which is stored in the *Config* class *PidFits*, thus methods in *PidFits* are often called during the reconstruction. The particle identification variables, presented in section 9.3, which depend only on calorimeter information are reconstructed and written to output files in this fashion, whereas multi detector particle identification variables are reconstructed during the global reconstruction. The global reconstruction application does not yet exists, but the application *RootEvent* (presented in section 6.1.4) fills its purpose until an official application has been completed.

A comment about persistency

An *EmCalHit* corresponds to an energy depositing hit in a sensitive volume, such as a fiber. An *EmCalDigit* corresponds to one photo multiplier tube. Since there are two PMTs connected to every cell, there can never be more than twice as many *EmCalDigits* as *EmCalHits*. Since there can be more than one hit per cell, one digit is often created by more than one hit. Also, since there is a threshold for when a digit is kept, there can be plenty of hits and no digits. Hence, there is no lower limit to how many digits per hits one can have.

Since there is no simple 1 to 1 relation between hits and digits, every hit keeps track of a list of digits it has participated in creating. Similarly every digit remembers which hits took part in its creation. In case a digit is removed for one reason or another, that digit is unassigned from all hits associated with it.

Since a digit is associated to a particular PMT, which in turn is associated to a particular cell, layer etc, one should ask one of the associated hits for its cell number or equivalent if that information is desired. Since a digit has always at least one hit associated to it, and all hits associated to a particular digit have identical cell parameters, it is best to ask the first hit in the list of hits for this kind of information.

7. BACKGROUNDS AND THEIR SIMULATION

There are a number of experimental challenges facing the Muon Ionization Cooling Experiment, and some of the hardest to cope with are backgrounds the in form of beam contamination. The reasons for the contaminations vary, but the main contributors to the impurities are intrinsic contamination, which is a remnant of the particle production, muon decay background, which cannot be avoided at these low velocities, and RF induced background, which causes massive exposure to X-rays for the detectors.

7.1 Pion contamination

Simulations using G4BeamLine [62] and TURTLE [63] have shown that the beamline configuration MICE will use will produce a rather pure muon beam. However due to the similar masses of muons and pions, some pions which have not decayed in the decay solenoid will survive the momentum selection in the bend and thus remain in the beam as it enters the straight section of the experiment. There are contributions from protons and electrons as well, but their transmission rate through the cooling channel is very small, and any remaining particles at the downstream end of the experiment can easily be rejected using the downstream particle identification analysis.

Since pions are hadrons, the energy loss in the absorbers does not match the energy loss of muons, and pion cooling performance will hence differ from muons. Some of the pions will decay in the cooling channel which is even worse, since the upstream detectors will measure the amplitude of a pion, and the downstream detectors will measure the emittance of a muon with an increased single particle emittance due to the decay process. In this case the downstream particle identification will correctly identify the particle as a muon, but it is insensitive to the pion decay process that has produced the event.

Upstream particle identification is achieved by the time of flight measurement between TOF0 to TOF1 (section 4.2.3), and a dedicated Čerenkov detector, CKOV1 (section 4.2.4). The time of flight can be compared with the measured momentum in the upstream spectrometer, and is hence a measurement of the particle mass. This procedure shows good performance, but due to the presence of a lead diffuser and the TOF1 material, there is an additional uncertainty on the momentum measurement in the upstream region. Furthermore as the beam momentum increases, the separation in time of flight between pions and muons approaches the detector resolution, and the performance of this particle identification procedure decreases as a result. The double aerogel Čerenkov detector will compensate for these short comings since it shows an excellent pion to muon separation capability in the high momentum region.

Tab. 7.1: The ratio of particle types in the beam at the target and TOF1 respectively, using the Sept´04 beamline design [58].

Particle	Target	TOF1
p^+	51%	0.4%
π^+	4.6%	0.4%
μ^+	0.01%	99.1%
e^+	0.3%	0.1%
n	36%	0%
γ	6.6%	0%
π^-	1.5%	0%
μ^-	0.01%	0%
e^-	0.4%	0%
Other	<0.01%	<0.1%

The pion contamination was intended to be measured during MICE Stage 1, where only TOF0, TOF1 and the calorimeter are installed. Simulations regarding this scenario have been performed by the author and are presented in section 8.6.1. It was intended to update these results using the more evolved Sandwich calorimeter design, as was done for electron identification in Stage 6. However it appears that the full calorimeter will not be delivered in time for Stage 1, and the measurement of the pion content in the beam will likely be performed using only a partial calorimeter, and hence the planned simulation effort was cancelled. For all other studies presented in this thesis, the upstream particle identification analysis is assumed to be perfect and the muon beam 100% pure at TOF1.

7.2 Muon decay background

Even if the incoming beam to the experiment would be absolutely pure, the nature of the particles MICE will use causes an irreducible background. When a μ^+ decays it produces two neutrinos, which do not interact with the detectors, and a positron. The positron will have a similar but significantly different momentum compared to the muon (shown in figure 7.1), and will hence induce a bias in the measured track properties. See section 5.1.1 for description of muon decay and its kinematics.

As figure 7.2 shows, in general a decay electron will have a larger single particle emittance (section A.2.2) than a muon of the same bunch, since the angular freedom in the center of mass frame is only limited by the polarization. This causes not only the single particle emittance measured for each event to be flawed, but also the measured beam emittance will be larger for a muon beam containing decay electrons than for a beam purely consisting of muons. Furthermore since the muon decay is a Poisson process, the number of electrons present in the beam increases exponentially with time, and hence there is

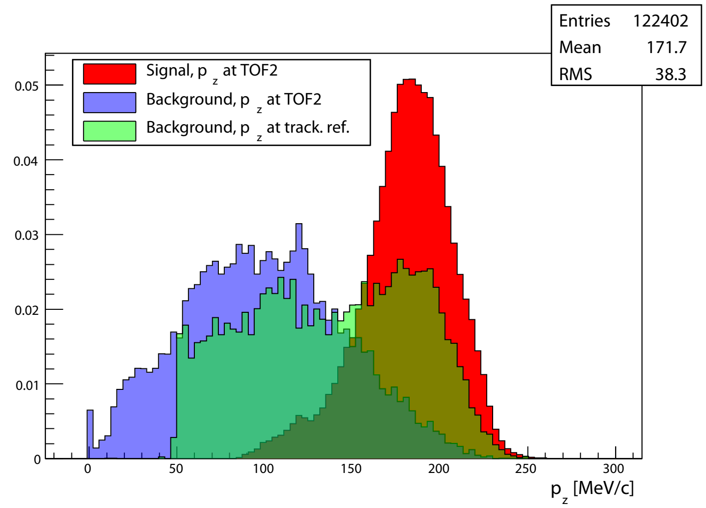

Fig. 7.1: Normalized distributions of longitudinal momentum for MICE Stage 6, active cooling channel in the 200 MeV/c beam setting. The red histogram shows the momentum distribution of muons at the entrance of TOF2, while the blue is the momentum of background events causing hits in TOF2 and the calorimeter. The green area illustrates the momentum of background events measured at the downstream tracker reference plane. Since many of the background events are decaying inside the tracker the last distribution shows significant overlap with the two other distributions. All values of p_z are unsmeared Monte Carlo truth.

an apparent heating of the beam if measured at two different locations even though the emittance of the muon sample is conserved.

This problem and how it is handled takes up a large part of this thesis, and is mainly presented in chapters 8 and 9. The findings presented in the latter chapter show that a detector dedicated to separating muons from electrons is necessary, and that the proposed detector with associated analysis program is sufficient for achieving the MICE objectives (see section 4.1).

7.2.1 PID and emittance measurement

The performance of the PID can be quantified in a number of ways; the separation of the signal and background samples, the efficiency of correctly identifying a background event at some reference signal efficiency, or the impact on the emittance reduction measurement of the experiment. Of these alternatives the latter is the most attractive quantity to obtain, but it is also the hardest to extract from the analysis.

Let $\langle\epsilon_s\rangle$ denote the average single particle emittance of the signal sample, and $\langle\epsilon_b\rangle$ is the average single particle emittance of the background sample. Furthermore let n_s and n_b be the number of signal and background events in each respective sample. The average

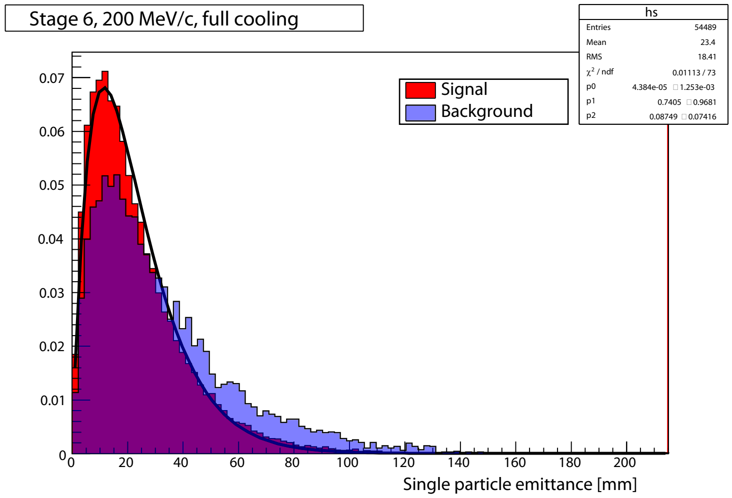

Fig. 7.2: Single particle emittance distribution for signal and background events respectively. Since the input beam was Gaussian distributed in four dimensional phase space, the single particle emittance is distributed according to a chi-square distribution with four degrees of freedom. The background, which mainly consists of positrons produced in muon decay, fills a larger phase space volume and thus introduces a systematic error on the emittance measurement. The average single particle emittance of the signal sample in this figure was 23.40 mm and the corresponding value for the background sample 32.66 mm.

single particle emittance thus measured is

$$\langle \epsilon' \rangle = \frac{\langle \epsilon_s \rangle n_s + \langle \epsilon_b \rangle n_b}{n_s + n_b} \tag{7.1}$$

which can be expressed in purity (see section A.1.8)

$$p = \frac{n_s}{n_s + n_b} \tag{7.2}$$

as

$$\langle \epsilon' \rangle = p \langle \epsilon_s \rangle + (1 - p) \langle \epsilon_b \rangle . \tag{7.3}$$

The relative systematic error on the emittance measurement is thus

$$\delta \equiv \frac{\langle \epsilon' \rangle - \langle \epsilon_s \rangle}{\langle \epsilon_s \rangle} = (1 - p) \frac{\langle \epsilon_b \rangle - \langle \epsilon_s \rangle}{\langle \epsilon_s \rangle}. \tag{7.4}$$

With the assumption that the average amplitude of background events are 50% higher than the corresponding quantity for signal events, this leads to a minimum purity of $p > 99.8\%$ in order to meet the experimental requirement that $\delta < 0.1\%$. Due to uncertainties on whether more background events will survive through the cooling channel in non-flip mode[1], a safety factor of 3 is adopted, equivalent to increasing the purity requirement to 99.933%.

[1] Studies performed by the author showed that half of the positron content of the beam is lost in three empty absorbers, most likely due to the diverging magnetic field lines in the flips.

Since it was not known a priori how the single particle emittance of signal events which were incorrectly rejected as background differs from accepted signal events, a conservative assumption that they have twice as large amplitude as the remaining events was used. Using the same argument as above, this led to a signal efficiency requirement of 99.9% or better.

The purity after background rejection depends on the efficiency of the particle identification and the intrinsic purity of the sample, i.e., the purity before any analysis is performed. The intrinsic purity is higher for higher energy beams, making the required rejection efficiency higher for the lower momentum beams than for the higher momentum beams.

7.2.2 Simulation of muon decay

The problem of the muon decay background was modeled and simulated in G4MICE [50]. The muon decay process was controlled by the default class in Geant4. Pure muon beams of various beam parameters were started at the downstream end of TOF1, and were propagated through the experiment toward TOF2 and the calorimeter. Depending on what stage was simulated, the material and electromagnetic fields between the two time of flight detectors differed, but in general the average muon travelled the distance in 40 to 50 ns at a β of 0.88. Comparing that to the muon life time, the expected electron impurity at the end of the experiment was approximately one percent, though the various objects and field flips encountered between the time of flight detectors reduced the net electron impurity by a factor of two. Since a full simulation of muon decay in flight is time and resource consuming, a second setup was prepared where the same muon decay process was used but with the life time set to 40 ns. This ensured that muons decayed sufficiently often to give the desired increase in number of background events, while not significantly distorting the longitudinal distribution of the muon decay which could arise should one decide to use an even shorter life time.[2] Should any such fast decaying muons still be left at the entrance of TOF2, they were filtered out and not used in the analysis.

The Simulation executable was run for about a week on the GRID which produced a signal sample of approximately 90000 signal events, and a background sample of about 9000 events[3]. The Monte Carlo data were digitized and special particle identification variables were created for every event. Half of the events were used to train an Artificial Neural Net, and the other half were used for performance evaluation. This process was repeated for every beam setting and experimental stage studied, generating hundreds of gigabytes of data. The analysis is presented in detail in chapter 9.

[2] This would cause a bias in the particle identification performance evaluation since particles which decay early are easier to correctly identify than background events produced further downstream.

[3] Every setup used 120000 normal decaying muons and an equal amount of fast decaying muons, but many particles were lost due to scraping or not fulfilling the *good event* requirements.

7.3 RF induced background

The Muon Ionization Cooling Experiment uses 201.25 MHz RF cavities in an inhomogeneous magnetic field of 1-3 T in combination with liquid hydrogen absorbers to reduce the emittance of a muon beam. Even though MICE will operate below the Kilpatrick limit, the electric field gradient in the cavities causes electrons to be emitted. When the electrons interact with the surrounding material, photons are created through bremsstrahlung. These photons cause a background in the detectors of MICE.

This section presents the origin of the electrons, calculations of their acceleration, and a model for the number of bremsstrahlung photons per electron emitted from the cavity. Together with photon rates measured in the MTA, this gives a prediction of the number of electrons emitted in MICE. Together with a simulation, this gives the predicted background rates in the MICE detectors.

Towards the end a semi-empirical model is presented that explains the gradient dependence on electron emission and photon rates observed in a large number of experiments during the last century.

7.3.1 Field emission

While MICE will operate at 8 MV/m, the expected peak surface field is 12 MV/m [58], which should be compared with the Kilpatrick limit for breakdown

$$f(\mathrm{MHz}) = 1.64E^2 e^{8.5/E} \tag{7.5}$$

which is $E \approx 15$ MV/m for a 201.25 MHz cavity. At local field gradients of 6–7 GV/m the tensile stress becomes equal to the tensile strength of copper, and the material fails which results in a breakdown event. This process is illustrated in figure 7.3. The Kilpatrick limit uses the Fowler-Nordheim theorem from 1928 which states that the current density of electrons tunneling through a potential barrier is proportional to the square of the electric field times an exponential increase with inverse field strength,

$$n_e(E) = \frac{A(\beta_{FN}E)^2}{\phi} \exp\left(-\frac{B\phi^{3/2}}{\beta_{FN}E}\right) \tag{7.6}$$

where A and B are constants [83]. The work function ϕ is the energy required to move an electron from a metal to a point immediately outside its surface, while

$$\beta_{FN} = \frac{E_{local}}{E_{surface}} \tag{7.7}$$

is a local field enhancement factor due to impurities and asperities of the surface (see figure 7.4). This model assumes that the free electron model is valid in the metal and that the temperature is zero Kelvin. The Fowler-Nordheim tunneling is also known as *field emission* and was first observed by Robert W. Wood in 1897.

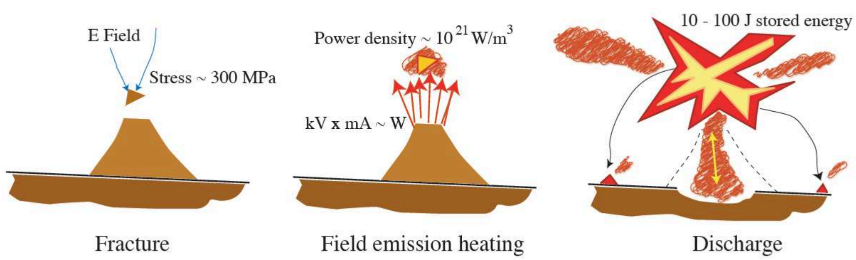

Fig. 7.3: An illustration of material failure in an asperity causing a breakdown event. The original asperity is destroyed in the process, leaving behind a crater and a number of smaller asperities. From ref [83].

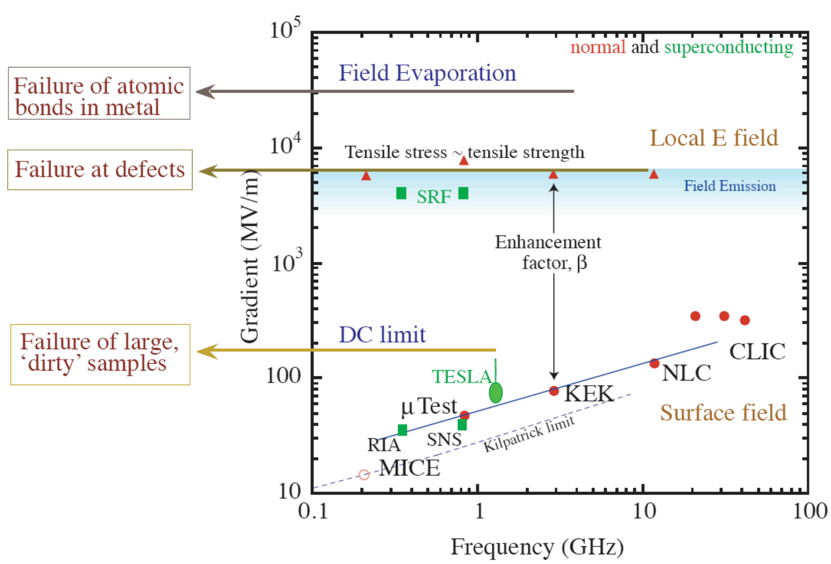

Fig. 7.4: At high local electric field gradients, field emission occurs. If the mechanical stress exceeds the tensile strength a breakdown event occurs. From ref [84].

At local electric field gradients just below the critical tensile stress, electrons are stripped off MICE RF cavity surfaces and accelerated along magnetic field lines. Should the electrons hit the detectors, they would create backgrounds to muon tracking and identification. However, the material in the absorbers halts the electrons before they hit the spectrometers. The main contributions to energy loss of electrons are ionization and bremsstrahlung. Bremsstrahlung will produce photons, to which the absorber material is mostly transparent.

An additional effect not accounted for in this chapter is *multipactoring*, which is a resonance phenomenon when the impact of the primary electron on a surface generates an avalanche of electrons, which in turn are accelerated in the other direction. A necessary condition is that the field should be directed in the opposite direction when the primary electron hits the far surface, and the most effective resonance is obtained when the field is at maximum strength. In other words, when the travel time for the primary electron corresponds to exactly half an RF period.

7.3.2 RF acceleration

Since emission depends very strongly on the electric field strength, it is assumed that the electrons are emitted from the RF cavity surfaces almost exclusively at maximum electric field, generating sharp peaks in the time distribution of emission. The time for each such peak depends on the phase shift between different cavities in an RF section. The phases are optimized for a μ^+ beam at 200 MeV/c, as described in table 7.2. The resulting acceleration of constant phase shift phasing (column A table 7.2) is shown in figure 7.5. This gives a distribution in time for the dark current, which is shifted with respect to the muons. The distribution of electron emission results in monochromatic peaks in the corresponding energy distribution, where the energy depends on from which cavity the electron was emitted, and the muon momentum for which the cavities was optimized. The energy spectrum of the electrons is independent of whether the experiment is cooling μ^- or μ^+, while the time distribution is shifted by half an RF period, 2.5 ns, with respect to muons of the opposite sign.

The RF cavities have 0.38 mm thick beryllium windows with a radius of 21 cm at the boundaries. The windows give an energy loss to the RF induced electrons. The energy gained by an electron when it has been accelerated to the outside of the RF section was calculated using Matlab, while the energy loss was calculated from NIST data.

These calculations resulted in six peaks in energy and time per linac for electrons going in the downstream direction. The corresponding number of RF background peaks in the upstream direction is two per linac. The reason for this behavior is that some electrons are turning around in the cavities, if they are emitted at positive field due to the phasing of the cavities. Previously 466 mm cavities were considered for the MICE experiment, and in this case, the point where the kinetic energy approaches zero occurs close to the beryllium windows so these electrons are killed in the windows and do not reverse in the direction towards where they were emitted. The results in terms of flight time and kinetic energy for the electrons are given in table 7.3. Should the cavities be phased using a G4MICE

Tab. 7.2: The phasing of individual RF cavities in a MICE linac, with respect to the most upstream RF cavity (cavity 1). The phases listed in column A correspond to a constant increment between neighboring cavities, and is the phasing that was used for calculating the energy used in the simulation. Column B is the result of a reference particle at 200 MeV/c according to G4MICE. The effect on the acceleration of muons is virtually negligible, but the different phasings affect the dark current energy spectrum.

Cavity	phase A [rad]	phase B [rad]
1	0	0
2	2.049	2.0633
3	4.098	4.1207
4	6.147	6.1705

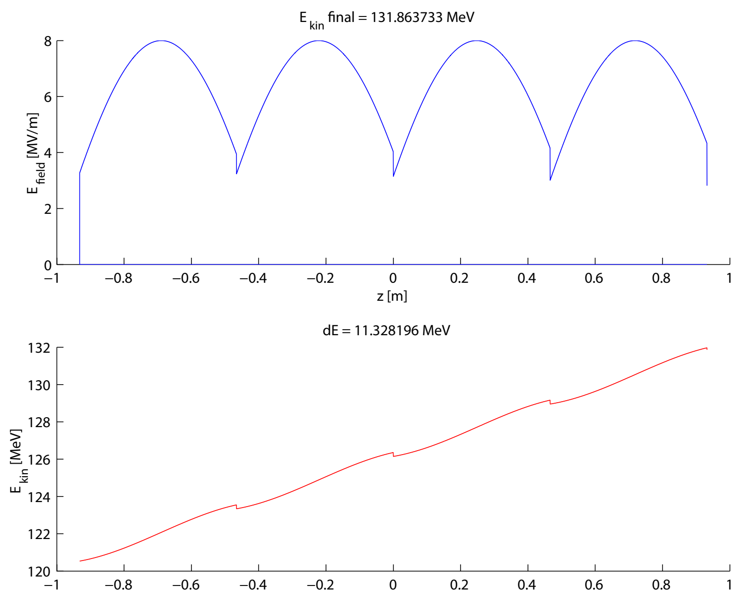

Fig. 7.5: Top: The electric field as seen by a μ^+ at 200 MeV/c, assuming all phases are set for a muon at constant momentum (column A in table 7.2). Bottom: The kinetic energy of the same particle. The energy increases due to the acceleration in the electric field, but also loses a fraction of the energy at the beryllium windows located at the cavity boundaries.

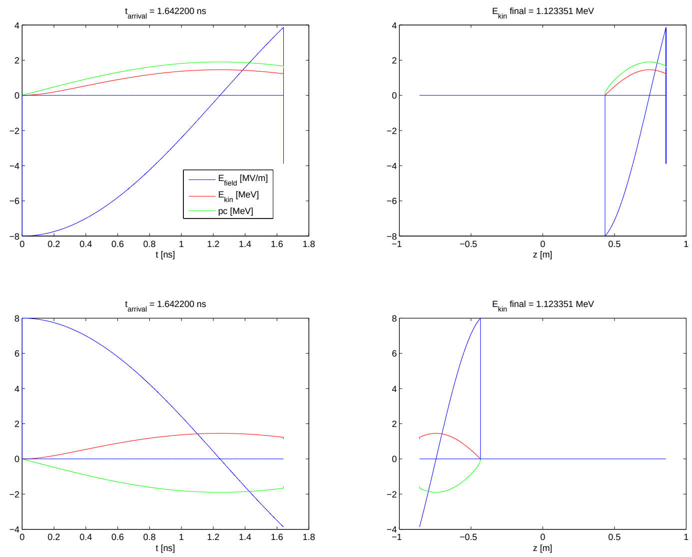

Fig. 7.6: Electrons accelerated in time dependent RF electric field of a 430 mm long cavity. Energy loss in the windows is included. Top: Electrons emitted at negative peak field (accelerated downstream). Bottom: Electrons emitted at positive peak field (accelerated upstream). Left: Time dependences. Right: z dependences.

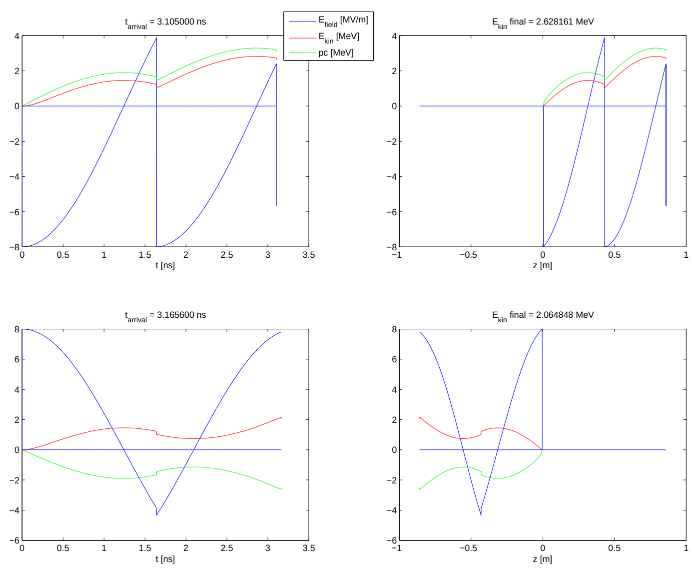

Fig. 7.7: Same as fig 7.6 but with two cavities. The phases of the cavities were set according to column B in table 7.2.

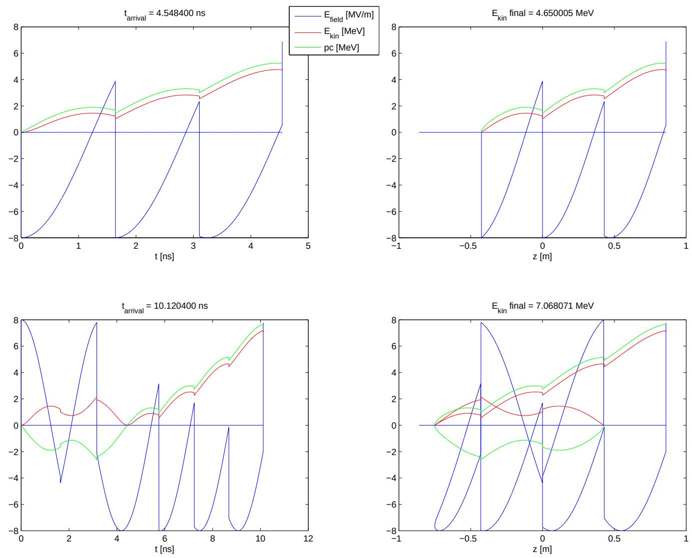

Fig. 7.8: Same as fig 7.6 but with three cavities. The phases of the cavities were set according to column B in table 7.2. Note that the direction of the electrons emitted upstream is reversed.

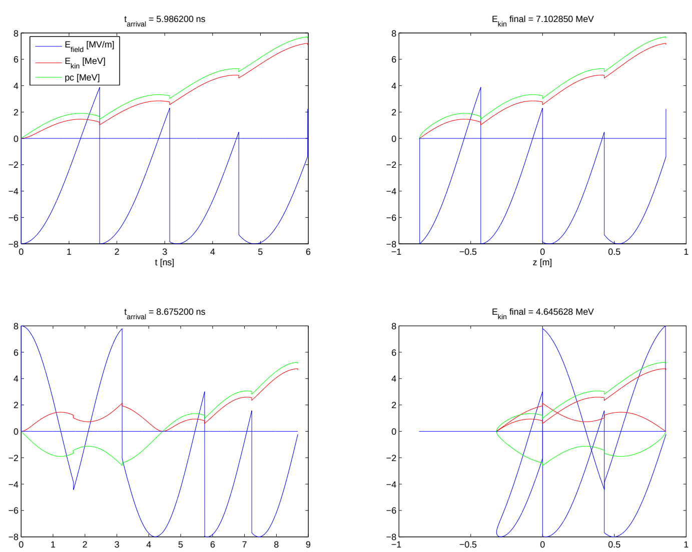

Fig. 7.9: Same as fig 7.6 but with four cavities. The phases of the cavities were set according to column B in table 7.2. Note that the direction of the electrons emitted upstream is reversed.

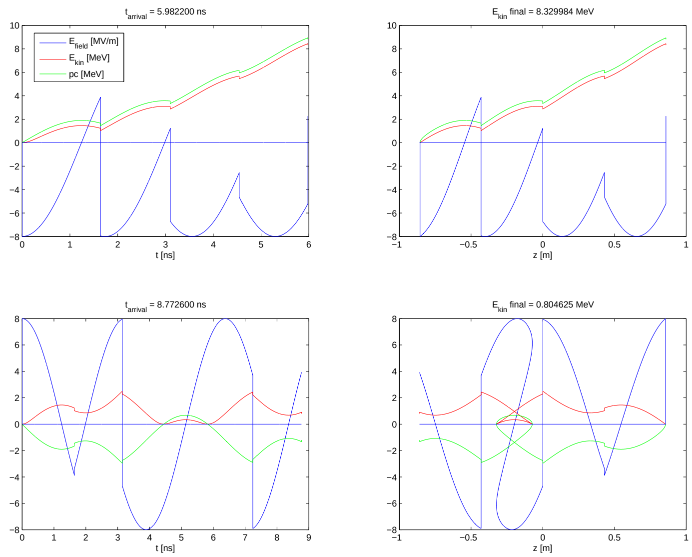

Fig. 7.10: Same as fig 7.6 but with four cavities. The phases of the cavities were set to accelerate a muon at $p = 140$ MeV/c. The direction of electrons emitted upstream is reversed twice, resulting in equal number of particles arriving in upstream absorber as downstream absorber.

reference particle, as presented in table 7.2, the minute differences in relative phases have no impact on the energy spectrum for electrons which are not reversed. However, the final kinetic energy of reversing electrons is very sensitive to the RF phases, as can be seen by comparing table 7.3 with table 7.4. As illustrated in figure 7.10, the electron acceleration for a linac optimized to accelerate a 140 MeV/c muon makes the upstream emitted electron reverse twice in the third cavity, thus resulting in an equal number of electrons arriving at both ends of the linacs.

Figures 7.6 to 7.9 show that the field with opposite polarity as a particle hits a window is never larger than half of the field strength on crest. The conclusion drawn from this is that the multipactoring effects are negligible compared to the initial field emitters, due to the strong dependence on the electric field strength. However, a similar avalanche mechanism can take place in the window belonging to a subsequent cavity, especially for electrons emitted at negative peak field, since the field of the subsequent cavity is nearly maximal in the accelerating direction at the time of the electron's arrival. This effect has not been accounted for, and could further increase the bremsstrahlung photon background emitted in the upstream direction.

7.3.3 Photon production

The fraction of the electrons emitted from the RF cavities making it through the absorbers is heavily suppressed due to energy loss in the liquid hydrogen. The energy loss

Tab. 7.3: Kinetic energy and time of flight from emission to exit of RF system as calculated in Matlab, using column A in table 7.2 for setting the phases of the cavities. The table also shows how many cavities the electron would have to traverse to reach the other side of the RF system, and if the particle direction was reversed due to the sign of the electric field.

Initial field sign	Cavities	Reversed	$E_{kin}[MeV]$	$TOF[ns]$
-1	1	no	1.125466	1.657
-1	2	no	2.626274	3.120
-1	3	no	4.629612	4.5635
-1	4	no	7.037191	6.0015
+1	1	no	1.125466	1.657
+1	2	no	2.036122	3.1815
+1	3	yes	2.224277	10.1535
+1	4	yes	4.706079	8.7085

Tab. 7.4: Same as table 7.3, but with the phases of the RF cavities set by a reference particle in G4MICE (column B in table 7.2). Smaller step length in the numerical calculation and a more recent version of Matlab are responsible for the small differences compared to table 7.3 in the one cavity cases. Reversing electrons spend longer time in the linac system, and are thus more sensitive to small differences in the phasings of individual cavities.

Initial field sign	Cavities	Reversed	$E_{kin}[MeV]$	$TOF[ns]$
-1	1	no	1.123351	1.6422
-1	2	no	2.628161	3.1050
-1	3	no	4.650005	4.5484
-1	4	no	7.102850	5.9862
+1	1	no	1.123351	1.6422
+1	2	no	2.064848	3.1656
+1	3	yes	7.068071	10.1204
+1	4	yes	4.645628	8.6752

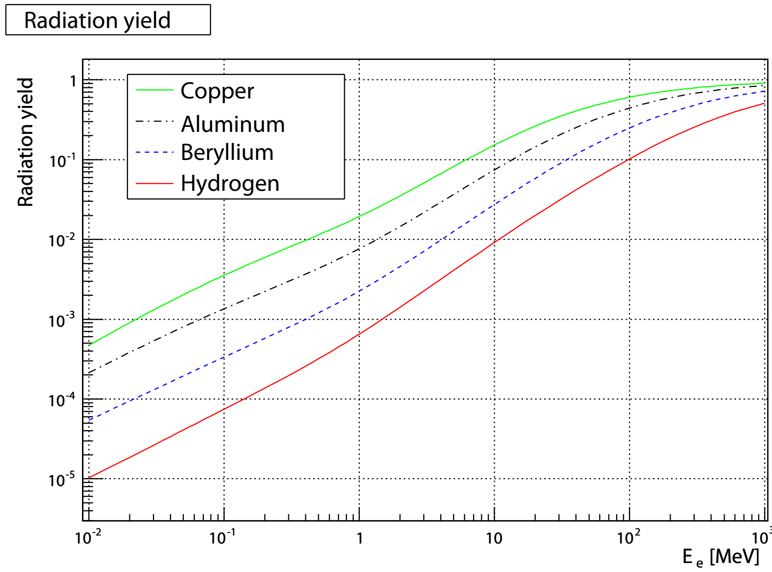

Fig. 7.11: The radiation yield as a function of electron energy, for four of the most important materials in the beamline. The radiation yield is the fraction of kinetic energy of the primary electron which is converted into photons through bremsstrahlung. The calculations are based on NIST data, which in turn is using Seltzer–Berger parameterization [74].

is dominated by ionization, but there is a contribution due to photons created through bremsstrahlung. These photons can in turn generate hits in the detectors. However since the energy is well below the critical energy, the conversion probability is small, as shown in figure 7.11. However, since the bremsstrahlung cross section increases with decreasing radiation length, the radiation yield increases for denser materials. This is important to MICE since the radiation length of aluminum is shorter than that for beryllium and liquid hydrogen, a factor 100 for aluminum compared to liquid hydrogen. This results in more than an order of magnitude higher radiation yield per unit length in the absorber windows than in the liquid hydrogen. Thus, thin low Z absorber windows not only reduce the multiple scattering of muons, but also minimize the RF induced background.

Since the cross sections for pair production, and subsequent annihilation, are much smaller than the cross sections for Compton scattering and photoelectric effect at the relevant energies, it is valid to assume that all photons are generated through bremsstrahlung, and that no secondary photons are produced by interactions between the material and a bremsstrahlung photon. Hence the radiation yield illustrated in figure 7.11 should be taken as an upper limit to the photonic background in the spectrometers per RF emitted electron.

Since the parameterization (5.38) contains infrared divergencies, it is not meaningful to discuss the number of photons below a certain energy. The energy density function however $t\mathrm{d}\sigma/\mathrm{d}t$ does not contain the divergencies and can thus be employed to calculate the fraction of photonic energy above a certain energy threshold. As can be seen in figure 5.11, the

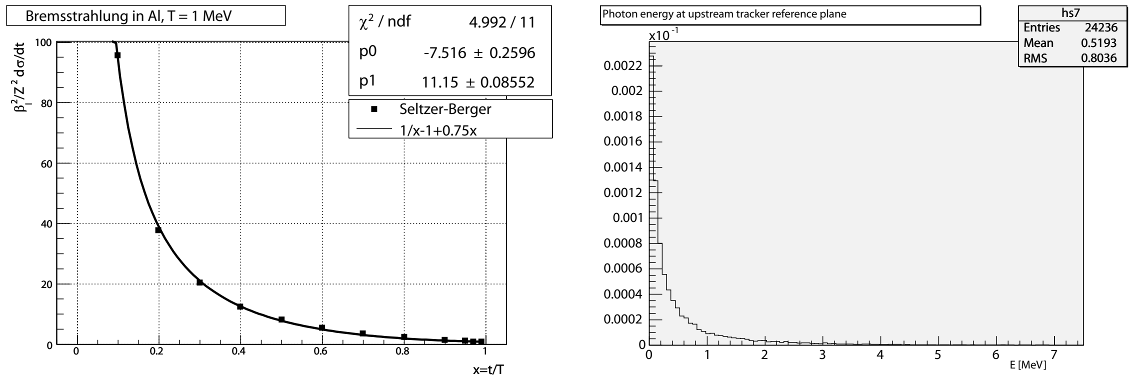

(a) Two parameterizations to Al data

(b) Spectrum from simulation

Fig. 7.12: (a) The energy spectrum of photons using data from reference [74], fitted with $y(x) = p_0 + p_1(x^{-1} - 1 + 0.75x)$. (b) The energy distribution at the upstream tracker reference plane of bremsstrahlung photons from RF induced background.

cross section depends rather modestly on the fraction of the electron energy with which the photon is created. Since the radiation yield and the initial electron emission shows much more dramatic dependencies on the experimental observables, it can be concluded that uncertainties in the energy distribution only contributes in higher order when compared to other effects. For example, in the example shown in figure 5.11, 51% of the photonic energy is above one quarter, 24% above one half, and 8% above three quarters of the electron energy.

A 1 MeV electron has a CSDA range of 2 mm in aluminum, and the absorber and vacuum windows each are 0.18 mm thick in the center, and thicker toward the window boundaries. This infers that a significant part of the energy loss of an RF electron will occur in the windows. With the higher radiation yield for low X_0 materials, many of the bremsstrahlung photons will be produced in the absorber and vacuum windows. Since the radiation yield increases with electron energy, while the fraction of energy lost in the aluminum windows decreases with electron energy, the effective photon production is subject to energy straggling, impact position and direction, and is difficult to accurately predict.

Assuming that all photons are produced in the inner absorber window of an outer absorber, the photon background is attenuated by 35 cm of liquid hydrogen, two thin aluminum windows and approximately 2 m of air before hitting the spectrometers. Using Beer's law (5.46) with tabulated NIST data, at 1 MeV the intensity is reduced by less than half a percent in the aluminum and approximately 1.5% in the air. The only significant attenuation occurs in the liquid hydrogen itself, where the intensity is reduced to approximately 73% of its original value. The total attenuation is therefore considered to give a factor of 0.7 to the original photon output, and less for lower initial energies.

7.3.4 MTA measurements

In order to study the breakdown processes and evaluate the prototype 201.25 MHz cavity, an experiment has been setup in the MuCool Test Area, *MTA*, at Fermilab. Among the topics studied are the influence of material and coating on the breakdown processes, and the maximum achievable electric field gradient as a function of the magnetic field strength.

Experimental technique

The setup consists of two different RF cavities, a 201.25 MHz MICE prototype cavity and an 805 MHz pillbox cavity. The latter is installed in a 5 T solenoid, and a set of special buttons with different shapes and coatings have been manufactured which are mounted in the center of the cavity window. This allows fast and uncomplicated change of experimental conditions necessary for studying the impact of magnetic fields and materials. The tested buttons used molybdenum-zirconium alloy, tungsten, copper and titanium nitride coating on copper base, but buttons using tantalum, niobium, niobium-titanium alloy and stainless steel has been manufactured and will also be tested.

The 201.25 MHz cavity is sandwiched between two thick aluminum plates to withstand atmospheric pressure. Due to the larger size of this cavity compared to the 805 MHz cavity, it cannot fit inside the bore of the solenoid. The magnetic field is instead supplied by an external coil. It is not known exactly how much the inhomogeneous magnetic field resulting from the positioning of the coil affects the experimental results. In the first quarter of 2009 a MICE coupling coil will be installed to reproduce the operational conditions of the MICE experiment. The experimental setup is illustrated in figure 7.13.

Contrary to the smaller cavity, the 201.25 MHz cavity does not have the option to exchange buttons to test the effects of different materials and coatings. Instead two sets of windows have been manufactured and tested. The first used flat titanium nitride coated copper windows, and the second set used curved titanium nitride coated beryllium windows similar to the MICE RF cavity window design. A total of 0.635 cm of copper and 3.6 cm of aluminum is found in the path of the particles emitted from the cavity. In addition, a disk of stainless steel of similar thickness to the copper vacuum window was placed between the cavity and the detectors. The stainless steel disk contained ports, which makes it hard to accurately estimate the amount of material a particle encounters as it is emitted from the cavity. Since the attenuation effect is limited, the stainless steel disk was not included in the analysis. This is equivalent to assuming that all particles are traversing the disk through the ports.

Photons emitted from the cavities are detected using nine scintillating counters with light guides and photomultiplier tubes. They are located in various locations around the cavities and provide information on the emission angles. A tenth detector is a two inch thick, 1.5 inch diameter, NaI crystal with a photomultiplier tube (named PMT16), which is positioned on the beam axis 4.7 meters from the center of the 201.25 MHz cavity. The NaI detector is used for measuring the energy spectrum of the photons, and was calibrated using the 1.17 MeV peak from a ^{60}Co source. At 13.29 meters distance from the center of the

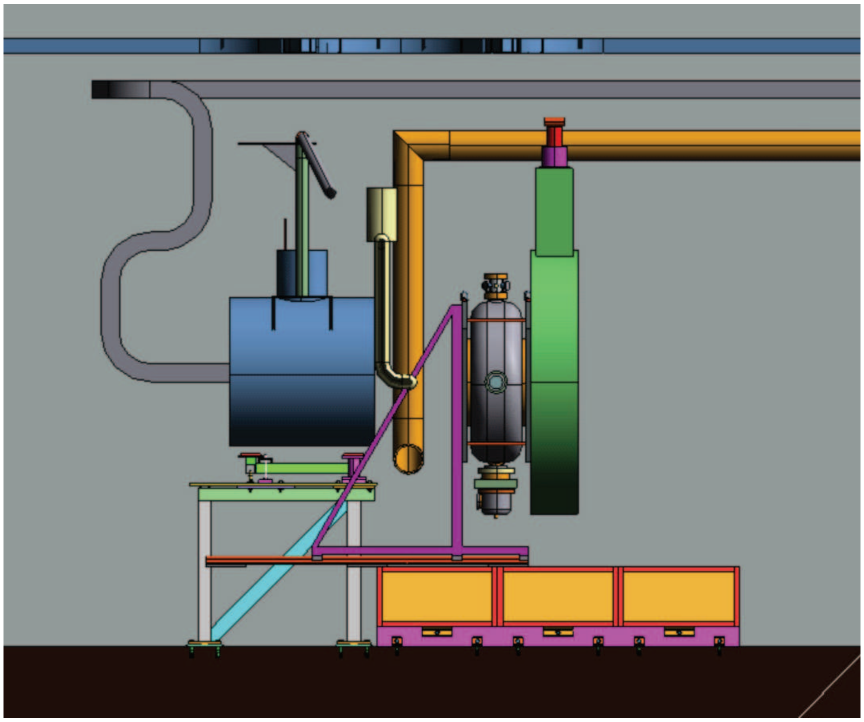

Fig. 7.13: The layout of the RF background measurements in the MuCool Test Area.

cavity, a 1 cm thick 10 by 10 cm plastic scintillator detector was positioned, approximately one meter below the NaI detector. This last detector was named PMT8 and was used to measure the photon counting rates.

As figures 7.12 and 7.14 show, the energy spectra agree well with the assumption that the photon production is dominated by bremsstrahlung in the material between the RF cavity and the detector. The kinetic energy gained by an electron emitted on crest given a field strength of 10.5 MV/m is $T = 1.811$ MeV and should be compared with the endpoint in figure 7.14. However the cross section for producing such an energetic bremsstrahlung photon is very small according to (7.20).

Maximum accelerating gradient achieved

The 201.25 MHz cavity reached 18 MV/m using the flat copper windows in the absence of magnetic field, producing very little spark damage. The same cavity reached 19 MV/m using the curved beryllium windows. The MICE operating gradient is 8 MV/m in the presence of 2–3 T magnetic field. Measurements using magnetic field will be performed for electric field strengths up to 16 MV/m and beyond.

The maximum achievable gradient as function of the magnetic field strength was evaluated with the 805 MHz cavity for a number of different button materials. Most of the titanium nitride coating was ripped off the surface due to a yet unknown mechanism, and the results are therefore not reliable. The molybdenum button consistently achieved higher

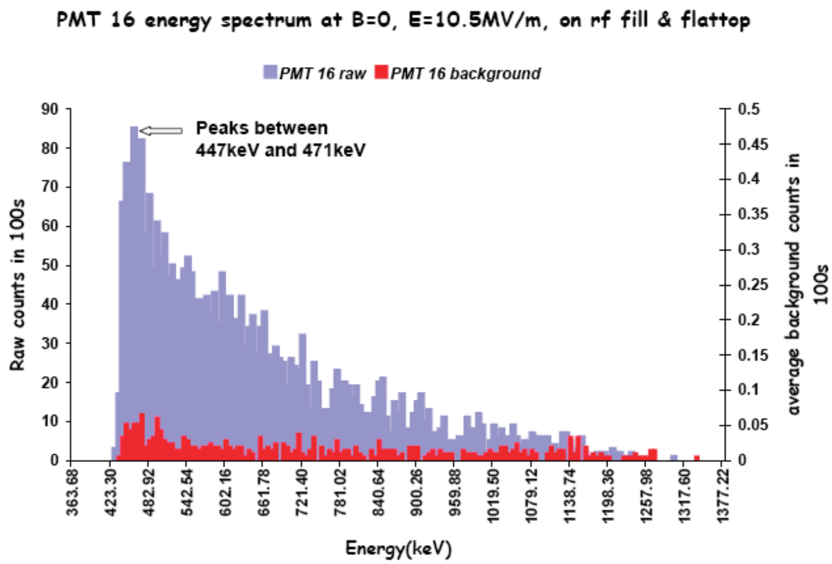

Fig. 7.14: The energy spectrum measured in the MuCool Test Area for the 201.25 MHz cavity.

gradients than the tungsten button for almost all magnetic field settings. The difference was of the order of 10%. From this it was concluded that molybdenum was a better material than tungsten.

Photon rates

For the photon counting rates, the button tests did not produce any statistically significant difference between different materials. At high electric field gradients the field emission follows the Fowler-Nordheim model for both cavities, and the results are compatible with previous measurements at LabG. At lower gradients resonance structures have been observed which are likely due to multipactoring. These effects could only be observed when the cavities were exposed to magnetic fields.

7.3.5 Photons per emitted electron in MTA

The photons are assumed to be generated by bremsstrahlung in copper, according to Seltzer–Berger parameterization for the energy distribution [74]. By reading off values in figure 7.11, the radiation yield in copper is $p_y = 3.21\%$ for a monochromatic electron beam of $T = 1.811$ MeV kinetic energy. Since

$$\langle t \rangle = p_y \cdot T \tag{7.8}$$

together with

$$\langle t \rangle = \int t \frac{\mathrm{d}\sigma}{\mathrm{d}t} \mathrm{d}t \tag{7.9}$$

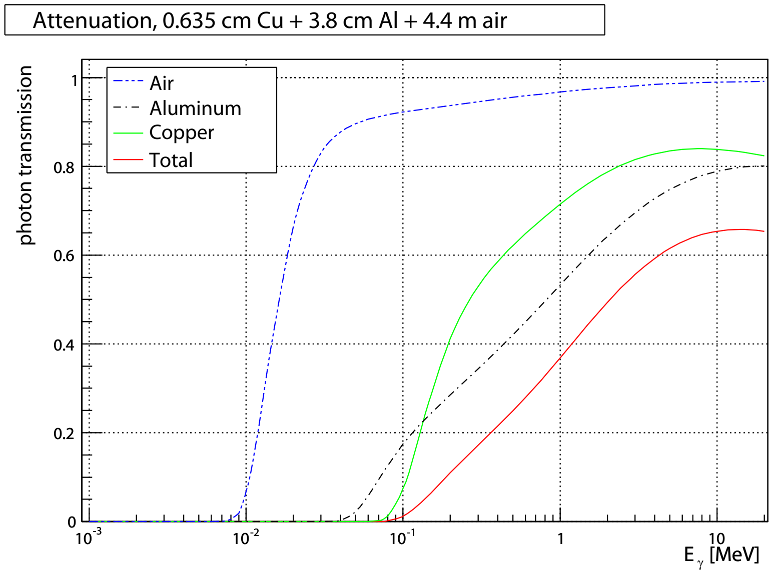

Fig. 7.15: Attenuation of photons from RF background in the MTA experiment.

the probability of generating a photon with fractional energy $x = t/T$ is

$$p_{gen}(x) = \frac{4}{3}T^2 p_y \left(\frac{1}{x} - 1 + \frac{3}{4}x\right) \tag{7.10}$$

if the parameterization from (5.31) is used.

Due to material in their path, the photons are attenuated. As figure 7.15 shows, the contribution to the attenuation form copper and aluminum is almost identical, while bremsstrahlung photons are produced in the copper. For high energies more than 50% of the photons survive to the detectors, while lower energy photons are quickly absorbed in the media, mostly due to the photoelectric effect. Figure 7.16 shows the energy spectrum after attenuation from photons from bremsstrahlung in copper. Note that the infrared divergencies are cancelled by the attenuation, though toward the high energy end of the spectrum, the function resembles the unattenuated cross section. In the simplification that all photonic energy in one event is gathered in only one photon, $p_{gen\&att} = 4.2\%$ of the electrons produce photons which survive the full distance to the detectors. With the requirement that the photon energy should exceed the detector threshold of 420 keV, the corresponding value would be 2.4%.

Assuming that the bremsstrahlung photons are emitted isotropically in a hemisphere, the detectors correspond to relative solid angles of

$$p_\Omega^{PMT8} = \frac{0.1^2}{2 \cdot 13^2 \pi} \approx 9.42 \cdot 10^{-6} \tag{7.11}$$

$$p_\Omega^{PMT16} = \frac{(0.0254 \cdot 0.75)^2 \pi}{2 \cdot 4.4^2 \pi} \approx 9.37 \cdot 10^{-6} \tag{7.12}$$

with distances of 13.0 m and 4.4 m respectively from the bremsstrahlung vertex.

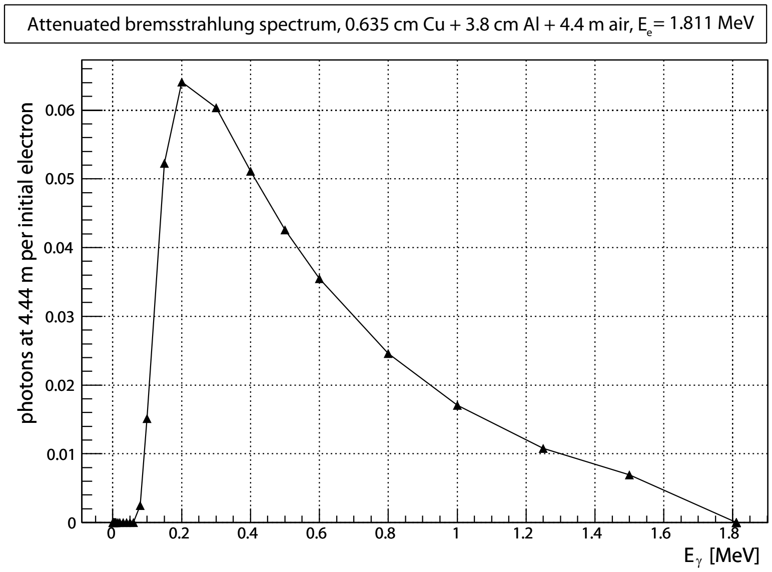

Fig. 7.16: The energy spectrum of bremsstrahlung photons, with attenuation effects included.

Since the density of polystyrene is 1.060 g/cm^3, and the mass attenuation coefficient is 0.06847 cm^2/g at a photon energy of 1.0 MeV, the interaction probability, p_{int}, in the 1 cm thick scintillator paddle is, according to Beer's law, 7.00%. At this energy Compton scattering is the dominating process. By approximating the Compton spectrum as flat until the Compton edge

$$E_{Compton} = E_\gamma \frac{2E_\gamma}{m_e c^2 + 2E_\gamma} \ , \tag{7.13}$$

the probability of the interaction energy deposition in the detector exceeding the threshold is

$$p_{cut} = 1 - \frac{E_{cut}}{E_{Compton}} = 1 - \frac{E_{cut}}{E_\gamma}\left(1 + \frac{m_e c^2}{2E\gamma}\right) \ . \tag{7.14}$$

For the case of $E_\gamma = 1.811$ MeV cut at $E_{cut} = 0.42$ MeV, p_{cut} is 65.9% [4]. The NaI detector is thicker, and made of denser material. Therefore, all photons arriving at the detector are assumed to interact with the crystal, and deposit all their energy in the sensitive region.

Together, these effects results in a translation from detected photons to emitted RF electrons,

$$\frac{n_\gamma}{n_e}(PMT8\ ) \ = \ p_{gen\&att} \cdot p_\Omega \cdot p_{int} \cdot p_{cut} \approx 1.04 \cdot 10^{-8} \tag{7.15}$$

$$\frac{n_\gamma}{n_e}(PMT16) \ \approx \ 2.25 \cdot 10^{-7} \tag{7.16}$$

which should be compared with MTA measured data, which is about 15 events in PMT8 per pulse at 10.5 MV/m field strength. Since the length of a pulse is 125 μs, and an RF

[4] The real threshold of PMT8 is unknown, this choice of E_{cut} implies an assumption that the threshold is identical to the one of PMT16.

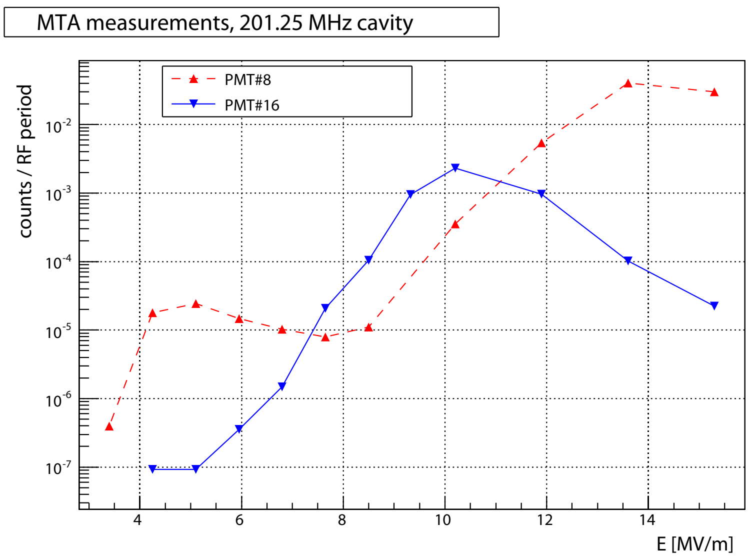

Fig. 7.17: The photon rates for PMT8 and PMT16 as a function of the gradient. Below E=4.5 MV/m the energy for an electron emitted on crest is at the PMT16 threshold. The threshold of PMT8 is unknown, but should it be identical to the prior, any counts below 4.5 MV/m would be due to noise and cosmic rays. At very high field strength, the detectors are saturated and the data are not reliable. PMT16 is saturated at lower field strength than PMT8.

period is 4.97 ns, there are 25 thousand RF periods per pulse, resulting in an average RF background event rate of $6.0 \cdot 10^{-4}$ photons per RF period. According to (7.15), this infers $5.8 \cdot 10^4$ electrons emitted per RF period[5] at this particular field strength.

Simulations of the MTA experiment

In order to cross check the results presented earlier, the MTA setup was modeled in G4MICE as two slabs of copper and aluminum, with the thicknesses 0.635 cm and 3.6 cm respectively. The surrounding volume was filled with dry air, and all particles reaching virtual planes corresponding to the detector positions were registered.

$3.54 \cdot 10^6$ electrons were fired parallel to the surface normal with a monochromatic kinetic energy of 1.811 MeV, corresponding to the electron acceleration if emitted on crest at 10.5 MV/m. This resulted in 56971 photons leaving the aluminum on the other side of the two slabs, hence the average number of photons per electron is 1.6%. This is smaller than the calculated $p_{gen\&att}$. One reason for this discrepancy is that the attenuation calculation did not take into account the longer path length of particles which are emitted at large angles from the surface normal. Since the detector is located on the beam axis and its

[5] Actually half period, since an equal amount of particles are emitted in the opposite direction, but there are no detectors on the opposite side of the cavity.

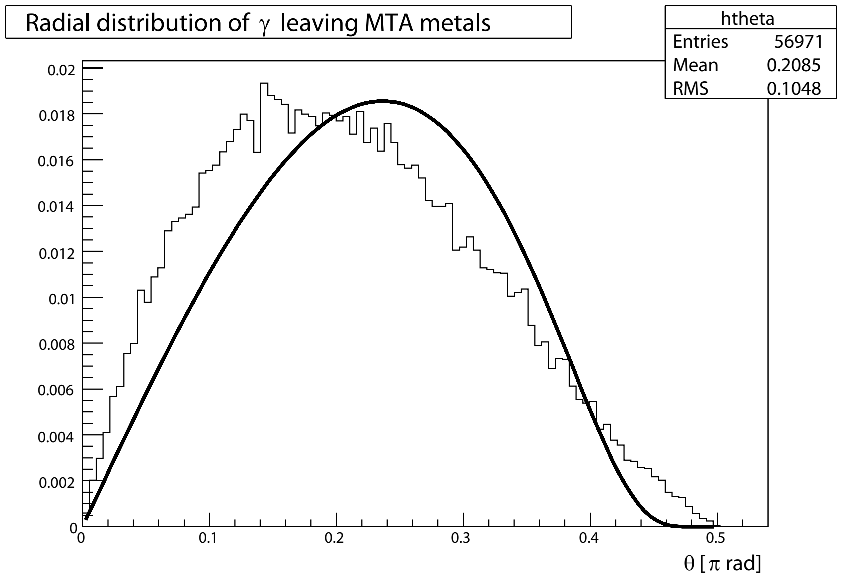

Fig. 7.18: The direction of bremsstrahlung photons leaving the metal surface, according to a G4MICE simulation of the MTA experiment. The solid line indicates the effect of increased attenuation for photons emitted at large angles, assuming no scattering and an isotropic angular distribution.

solid angle is very small, this effect would not be seen experimentally, unless the detector is moved.

Due to the large bremsstrahlung angles, only 5092 of the photons hit an area given by a circle of 1 m radius at the position corresponding to the NaI detector, of which 2111 photons had energy exceeding the PMT16 threshold of 420 keV. Assuming that the photon density at this virtual disk is homogeneous, together with the dimensions of the NaI detector, the number of photons above threshold per initial electron hitting the NaI detector is

$$\frac{n_\gamma}{n_e}(PMT16) \approx 2.16 \cdot 10^{-7}. \tag{7.17}$$

Using the same assumptions regarding the interaction probability in the detector as presented earlier, the corresponding quantity at PMT8 is

$$\frac{n_\gamma}{n_e}(PMT8) \approx 1.05 \cdot 10^{-8}. \tag{7.18}$$

which should be compared to (7.15). Hence, the calculations indicate 4% higher effective photon gain in PMT16 than the simulation, which given the many uncertainties involved is considered more than an adequate agreement. For PMT8 the agreement is even better; the calculations produced less than 0.4% lower gain than what was obtained by simulation. However, the PMT8 data is very sensitive to the poorly known threshold energy, the interaction probability in the detector and other assumptions that were made for both the calculated rate and the analyzed data. In addition, the experimenters have stated that

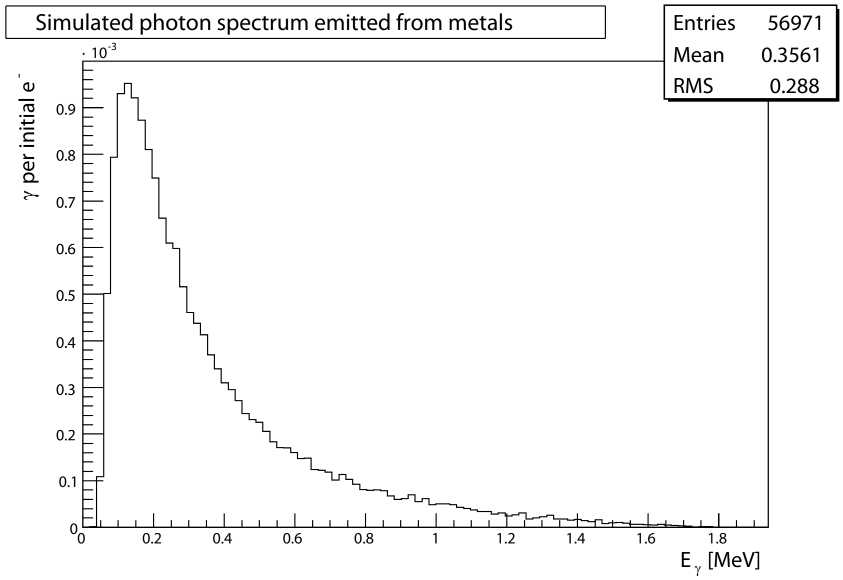

Fig. 7.19: The energy spectrum of bremsstrahlung photons, leaving the metal surface, according to a G4MICE simulation of the MTA experiment. The spectrum was generated by 3.7 million monochromatic electrons incident towards the metals at a kinetic energy of 1.811 MeV. The distributions resembles the calculated distribution shown in figure 7.16, but higher energy photons are less numerous than calculated.

PMT16 data is more reliable than PMT8 data, as long as it is not saturated. For these reasons, the PMT16 data is considered the most reliable and can be used to estimate the number of electron initially emitted from the cavity.

The same simulation also produced the energy spectrum for photons leaving the metal slabs. By comparing figure 7.16 with figure 7.19, it is clear that the number of high energy photons is overestimated in figure 7.16. There are two reasons for this:

- The calculations assumes the photon does not suffer energy loss, it is either absorbed or not. In reality, Coulomb scattering produces photons with lower energy, thus shifting the spectrum to low energy.

- The increased path length in the material for photons at large angles, implies a larger integrated cross section for processes giving energy loss.

The agreement between figure 7.14 and figure 7.19 is, however, quite good.

Since the radiation yield and the energy spectrum depend on the energy of the primary electron, an identical simulation run was launched with electron kinetic energy of 1.226 MeV, which is the energy of an electron emitted at peak field for 8 MV/m field strength[6].

[6] This is slightly higher than the value given in table 7.3 since these electrons are not subject to energy loss in a beryllium window.

Of 3.48 million initial electrons, 1969 produced photons in a one meter radius virtual plane corresponding to the placement of PMT16. Of these photons, 549 had energy exceeding the detector threshold 0.42 MeV. This resulted in an effective number of photons detected per initial electron,

$$\frac{n_\gamma}{n_e}(PMT16)\bigg|_{8\ \mathrm{MV/m}} \approx 5.72 \cdot 10^{-8} \tag{7.19}$$

hence only a quarter of the same quantity corresponding to 10.5 MV/m. According to MTA measurements, there are $4.03 \cdot 10^{-5}$ photons per RF period[7] at 8 MV/m. This value divided by the background efficiency (7.19) resulted in 705 electrons emitted from the cavity per RF half period. Expressed in frequency this is 142 GHz of electrons per direction.

To validate the Geant4 results, an additional study using EGSnrc [85] was planned. Since the manuals of the respective Monte Carlo packages describe the implementation of bremsstrahlung almost identically, the benefit of this endeavor was considered not worth the effort.

7.3.6 Simulation of RF background in MICE

The RF induced background was studied in 2004, by G4MICE [50] based on Geant4.5.2.p02 [61]. The initial energy spectrum of the electrons was given by table 7.3. Due to the low effective photon yield, the problem was simulated for two weeks on one hundred computers at a new computer farm at RAL. The implementation of many important processes changed with a new Geant4 release a year later, and the same simulation setup was resimulated with Geant4.6.2.p02. Since this second study had to be performed locally, the number of events was limited. The resulting rate of photons in the downstream tracker was 11% higher. Other rates were also somewhat higher, but those results suffer from small statistical samples.

Geometry

The background electrons were generated at the four beryllium windows next to an absorber. The absorbers, the absorber and vacuum windows had spherical shapes in G4MICE as shown in figure 7.20. The particles were read out at the tracker reference planes, which were placed at the entry to the trackers on the side which is closest to the cooling channel.

Simulation results

As expected, the most numerous background particles in the spectrometers were photons, even though the photon rate is attenuated by the absorbers and other material in the beamline. See tables 7.5 and 7.6. Photons have a relatively small probability to create a

[7] The data were derived from data collected during the 88.6 μs long RF flat top, not the full 125 μs long pulse.

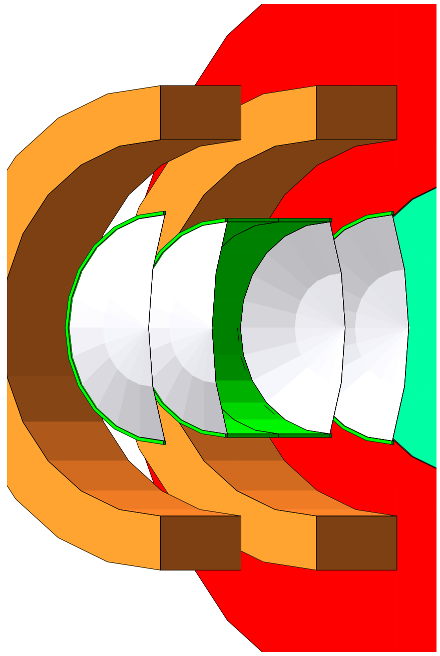

Fig. 7.20: Cut picture of an absorber in the G4MICE version used for the RF background studies. The liquid hydrogen is invisible here. The default absorber design in G4MICE-0.9.17 used spherical windows of a curvature radius of 30 cm for absorber windows, and 32 cm for vacuum windows.

hit in the detectors, making the experiment more sensitive to background in the form of electrons.

Simulations show that, due to geometry, less than 20% of the photons leaving the vacuum windows toward the spectrometers will arrive at the tracker reference planes, and those that do will have a radial distance from the beamline which is typically a factor two larger compared to the same distance when leaving the vacuum windows. Electrons leaving the cavities will hit the spectrometers since they follow the magnetic field lines.

Due to the phase asymmetry, up- and downstream shown in figures 7.6 to 7.10, the particles hitting the downstream spectrometer are more numerous and have higher energies than in the upstream case. The expected upstream to downstream photon rate is approximately 28% higher than what was expected based on arguments presented in previous subsections.

The energies of the bremsstrahlung photons follow approximately the distribution given by (5.31), since the low mass of intermediate material makes the background only modestly attenuated. As figure 7.12 shows, this resembles an exponential function. In the MICE linac the energies of the electrons as they interact with the absorbers depends on how many cavities they have travelled through, thus the photon energy distribution is a sum over the i energy states.

$$\frac{\mathrm{d}\sigma}{\mathrm{d}t} \propto \sum_i w_i \left(\frac{1}{x_i} - 1 + 0.75 x_i \right) \qquad , \; x_i = \frac{t}{T_i} \tag{7.20}$$

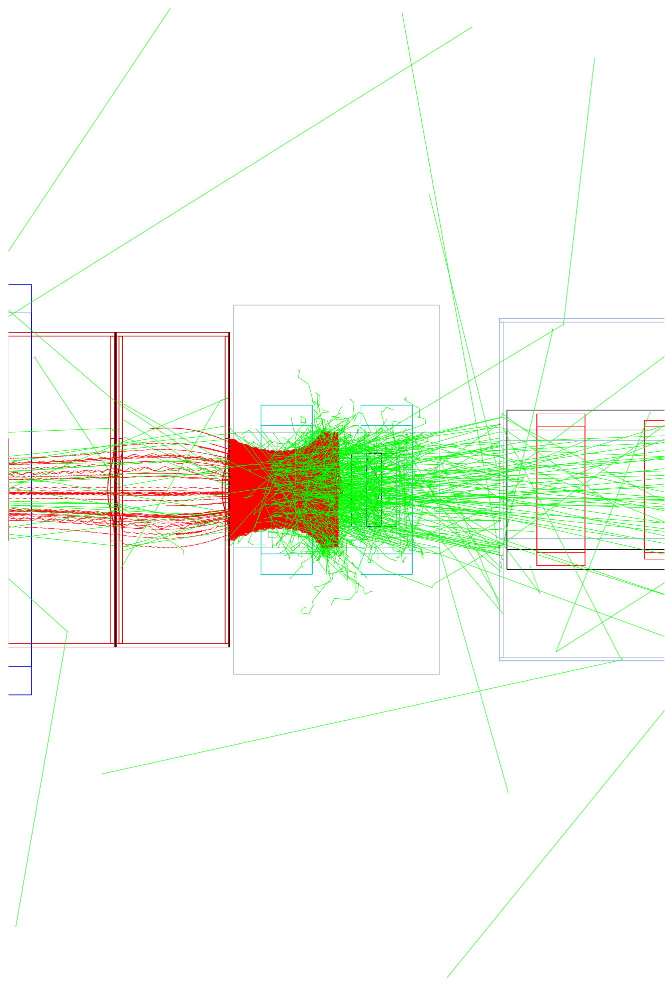

Fig. 7.21: RF background event visualized in G4MICE. Electrons are emitted at the beryllium windows and follow the field lines to the absorber. There they lose energy and sometimes produce bremsstrahlung photons. The photons have a fair chance of reaching the spectrometers. The particle rate corresponds to the average over 3.9 ns, using initial electron energies as calculated in Matlab. Red: negative particles. Blue: positive particles. Green: neutral particles.

where w_i is a relative weight between different electron energy peaks. As (7.20) shows the maximum photon energy which can be obtained is equal to the maximum initial energy T_i of the generated RF electron (here approximately 7 MeV).

Tab. 7.5: Rates of RF induced background at the tracker reference planes, G4MICE compiled with Geant4.5.2.p02. The rates are given per total number of initial electrons generated in the MICE cooling channel, Stage 6.

Particle	Downstream per generated	Upstream per generated
e-	$5.76 \cdot 10^{-6}$	$1.72 \cdot 10^{-7}$
gamma	$8.315 \cdot 10^{-4}$	$6.934 \cdot 10^{-5}$

Tab. 7.6: Rates of RF induced background at the tracker reference planes, G4MICE compiled with Geant4.6.2.p02. The rates are given per total number of initial electrons generated in the MICE cooling channel, Stage 6. These values were obtained using lower statistics than the values presented in table 7.5.

Particle	Downstream per generated	Upstream per generated
e-	$1.03 \cdot 10^{-5}$	$1.14 \cdot 10^{-6}$
gamma	$9.02 \cdot 10^{-4}$	$1.04 \cdot 10^{-4}$

Using the number of electrons emitted from an RF cavity derived from the MTA measurements as outlined earlier, the total number of electrons emitted during a MICE RF period can be calculated. With two linacs, each consisting of four cavities, and two half periods per period, the total number of emitted electrons is

$$n_e = 2 \cdot 4 \cdot 2 \cdot 705 \approx 1.13 \cdot 10^4 \tag{7.21}$$

per RF period, equivalent to

$$f_e \approx 2.27 \text{ THz}. \tag{7.22}$$

Using the MICE $n_\gamma / n_e = 9.02 \cdot 10^{-4}$ in the downstream direction from table 7.6, the photon rate in the downstream tracker reference plane is thus 2.0 GHz, and between a factor 9 to 12 lower in the upstream direction (depending on which simulation to rely on). The statistical sample for electrons arriving at the tracker reference planes is limited, and the results are thus less reliable, but the worst rate obtained is in the downstream direction at around 23 MHz.

7.3.7 The dependence on field gradient

Looking at the MTA PMT16 data in figure 7.17 three general regions can be identified. At very low gradients noise and cosmic ray background dominate the counting rate, effectively

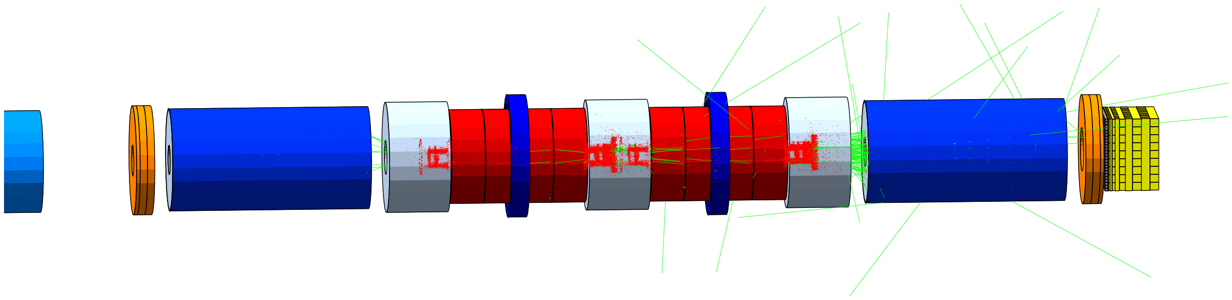

Fig. 7.22: This figure is a G4MICE snapshot of the RF induced background, with a rate corresponding to 3.9 ns. A large number of electrons and photons are interacting in the absorbers. Some of these bremsstrahlung photons are making hits in the spectrometers and time of flight detectors. As explained in the text, the highest rate of background is in the downstream direction.

masking the RF induced background. At high gradients the detector is saturated and does not give useful information on the rate of bremsstrahlung photons. In the central range, $5.95 \geq E \geq 9.32$ [MV/m], the rate depends very strongly on the gradient E

$$n_\gamma \propto E^{16.5} \quad (\chi^2/ndf = 0.3752/2). \tag{7.23}$$

Over the last century a large number of experiments have reported often conflicting reports of the value of the exponent in (7.23). Values between 9 and 20 have been published [86]. This section shows that the ambiguities are due to effects described in previous sections which have not been accounted for, thus resolving the conflict between different sets of data.

Photon to electron ratio as function of gradient

Most importantly, the energy to which an electron is accelerated depends on the accelerating field gradient. As figure 7.23 illustrates, there is a sharp cut off at low fields. This is because the particle is not accelerated enough to reach the opposite side of the cavity before it is decelerated. These electrons will in vacuum be trapped inside the cavity, oscillating back and forth. In reality they could cause resonance effects when colliding with the surface from which they were emitted. The cut off implies that the exponent is initially very large and at higher gradients the electron kinetic energy is proportional to the electric field gradient.

Another contributing factor is that both the radiation yield (figure 7.11) and the photon transmission probability (figure 7.15) increase with higher energy, thus with increasing electric field gradient. In addition the average energy of photons hitting the detector increases, giving a larger fraction of photons which are above the detector threshold. When all these effects are combined the photon per initial electron ratio depends on the field

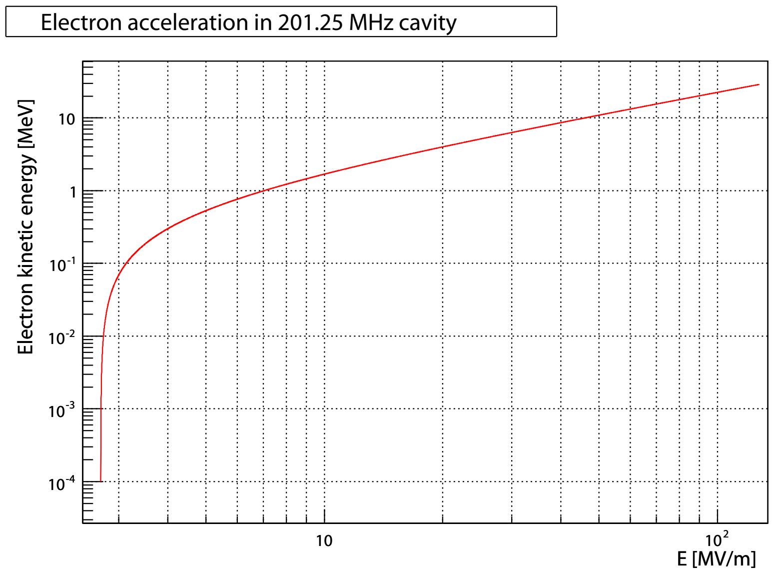

Fig. 7.23: Electron acceleration as a function of electric field gradient in one 201.25 MHz cavity. Calculated in numerically in Matlab.

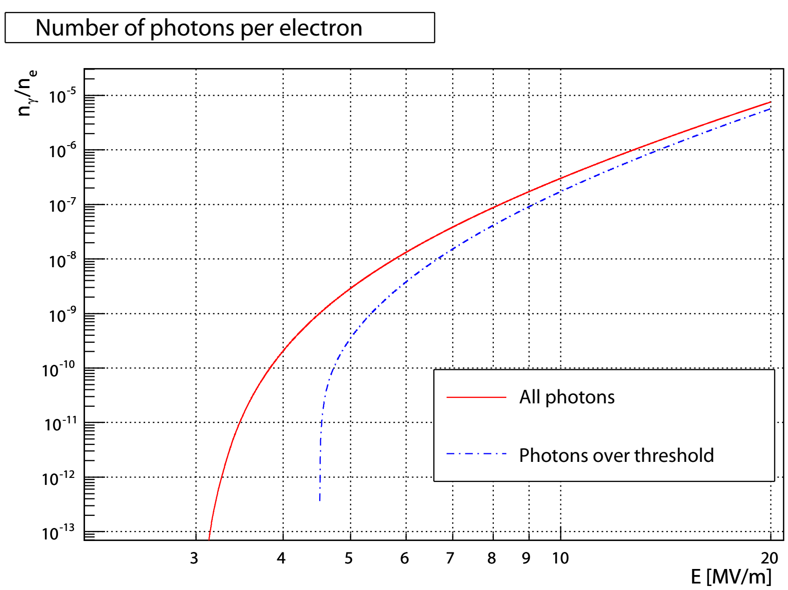

Fig. 7.24: The number of photons hitting the NaI detector (PMT16) per number of electrons emitted from the cavity as a function of the field gradient. The vertical scale takes the detector solid angle into account.

gradient as

$$\frac{n_\gamma}{n_e} \propto E^{7.65} \quad (\chi^2/ndf = 4.445/1077), \tag{7.24}$$

fitted[8] from calculations presented in figure 7.24.

The remaining exponent $16.5 - 7.65 \approx 8.85$ cannot be explained by the effects giving the gradient dependency of the n_γ/n_e ratio. Instead, this factor is most likely caused by the creation of new emitting sites and the activation of old emitting sites, both effects adding to the number of electrons emitted from the cavity, n_e. A number of experiments [83, 86, 87] have published

$$flux \propto E^{9.6} \tag{7.25}$$

for cavities operating at much higher field gradients. At these gradients the electron energy is almost linear with the gradient and the resulting photon energy is large enough that virtually all photons are above the detector thresholds, while the attenuation of photons is only modestly depending on the photon energy. Thus the only remaining factor is the radiation yield, which when deducted gives an exponent of approximately 8.9. This value is close enough to the estimated exponent due to field emission $n_e \propto E^{8.85}$ that we conclude that the 201.25 MHz data at 8 MV/m is consistent with 805 MHz data at 100 MV/m [83, 86]. This model should be universally applicable.

Effective field emission as function of gradient

If the number of emitting sites and their respective field enhancement were constant the leading term in (7.6) suggests that the emission of electrons should be proportional to the square of the electric field gradient. The surface of a cavity is however laden with asperities of varying β_{FN}. As the surface field gradient E increases asperities at subsequently lower β_{FN} become "activated" as E_{local} approaches the field emission region. By performing a log-log plot on figure 7.25 the density of asperities depends on β_{FN} as

$$\rho(\beta_{FN}) \propto \beta_{FN}^{-3.09} \tag{7.26}$$

which implies that the effective field emission due to pre-existing emitting sites increases with E as

$$n_e(\mathrm{pre-existing}\ \beta_{FN}) \propto E^{2 \cdot 3.09} \tag{7.27}$$

where the exponent 2 comes from the leading term of Fowler-Nordheim tunneling.

When a very high local electric field causes the mechanical stress to exceed the tensile strength a breakdown occurs and the asperity is destroyed, as illustrated in figure 7.3. It has been observed [84, 88, 89] that breakdown events cause craters to be created on the surface, surrounded by a large number of smaller asperities. When conditioning a cavity, the asperities with the largest enhancement factors are burned off, allowing increasingly higher maximal gradient to be maintained [90]. Unfortunately this also produces new asperities with lower β_{FN}.

[8] This is based on the assumption of the existence of a detector threshold. The corresponding scaling law in the same interval for 100% detection efficiency is $E^{6.23}$, $\chi^2/ndf = 1.204/1077$.

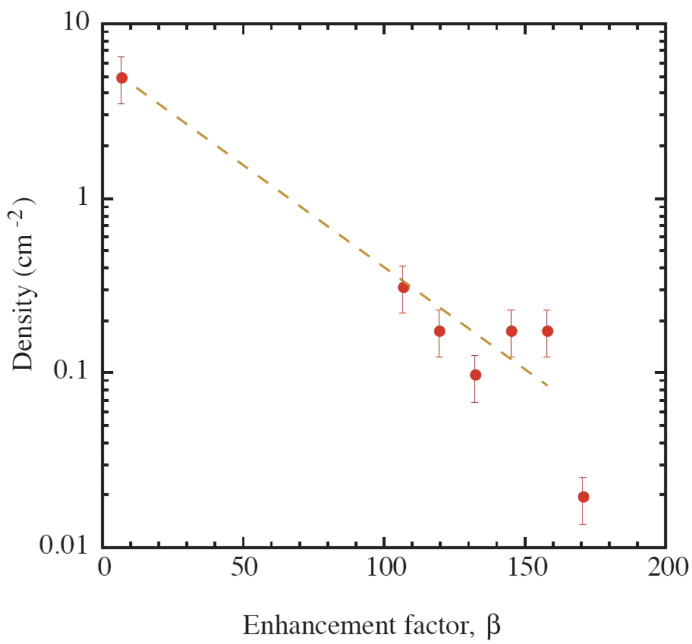

Fig. 7.25: The density of asperities causing field enhancement. From ref [84].

Although the relation between creation of new low β_{FN} asperities and the annihilation of high β_{FN} asperities is far from straightforward, it is reasonable that the process should be proportional to the occurrance of breakdown events. Quoting Döbert [89]

> *"The slope of the fitted curve is one decade in breakdown rate for 7 MV/m of average gradient..."*

gives a factor

$$n_e(\text{new } \beta_{FN}) \propto E^{2(1/\log_{10} 7)} = E^{2 \cdot 1.18} \tag{7.28}$$

due to the creation and destruction of emitting sites.

The combined effect of the activation of pre-existing asperities and the creation of new asperities thus gives an exponent 8.5, which should be compared with 8.9 in the previous section. When the model for $n_\gamma / n_e(E)$ is multiplied by the model for $n_e(E)$ the resulting photon rate in the detector n_γ according to this model shows good agreement with PMT16 data. This is shown in figure 7.26.

Magnetic field effect

If the cavity is subject to magnetic field the Lorentz force [84] created by the electron current increases the chance of breakdown. This is expected to further increase the background rates. Unfortunately the 201.25 MHz cavity could not yet be tested in a magnetic field. The 805 MHz cavity was however operated at a number of field settings, and it was found [91] that the counting rate was proportional to $e^{0.9251B}$, where B is the magnetic field

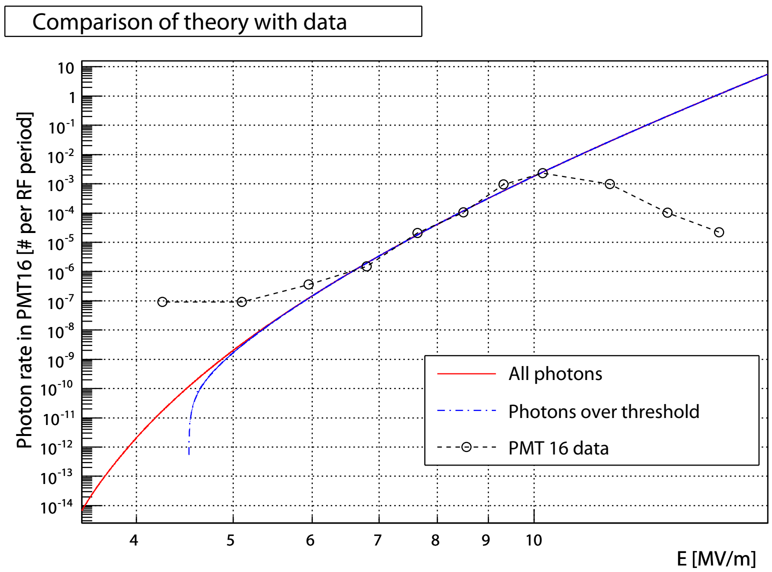

Fig. 7.26: Comparison between MTA PMT16 data with the predicted number of photons using the bremsstrahlung model combined with the empirical field emission model. At low E noise and cosmic ray background dominates, and the detector is saturated at high E. The central region shows good agreement. The rate given by the model was scaled by an overall constant 2500.

strength in tesla. If this law is also valid for the 201.25 MHz cavity, which will operate in approximately three tesla, the rates calculated here would increase by an additional factor of 16.

Heating of absorbers

If the rates of RF induced electrons is extremely large, a temperature increase in the liquid hydrogen absorbers could be observed. Since the central absorber is exposed to half of the total number of RF induced electrons, independent of whether the electrons are reversing in the linacs, it would be the absorber most at risk. The average kinetic energy of the electrons in table 7.4 is 3.80 MeV, and assuming that the energy carried away by bremsstrahlung photons is negligible, the average power is

$$\langle P_{heat} \rangle = \frac{f_e}{2} \langle E_{kin} \rangle \, d \approx 4.317 \cdot 10^{15} \text{ eV/s} \approx 0.691 \text{ mW} \tag{7.29}$$

where the RF duty factor $d = 10^{-3}$ was used. When magnetic field is applied the flux of electrons, and thus the heat, is expected to increase by an order of magnitude. This is negligible compared to the heat removal capacity of the absorber design (page 65), and thus not a problem for the experiment.

In a full scale Neutrino Factory cooling channel the gradient is approximately 16 MV/m [28]. Using the model described in this section the emission of electrons will rise by

$2^{2(1.18+3.09)} \approx 372$, while the average electron energy increases by a factor 2.6. In addition the duty factor of a Neutrino Factory is $d = 0.19\%$ [28]. The effective heat is thus expected to be approximately 1.3 W, not counting the additional field emission due to magnetic field. The heat dissipation of a Neutrino Factory absorber will be approximately 300 W [28]. The absorbers will thus be able to cope with the RF induced heat, even if the rates are increased by an order of magnitude due to the magnetic field.

7.3.8 Conclusions

While it is possible to achieve accelerating gradients much higher than required for the MICE experiment, the background in terms of bremsstrahlung photons quickly becomes a major obstacle. The heat in the absorbers due to field emission is, however, not a problem.

Prior to the MTA measurements, it was assumed based on LabG data that the number of electrons emitted from an RF cavity was 8 per period and direction. The analysis shows that the previously expected number of electrons emitted from the cavity was underestimated, by a factor 88. The many approximations introduce uncertainties in the estimate. A particular problem is the sensitivity to the electric field strength, which implies that it must be measured very accurately if one is to estimate the background rates in a MICE working condition.

As previously mentioned, another source of background in MICE is the avalanche effect which occur if an electron knocks off more electrons in an adjacent cavity. This is similar to multipactoring, but with the additional problem that it is not restricted to low field strengths, since the RF cavity phases are set to accelerate relativistic particles. Based on a different cavity, the background rates are expected to increase by an order of magnitude when the magnetic field is applied.

There are a number of techniques available to reduce the field emission. If the number asperities with high enhancement factors can be reduced by chemical, mechanical or electrical polishing prior to conditioning the background rates would decrease. If the tensile strength of the surface would increase by titanium, molybdenum or tungsten coating the breakdown rates would decrease, and thus also the creation of new asperities. However the shape of the asperities strongly influences the field emission, and it is not clear the shape is related to the tensile strength. A third route to decrease field emission is to use high pressured gas in the cavities. This causes low energy electron to recombine before they can be accelerated in the linac.

Since detectors such as the time of flight stations, are designed to measure muons which deposit a few MeV of energy loss, while the RF induced background occupies the low energy region, much of the background effects could be avoided by setting a high energy threshold. However this would reduce the performance of the muon track measurements. If the rates are high enough, the photon energy integrated over an open gate can obscure the muon signal and pose a real problem. Even though only about a few percent of the photons interact with the detector, and the average energy deposition is very low, the total photonic energy deposition is comparable to, or exceeding that of a muon track. This can be demonstrated by the following Gedankenexperiment: Assume 2 GHz photon flux in the downstream tracker reference plane, and that 10% of these arrive at TOF2. Of the photons hitting the detector only 10% interact and give an energy deposition of 0.5 MeV. The open gate of TOF2 is 500 ns, which gives a total photonic energy deposition of 5 MeV, which is about half the energy deposition of a muon track.

Simulations of the scintillating fiber tracker have shown [92] that it is more sensitive to background in the downstream tracker since the direction of the electrons is parallel to the muons. The same simulations were based on much lower background rates, and the problem would need to be resimulated with the new reconstruction software before any firm conclusions can be drawn.

8. CALORIMETER DESIGN

As discussed in section 7.2, the presence of electrons produced by decaying muons introduces systematical errors on the emittance and cooling measurements. The particle identification was originally intended to be performed using a dedicated Čerenkov detector followed by a sampling calorimeter. The total cost of these devices was considerable, and the calorimeter was not optimized for the MICE running conditions. A study was performed in an attempt to improve the performance, while at the same time minimizing the cost of the calorimeter.

This chapter is a summary of the conceptual design of the calorimeter, and the work performed to compare the performance of the original calorimeter design with a new design, invented by the author and Jean-Sebastien Graulich, Geneva University. The performance improvement showed that the latter design is superior in all cases studied, and was thus chosen as the base line calorimeter for the Muon Ionization Cooling Experiment.

8.1 *Principles of calorimetry*

There are various methods of measuring the energy of a particle, and in MICE we rely on the scintillation mechanism in plastic scintillators. The final amplitude in the readout depends on a number of parameters. The most important feature is that the number of scintillation photons produced is proportional to the energy lost by the particle in the detector. Both the number of particles produced in an electromagnetic shower and the number of scintillation photons per charged particle track follow Poisson distributions. Therefore the variance σ_E^2 is proportional to the energy E, and the energy resolution is given by

$$\frac{\sigma_E}{E}(Poisson) = \frac{a}{\sqrt{E}} \tag{8.1}$$

where a is a constant which characterizes the calorimeter performance. It follows that low energy loss gives worse relative energy resolution, ultimately diverging for zero energy beams. In addition to this effect, electronic noise gives a contribution to the resolution independent of the energy,

$$\frac{\sigma_E}{E}(noise) = \frac{b}{E} \tag{8.2}$$

but this is usually a second order effect which becomes significant only at high energy.

At high energy, resolution is lost due to longitudinal leakage, i.e., the particle or the associated daughters spill out of the active volume at the back end of the calorimeter. Such longitudinal leakage gives larger σ_E than transverse leakage for identical fractional loss. To first order the longitudinal leakage depends on the energy loss at the shower maximum, t_{max}, which in turn is proportional to the energy. In this approximation the energy resolution due to leakage scales as

$$\frac{\sigma_E}{E}(leakage) = c. \tag{8.3}$$

Thus a useful parameterization for the energy resolution of a calorimeter is

$$\frac{\sigma_E}{E} = \frac{a}{\sqrt{E}} + \frac{b}{E} + c \tag{8.4}$$

where each of the constants a, b and c have a physical meaning.

In order reduce the leakage term in a finite size detector, the stopping power can be increased by interleaving the sensitive volumes with dense material. Such mixed detectors made of active parts with low stopping power and passive parts with high stopping power, are called sampling calorimeters. However, the geometry of the sampling calorimeters introduces a substantial loss of energy in the passive parts, which usually dominates the energy resolution of sampling calorimeters. The energy deposition in the material is dominated by low energy electrons, which have a very short range and are often confined to the passive material. While the variance in the number of photons produced is proportional to the critical energy E_c (5.29), which is inversely proportional to Z, the range is proportional to the radiation length X_0, hence proportional to A/Z^2. The relative energy resolution is thus proportional to the square root of tZ/A, where t is the thickness of the passive material. The passive material in a sampling calorimeter should therefore be

- as thin as possible
- made of as dense material as possible

in order to improve the energy resolution. Furthermore it is important how the microstructure is arranged in a sampling calorimeter in order to reduce channeling effects[1].

8.2 KLOE calorimeter

The electron positron collider $DA\Phi NE$ was designed to study $\mathcal{CP}$ violation in the neutral kaon system, and operated with a center of mass energy around 1 GeV. The KLOE experiment was constructed to detect K_L produced in Φ decay and measure its decay channels. Since photons are produced in the decay of π^0 as well as in Φ related processes, the calorimeter was optimized to measure the energy and vertex of photons.

The KLOE calorimeter was a sampling calorimeter with grooved lead sheets and glued scintillating fibers [61]. Studies had shown that a better performance could be obtained by this "spaghetti" structure of fibers, than with a "lasagna" structure of lead and scintillator

[1] Tracks at certain angles might encounter different amounts of passive material than the average track, leading to undesired resonances in sampling fraction and energy loss.

sheets. The sampling fraction of the detector was 13%, and the energy resolution of the calorimeter was[2]

$$\frac{\sigma_E}{E} \approx \frac{5\%}{\sqrt{E[\mathrm{GeV}]}} \tag{8.5}$$

according to a test beam at PSI using electrons, muons and pions in the momentum range 100 to 450 MeV/c. The presence of lead in the calorimeter made it opaque to photons and thus it was a good at measuring the energy of photon events which would otherwise be lost in a more transparent material such as plastic scintillator. The drawback was that a large fraction of particle energies were lost in the lead, thus limiting the energy resolution for muons and other particles of interest.

8.3 The calorimeter's role in MICE

It is important to remember that the so called calorimeter in MICE is not primarily intended to be used for energy measurement. Its main objective is to provide separation capability between muons and decay positrons. In addition to this primary task, it should also be able to separate muons from pions, x-rays and electrons. As a bonus, it would be useful if the calorimeter could give independent information on the particle momentum, through means such as range or barycenter in the calorimeter.

Having said that, there is indeed an interest for good energy resolution with the calorimeter, since particles can be identified by comparing the momentum measured in the tracker with the energy measured in the calorimeter. As was shown in the previous section, the relative energy resolution gets worse for lower energy, so relying on matching the energy to the momentum will not be a good PID method for low momentum. As an example; at the lowest momentum beam setting according to the run plan, the momentum of the muons is

$$p = 140 \pm 14 \text{ MeV/c} \tag{8.6}$$

in the center of the central absorber, which means that the three standard deviation lower limit will occur at around 98 MeV/c, i.e., 38.5 MeV kinetic energy. There is one half absorber worth of energy loss to deduct from that, and at 40 MeV

$$-\frac{\mathrm{d}E}{\mathrm{d}x\rho} = 6.539 \text{ MeVcm}^2\text{g}^{-1} \tag{8.7}$$

$$\rho = 0.07080 \text{ gcm}^{-3} \tag{8.8}$$

$$x = 17.5 \text{ cm} \tag{8.9}$$

hence the kinetic energy after the cooling channel is 30.4 MeV. At this velocity, a muon loses approximately 4 MeV in the spectrometer. It has therefore 27 MeV kinetic energy at the entrance of TOF2. A muon at 30 MeV has a CSDA range in polystyrene of 4.6 cm [93], and even shorter for lower energies. The baseline design of TOF2 is 5 cm thick, so

[2] Can be compared with ATLAS ECAL $\frac{\sigma_E}{E} = \frac{0.10\sqrt{\mathrm{GeV}}}{\sqrt{E}} + \frac{0.28\ \mathrm{GeV}}{E} + 0.0035$.

the slowest muons are actually stopped in TOF2. Performing this exercise on a nominal 200 MeV/c muon, the resulting energy of the particle hitting the calorimeter is 97 MeV, or 173 MeV/c.

This exercise tells one very important thing: *Particle identification should be performed on muons which have momentum starting from zero as they enter the calorimeter!* Equation (8.5) diverges, and relying exclusively on the energy deposited in the calorimeter for particle identification would hence not work. Typically the muon momentum in the KLOE calorimeter was much higher than in MICE, for example the $K^{\pm} \to \mu^{\pm}\nu$ gives a muon momentum between 280 and 320 MeV/c, and the experimental technique must be adjusted accordingly to suit the MICE conditions.

8.4 Two calorimeter designs

In the original MICE proposal, the separation between μ^+ and e^+ was performed using a calorimeter and a Čerenkov detector, called CKOV2. Together with the information given by the spectrometers and the time of flight system, this was thought to be enough to remove any significant bias to the emittance measurement.

8.4.1 KLOE-light

The baseline design for the calorimeter was a lead and fiber "spaghetti" design, similar to what was used in the KLOE experiment. Since the energy of the particles is lower than in KLOE, the ratio of fiber to lead has been adjusted by making the lead foils thinner. This design is henceforth called KLOE-light, or KL for short.

A KLOE-light layer was segmented transversally in thirty different cells. Each cell was 4 by 4 cm, and 120 cm long.[3] There were four identical layers, and each layer was oriented perpendicular to its closest neighboring layers. Every cell was read out at both ends by PMTs, thus making the total number of channels equal to 240. When the study presented in this chapter was performed, there was no decision taken for the front end electronics, but it was assumed that ADC and TDC information would be available.

8.4.2 Sandwich

Due to the low energy of the muons, and the limited particle identification performance obtained in simulations using the KLOE-light calorimeter (section 8.6), an alternative design has been proposed. This design is made of a front layer identical to the KLOE-light, and ten layers of fully active plastic scintillator. The thicknesses of the plastic layers are 1, 2, 3, 4, 6, 8, 10, 12, 12, 12 cm respectively. The thicknesses were chosen such that the resolution of the range of the muons is still reasonable at low momentum. The transverse segmentation of the plastic has been chosen such that the total number of channels is identical to the KLOE-light baseline. This design was called Sandwich, or SW for short.

[3] The transverse dimensions of the cells have been changed in the final design to 4.4 by 92.4 cm.

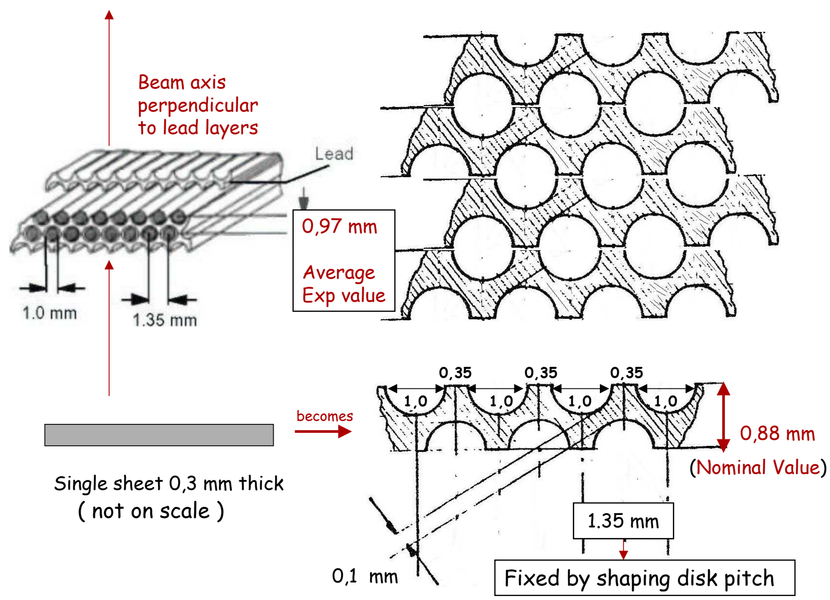

Fig. 8.1: The microstructure of the KLOE-light. The scintillating fibers are glued to grooved lead foils, and read out on both ends by photomultiplier tubes.

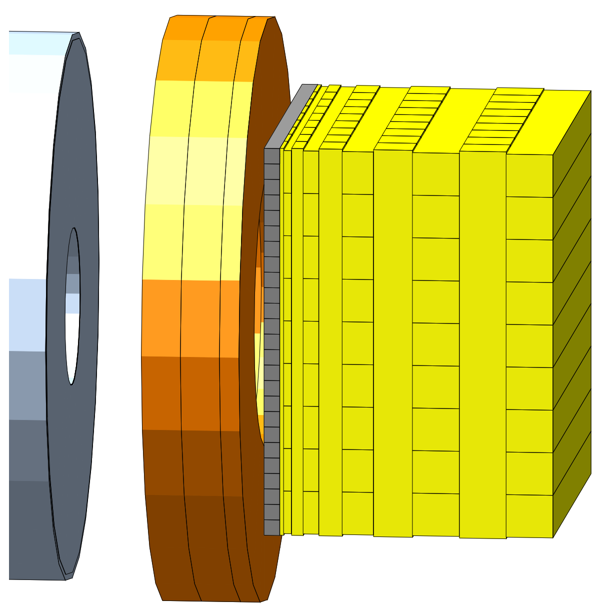

Fig. 8.2: The Sandwich calorimeter design as implemented in G4MICE (grey and yellow). During the design evaluation presented in this chapter, the iron shield (orange) encasing TOF2 was not yet invented. See chapter 10 for discussion on related topics.

An incoming positron or electron will lose most or all of its energy in the preshower layer, and generate an electromagnetic shower in the process, as described in section 5.4. The photonic content of an electromagnetic shower increases with shower depth, but since the absorption coefficient for pair production is inversely proportional to the radiation length, the low Z of the chemical components of plastic scintillator makes the layers following the preshower mostly transparent to the photons. Thus an electromagnetic shower event will have a very different longitudinal profile compared to a muon event in the calorimeter, which makes it possible to distinguish between signal and background events, even when the energy of the incoming particle is only a few times the critical energy in lead.

The principle advantages of the SW over the KL are that the prior samples more of the particle energy, muons are not punching through, and the range resolution is better. In addition to this, it is easier and cheaper to manufacture.

8.4.3 Longitudinal size and segmentation of SW

Since the radiation lengths of the fibers and the glue is much longer than the radiation length of lead, 41 cm compared to 0.56 cm, the lead content in the preshower layer dominates the electromagnetic shower production. The preshower layer has the same structure as the four layers in the KL design, and by reading figure 8.1 one can conclude that the preshower layer volume consists of approximately 33.9% lead. With a preshower thickness of 4 cm as in the KL design, the average amount of lead traversed by a straight trajectory is thus 1.35 cm, or 2.42 radiation lengths. Using (5.59) with the critical energy $E_c(Pb) = 7.79$ MeV implies that the thickness of a 4 cm preshower layer corresponds to the depth of the shower maximum for electrons with the kinetic energy

$$E = E_c e^{\frac{\Delta z}{X_0}+0.5} \approx 145 \text{ MeV}. \tag{8.10}$$

Hence the shower maximum of most background events is located inside the preshower layer, while only very high energy showers still develop in the back of the preshower layer. This suits the experimental conditions of MICE.

The total thickness of the Sandwich calorimeter was chosen with the muon range in mind. A back of the envelope calculation of the range gave that 70 cm of plastic after the preshower layer would be enough.[4] This was later compared with simulation, and in figure 9.12, the stopping depth of the muon is plotted as a function of the $\beta\gamma\cos\theta$ of muons in plastic[5]. See also figure 9.9. 70 cm of plastic were concluded to be enough to stop muons up to around 270 MeV/c. Simulations show that only 1.9% of all good muon events for the highest momentum beam will have $p_z \geq 270$ MeV/c at the entrance of the calorimeter. For the nominal momentum of 200 MeV/c the muon will likely stop in the center of the calorimeter, and the track will be even shorter when the energy loss in upstream volumes has been accounted for.

[4] A preshower layer of 4 cm followed by 70 cm of polystyrene corresponds to a total of 4.2 radiation lengths, and the polystyrene corresponds to 1.4 times the mean free path length of photons created in the preshower layer.

[5] The volume contained only 70 cm of plastic scintillator so the graph is cut off at very high momenta.

The longitudinal segmentation was chosen to have a relative resolution on the range as constant as possible, or at least that the resolution would be a monotonic function of the particle range. That means thinner layers in the beginning and thicker towards the end of the calorimeter. Ideally the first plastic layer should be infinitesimally thin, but one centimeter was considered the thinnest practical thickness. Ten layers were considered required to reconstruct the range. The argument that the Sandwich calorimeter should not use more PMTs than the KL meant that nine scintillator slabs per plastic scintillator layer could be employed.

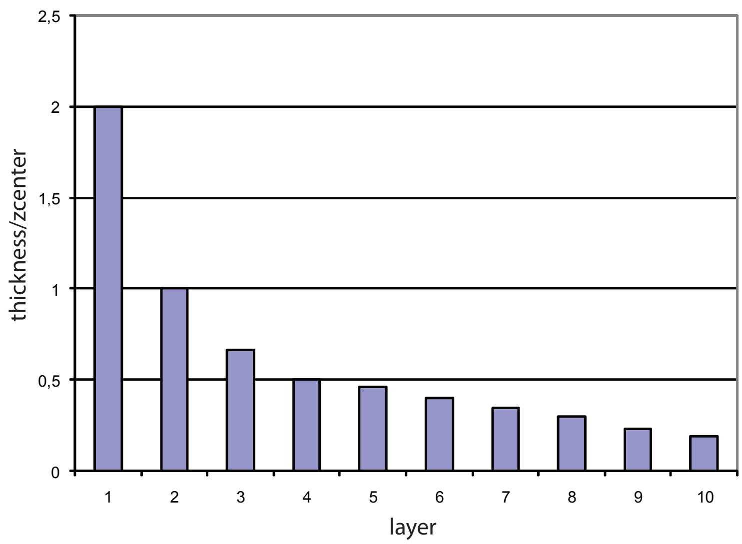

Fig. 8.3: The relative resolution of the range of particles in the plastic part of the Sandwich calorimeter depends on the thickness of the layer at the stopping position and the placement of the last hit layer. X-axis: layer number. Y-axis: a quantity proportional to the relative resolution.

8.4.4 History and naming convention

The original design was named KLOE-light by Ludovico Tortora, since it is similar to the design used for KLOE but with thinner lead sheets. The Sandwich design was originally plastic layers sandwiched between two layers identical to those used for KLOE-light. A similar design without the back end layer was called Smörgås[6], which means open sandwich in Swedish. The back end layer was intended for capturing photons from electromagnetic showers generated in the preshower layer. However the performance to cost ratio was too low, and the original Sandwich design was scrapped. Sandwich was already the established name of the contender to KLOE-light, so the Smörgås design inherited its name.

To add to the confusion, the abbreviations KL and SW are often incorrectly used to describe the preshower layer and the plastic part of the Sandwich design. In addition

[6] Webster's: Main Entry: smorgasbord Function: noun Etymology: Swedish smörgåsbord, from smörgås open sandwich & bord table

the name EMCal, originally meaning electromagnetic calorimeter, was also recycled as Electron–Muon calorimeter.

In this thesis and in any publications by the author, SW and KL are two different *conceptual designs* of the physical EMCal, and not physical subcomponents of the same detector.

8.5 Description of methodology

The purpose of this study was threefold; it aimed to

- evaluate the performance of the baseline calorimeter design
- find ways to improve the performance
- reduce the total cost of the particle identification system.

The first objective was obtained by implementing the KLOE-light design in as much detail as possible in a series of realistic simulations. This was performed in G4MICE, compiled with Geant4.7.1.p01 libraries. It was performed in steps, as outlined in section 6.1. The focus on was the running conditions for MICE Stage 6, as it is the final Stage for the experiment and will give the most relevant information for the construction of a Neutrino Factory cooling channel. A smaller effort was made to study the separation of muons and pions in Stage 1, since the beam composition and properties must be understood before the experiment can enter the cooling measurement phase.

The second objective was met by reasoning based on physical principles, which led to an alternative conceptual design. This was evaluated in a manner identical to the baseline design in order to allow for a fair comparison between the two designs.

The third objective was achieved by imposing a cost restriction on any alternative design that was equal to or less than that of the baseline design. Due to the uncertainty on the available frontend electronics and their cost, the same electronics and number of channels were assumed. As a last step towards the cost reduction, the improvement on the global experimental performance by adding CKOV2 were reviewed.

8.5.1 Simulation inputs and geometry

For Stage 1, only TOF0, TOF1 and the calorimeter were present in the beamline[7]. In the simulation, this was modeled by setting the distance between TOF1 and TOF2 to 648 cm, center to center, and all electric and magnetic fields were turned off. The beamline was filled with air. The calorimeter was placed immediately downstream of TOF2, but there was a distance left between them, corresponding to the space needed for CKOV2. The beam was started just upstream of TOF0, with pions and muons with flat p_z distributions between 100 and 300 MeV/c.

[7] Since this study was performed, a spectrometer without its solenoid will, in addition, be present for Stage 1.

For Stage 6, the full MICE cooling channel was modeled. However, we did not want to complicate the issue with reconstruction of phase in the RF, which requires sophisticated use of reconstructed momentum and TOF, so the absorbers were left empty and the RF field was turned off. The calorimeter was placed at the same distance to TOF2 as the corresponding distance to TOF1 in Stage 1.

A series of beams corresponding to the run plan of MICE was used. The beams used were unmatched 6π mm beams of longitudinal momenta of 140, 170, 200, 240 MeV/c with a standard deviation of 10%. There was also a beam generated in TURTLE by Kevin Tilley for the collaboration meeting at RAL in 2005. This beam was diffused by a 7.6 mm lead diffuser positioned 6078 mm upstream of the center of the central absorber. The "TURTLE beam" had $p_z^{TOF1} = 236 \pm 26$ MeV/c.

The Simulation executable gives the Monte Carlo truth values, but before proceeding with a performance measurement, one must take errors and biases introduced by the front end electronics into account. This was handled in the G4MICE application Digitization (see section 6.3.2).

8.5.2 Analysis

The performance analysis of the two calorimeter designs was also a test bed and development area for the downstream particle identification. The final analysis is presented in chapter 9, though some features were different or missing during the work presented in this chapter.

Before any analysis could begin, beams of ten thousand events were simulated and digitized, in order to find good variables for doing particle identification. These beams had very wide distributions so as to map all beam conditions. The variables should provide maximal data reduction while keeping the loss of information minimal, and were selected according to the principles described in section 9.3.4.

Once the variables had been chosen, fits were made for all expected values. The fits were used to create "discrepancy variables"[8]

$$D = (measured - expected)/measured, \tag{8.11}$$

where zero means very muon like. An event which has both the expected and the measured value at zero (or below a certain threshold) is assigned $D = 0$, while an event which has the measured but not the expected value at zero, was assigned $D = 1$. Naturally, the inverse situation also results in $D = 1$ by applying equation 8.11.

Since the rest of the analysis was performed in ROOT, the output files of Digitization were converted to ROOT trees using the RootEvent application (section 6.1.4). This application also tagged the events as good or bad.

Since simple cuts proved useless for pion-muon separation as well as electron-muon separation, the problem was analyzed with an Artificial Neural Network (see section D.2). For every scenario, the muon sample was merged with the background sample, and an

[8] This quantity was later replaced with *asymmetry* (see section A.1.6).

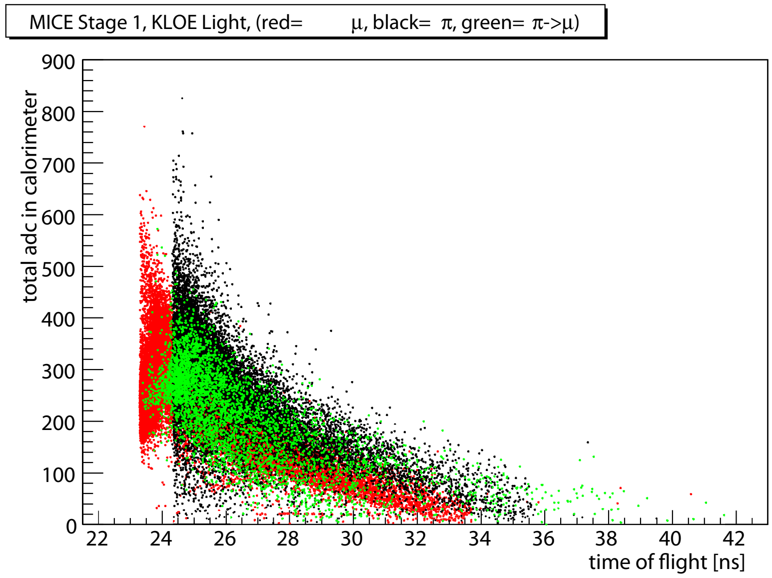

Fig. 8.4: The total number of ADC counts in the KL calorimeter as a function of the time of flight. Red is for muons, black for pions and green is pions decaying into muons between the TOFs.

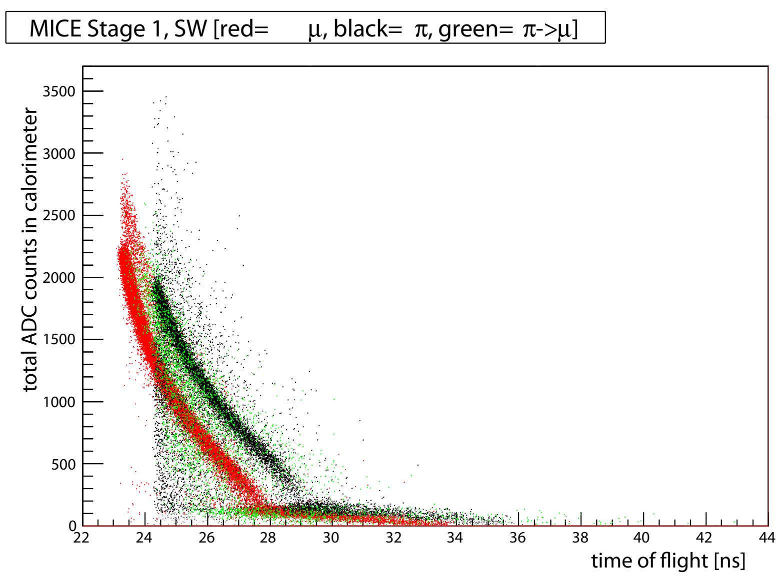

Fig. 8.5: The total number of ADC counts in the SW calorimeter as a function of the time of flight. Red is for muons, black for pions and green is pions decaying into muons between the TOFs.

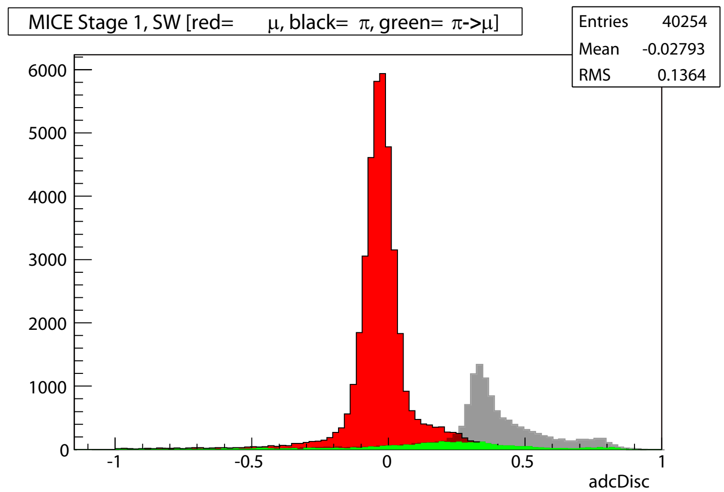

Fig. 8.6: The number of ADC counts corresponds to the energy lost in the calorimeter, and can be matched with the time of flight of the particle. Using the measured time of flight, it is possible to give an expected amplitude in the calorimeter, since the mass of a muon is a known quantity. The discrepancy variable (8.11) is chosen such that an event which looks like a muon should have the value 0. This figure illustrates how the pion distribution (black) peaks at a different value, due to its different mass. Naturally, pions decaying into muons between the TOF detectors are positioned between the muon and pion peaks. Green is pions decaying into muons between the TOFs.

Artificial Neural Network was trained on half of the merged and filtered sample (called the training sample). The Artificial Neural Network performs a fit to a function which is equal to one for signal events and zero for a background event. The fitted value it assigns the event is a floating point number and can thus be interpreted as a signal weight. The fit parameters obtained from the Artificial Neural Network were written to disc, such that it is easy to go back to an older fit if necessary.

Using the fit parameters acquired by the Artificial Neural Network, a weight was assigned to all the events which were not part of the training. This sample is called the test sample and it is used for evaluating the performance. By making cuts along the signal weight, the signal efficiency and the purity trace out a curve. Ideally, the purity after the analysis should be at 100% while not losing any efficiency.

The analysis method is more thoroughly explained in chapter 9, which also contains the results of the more refined analysis method which was performed after this initial study. There are differences between the method presented here and in chapter 9 however:

- The method presented here did not have calorimeter hits as a requirement for *good event*.

- The method presented here did not have track confinement in the tracker active region as a requirement for *good event*.

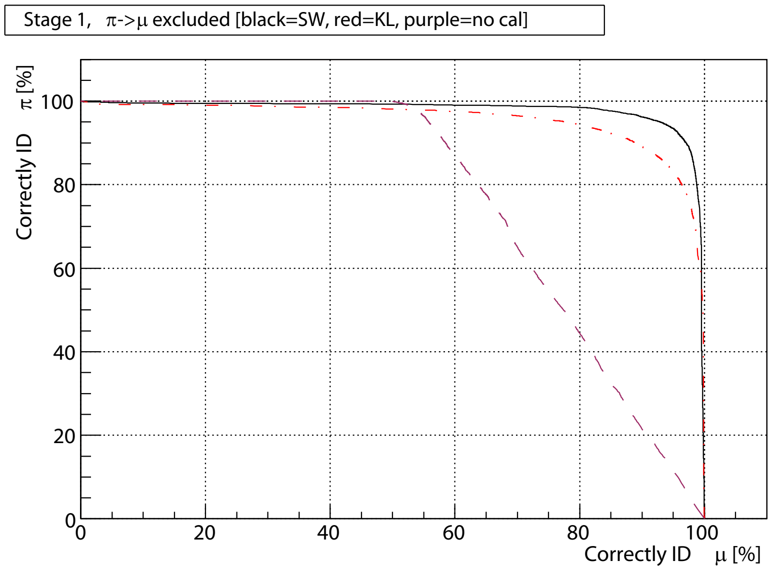

Fig. 8.7: The PID performance in Stage 1. Solid black line indicates SW, dash-dotted red line indicates KL, while dashed purple line is the performance using time of flight information only. Pions decaying to muons between the time of flight stations are ignored in this plot.

- The method presented here used *discrepancy* instead of *asymmetry* for multi detector variables.

In addition, all fits have been updated due to changes in the field map, positions of detectors etc.

8.6 Performance

The objective of the particle identification analysis, for which the calorimeter is a key component, is to reduce the bias on the cooling measurement to an acceptable level. As discussed in section 9.6, this requires a high performance expressed as a minimum purity of 99.8% at a reference signal efficiency of 99.9%. This section therefore evaluates the background rejection efficiency for both calorimeter designs at the given reference signal efficiency.

8.6.1 Stage 1

In Stage 1, the objective is to measure the pion content in the muon beam. The momentum is considered unknown, so all the longitudinal momentum is distributed with a flat distribution between 100 and 300 MeV/c. Particles with larger longitudinal momentum have a larger probability to reach the end of the experiment, and be tagged as good events, so the flatness is not conserved in the final analysis.

The network architecture used for the Artificial Neural Network was `6:7:1`[9]. The six inputs were:

- tof
- adcDiscrepancy
- rangeDiscrepancy
- adcQ(0)
- adcProd(0)
- highQ

One difference for Stage 1 compared to Stage 6 was that there were no spectrometers present, but the absence of cooling channel makes the time of flight a good substitute for the longitudinal momentum. Thus, the time of flight was used for reconstructing the longitudinal momentum, and then the analysis continues exactly as in the Stage 6 case. The resolution of the time of flight was a Gaussian with 70 ps standard deviation. There were no transverse variables, which is something which could be improved later. As figure 8.7 shows, the SW design performed better than the KL design, and time of flight alone was not enough to give an adequate particle identification.

Similar to what was done for Stage 6 in chapter 9, the particle identification performance in Stage 1 would benefit from the more developed and optimized analysis algorithms. However, the production of the calorimeter will likely only be partially completed by the time MICE starts taking data in Stage 1. It is unknown how many layers will be present when the first beam is delivered, so it is hard estimate the actual performance of the device, and any new simulation would be subject to arbitrary assumptions.

8.6.2 Stage 6

Just like in Stage 1, simple cuts on the variables did not help much and were therefore not used in Stage 6. Instead Artificial Neural Networks were used to fit the particle ID as a function of the input variables. For the lowest momentum a `9:5:2:1` architecture was used, and for all other cases `8:7:1` was used. The barycenter is strongly correlated with the range, and it is usually not necessary to include them both, but for the 140 MeV/c beam, having a barycenter discrepancy variable did improve the results slightly.

Comments on results

The most striking property of the results for Stage 6 was that over the full spectrum, the SW design performed better than the KL counterpart.

[9] That means there were six input variables, one hidden layer of seven variables, and the single particle ID tag variable as output.

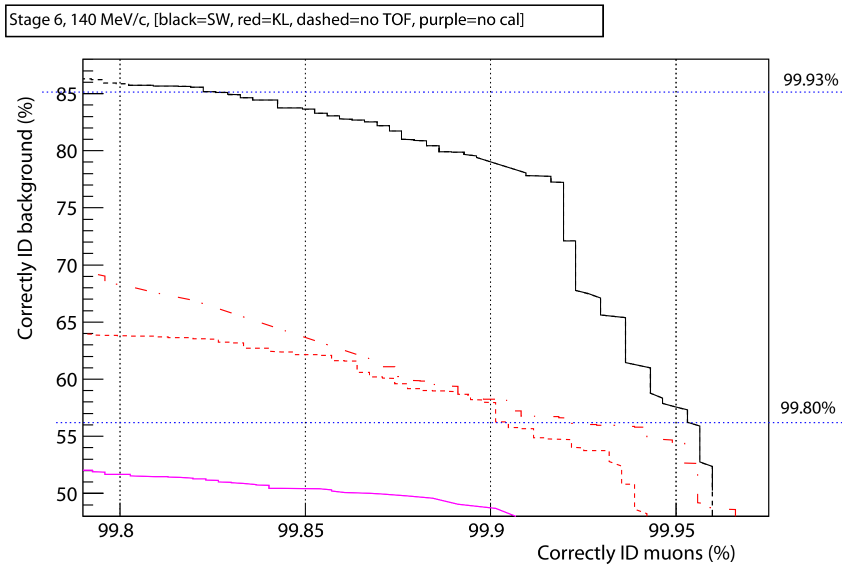

Fig. 8.8: The PID performance in Stage 6, $p_z^{TOF1} = 140{\pm}14$ MeV/c. The solid black line indicates the performance using SW, while the dash-dotted red line is the performance using KL. The dashed red and black lines are the performance using KL and SW without TOF information respectively, and the purple solid line is the performance when no calorimeter is used. The blue lines correspond to 99.8% and 99.933% purity respectively.

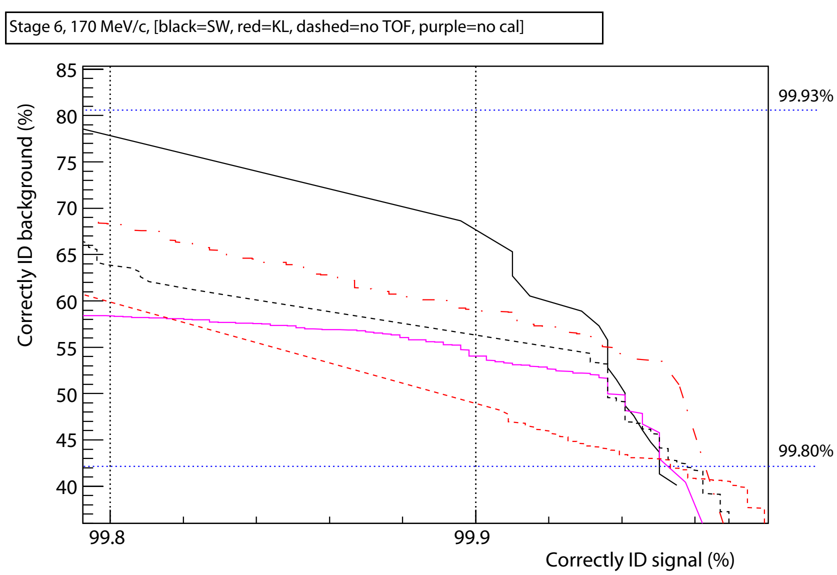

Fig. 8.9: The PID performance in Stage 6, $p_z^{TOF1} = 170{\pm}17$ MeV/c. The solid black line indicates the performance using SW, while the dash-dotted red line is the performance using KL. The dashed red and black lines are the performance using KL and SW without TOF information respectively, and the purple solid line is the performance when no calorimeter is used. The blue lines correspond to 99.8% and 99.933% purity respectively.

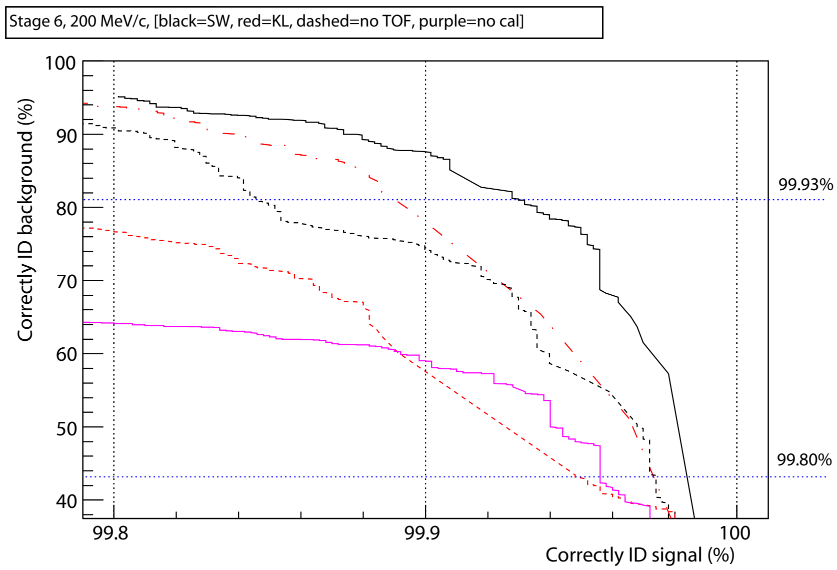

Fig. 8.10: The PID performance in Stage 6, $p_z^{TOF1} = 200 \pm 20$ MeV/c. The solid black line indicates the performance using SW, while the dash-dotted red line is the performance using KL. The dashed red and black lines are the performance using KL and SW without TOF information respectively, and the purple solid line is the performance when no calorimeter is used. The blue lines correspond to 99.8% and 99.933% purity respectively.

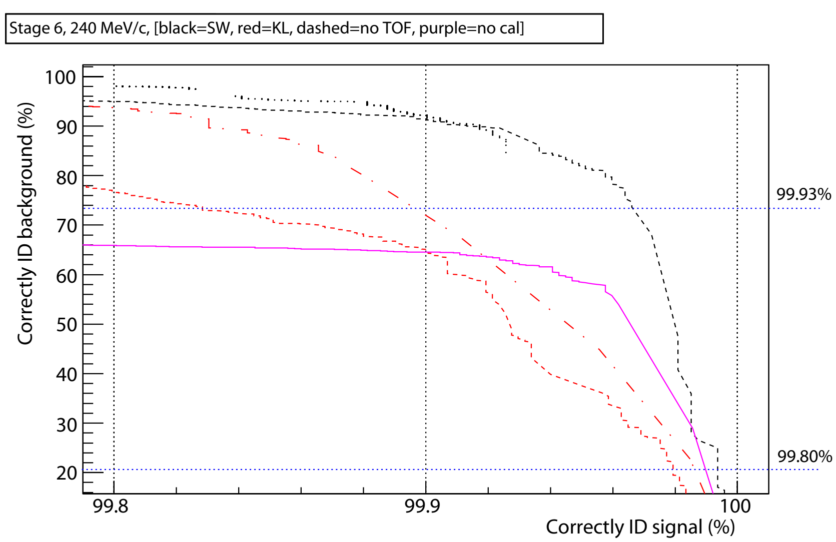

Fig. 8.11: The PID performance in Stage 6, $p_z^{TOF1} = 240 \pm 24$ MeV/c. The black markers indicate the performance using SW, while the dash-dotted red line is the performance using KL. The dashed red and black lines are the performance using KL and SW without TOF information respectively, and the purple solid line is the performance when no calorimeter is used. The blue lines correspond to 99.8% and 99.933% purity respectively.

Initial mom.	No cal., with TOF	KL, no TOF	SW, no TOF	KL, with TOF	SW, with TOF
140 14 MeV/c	47.8%	56.2%	79.5%	58.2%	79.5%
170 17 MeV/c	54.1%	48.8%	56.4%	59.0%	67.8%
200 20 MeV/c	59.0%	57.3%	74.2%	79.4%	87.6%
240 24 MeV/c	64.5%	65.0%	91.4%	80.0%	92.2%
TURTLE				83.5%	

Not meeting req. Meeting basic req. Meeting safety req.

15

Fig. 8.12: Summary table for Stage 6. The numbers correspond to how much of the background is rejected at 99.9% signal efficiency. Slide from presentation by Rikard Sandström at MICE collaboration meeting 2006 in Osaka.

Initial mom.	No cal., with TOF	KL, no TOF	SW, no TOF	KL, with TOF	SW, with TOF
140 14 MeV/c	0.24%	0.20%	0.093%	0.19%	0.093%
170 17 MeV/c	0.17%	0.19%	0.17%	0.16%	0.12%
200 20 MeV/c	0.14%	0.15%	0.091%	0.073%	0.044%
240 24 MeV/c	0.089%	0.088%	0.022%	0.050%	0.020%
TURTLE				0.070%	

Not meeting req. Meeting basic req. Meeting safety req.

16

Fig. 8.13: Summary table for Stage 6. The numbers correspond to the impurity after PID at 99.9% signal efficiency. Slide from presentation by Rikard Sandström at MICE collaboration meeting 2006 in Osaka.

The general tendency is that for higher momentum, not only does the intrinsic purity increase, but also the background rejection capability improves. Thus, at higher momentum, identifying muon decay is not a problem. The problem resides at lower momentum.

If the momentum is low enough however, a muon will never traverse the first lead-fiber layer but will be contained within it. Since this is not true for a positron, that gives a veto on the particle identification. At slightly higher momentum, a muon sometimes spills over into the second layer, and the behavior looks dangerously similar to an electromagnetic shower. With the experimental setup simulated here, this dip in performance occurs around 150 MeV/c at the entry to the calorimeter. According to (8.10) electrons at 145 MeV/c cause electromagnetic showers with the shower maximum on the boundary between the preshower layer and the first plastic layer. Due to energy loss on the way from the TOF1 exit, the 170 ± 17 MeV/c beam momentum is 148 ± 22 MeV/c at the exit of TOF2, hence we should expect to see this minima in performance for this beam. Looking at the results, this was also the case.

It is hard to remove the behavior by changing geometry; if one tries to push it to lower momentum by making the first layer lighter or thinner, more primary incident positrons will penetrate the first layer and make tracks in the following layers. If one would make the first layer thicker or heavier more muons would be stopped in the first layer and thus push the dip into the central momentum region at 200 MeV/c. It is possible to get rid of this by improving the analysis itself rather than the geometry, but this effect must be taken into account when optimizing the segmentation of the calorimeter. With the modular approach to track propagation used in the more refined analysis presented in chapter 9, and with updated fits which took this transition region into special consideration, the dip in performance for the 170 MeV/c beam disappeared.

8.6.3 Analysis of PID failure

The main problem with the downstream electron–muon identification in Stage 6 is to maintain the very high efficiency of 99.9%. By looking at figure 9.25 one does notice that some signal events receive a muonness weight such that they look very much like background events. Since 99.9% of the signal is supposed to be accepted, this implies that the cut must be done in the close vicinity of the background peak at 0, and hence a lot of background events are also accepted as signal events.

In order to study the severely misidentified signal events, the 200 MeV/c beam was studied in closer detail. In the test sample of this beam (the half not used for neural net training), there were 49786 good signal events, of which 112 had a severe mis-PID. Those values corresponds to efficiency = 99.78%. Of these, 54 were muons decaying so close in time to the particle track in the calorimeter, that it was not possible to distinguish two separate peaks based on TDC information. The only possible remedy to this is to change the TDC threshold. However it is hard to imagine how misidentifying these events will introduce a bias on the emittance measurement.

There were also 14 positrons and 6 electrons at the first calorimeter hit of the event. Those numbers could be reduced by making the distance between TOF2 and the calorimeter smaller, preferable as small as possible. The same conclusion is valid for the 38 events which never hit the calorimeter. Some of these are muons without the necessary kinetic energy to traverse TOF2, others are muon decays inside or after TOF2.

This prompted two actions to solve the problem of particle identification failure:

- The calorimeter was pushed as close as possible to TOF2.
- *Good event* was redefined as an event that gives reasonable hits in the trackers & tofs & calorimeter.

The first point could be achieved if CKOV2 were absent, but this more upstream position also put the photomultipliers in a higher magnetic field. The second point could in principle introduce a bias since the effective cut off at low energies is increased. However as the study in chapter 10 showed, these extremely low energy particles are very problematic to collect anyway, and can safely be tagged as *bad events*.

8.6.4 Implications of this study

Although the main objectives of this study were to make a decision on the general design philosophy of the calorimeter and evaluate its performance, the good particle identification performance obtained suggested that the downstream Čerenkov detector, CKOV2, was redundant. A decision was taken to remove CKOV2 and fix the calorimeter design to SW. This allowed the calorimeter to be placed closer to TOF2.

9. PARTICLE IDENTIFICATION ANALYSIS

One of the sources of background with the potential to impose a systematic error larger than the specified experimental precision is muon decay, which produces an electron of similar but different track properties as the original particle (see section 5.1.1). If the decay occurs upstream of TOF1, the event can easily be rejected using the Čerenkov detector and the measured time of flight. For muon decay further downstream this is not so easy, and a more sophisticated analysis is necessary to meet the experiment requirements. This chapter describes the analysis developed by the author to cope with muon decay background in the downstream region of MICE.

9.1 Energy loss predictions

In order to predict the particle energy and momentum at a given detector, the momentum measured in the spectrometers was used together with the Bethe-Block function,

$$-\frac{dE}{dx} = \frac{4\pi}{m_e c^2} \cdot \frac{nz^2}{\beta^2} \cdot \left(\frac{e^2}{4\pi\varepsilon_0}\right)^2 \cdot \left[\ln\left(\frac{2m_e c^2\beta^2}{I \cdot (1-\beta^2)}\right) - \beta^2\right] \tag{9.1}$$

which was used to fit the energy loss seen in the simulation. Due to problems with convergence of the fitting procedure when using logarithmic dependencies, equation (9.1) was Taylor expanded before the fit,

$$\frac{dE}{dx} = \frac{k_{-2}}{\beta^2} + \frac{k_{-1}}{\beta} + k_0 + k_1\beta + k_2\beta^2 + \mathcal{O}(\beta^3). \tag{9.2}$$

Since the track is not always perpendicular to the surface of the volume for which the energy loss is supposed to be calculated, a path length correction due to the angle must be accounted for,

$$l = \frac{\Delta z}{\cos\theta} \tag{9.3}$$

where Δz is the thickness of the volume in the longitudinal direction, and θ is the measured or predicted incident angle of the track to the surface.

In addition to losing energy, the particle direction is changed by a small amount by transverse magnetic fields, multiple scattering and other processes. The analysis used a very simple model for this scattering since the effect on the particle identification capability is limited, and relied mostly on the mean value of $\Delta\theta$ for rotating the Lorentz vector. These values are listed in table 9.2, and two of the fits are shown in figures C.5 and C.6. For

Tab. 9.1: Energy loss fitted with Taylor expanded Bethe-Block function (9.1). The fit for volumes marked with † is the energy loss in MeV per cm, where the length l is defined in equation (9.3). For the other fits, the thickness of the volume and the path length correction due to incident angle are already included. One might expect the energy loss of the two spectrometers to be identical, but one very important difference is that the input β in the upstream spectrometer case is measured *after* the energy loss. Furthermore, the dependency on β is fairly linear in this region, and β is close to 1, which cause the different terms to cancel in the Taylor expansion. The fits are shown in figures B.1 to B.5.

Volume	k_{-2}	k_{-1}	k_0	k_1	k_2
TOF1→diffuser	0.5946	-1.434	0.6556	0.9006	-0.6432
Diffuser†	-57.7	162.2	-24.85	-188.1	121.4
SciFi0	1.344	0.2889	-0.2327	-0.1245	0.6842
SciFi1	-8.49671	48.1395	-85.2172	65.6883	-18.1637
TOF2†	112.494	-520.188	917.926	-722.081	213.905
EMCal0	119.106	-175.564	-37.1309	164.933	-50.0836

high density volumes like the calorimeter, the dominating cause of the change in angle is physical processes, while between the tracker reference plane and time of flight station, magnetic field effects dominate.

Several such volumes, such as the spectrometers, TOF2 and the preshower layer of the calorimeter, had individually fitted parameters in order to predict the energy loss. For predicting the Lorentz vector after volume number n, the predicted Lorentz vector was calculated after volume number 1, which gave input to the predicted Lorentz vector fits after volume 2 etc. The advantage of this modular method compared to a global fit is that should one change the design of a volume, only the fits of that volume must be changed. Better still, should only the thickness of a module change, equation (9.3) shows that no

Tab. 9.2: The difference in angle from beam axis due to the muon interacting with passive material and nonzero transverse magnetic fields. The scattering in TOF2 and the diffuser is neglected in the analysis. The diffuser in question is a 4.2 mm thick lead diffuser.

Volume	$\Delta\cos\theta =$	Correction
TOF1→Diffuser	-0.003917 ± 0.008971	$-0.390 + 0.3929\cos\theta$
Diffuser	$-6.11 \cdot 10^{-4} \pm 0.01189$	$-0.3219 + 0.3272\cos\theta$
Diffuser→SciFi0	-0.01467 ± 0.01682	$-0.511 + 0.5131\cos\theta$
SciFi1→TOF2	0.02376 ± 0.03481	$0.7174 - 0.7241\cos\theta$
TOF2	0.00104 ± 0.00904	-
EMCal0	-0.02778 ± 0.06724	$-0.2572 + 0.234\cos\theta$

change at all in the energy loss fit needs to be performed.

The predicted Lorentz vector assumed that the mass of the particle was one muon mass, while the momentum was the experimental momentum given by the spectrometers or propagated through volumes with energy loss. Thus the quantities used were

$$\beta_\mu = \frac{1}{1 + \frac{m_\mu^2}{E_\mu}} \tag{9.4}$$

and

$$E_\mu = \sqrt{p^2 + m_\mu^2} \quad , \; p = |\mathbf{p}|. \tag{9.5}$$

The beam used for extracting these fit parameters was a custom made beam designed to fill the full phase space. The 10 MeV/c binning is visible as an artifact in figures B.1 and B.2. The beam is more extensively described in section 10.1.

9.2 TOF and tracker resolutions

Since at this writing there is no functioning tracker or TOF reconstruction, tracker and time of flight information were smeared using Gaussian values. For the time of flight, the Monte Carlo truth value was used smeared with a 70 ps standard deviation.

For the spectrometer, the transverse position resolutions were set to

$$\sigma_x = \sigma_y = 0.5 \text{ mm} \tag{9.6}$$

and the transverse momentum resolutions were

$$\sigma_{p_x} = \sigma_{p_y} = 2.0 \text{ MeV/c}. \tag{9.7}$$

These values were used for smearing the longitudinal momentum resolution. In order to make the values agree with the presentations given by Malcolm Ellis at the MICE collaboration meeting at LBNL in 2005 [81], the simple formulae used were rescaled by a constant factor. The final resolution that was used was

$$\sigma_{p_z} = 0.209\sqrt{2}\sigma_{p_x}\frac{p_z}{p_t} \tag{9.8}$$

where

$$p_t = \sqrt{p_x^2 + p_y^2}. \tag{9.9}$$

From equation (9.8) it can be noted that for straight tracks the resolution becomes worse. For many of the expected values of measurables in the calorimeter, the resolution on longitudinal momentum in the downstream spectrometer is crucial for the performance of the PID. In other words, the matching of measured momentum to other detectors will suffer from poor tracker resolution for certain tracks.

The software which performs the particle identification analysis is already prepared to use the actual reconstructed quantities from the spectrometer and the time of flight

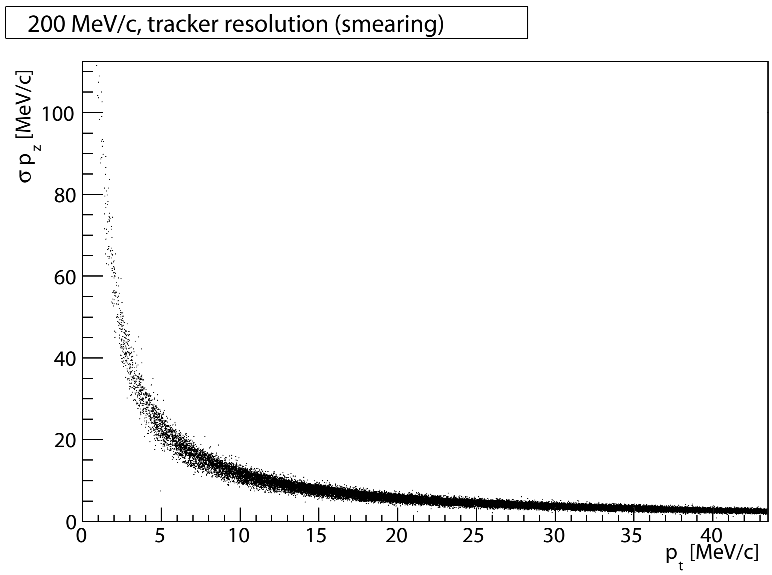

Fig. 9.1: The tracker resolution was synthesized by Gaussian p_t resolution and equation (9.8) for p_z resolution. Plotted here is the longitudinal momentum resolution as a function of the true value of transverse momentum in a tracker for a 200 ± 20 MeV/c, 6 π mm beam.

Tab. 9.3: Preliminary tracker resolutions with updated Reconstruction software [68]. Results are consistently better than the old study suggested [81], in particular for the transverse momentum resolution. The figure of merit is the resolution divided by the standard deviation of the sample. These results should be compared with the results obtained with a TPG (table 6.2).

Tracker	resolution	figure of merit
$\sigma_x = \sigma_y$	0.37 mm	1.7%
σ_{p_t}	1.06 MeV/c	7.4%
σ_{p_z}	3.89 MeV/c	13.7%

stations, once the reconstruction comes online. Preliminary results show consistently better resolutions [68] than the previous results, thus the track prediction at the calorimeter and the expected time of flight should be better than what has been assumed for the results presented in this thesis. The most recent tracker resolutions are shown in table 9.3. While the position resolution is almost identical to the corresponding values of a short neon based TPG, the momentum resolutions still have a long way to go before they are comparable with a TPG.

9.3 PID variables

Any experiment collects an amount of data. Since the *information* increases with number of observations, given that the information is conditional on what we want to learn from the experiment and that the information is related to the precision[1], it is desirable to use large amounts of data. In order to make the collected data useful one must find a method to maximize the data reduction while minimizing the loss of information [94]. In this analysis this is achieved by expressing the data in special variables. A variable which is a function of the data is called by statisticians a *statistic*. The task of finding a suitable particle identification algorithm can therefore be expressed as finding sufficient statistics with minimal loss of information.

9.3.1 signal

This variable is the particle identification Monte Carlo truth and is what the analysis is trying to reconstruct using measured detector variables. It is set to 0 for background events and 1 for signal events. A signal event is defined as a muon in TOF1, TOF2 and the calorimeter. This can be referred to as a probability density function $f(signal)$ which is a delta function at $signal = 1$ for signal events, and at $signal = 0$ for background events.

9.3.2 badness

The *badness* variable is a tag assigned to each event which describes whether the event can be interesting for data taking or not. If an event is a *good event*, i.e., an event which will not immediately be rejected before analysis, the badness is set to 0. If, however, any of the reconstructed event properties indicate that the event is bad, badness is incremented by 1. Should any of the Monte Carlo truth event properties flag the event as bad, it is instead incremented by 2. Thus should both reconstructed and MC truth event properties agree that the event is bad it will have $badness = 3$. This allows selecting MC truth tagged good events by requiring that the badness is less than two, and reconstruction tagged good events by choosing events where *badness* is even.

The list of requirements for classifying an event as a good event is this:

- The time of flight between TOF1 and TOF2 must be larger than 10 ns.

[1] This is the Fisher definition of information [94].

- The time of flight between TOF1 and TOF2 must be larger than the corresponding average velocity of half light speed in vacuum.
- The time of flight between TOF1 and TOF2 must be smaller than the corresponding average velocity of light speed in vacuum.
- The longitudinal momentum in both spectrometers must be larger than 50 MeV/c.
- The longitudinal momentum in both spectrometers must be smaller than 400 MeV/c.
- If the first hit in the calorimeter is a muon, there must be a muon hit in TOF2 as well.[2]
- The track must be contained inside the active radius of both spectrometers. This is ensured by equation (9.10).

$$\rho_0 + R < \rho_{max} \tag{9.10}$$

ρ_{max} is the tracker active radius (15 cm), R the gyroradius

$$R = \frac{p_t}{|q|B} \tag{9.11}$$

and ρ_0 the Larmor center of the track

$$\rho_0^2 = \rho^2 + R^2 + 2s_1 s_2 R(xp_y - yp_x)\ . \tag{9.12}$$

s_1 is the electric charge sign of the muons and s_2 the polarity of the magnets.

The values used for these cuts were not chosen such that they would remove any of the background, but to remove undesired events which would not be used for emittance calculations anyway. In order to not introduce unnecessary bias, the cut values are conservative and pass most unscraped events through as good events.

9.3.3 Out0

When *signal* is reconstructed the resulting value is called $Out0$. It can take any real value between minus and plus infinity. The events sum up to give a probability density function $g(Out0)$, which should look like the corresponding function with *signal* as argument, i.e., have a peak at 0 for background events and a peak at 1 for signal events. By making a selection, such as a simple cut, on this variable it is possible to divide the space $\Re$ in a critical region w and a region of acceptance $\Re - w$. The standard deviation of the background and

[2] If TOF2 is too small, some muons will miss it while still hitting the calorimeter. This causes the event to look like a muon event in the calorimeter but it will still be tagged as a bad event. Sometimes there are hits in TOF2 from back propagation of secondary particles from the impact in the calorimeter, introducing a bias on the time of flight measurement. This observation prompted a study of the optimal detector sizes, presented in chapter 10.

signal distributions on $Out0$ is a simple measure of the discriminating power of the particle identification algorithm, but looking at the separation, or simultaneous efficiencies of both distributions for a given value of $Out0$, is usually more interesting to the experiment. An example of such a function is shown in 9.22.

Using the signal event as the null hypothesis, the *level of significance* of the test, which is the probability that $Out0$ falls in the critical region when the null hypothesis is true, coincides with the signal inefficiency. Usually the level of significance is defined by the experimenters, which gives the *power of the test* for the specific level of significance. The power of the test is the probability that $Out0$ falls in the critical region, or in this specific case, the fraction of background events rejected.

9.3.4 Variables used for fitting

In order to make the particle identification algorithm both powerful and efficient a number of input variables must be carefully selected to be used as parameters for fitting the PID function $signal(x)$. A good candidate can be identified by its *separation* (section A.1.4) of signal and background events; a separation close to 1 is a very good candidate, where as if the separation is close to zero the overlap of the two probability density functions is too large to provide meaningful information of the differences between the two samples.

Another criterion is the *correlation* (section A.1.5) between the statistic and other statistics used for the fit. Should the correlation be very high between two variables, one of the variables is likely not needed. Figure 9.2 shows an example of the correlation matrices used for spotting significant correlations between PID variables.

Some of the variables used are *single detector variables*, meaning that the statistic depends on information given by one single detector only. Other variables depend on two or more detectors in such a way that given the information in detector A, the variable describes how consistent the response of detector B is with the hypothesis that the event was a signal event. The *asymmetry* between the measured value and the expected value is defined as in section A.1.6, but with the additional option of using thresholds, thus avoiding the divergence when the denominator is zero. The definition of the asymmetry with threshold becomes

$$d \equiv \begin{cases} 0 & \text{if } a_e = a_m \\ \frac{a_m - a_e}{a_m + a_e} & \text{if } a_e > T \,\&\, a_m > T \\ 0 & \text{if } a_e < T \,\&\, a_m < T \\ 1 & \text{if } a_e < T \,\&\, a_m > T \\ -1 & \text{if } a_e > T \,\&\, a_m < T \end{cases} \tag{9.13}$$

where a_m is the measured quantity, a_e is the expected, and T is a threshold. In other words, this says that $d = 0$ if both are the same, regardless of threshold, $d = \pm 1$ if one of the two is below threshold but not the other, and finally if both are above threshold, d describes the fractual difference between the expected and measured quantities.

It is usually hard to find a set of uncorrelated variables with high separation for all the beam settings of the experiment. The variables based on calorimeter values are naturally

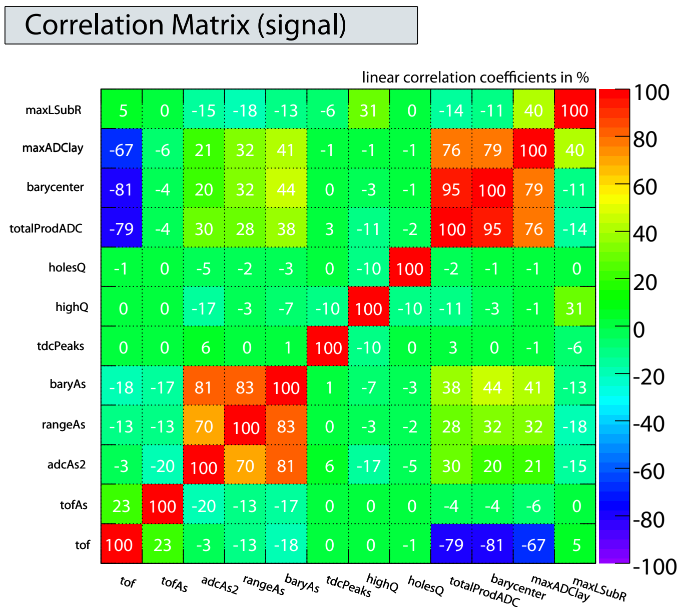

Fig. 9.2: Example of correlation matrix, in this case the signal sample for the setup 200 MeV/c. Ideally this matrix should be zero in all off diagonal elements. When looking at the background sample the correlations for the calorimeter specific variables have disappeared. Due to technical reasons two of the variables used in the analysis were not included in this figure.

better for higher energies since the particle interacts more with the detector, while for a setup with time dependent RF fields, the time of flight gets worse. In this study identical variables were used for all the studied samples, while at a later stage it would be reasonable to adapt the choice of variables to every case individually.

tof

This statistic is the time of flight between the downstream end of TOF1 and the upstream end of TOF2. It uses the Monte Carlo truth value, smeared with a Gaussian function with standard deviation equal to the resolution specified in the Technical Reference Document [58], 70 ps.

tofAs

The asymmetry between the time of flight and the expected time of flight uses assumptions and motivations discussed in appendix C. The expected time of flight uses the longitudinal velocity

$$\beta_z = \frac{p_z}{\sqrt{p^2 + m_\mu^2}} \qquad , \; p = |\mathbf{p}| \tag{9.14}$$

where the mass m_μ is always assumed to be the muon mass, and the momentum is given by the expected momentum given the measured momentum in the spectrometers. To first

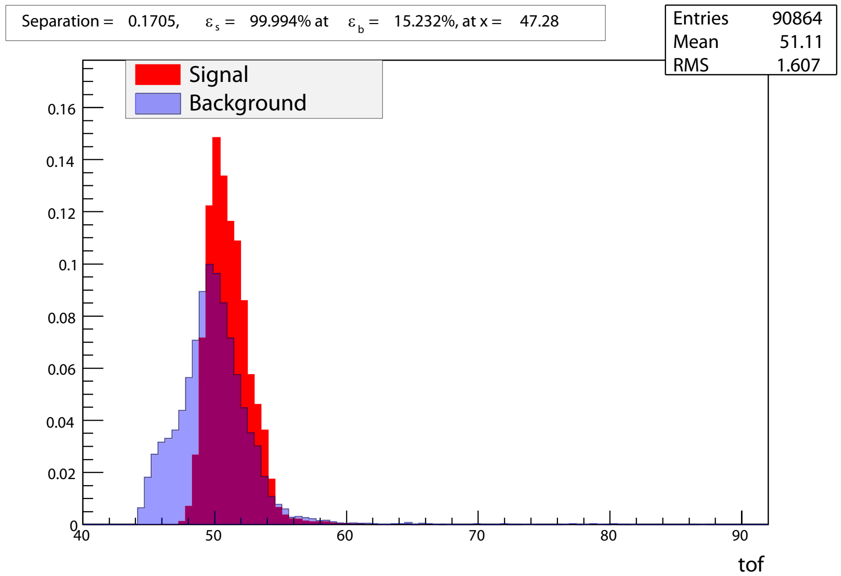

Fig. 9.3: The time of flight for a 200 MeV/c beam.

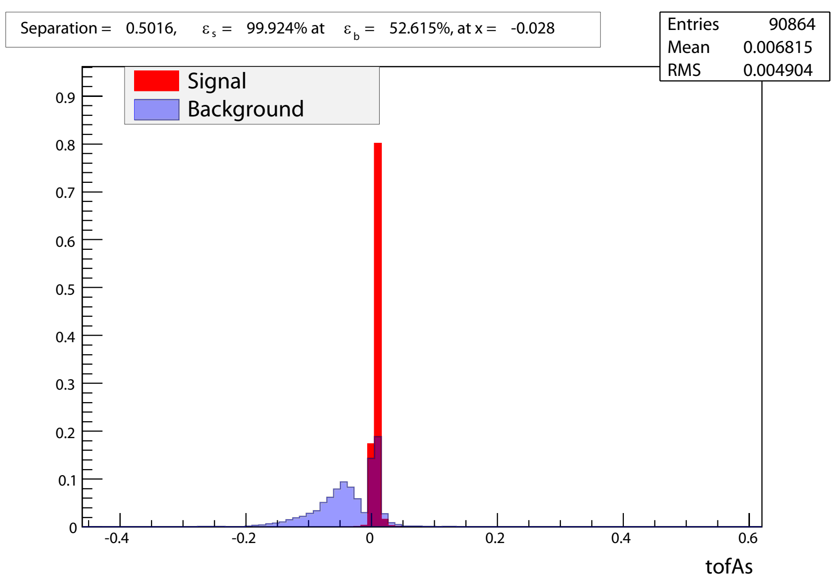

Fig. 9.4: The time of flight asymmetry for a 200 MeV/c beam.

Tab. 9.4: The corrections to the expected time of flight, based on a field map with an empty cooling channel and optimized for $\beta = 42$ cm and $p_z = 200$ MeV/c.

Volume	$x = \sin\theta_{up}\tan\theta_{up}$	$x = \sin\theta_{dn}\tan\theta_{dn}$	$x = \Delta\sin\theta$
TOF1→Diffuser	-	0.001429	-
	-	$-0.1468x$	-
	-	$-0.6993x^2$	-
Diffuser	-	-	-
Diffuser→SciFi0	-	-0.002466	-
	-	$+0.4185x$	-
	-	$+0.7192x^2$	-
SciFi1→SciFi1	0.2274	0.2386	-0.6512
	$-2.966x$	$-1.651x$	$+0.491x$
	$-2.927x^2$	$-14.64x^2$	-
	-	$+14.2x^3$	-
	-	$-4.281x^4$	-
SciFi1→TOF2	-0.006438	-	-
	$+0.48614x$	-	-
	$+0.94976x^2$	-	-

order the expected time of flight is given by

$$t' = \frac{\Delta z}{c(\beta_z^{up} - \beta_z^{down})}(\ln(c\beta_z^{up}) - \ln(c\beta_z^{down})) \tag{9.15}$$

for all regions. A number of corrections are added to this initial expected time of flight, which are summarized in table 9.4. See appendix C for their motivation.

adcProd.At(0)

This statistic is the product of the ADC counts of the left and right side of the calorimeter, divided by the sum of the left and right side

$$a_p = 2\frac{a_L a_R}{a_L + a_R} \ . \tag{9.16}$$

A factor of two is present for normalization. The product of the two sides of the same scintillator negates the attenuation effect of the hit position when energy deposition is reconstructed.

$$\begin{aligned} \sqrt{a_L a_R} &\propto \Delta E\sqrt{e^{-x/\lambda+(x-l)/\lambda}} \\ &= \Delta E\sqrt{e^{-l/\lambda}} \propto \Delta E \end{aligned} \tag{9.17}$$

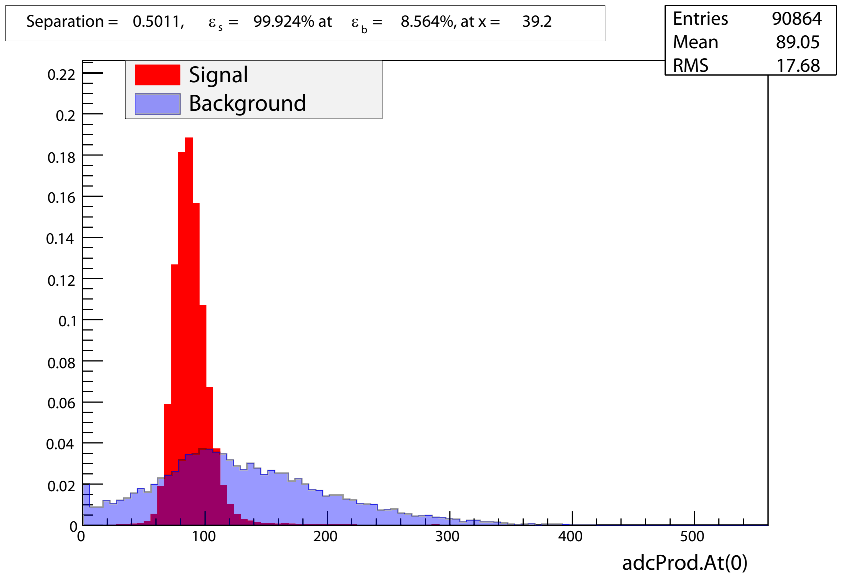

Fig. 9.5: The ADC product in the preshower layer of the calorimeter for a 200 MeV/c beam.

Experimentally it is usually better to divide by the mean value of the two sides than take the square root [95], thus arriving at equation (9.16).

If there are hits in more than one cell of a layer of the calorimeter, the energy deposited in layer l is proportional to the sum of the $a_{p,i}$ over all cells i of the layer,

$$A_l = \begin{cases} 2\sum_i \frac{a_{L,i}a_{R,i}}{a_{L,i}+a_{R,i}} & \text{if } a_{L,i}+a_{R,i} \neq 0 \\ 0 & \text{if } a_{L,i}+a_{R,i} = 0. \end{cases} \tag{9.18}$$

The variable *adcProd.At*(0) is the value A_l for layer 0, the preshower layer.

totalProdADC

This statistic is proportional to the energy deposited in the active regions of the calorimeter, and is hence the sum over *adcProd.At*(l) for all layers l,

$$A_{tot} = \sum_l A_l \tag{9.19}$$

where A_l is given by (9.18).

adcAs2

This statistic is the asymmetry between the expected and measured *totalProdADC* (see section 9.3.4). The expected value is derived from the expected Lorentz vector at the entrance of the calorimeter which gives an expected energy loss in the preshower layer. A

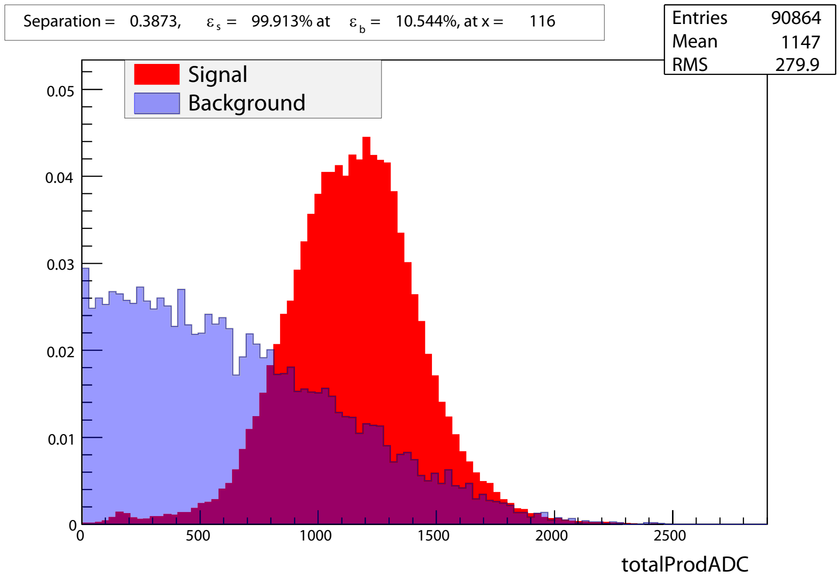

Fig. 9.6: The total ADC product in the calorimeter for a 200 MeV/c beam.

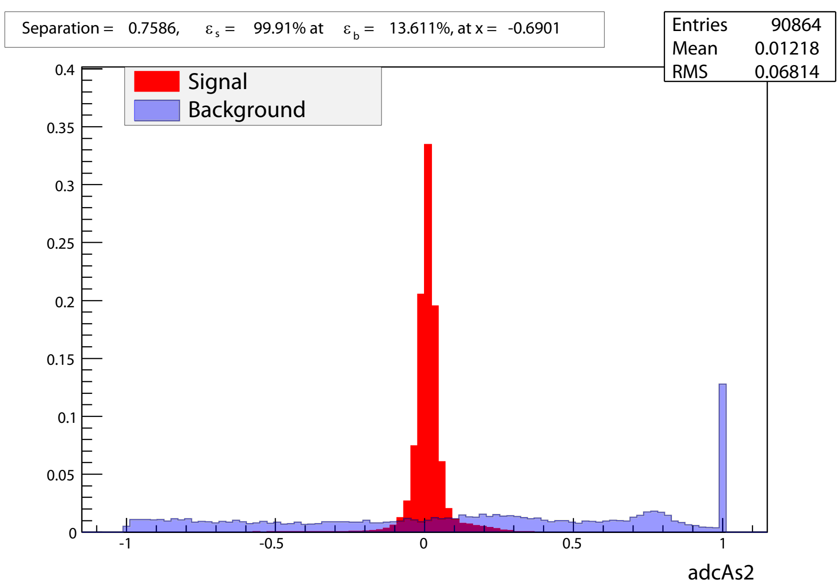

Fig. 9.7: The ADC asymmetry in the calorimeter for a 200 MeV/c beam.

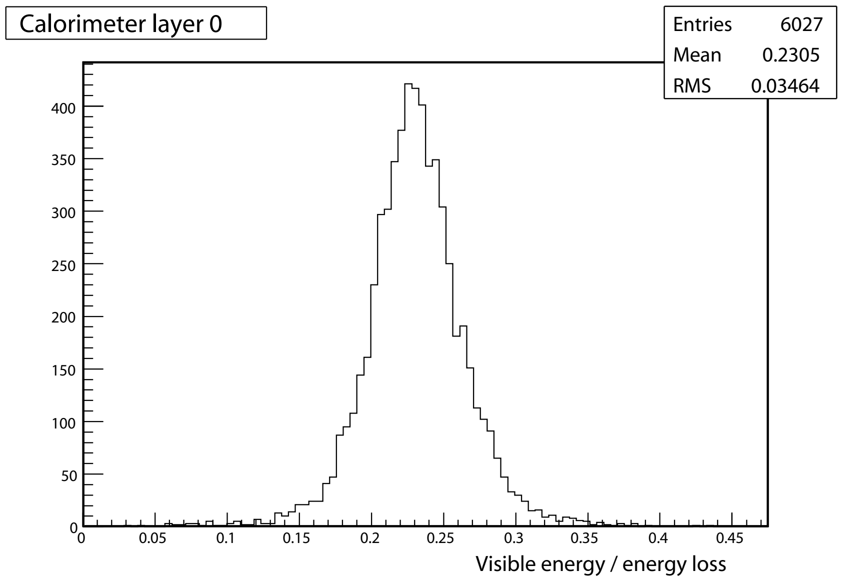

Fig. 9.8: The fraction of the energy lost in the preshower layer of the calorimeter which is sampled by the scintillating fibers. From G4MICE simulation.

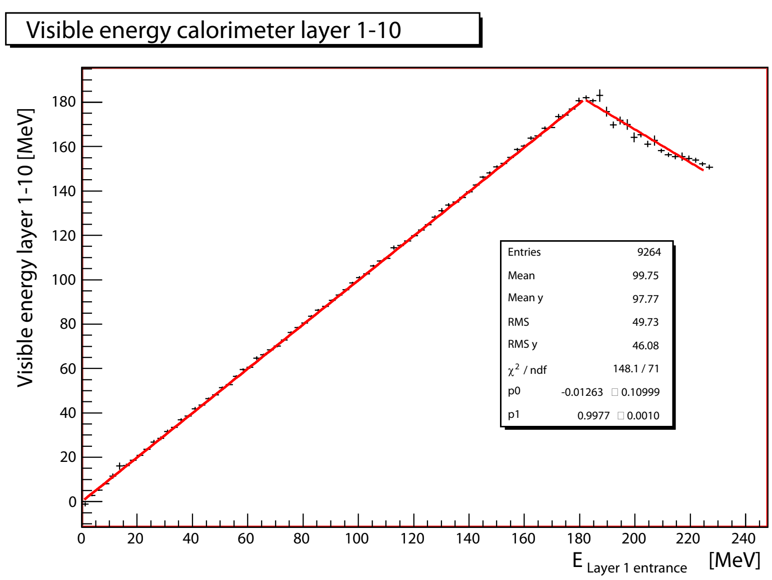

Fig. 9.9: The visible energy in layers 1-10 of the calorimeter as a function of the kinetic energy at entrance of layer 1. Since the plastic scintillator is fully active, a linear dependency is expected with gradient equal to unity. For high energy particles, energy deposition falls due to longitudinal leakage.

certain fraction of the energy loss is sampled and the total visible energy in the calorimeter depends on whether the particle is expected to punch through the back of the calorimeter.

The expected energy loss in the preshower layer uses the fits listed in table 9.1, and 23.05% of this energy is assumed to be sampled by the scintillating fibers, as shown in figure 9.8. For the subsequent layers, the visible energy is

$$E_{vis} = \begin{cases} 0 & \text{if } E_{kin} \leq 0 \\ 0.997710 E_{kin} & \text{if } 0 < E_{kin} < 182 \text{ MeV} \\ 316.532 - 0.744172 E_{kin} & \text{if } E_{kin} \geq 182 \text{ MeV.} \end{cases} \tag{9.20}$$

The fits are shown in figure 9.9.

The expected energy deposition is translated into a corresponding estimated mean number of ADC counts using

$$\langle A \rangle \approx k_{amp} \epsilon_{qe} \epsilon_{col} \epsilon_{lg} \frac{\Delta E}{w} \frac{e}{C} \left(n_l e^{-\frac{d}{\lambda_l}} + n_s e^{-\frac{d}{\lambda_s}} \right) \left(Q(3, t_0/\tau) - Q(3, t_1/\tau) \right) \tag{9.21}$$

where k_{amp} is the mean amplification of the PMTs, ϵ_x is the quantum efficiency, collection efficiency and light guide efficiency respectively, ΔE is the energy deposition, w the mean energy for creating a scintillation photon, e is the electron charge, C is charge per ADC count, and λ_l and λ_s are the two attenuation lengths with normalized weights n_l and n_s. These parameters are the same as those used as input for the simulation of the calorimeter digitization, which is described in section 6.3.2. $Q(3, t/tau)$ is the normalized incomplete gamma function

$$Q(a, x) = 1/\gamma(a) \int_x^\infty t^{a-1} e^{-t} dt \tag{9.22}$$

which describes the integrated charge function (6.19) over time. For large integration range, $Q(3, t_0/\tau) - Q(3, t_1/\tau)$ approaches unity. The parameter d is the distance between the hit to the read out and it is assumed to be half the detector width, i.e., the hit is assumed to have occurred on the beam axis.

The assumption that the mean values of all random processes can be multiplied, as in equation (9.21), to give the correct answer was confirmed by comparing equation (9.21) to the simulation. Both the equation and the simulation gave, on average, 13.6 ADC counts per MeV visible energy, thus the estimator is unbiased.

adcQ.At(0)

This statistic is proportional to the fraction of the energy deposited in layer 0 compared with total energy deposited in the calorimeter. The fraction is defined as

$$q_l \equiv \begin{cases} A_l / A_{tot} & \text{if } A_{tot} \neq 0 \\ 0 & \text{if } A_{tot} = 0 \end{cases} \tag{9.23}$$

where A_{tot} is given by (9.19). It is a measure of how front heavy the event is, and since electrons shower in the lead of layer $l = 0$, they give much higher values of q_0 than muons. However at low energies, the muons have very short range and the overlap with electrons is significant.

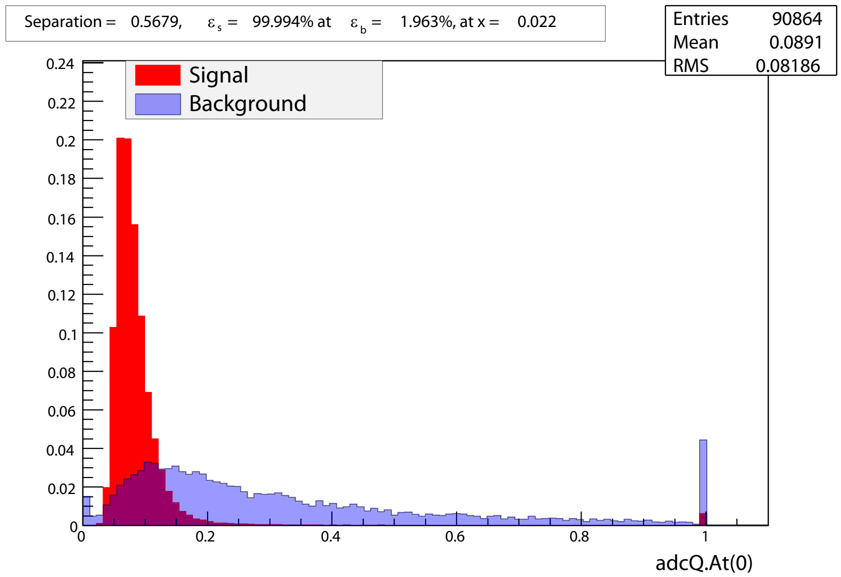

Fig. 9.10: The fraction of the ADC counts found in the preshower layer for a 200 MeV/c beam.

rangeAs

The *rangeHT* statistic is defined as the last layer with a high level layer digit in the calorimeter, so the *rangeAs* statistic describes the asymmetry between expected and measured value of *rangeHT*. Since *rangeHT* is numbered according to the layer numbering convention, $rangeHT = 0$ means the preshower layer. For this reason *rangeAs* is actually defined as the asymmetry between the expected and measured values of $rangeHT + 1$. The expected range is calculated in length units and converted into discrete layer numbers before the comparison.

The expected range uses the predicted Lorentz vector at the exit of layer 0,

$$r = \begin{cases} l_0 + 1.50433\beta\gamma\cos\theta + 14.2086(\beta\gamma\cos\theta)^2 & \text{if } \beta\gamma\cos\theta > 0 \\ +121.749(\beta\gamma\cos\theta)^3 - 46.1066(\beta\gamma\cos\theta)^4 & \\ +4.68409(\beta\gamma\cos\theta)^5 & \\ \frac{l_0}{2} & \text{if } \beta\gamma\cos\theta \leq 0 \end{cases} \tag{9.24}$$

where l_0 is the thickness of layer 0. See figure 9.12. Since an event is considered *bad* (section 9.3.2) if there are no hits in the calorimeter, a good event always has some hits in the calorimeter and, therefore, a range that corresponds to the center of the preshower layer or beyond.

maxADClay

This statistic is the layer number which contains the highest energy deposition per layer thickness, in other words the layer with the highest $\mathrm{d}E/\mathrm{d}x$. The algorithm compares the number of ADC counts A_l in each layer, as in (9.18), to find and tag the *maxADClay* layer.

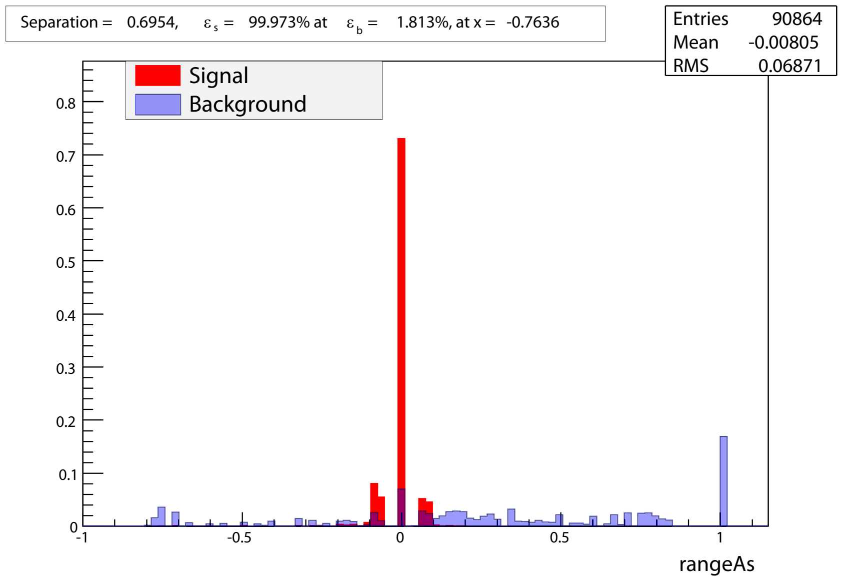

Fig. 9.11: The range asymmetry in the calorimeter for a 200 MeV/c beam.

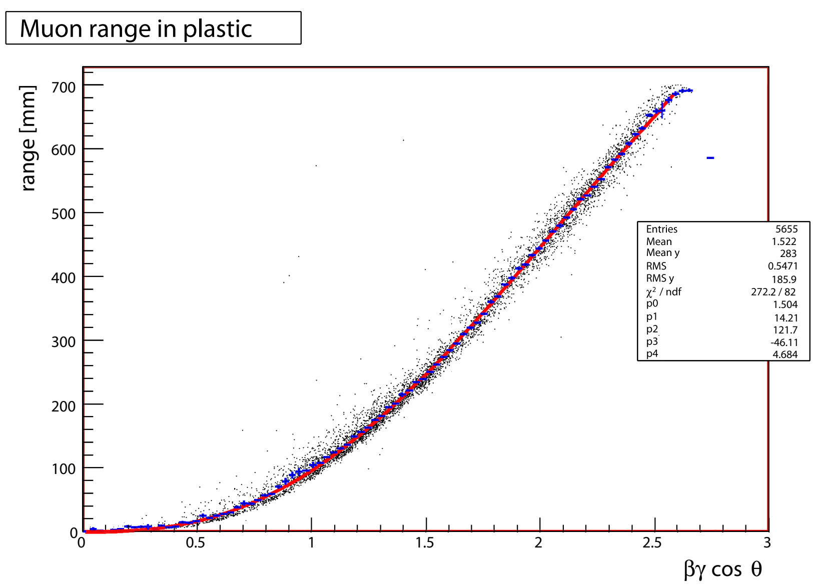

Fig. 9.12: The longitudinal range in layers 1 to 10 of the calorimeter as a function of $\beta\gamma\cos\theta$ at the entrance of layer 1. At very high energies the muons are punching through and thus the range measurement is saturated at the full $\Delta z = 70$ *cm*.

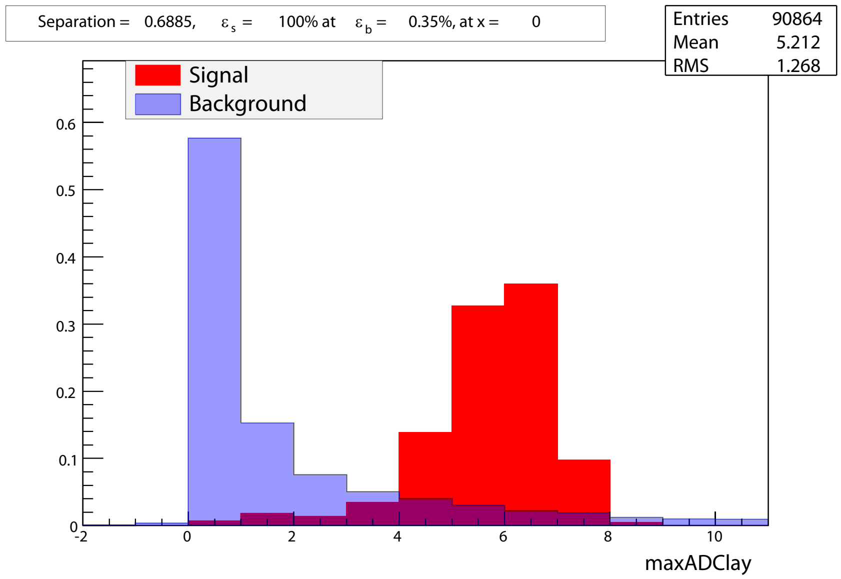

Fig. 9.13: The maximum ADC layer of the calorimeter for a 200 MeV/c beam.

The preshower layer is different from the other layers in that it only samples around 20% of the energy, and that the dE/dx is higher. The combination of these two effects means that the number of ADC counts in this layer is divided by 0.6789 in order to make the comparison with the other layers. The need for this correction can be seen in figure 9.14; all distributions should converge towards the same value at very high z, corresponding to a minimum ionizing particle.

This statistic is used as a Bragg peak identifier. For muons the Bragg peak is found at the end of its track, while electrons typically induce a shower maximum at around two radiation lengths[3], thus confining the *maxADClay* to the beginning of the electromagnetic shower.

maxLSubR

This statistic indicates the length of the tail of the track in the calorimeter. It is the *maxADClay* variable minus the last layer with nonzero hits. Since a muon will normally not create long range secondaries, a signal event should have the value 0, or -1 when some of the energy is spilling over into the neighboring layer. For an electromagnetic shower however, the shower content after the maxima consists mainly of photons. The photons generate hits with low energy loss at large detector depths. For this reason this statistic is one of the best variables for particle identification for low energy beams.

[3] Using (5.59) for lead, $E_c(Pb) = 7.79$ MeV and $E = 100$ MeV yields $t_{max} = 2.05X_0$. See also section 8.4.3.

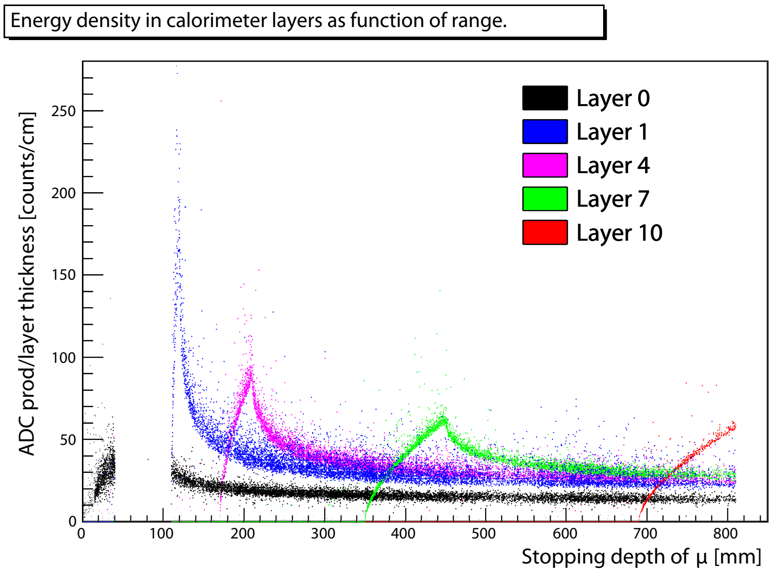

Fig. 9.14: The horizontal axis shows the longitudinal position of the end of the muon track, and the vertical axis indicates the *adcProd* variable divided by the thickness of its corresponding layer. This specific simulation contained an air gap between layer 0 and the other layers, as can be seen in the plot. The values used in the PID algorithm (not shown here) are modified for layer 0, due to its lower sampling ratio and higher energy loss per unit length. After this modification, the distributions on the far right converge toward the same value.

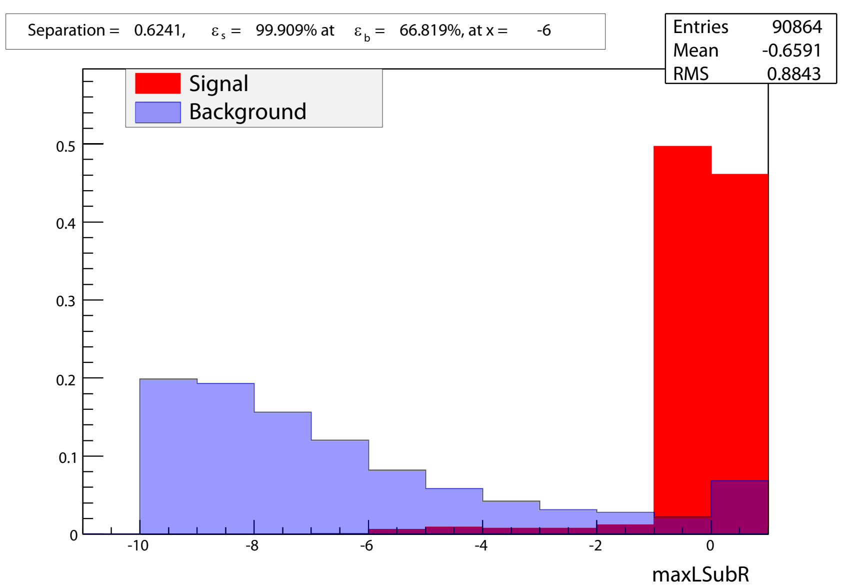

Fig. 9.15: The maximum ADC layer minus the last hit layer in the calorimeter, the tail distribution, for a 200 MeV/c beam.

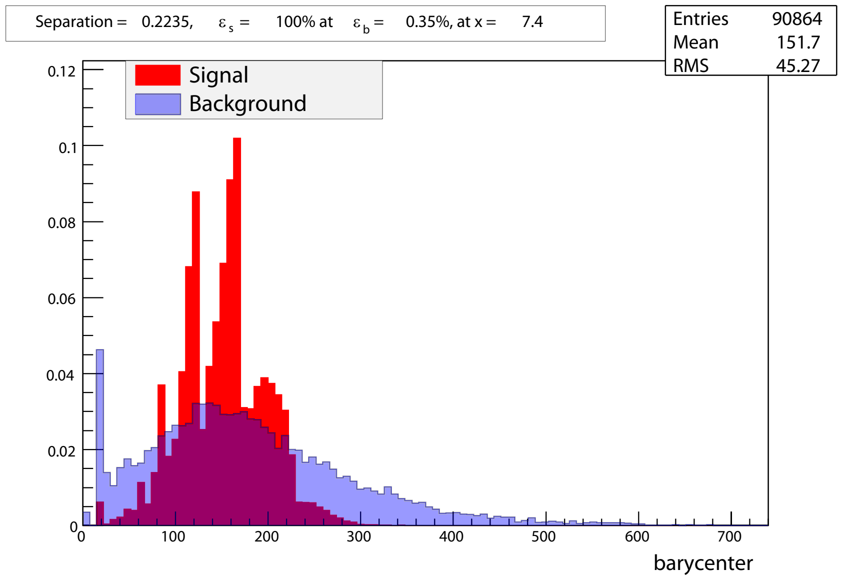

Fig. 9.16: The barycenter in the calorimeter for a 200 MeV/c beam.

barycenter

The barycenter is a weighted mean of the track's longitudinal position in the calorimeter,

$$b = \sum_l A_l d_l = \sum_l A_l \left(\frac{\Delta z_l}{2} + \sum_i^{l-1} \Delta z_i \right) \tag{9.25}$$

where Δz_i is the thickness of layer i. Since electromagnetic showers are front heavy while the energy deposition from muon tracks are more evenly distributed, the barycenter can distinguish between the two phenomena even though the actual range of the tracks are identical.

It was found that the best use for the barycenter was for low energy, since muons are confined to the first layer, while electromagnetic showers can generate hits deep in the plastic scintillator region of the calorimeter.

baryAs

This statistic is the asymmetry between the expected and measured barycenter of the calorimeter. It uses the predicted Lorentz vector after the preshower layer in the calorimeter to estimate what the barycenter should be under a muon track hypothesis, and compares

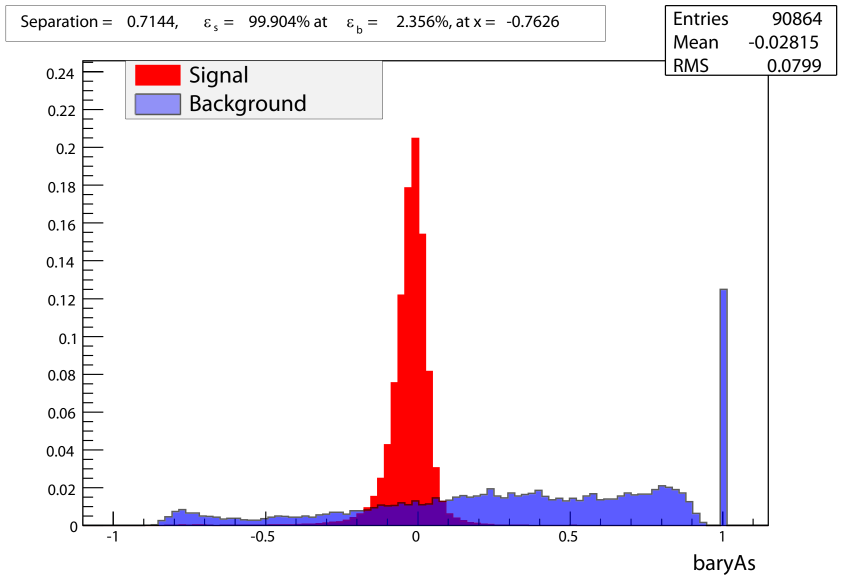

Fig. 9.17: The barycenter asymmetry of the calorimeter for a 200 MeV/c beam.

that with the measured barycenter. The expected value for barycenter is

$$b_e = \begin{cases} \frac{\Delta z_0}{2} & \text{if } \beta\gamma\cos\theta \leq 0 \\ \Delta z_0 - 8.268307 - 11.895816\beta\gamma\cos\theta & \text{if } 0 < \beta\gamma\cos\theta < 2.5 \\ +70.249759(\beta\gamma\cos\theta)^2 & \\ +14.155903(\beta\gamma\cos\theta)^3 & \\ -6.172258(\beta\gamma\cos\theta)^4 & \\ \Delta z_0 + 1946.499090 - 1087.370892\beta\gamma\cos\theta & \text{if } \beta\gamma\cos\theta \geq 2.5 \\ +185.505118(\beta\gamma\cos\theta)^2 & \end{cases} \tag{9.26}$$

where the barycenter is expressed in millimeters, and where Δz_0 is the thickness of layer 0. The measured barycenter is given by (9.25).

tdcPeaks

The *tdcPeaks* statistic is an integer value describing the number of individual TDC signals in the calorimeter. A value of two or more can occur if either a muon stops and then decays within the open gate, or if more than one particle arrives in the same cell of the detector, but separated far apart in time so that the TDC registers the two particle tracks independently of each other.

The separation of this variable is very poor since both signal and background events normally do not give more than one peak. However it is very useful for detecting muons decaying in the open gate. The muon decay events would otherwise give a measured energy deposition, track length, etc which would be inconsistent with ordinary signal events. No study has been made of pileup of events in the calorimeter, but there will be a substantial contribution from muons decaying during the open gate of other events, thus giving

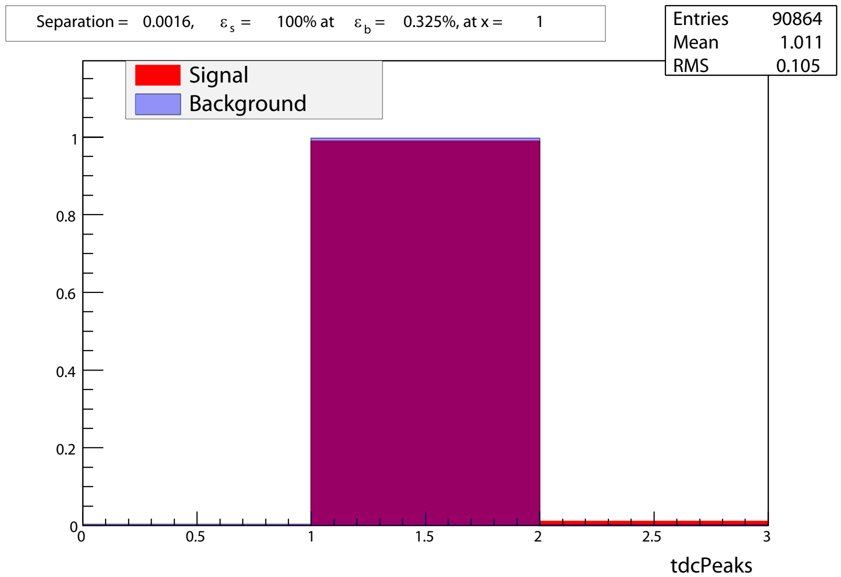

Fig. 9.18: The TDC peak distribution of the calorimeter for a 200 MeV/c beam.

$tdcPeaks > 1$. In practice any such event would likely be considered a *bad event*, and not tagged for PID analysis.

The TDC threshold used for the results in this report was 0.25 pC, which was changed to 1.84 pC. The reason for this change was that too many muon decays at rest were only seen as one continuous signal in the calorimeter, since the threshold was too low. For polystyrene, 83% of the distribution has $\mathrm{d}E/\mathrm{d}x > 2$ MeV/cm, which corresponds to 1.84 pC/cm at the highest point of the charge as function of time curve. This threshold should be sensitive to the thickness of the layer, but was chosen to correspond to the thinnest layer which is 1 cm thick. The risk of not reaching the threshold is small, since the energy loss is higher at the Bragg peak. In other words, the energy deposition in the layer where a muon decay eventually will occur is higher than the energy deposition of a minimum ionizing particle which passes through the layer.

highQ

The *highQ* statistic is the number of high level layer digits divided by any level layer digits in the calorimeter. An any level layer digit is 1 if the layer contains any digits at all, and a digit is created as soon as the ADC amplitude originating from an energy deposition exceeds the hardware threshold. A high level layer digit is similar, but it is a software trigger requiring an ADC amplitude corresponding to 72.5 keV/mm for layer 0 and 150 keV/mm for layers 1-10. The thresholds are set such that a charged particle track will create high level layer digits, while the energy deposition from photons will not be high enough to reach the threshold. If there are no calorimeter digits at all in the event, this variable is set to -1.

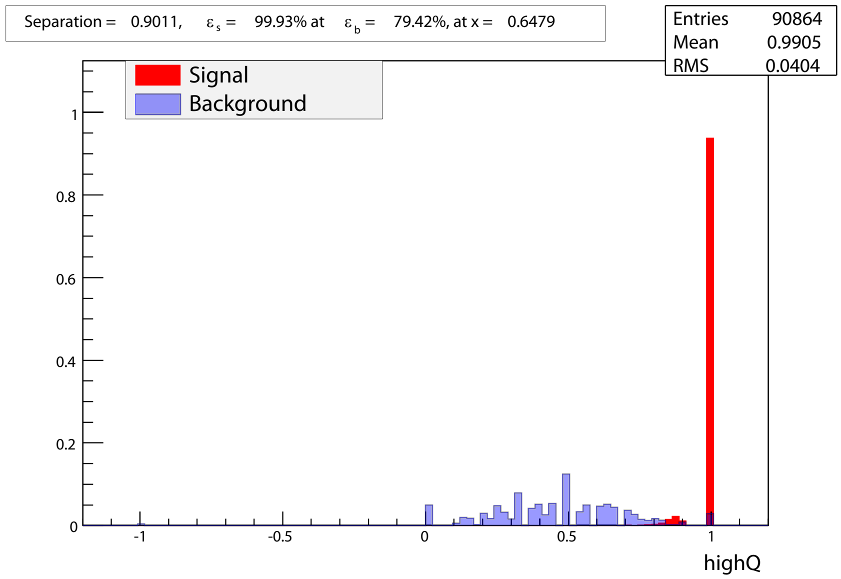

Fig. 9.19: The high level layer digit ratio distribution for a 200 MeV/c beam.

Since muons normally make continuous tracks until they reach their stopping positions, the *highQ* of signal events will be close to 1. An electromagnetic shower will however generate low level layer digits in the deeper parts of the calorimeter, pushing *highQ* towards 0. This variable provides the particle identification with an excellent rejection power, also when no other detectors apart from the calorimeter are used for the particle identification.

holesQ

Similar to *highQ*, this statistic uses the definition of high level layer digits to separate signal from background. It compares the number of layers with high level digits with the *maxADClay* variable, the Bragg peak tagging variable.

$$holesQ = \begin{cases} \frac{n_h}{l_{max}} & \text{if } l_{max} > 0 \\ 0 & \text{if } l_{max} = n_h = 0 \\ -1 & \text{if } l_{max} = 0 \ \&\ n_h \neq 0 \end{cases} \tag{9.27}$$

It describes how much of the track up until the Bragg peak layer (tagged with *maxADC-lay*) does not consist of high level layer digits. A continuous track from a charged particle should not contain any such holes in the track, but photons will sometimes pass through a few layers before making a hit. Hence *holesQ* is expected to be 0 for signal events. Naturally the discriminating power of this variable is reduced in the case of very short track lengths, i.e., low incoming momentum.

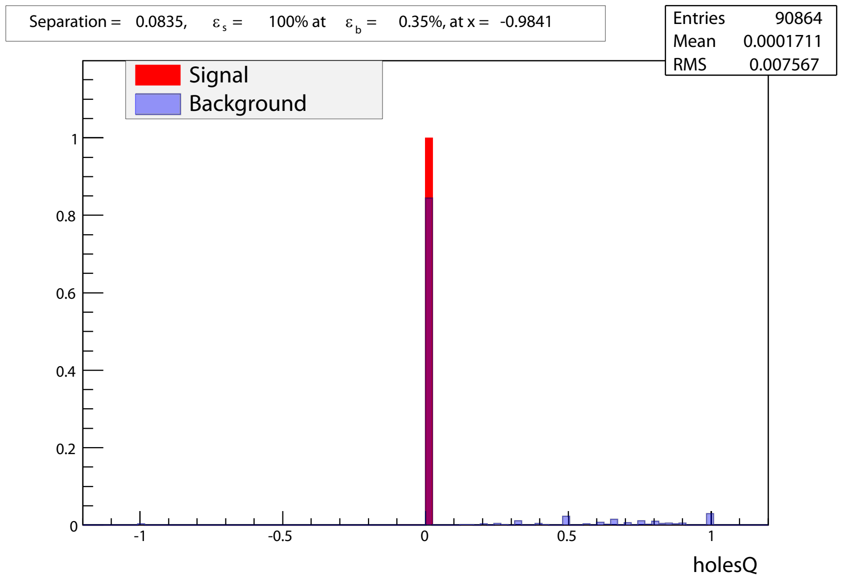

Fig. 9.20: The hole ratio in the calorimeter for a 200 MeV/c beam.

9.3.5 Evaluation of variables

The variables used for particle identification can be ranked with respect to separation and background rejection capability at a given signal efficiency, thus treating every variable as isolated from all other variables. This is done in table 9.5. As can be seen from the background rejection at the reference signal efficiency, no single variable performs sufficiently for all experimental scenarios. It is therefore more meaningful to use the variables in conjunction with the other variables. However it is hard to draw accurate conclusions from table 9.5 on the importance of a variable in a multi dimensional analysis, since the correlation must also be taken into account. Furthermore certain variables suffer from poor separation, but can still be powerful as a strict veto.

A statistic with a good performance over the full range of beam momenta is the *highQ*, which uses the energy density profile of the tracks to separate muons from electromagnetic showers. Another good statistic is the *maxLSubR*, which essentially is a measurement of the length of the longitudinal tail of the track. This is one of the very few techniques which works when the muon has an energy too low to punch through the preshower layer in the calorimeter. Interestingly the *barycenter* variable performs well for low energy but loses functionality as the momentum increases, a behavior opposite to the general trend. An advantage of these three variables is that they depend exclusively on the calorimeter information. Hypothesis testing by combining the information given by different detector systems is a very powerful technique, as demonstrated in the asymmetry variables.

While the *tdcPeaks* statistic shows very poor performance, it is still powerful as a veto, and it will likely be used to set the event *badness*. Most times when it gives a value larger than one it is due to pileup of events, not muons decaying in its own calorimeter time window. The statistic *holesQ* is the least useful statistic and can likely be removed

Tab. 9.5: Summary of particle identification variables. The separation [%] (defined in A.1.4) is indicated to the left. The background rejection [%] at 99.9% signal efficiency or higher is quoted in parenthesis. The variables are ranked with respect to separation for the 200 MeV/c beam. The right columns show the dependencies on time of flight, tracker reconstruction and EMCal information respectively.

	Central momentum [MeV/c]				Detector dep.		
Statistic name	140	170	200	240	tof	track	cal
highQ	84.1(0.5)	87.8(44.7)	90.1(79.4)	88.9(83.8)			x
adcAs2	57.5(4.2)	66.2(10.6)	75.2(13.6)	77.0(18.0)		x	x
baryAs	76.3(0.1)	71.7(1.2)	71.4(2.4)	72.2(3.4)		x	x
rangeAs	62.1(0.2)	66.1(1.3)	69.5(1.8)	68.9(5.9)		x	x
maxADClay	7.8(0.5)	48.7(0.3)	68.9(0.4)	71.4(0.3)			x
maxLSubR	48.0(17.8)	61.2(53.0)	62.4(66.8)	61.4(42.0)			x
adcQ0	29.1(6.9)	28.3(3.4)	56.8(2.0)	68.3(1.2)			x
tofAs	44.0(35.7)	47.3(43.4)	50.2(52.6)	53.4(58.4)	x	x	
adcProd0	18.2(4.1)	32.9(11.4)	50.1(8.6)	56.8(4.7)			x
totalProdADC	0.6(0.0)	18.6(5.5)	38.7(10.5)	47.5(9.5)			x
barycenter	59.0(45.3)	33.3(0.3)	22.4(0.4)	18.9(0.3)			x
tof	19.5(19.6)	16.6(20.3)	17.1(15.2)	17.3(21.1)	x		
holesQ	8.3(0.5)	8.7(0.3)	8.4(0.4)	7.4(0.3)			x
tdcPeaks	0.2(0.5)	0.1(0.2)	0.2(0.3)	0.1(0.2)			x

without significant loss of performance. It could still be useful for photon detection should the energy loss in the TOF2 be sampled and used as two initial calorimeter layers.

For time consumption issues, it is desirable to use a minimal set of information for performing the particle identification, and table 9.5 suggests that each beam setting might benefit from different statistic selections. A first choice was to use the subset of variables which only depend on the calorimeter. The results of that study are presented in table 9.6.

9.4 Global event reconstruction

All the fits used to create the input variables are stored in the PidFits class, which is situated in the Config area in G4MICE. The reconstruction application reads in values from the output of the Digitization application, and creates all the variables listed in section 9.3 which do not depend on more than one detector.

The plan has always been to create an application which reads in a preconfigured Artificial Neural Network configuration, and uses the reconstructed parameters to assign a variable which should be as close to 1 as possible for a signal event and 0 for a background event. The output of the PID application would then be used as input to the analysis which calculates the emittance of the beam. At the moment, however, this has not yet been realized, but it should be a fairly small project for a person skilled in C++ programming.

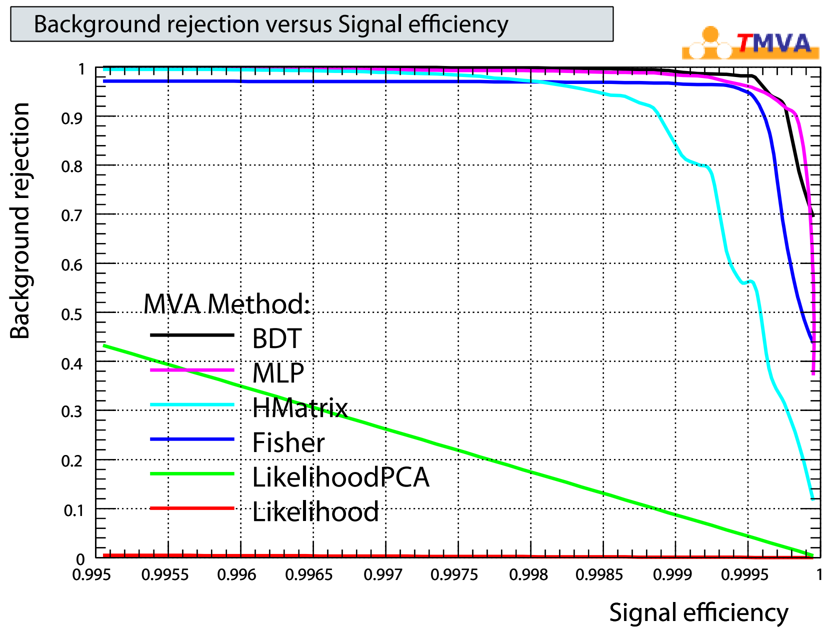

Fig. 9.21: The 200 MeV/c setup tested with a variety of fitting methods. At the reference signal efficiency of 99.9% the two best methods are Boosted Decision Trees (BDT) and Multi Layer Percepteron Artificial Neural Networks (MLP ANN), with BDT performing marginally better.

9.5 Fitting tools

In order to make use of the variables presented in section 9.3, the *signal* variable is fitted with the detector based variables as arguments. By looking at the separation and the efficiency of correctly identifying background events quoted in table 9.5, it is obvious that no single variable is powerful enough that a simple cut could achieve sufficient performance. A number of different tools have been tested to evaluate the performance and the ease of use. First a multidimensional Gaussian fit was performed by a custom written C macro. This worked somewhat well for simple problems but difficulties arose when the number of input parameters, and hence dimensions of the problem, increased. Furthermore it was cumbersome to individually adapt every fitting dimension if one was not operating with the assumption that the distributions where Gaussian.

Due to the demand for a more suitable multidimensional fitting procedure, the ROOT package TMVA [96] was used on the 200 MeV/c sample. Since TMVA was still in early development, the author had to perform a number of modifications to the open source package to achieve the desired functionality. The results of this study are illustrated in figure 9.21. The most powerful methods were Artificial Neural Networks (ANN) and Boosted Decision Trees (BDT), and ANN was the preferred choice since it is more conventional than the rather new but powerful BDT method. In the case when an ANN has no hidden layers it is identical to the Fisher method, which was the third best of the tested methods. Should the problem have been linear, the ANN and Fisher methods would have given identical results, hence the difference between the two methods is an indicator of the nonlinearities of the system.

No other methods performed sufficiently well, and for a conventional maximum likelihood fit it was not possible at all to obtain the reference signal efficiency while rejecting any background. It was therefore concluded that ANN is the method of choice, and if increased transparency is desired, the Fisher method is a good fall back option at a moderate expense of particle identification performance. The Artificial Neural Networks and the Fisher discriminant method are described in appendix D.

The exact ANN architecture used was to some extent decided after trial and error. Using only one hidden layer did not give satisfactory results due to the nonlinearity of the problem, but two hidden layers proved sufficient. The number of neurons per hidden layer were increased from initially seven and five respectively to $N+1$ and N, where N denotes the number of input variables. This was done following discussions with the developer of the ROOT Multi Layer Percepteron ANN software. Also TMVA's general purpose ANN uses this architecture.

The input variables were, as previously stated, chosen due to good separation and low correlation to other variables. However the choice of input variables in the analysis is not optimized, and there is probably some redundancy in the setup. It would be of interest for the experiment if the particle identification method could completely decouple from all detectors but the calorimeter, so the ANN fits using only calorimeter dependent quantities were performed on the same samples as when all input variable candidates were used.

The choice of the number of epochs used in the ANN training was chosen to be 500, since it was discovered that 100 or 200 epochs were not enough to fully train the ANN, and at 1000 epochs the effects of overtraining were significant. It was therefore no longer possible to obtain 99.9% signal efficiency. For the 240 MeV/c beam, overtraining already occurred at 500 epochs, so the training for this setting was reduced to 250 epochs as described in section 9.6.4.

9.6 Performance

The beams studied are unmatched 6π mm emittance beams at 140, 170, 200 and 240 MeV/c, with longitudinal momentum spread of 10% of the central momentum. The field map and detector positions used for the study were the G4MICE defaults in December 2006, with empty absorbers and the RF field turned off.

The ANN outputs are plotted in figures 9.22, 9.24, 9.25 and 9.26 with the background rejection efficiency at the reference signal efficiency indicated in the headers. However the displayed values are sometimes a few per mille too pessimistic due to the limited precision of the numerical cut finder. As figure 9.23 exemplifies, the output of the ANN was used for setting a cut c such that all values larger than c are considered signal events and events with values below c are treated as background. An alternative to this is to use the likelihood ratio (see section A.1.3), for a bin given by the output variable, as a weight in the emittance calculation. This idea has never been thoroughly tested in MICE but remains an interesting possibility. The performance is summarized in table 9.6 and figure 9.27.

9.6.1 140 MeV/c

At the lowest momentum setting, muons are rarely making it past the preshower layer of the calorimeter. Due to the low energy of the muon and the low sampling fraction of the preshower layer, the relative energy resolution, σ_E/E, is very poor. The range in the calorimeter and related variables is likewise of very limited use, and the time of flight asymmetry suffers from the fact that the model used does not fully apply to this low momentum. Clearly, this is the hardest beam setting for doing particle identification.

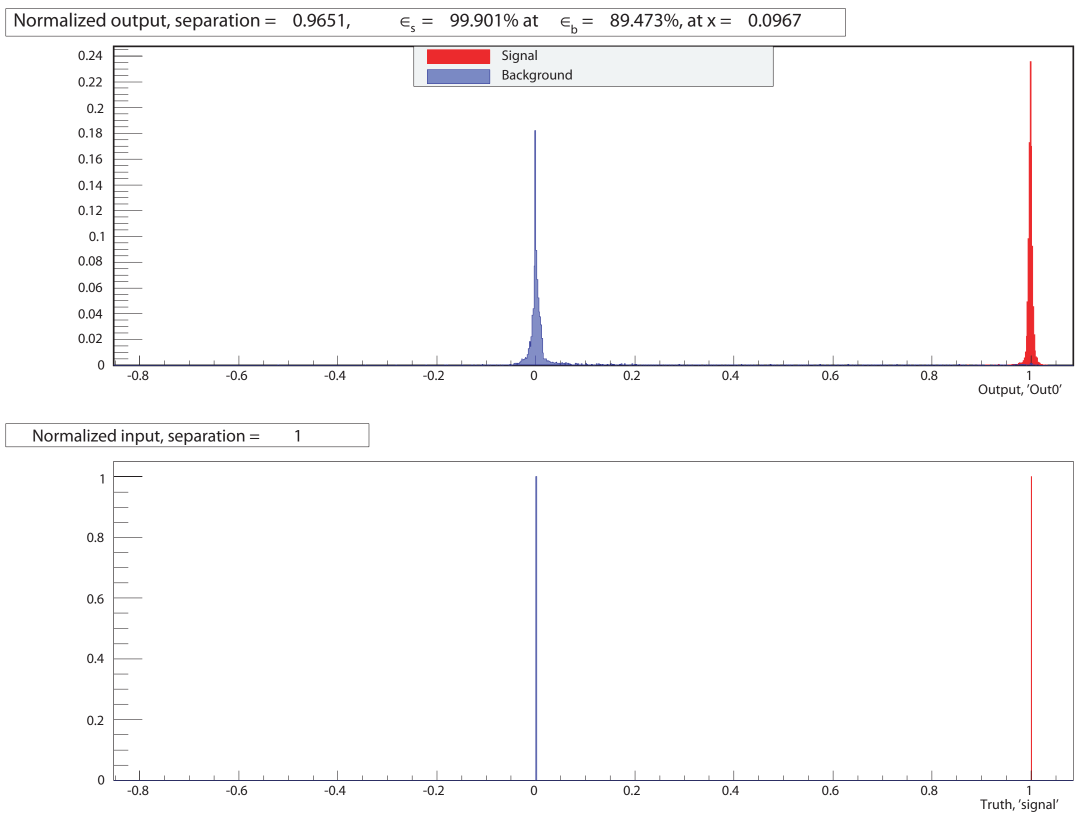

Fig. 9.22: The two probability density functions coming from the output of the neural network fit used in the particle identification algorithm for the 140 MeV/c beam. The bottom figure shows the truth particle ID, which the top figure tries to reproduce. For the purpose of clarity, the distributions are normalized in the sense that $\sum_i f_i = 1$, not $\sum_i f_i \Delta x = 1$. The separation of the two distributions is quoted in the header. Also the efficiency of the selection $x > x_0$ (acceptance) for the signal sample, and efficiency of $x < x_0$ (rejection) for the background sample, are indicated in the header. A very small contamination is visible at $x = 1$, which is a remnant of overtraining. The false background content due to overtraining is too small for visual detection in this figure.

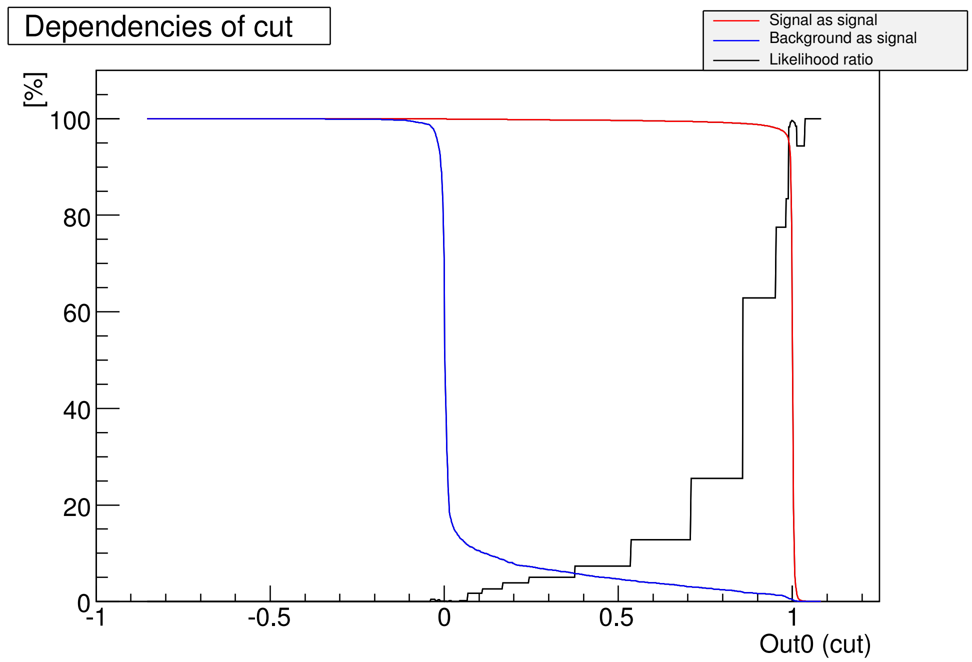

Fig. 9.23: The fraction of signal and background which is accepted as a function of a cut on the x-axis for the 140 MeV/c beam. The likelihood ratio is also included in the figure.

The intrinsic purity was 99.56%, which makes the required rejection efficiency 54.5% and the safety requirement 84.5%. At the reference signal efficiency of 99.9%, 89.5% of the background is correctly identified, and hence both the basic and the safety requirements are fulfilled. The safety factor achieved is 4.3 and the resulting purity of the sample is 99.954%.

When using input variables which only depend on information from the calorimeter, 69.6% of the background is correctly identified at 99.9% signal efficiency, which is enough to meet the basic requirement but not the safety requirement.

9.6.2 170 MeV/c

At this momentum muons are sometimes stuck in the preshower layer just like in the 140 MeV/c case, but more often than not the muons penetrate into the subsequent plastic layers. This make the performance better than in the 140 MeV/c case since many of the variables which showed little or no separation for low momentum are starting to give useful information regarding the nature of the event.

The intrinsic purity was 99.59%, which makes the required rejection efficiency 51.6% and the safety requirement 83.9%. At the reference signal efficiency of 99.9%, 96.0% of the background is correctly identified, and hence both the basic and the safety requirements are fulfilled. The safety factor achieved is 12.0 which is almost three times as good as for the 140 MeV/c beam.

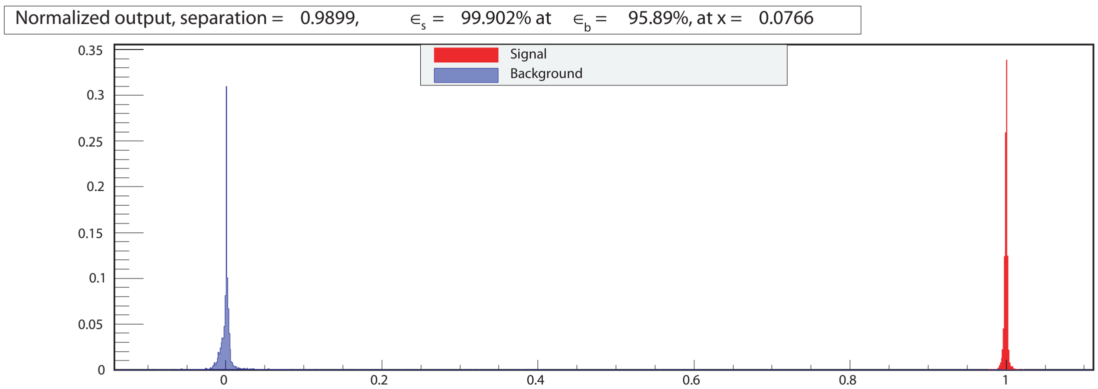

Fig. 9.24: The output of the neural net fit for the 170 MeV/c beam.

When using input variables which only depend on information from the calorimeter, 89.9% of the background is correctly identified at 99.9% signal efficiency, which meets both basic and safety requirements and is comparable to the performance with all input variables for the 140 MeV/c case.

9.6.3 200 MeV/c

For the 200 MeV/c beam, which is the MICE experiment's nominal momentum, the muons are, with few exceptions, always reaching deep into the calorimeter. The typical muon stops between the 4th and 7th layer, making well behaved tracks through the plastic which are useful for variables such as $highQ$. Also since the majority of the energy deposition is in the fully active region of the calorimeter variables such as $adcAs2$ are useful.

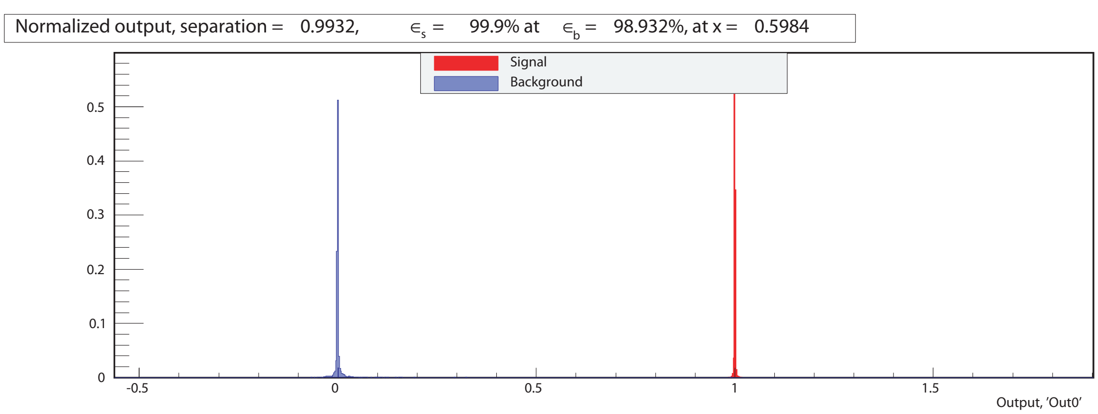

Fig. 9.25: The output of the neural net fit for the 200 MeV/c beam.

The intrinsic purity was 99.63%, which makes the required rejection efficiency 46.5% and the safety requirement 81.3%. At the reference signal efficiency of 99.9%, 98.9% of the background is correctly identified, and hence both the basic and the safety requirements are fulfilled. The safety factor achieved is 50.9.

For the same set but trained on calorimeter variables only, 97.5% of the background is rejected at 99.9% signal efficiency. That corresponds to a safety factor of 21.5.

9.6.4 240 MeV/c

For the highest beam setting muons are making full use of the calorimeter. They usually stop between the 5th and 10th layer, and occasionally punching through the calorimeter. The high energy deposition together with a substantial track length make particle identification easy. Due to slight overtraining, the number of epochs were reduced to 250, which gave approximately identical rejection power at the reference signal efficiency as the standard 500 epochs, but made the emittance bias curves smoother.

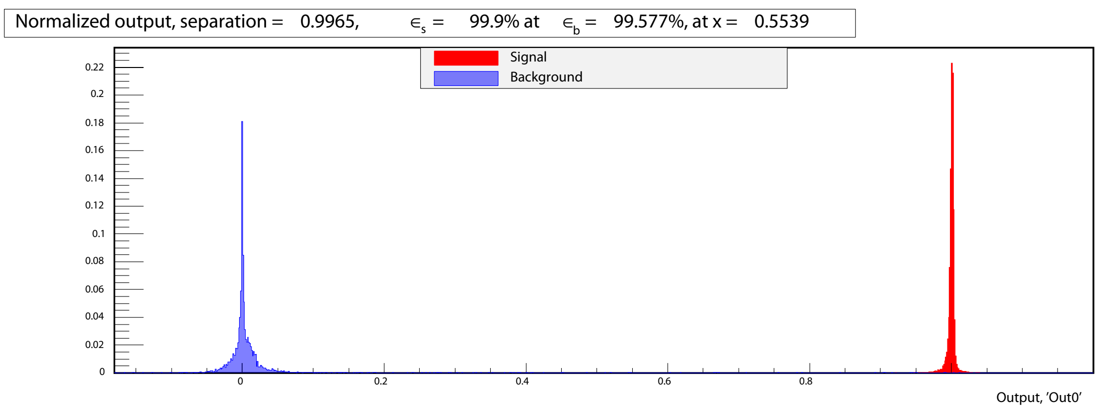

Fig. 9.26: The output of the neural net fit for the 240 MeV/c beam. Due to fewer training epochs the peaks have wider distributions, but the performance at the reference efficiency is marginally better due to less overtraining.

The intrinsic purity was again 99.63%, which makes the required rejection efficiency 46.4% and the safety requirement 81.3%[4]. At the reference signal efficiency of 99.9%, 99.7% of the background is correctly identified, and hence both the basic and the safety requirements are fulfilled by a good margin. The safety factor achieved is 179.1.

For the same set but trained on calorimeter variables only, 98.6% of the background is rejected at 99.9% signal efficiency. This performance is comparable to the 200 MeV/c case with all input variables active.

9.6.5 Analysis of failure

A large portion of the signal events which are severely misidentified are muons decaying inside the open gate of the calorimeter data taking. The recipe for handling this phenomenon has been to use the *tdcPeaks* variable to tag the muon decay. However if the

[4] This is achievable with a simple cut on the *highQ* variable. See table 9.5.

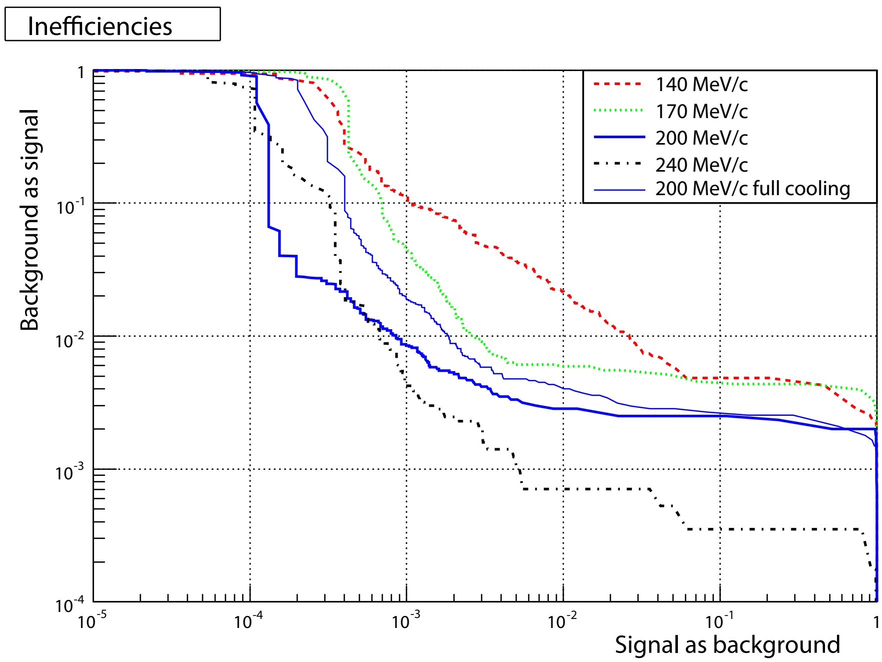

Fig. 9.27: The particle identification inefficiencies. In addition to the four different beam momenta discussed in this section, a fifth beam using filled absorbers and active RF fields is included. This beam was used for cooling studies described in section 9.7.

Tab. 9.6: Summary of particle identification performance. The intrinsic purity is the purity of good events before particle identification. Two efficiencies for background identification are presented, one when all input variables are used, and the other when only the calorimeter is used for performing the particle identification. Both values are for a signal efficiency of 99.9%.

Central momentum	Intrinsic purity	Rejected background	
		All variables	EMCal only
140 MeV/c	99.56%	89.5%	69.6%
170 MeV/c	99.59%	96.0%	89.9%
200 MeV/c	99.63%	98.9%	97.5%
240 MeV/c	99.63%	99.7%	98.6%

threshold is too low or the decay too close in time to the stopping muon, the TDC cannot distinguish the two signals. The results here likely have too low a threshold, but due to time constraints the particle identification performance under an improved TDC threshold has not been examined.[5]

9.7 PID and emittance measurement

Although the results in section 9.6 show that the performance of the particle identification algorithm is more than adequate in terms of efficiency and purity, the real test is the impact the contamination has on the emittance measurement. As figure 7.2 illustrates, a typical background event from a muon decay between TOF1 and TOF2 has a larger single particle emittance than the average signal event, so the impurities present in the beam appear to heat the beam. On the other hand, the signal events which are incorrectly tagged as background are usually ill behaved muons, which just like the background events have a higher amplitude than a typical signal event. Hence losing the outliers in the signal sample tends to give a measured emittance which is cooler than the full signal sample. Thus, in principle, it is possible that the two contributions cancel out in the emittance calculation, and the emittance measured is unbiased despite the presence of misidentified events.

The purpose of the MICE experiment is however *not* to measure the *emittance* of a beam, but to measure the cooling, *the emittance reduction*, of a beam. This means that even though there might be a bias on the emittance measurements, the emittance change measurement might still be unbiased if the emittance measured upstream and downstream are equally biased. This is very important to keep in mind not only for bias originating from particle identification failure, but also from scraping. In the latter case, the scraping muons will have high amplitude in the upstream spectrometer, and thus the emittance will be high upstream. Since they are scraped, they do not contribute to the emittance downstream, and naively looking at the difference in emittance will give the impression that the beam has cooled. Since MICE is a particle by particle experiment, the scraped events can be tagged as *bad* and thus they do not contribute to the emittance change measurement. For a Neutrino Factory one might still be interested in how much of the beam was scraped in the cooling channel, but those considerations are outside the scope of this thesis. See section 9.8 for evaluation of the systematic errors on the cooling measurement.

9.7.1 Method

The emittance was calculated using the Analysis package of G4MICE, using the Monte Carlo truth values at the tracker reference planes. The same files that were used for evaluating the particle identification performance were used as input for the emittance calculations. Since those files had an increased amount of background in order to help the training of the neural net, the background events were given a weight between 0 and

[5] The results were simulated, but due to technical difficulties reading in the results, the evaluation of the impact on performance had to be canceled.

1, where signal events had this weight equal to unity, when the covariance matrix was calculated. In order to cross check that this was done correctly the intrinsic purity of the beam was compared with the purity using the full sample but with reweighted background. As a second check, changing the weights for all events by an equal but arbitrary amount left the emittance invariant.

Since the files used to evaluate the particle identification performance (presented in section 9.6) were not simulated with an active cooling channel, it was only meaningful to examine the bias on the emittance measurement. In order to examine the bias on the cooling, a separate setup was used, which is described in 9.8. The corresponding bias on the emittance measurement is presented in figures 9.28 and 9.29 together with the other configurations.

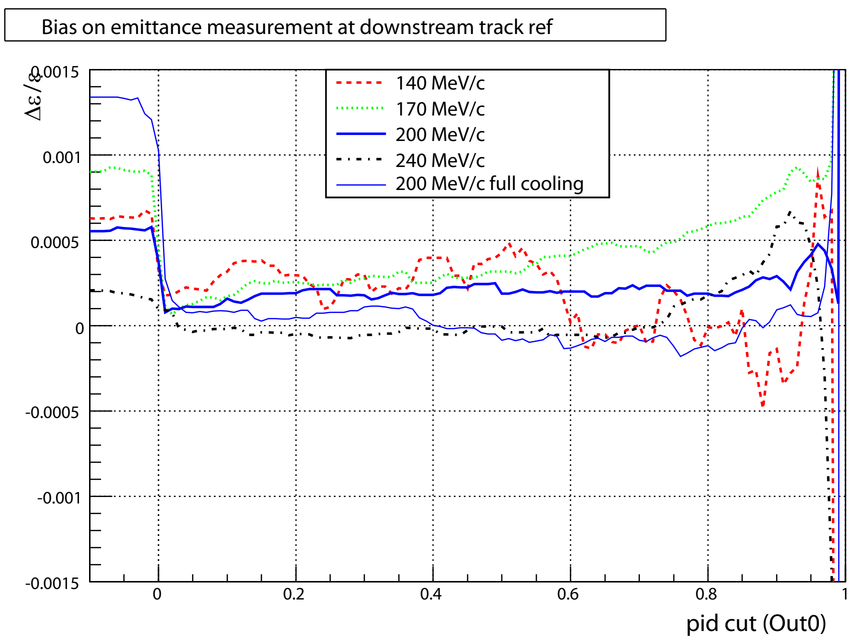

Fig. 9.28: The bias on the emittance measurement at the downstream tracker reference plane as a function of Out0, the output of the particle identification analysis.

9.7.2 Comments on results

The results of this study show that the impact of the muon decay background is moderate at the tracker reference planes, and that the particle identification algorithm, beyond a doubt, reduces the emittance measurement bias to a level the experiment can cope with. However there is one big problem with this line of reasoning. The emittance measured was taken from the tracker reference planes, which are close to the cooling channel. Since a huge fraction of the background giving *good events* comes from muon decay inside the downstream spectrometer solenoid, these late decay events do not contribute to the bias

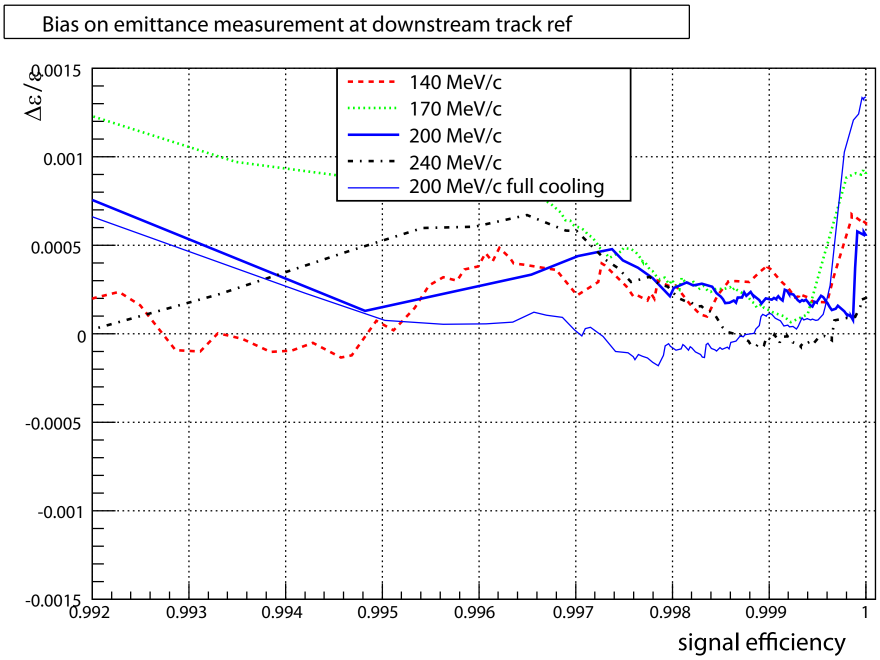

Fig. 9.29: The bias on the emittance measurement at the downstream tracker reference plane as a function of the signal efficiency. The bias is minimized for high values of the signal efficiency, approximately at 99.9% efficiency for most beams.

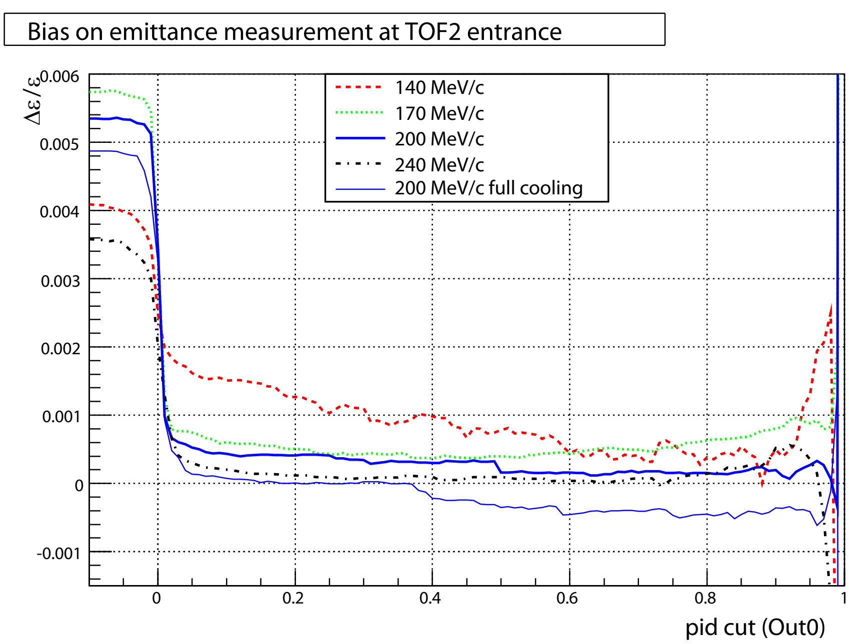

Fig. 9.30: The bias on the emittance measurement at the upstream TOF2 reference plane as a function of Out0, the output of the PID analysis.

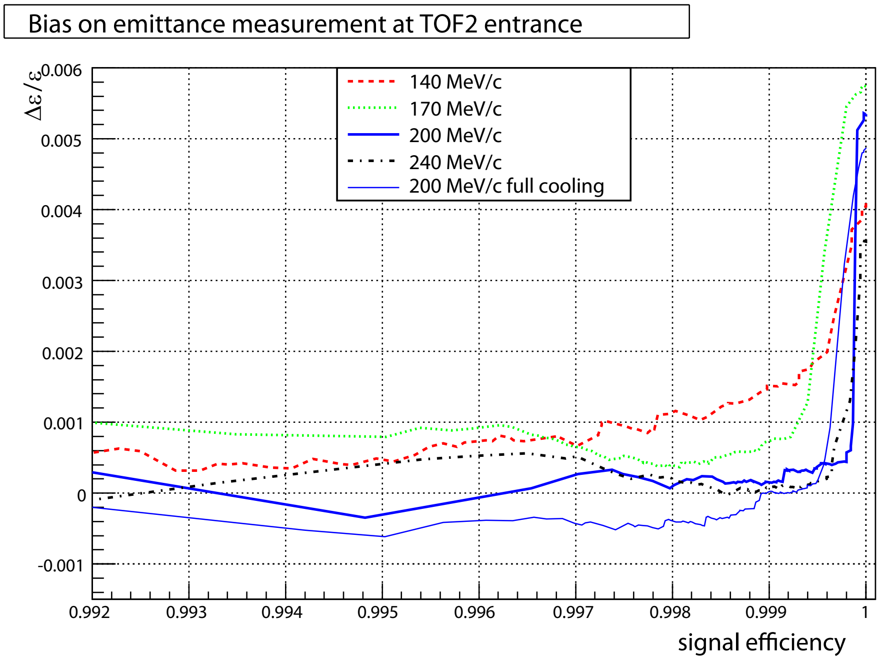

Fig. 9.31: The bias on the emittance measurement at the upstream TOF2 reference plane as a function of the signal efficiency.

of the emittance measurement. Should one measure the reference emittance further downstream, the bias would be larger. As figures 9.30 and 9.31 show, calculating the emittance at the entrance of TOF2 instead of the tracker reference plane would give a factor of three to twenty larger bias on the measurement. Furthermore, since the events which decay inside the active region of the tracker might give a very strange momentum measurement, the best way to evaluate this is to use the real tracker reconstruction, which unfortunately is yet to be made fully functional. However even if the emittance at TOF2 is used, it is still no problem to reduce the systematic errors on the emittance measurement to less than one in a thousand.

It is useful to compare the emittance measurement bias originating from misidentification of events with other sources of systematic errors. For example, while looking at the contribution from the tracker resolution during the emittance measurement, the bias from background contamination is of the same order or larger before particle identification is performed. After identification, however, the bias from wrong assignment of signal-background tags is vanishingly small in comparison with the errors from the transverse momentum measurement, shown in figure 9.32. This raises another point; the systematic error originating from the momentum measurement is much too large with the given resolution on transverse momentum, and does not meet the design requirements of the experiment. However due to the systematic nature of the bias there are measures one can use to correct for a large part of this shortcoming, obtaining less than one per mille bias provided that all phase space variables are known to 14% or better of their root mean

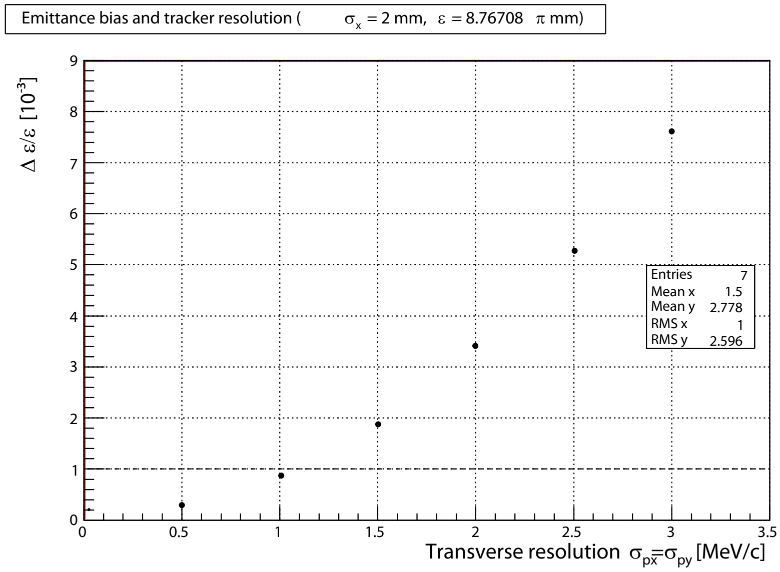

Fig. 9.32: The systematic errors on the 4D emittance measurement as a function of the tracker resolution. The required momentum resolution, assuming no corrections, is 1 MeV/c or less. Furthermore the effect of the spatial resolution is negligible.

square [97]. In addition, recent developments on the tracker reconstruction show much better resolutions [68].

9.8 PID and the cooling measurement

Since the MICE experiments ultimate objective is to demonstrate ionization cooling, it is crucial to the experiment to know what precision it is possible to obtain on the cooling measurement and where the different sources of uncertainty come from. In this thesis the term *cooling* is used to mean the fractional difference between the transverse emittance upstream and downstream of the cooling channel, divided by the transverse emittance upstream,

$$cooling \doteq \frac{(\epsilon_{down} - \epsilon_{up})}{\epsilon_{up}} \tag{9.28}$$

where ϵ denotes the transverse emittance. Similarly *cooling bias* is used for the precision of the cooling measurement

$$cooling\ bias \doteq \frac{\Delta(\epsilon_{down} - \epsilon_{up})}{\epsilon_{down} - \epsilon_{up}} = \frac{(e_{down} - e_{up}) - (\epsilon_{down} - \epsilon_{up})}{\epsilon_{down} - \epsilon_{up}} \tag{9.29}$$

where ϵ is the true emittance (without contamination), and e is the measured emittance (with contamination). Hence a negative value on the cooling bias means that the experiment is undervaluing the cooling performance. Since e is a function of the particle identification analysis, it allows making plots of cooling bias as a function of the signal efficiency, which is an experimental observable.

9.8.1 Method

In order to make a study involving the cooling measurement meaningful, the four previously used beams could not be used since they were not properly matched with the magnetic field; they used empty absorbers and the RF field was turned off. Instead a beam was matched using the G4MICE application *Matcher* into a field configuration assuming 207 MeV/c muons before the cooling channel, $\beta_\perp = 42$ cm (see (3.38)), with a fully active MICE Stage 6 cooling channel.[6]

The result was a higher transmission rate than for the unmatched beams, and while the other beams showed a considerable emittance growth, this beam cooled between the tracker reference planes. However the expected 10% cooling was not obtained. The cooling was measured to about 3%. A great deal of effort has gone into understanding this result, and the conclusion is that the particles arriving too far away in time from the reference particle are not reaccelerated in the RF field. This causes the energy-time ellipse to be deformed and the long tail at high time and low energy has larger single particle emittance than the particles in the RF bucket. This is largely a remnant of the fact that the beam is starting with a Gaussian distribution in time at TOF1 with a standard deviation of 0.6 ns, which is realistic if not too small compared to a Neutrino Factory. With the 5 ns period of the RF cavities, it is clear that this effect is a real feature of the experiment and in order to achieve 10% cooling, some cuts must be made on the distribution.

9.8.2 Results

In order not to confuse the cuts that must be made to obtain improved cooling with the particle identification selection of events, all *good events* were used and the corresponding cooling bias measured as a function of the particle identification output $Out0$ and the signal efficiency. The results are shown in figures 9.33 and 9.34.

This setup gave 99.67% intrinsic purity, slightly better than the unmatched beams without an active cooling channel. The improvement was partly due to the fact that the cooling channel removes more background and partly due to the improved transmission of muons. The amount of background rejected at 99.9% signal efficiency was 98.1%, lower than the corresponding value with 200 MeV/c beam without active cooling channel. This is due to energy loss in the last absorber, which reduces the effective momentum of muons at the entrance of the calorimeter.

The bias on the cooling measurement originating from background contamination is of the order of 4.5%. Since the design requirement of the experiment is a precision of 1%, this proves that particle identification is necessary. After particle identification has been performed, the bias is rather flat around zero bias, $9.2 \cdot 10^{-4} \pm 9.0 \cdot 10^{-4}$ for $0.05 < Out0 < 0.95$. The observant reader might have noticed that the large improvement on the precision of the emittance is found at the same values of signal efficiency as for the cooling measurement, which in turn is close to the reference efficiency of 99.9%. The flatness of

[6] The Matcher application was created by Chris Rogers, while the field map was created by Holger Witte, both RAL.

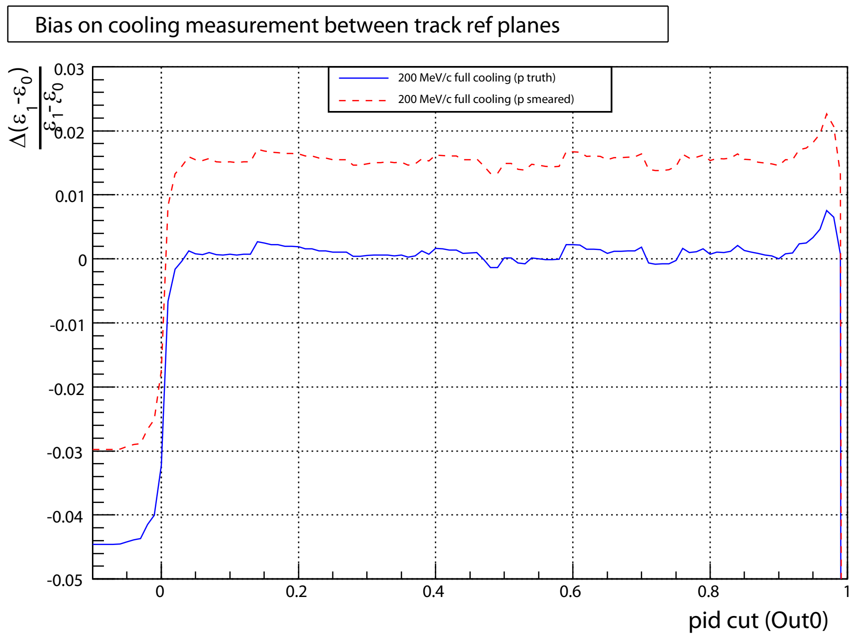

Fig. 9.33: The systematic error on cooling measurement from particle identification. The blue curve indicates the bias when the Monte Carlo truth information in the tracker reference planes is used, and the red curve is when the emittance is calculated using smeared tracker values. See section 9.2.

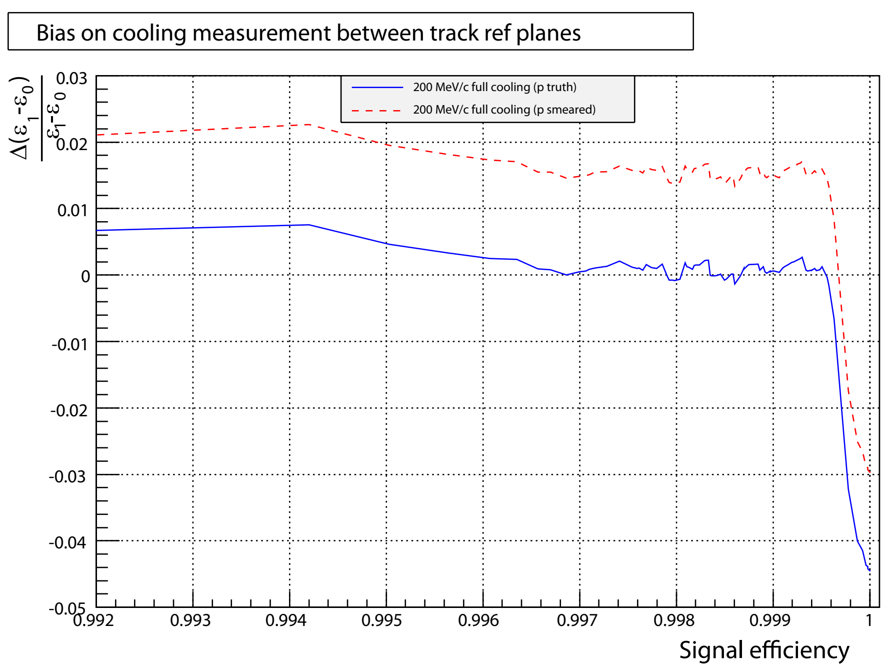

Fig. 9.34: Same as figure 9.33 but with the signal efficiency on the horizontal axis.

the curves below this value is good news since it makes the exact spot where the separation between signal and background events is made less crucial.

While these results use the Monte Carlo truth information for calculating the cooling, the results are rather different if one takes into account the effect of the tracker resolution. As the red curves in figures 9.33 and 9.34 show, the spectrometer imperfections systematically cause the measured cooling to be larger than it actually is. The contribution to the cooling measurement bias is larger for uncorrected contamination than the contribution from tracker resolution, but after particle identification, the remaining bias from misidentified background is negligible compared to the spectrometer imperfections. However as mentioned earlier there are strategies for how to cope with this issue.

The conclusion of this study is essentially the same as that in section 9.7, namely that it is indeed necessary to identify events, and that the particle identification algorithm performs satisfactory. However the real tracker reconstruction was not used and we have already seen that the emittance measurement bias depends strongly on exactly where the emittance is calculated, so it is natural to assume the same is true for the cooling measurement bias. Due to the presence of the diffuser, it is not possible to compare observe cooling between TOF1 and TOF2. The systematic error on the downstream emittance measurement typically worsened by one order of magnitude when looking at the entrance of TOF2 compared to the downstream tracker reference plane due to the muon decay between these two positions. It would be reasonable to expect the cooling measurement to give a similar deterioration when taking decay inside the trackers also into account. In the range $0.05 < Out0 < 1$ of figure 9.33, the root mean square of the cooling bias is approximately $1.0 \cdot 10^{-3} \pm 1.3 \cdot 10^{-3}$, implying that a one order of magnitude deterioration of the cooling measurement would give approximately 1% error, which is the MICE cooling measurement precision objective.

9.9 Summary

The most important instrument for identifying particles in the downstream region of MICE is the calorimeter. By using the calorimeter in conjunction with the trackers and the time of flight detectors, a very clean muon sample can be obtained.

The particle identification presented in this chapter can reduce the effect of muon decay to acceptable levels. When measuring the emittance at the downstream tracker reference plane, the systematic error on the emittance measurement can be kept below 0.4‰ for all setups studied. However a large portion of the positrons which hit the downstream detectors are created by muons decaying inside the downstream tracker solenoid. The systematic error on the emittance at the entrance of TOF2 is thereby increased, but the particle identification can still keep the emittance bias below the 1‰ specification. However it is unknown how the tracker reconstruction will treat tracks of muons which decay between the tracker stations, and this effect should be studied again when the tracker reconstruction is fully functional.

The systematic error on the cooling measurement without particle identification is around 4.5% for the nominal MICE beam. It can with ease be kept below 1% using the particle identification algorithms described in this chapter. However just as with the emittance measurement, the behavior of the tracker reconstruction for muon decaying inside the trackers is unknown, and could pose a challenge to the MICE objective of measuring the cooling with a precision of 1%.

9.9.1 Remark about reference efficiency and purity

As described in section 7.2.1, the reference signal efficiency was 99.9% while the target purity was 99.8%. By examining figure 7.2, it is clear that the assumption that the average single particle emittance of background events is 50% larger than the corresponding quantity for the signal events is correct. Using the values from that plot together with (7.4) one would expect the setup to give a relative systematic error on the emittance measurement equal to 0.130% if no particle identification was performed. Comparing this with figure 9.28 (200 MeV/c full cooling), where the corresponding quantity is 0.134%, shows that this line of reasoning is valid, and the purity requirement is just and fitting. However the muon decays after the downstream tracker reference plane will further increase the average amplitude of the background sample if it is measured further downstream, thus the purity requirement should hence be increased in order to achieve sufficiently low bias on the emittance measurement.

On the other hand, the same setup gave an average single particle emittance of 20.5 mm for signal events rejected by the 99.9% efficiency cut. This is much closer to the average of 23.4 mm for the total signal sample than was assumed when imposing the efficiency requirement in section 7.2.1. This leads to the conclusion that the efficiency requirement is too strict, and that the reference signal efficiency can be lowered in order to increase the purity.

10. SCRAPING

While investigating the particle identification performance, a study was launched with the objective of determining where the muon decay background was occurring for positrons which were not lost on the way to the downstream detectors. This led to the discovery by the author that the TOF2 active area was too small compared to the rest of the experiment, which in turn triggered a search for optimal detector sizes for the whole downstream region.

10.1 Cryostat

Outside the tracker active area is the cryostat for the tracker solenoid. Between the tracker active area (with radius 15 cm) and the cryostat inner wall (at 20 cm) is a cabling area containing clear fibers for the spectrometer. Initially it was thought that the cryostat would be obstructing the path of the muons, but its exact position was not well known and the author showed that the amount of scraping was strongly depending on this parameter.

After a technical drawing for the cryostat was circulated, the positions and dimensions of the whole tracker area were updated in the simulation software, and a new simulation was commenced. The results were generated by creating a beam with combinations of momentum and positions as

$$\begin{cases} p_z & = \{100, 110, \ldots, 350\} \text{ MeV/c} \\ x' & = \{-0.35, \ldots, 0, 0.05, \ldots, 0.35\} \\ y' & = \{-0.35, \ldots, 0, 0.05, \ldots, 0.35\} \\ x & = \{-5, 0, 5\} \text{ mm} \\ y & = \{-5, 0, 5\} \text{ mm} \\ z & = -6524.5 \text{ mm} \end{cases} \tag{10.1}$$

in order to fill the full phase space. This caused considerable scraping and raised questions regarding the acceptance of the experiment[1]. Only muons which fulfill the requirements for being *good* events where used to define the radial distributions at the cryostat and various other positions in the downstream region.

The updated geometry gave a lesser amount of cryostat scraping as a result. See figure 10.1. The number of *good* muons going through the cryostat wall was negligible, but there were still some *good* muon tracks going through the cabling area.

[1] The emittance at the downstream tracker reference plane obtained with this beam was 13.9 π mm.

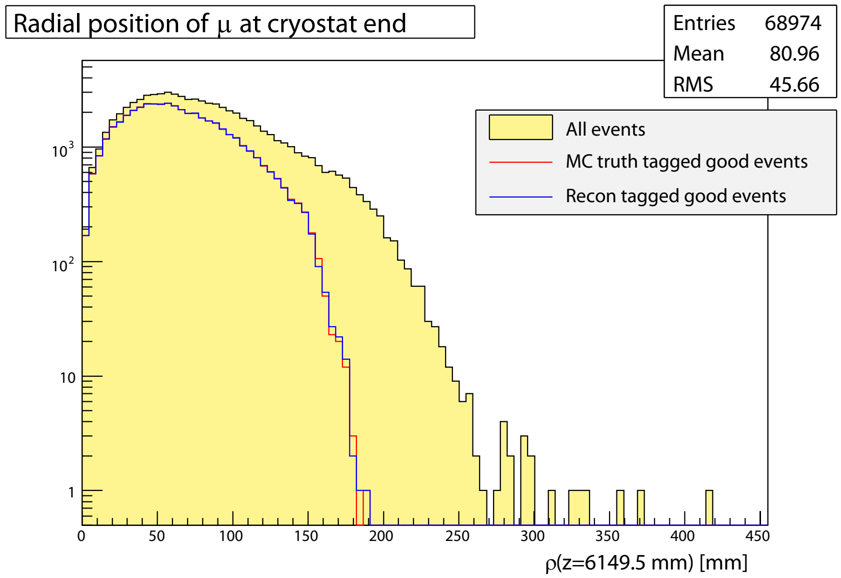

Fig. 10.1: Radial positions of muons at the end of the cryostat. The yellow area is for all muon events, while the blue and red curves indicate the events which are *good* muon events. The different colors indicate whether the goodness of event tagging uses Monte Carlo truth values or smeared tracker values.

10.2 TOF2 and iron shields

Since TOF1 and TOF2 are situated in a magnetic field of considerable strength, the two detectors are encased in cylindrical iron shields to protect the photo multipliers tubes. For TOF2, the upstream of the two shields is 10 cm thick and the shield downstream of the detector is 5 cm thick. The clear space between the shields is 10 cm, which is the minimum distance which allows easy mounting of TOF2. These values together with information from technical drawings of the cryostat fixed the positions of all volumes in the TOF2 area.

10.2.1 Full phase space beam

The full phase space beam (see section 10.1) was fired through the experiment using a field map assuming one 10 cm shield of radius 50 cm optimized for 200 MeV/c muons. The iron shields were not physically present in the simulation. The area of TOF2 was made very large in order to give the correct energy loss and scattering for muons passing through the detector and approaching the second iron shield. The radial positions were registered for upstream and downstream surfaces of both iron shields and TOF2, and the results are shown in figures 10.2(a) to 10.2(c). While the maximum radius at the cryostat end was 19 cm, the maximum radius grew to 35 cm at the entrance of the first shield, and continually increased until the beam leaves the second shield at a maximum radius of 45 cm. Since this beam is not realistic, but an attempt to run as wide a beam through

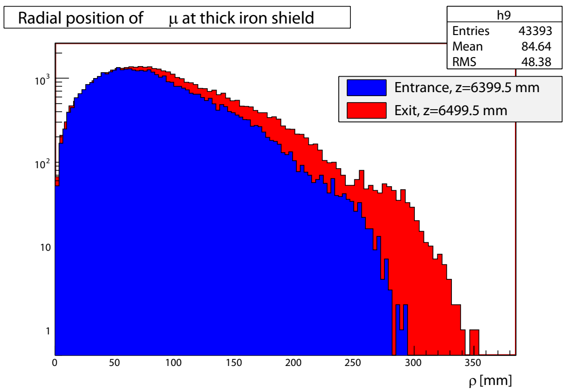

(a) 1st shield.

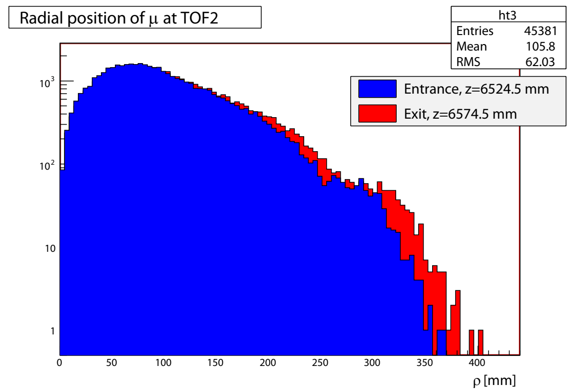

(b) TOF2

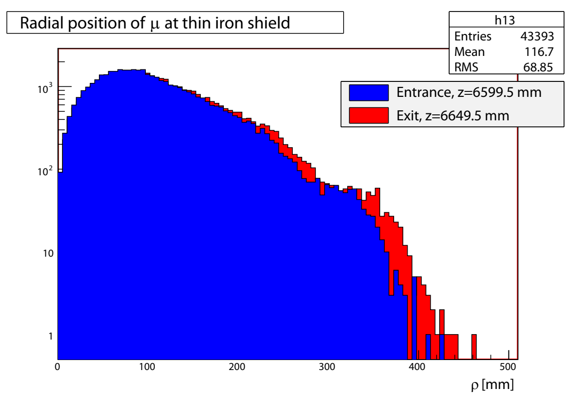

(c) 2nd shield.

Fig. 10.2: The radial positions at the entrances and exits of the volumes in the TOF2 region, using the full phase space beam. The radius of the beam grows with increased longitudinal position.

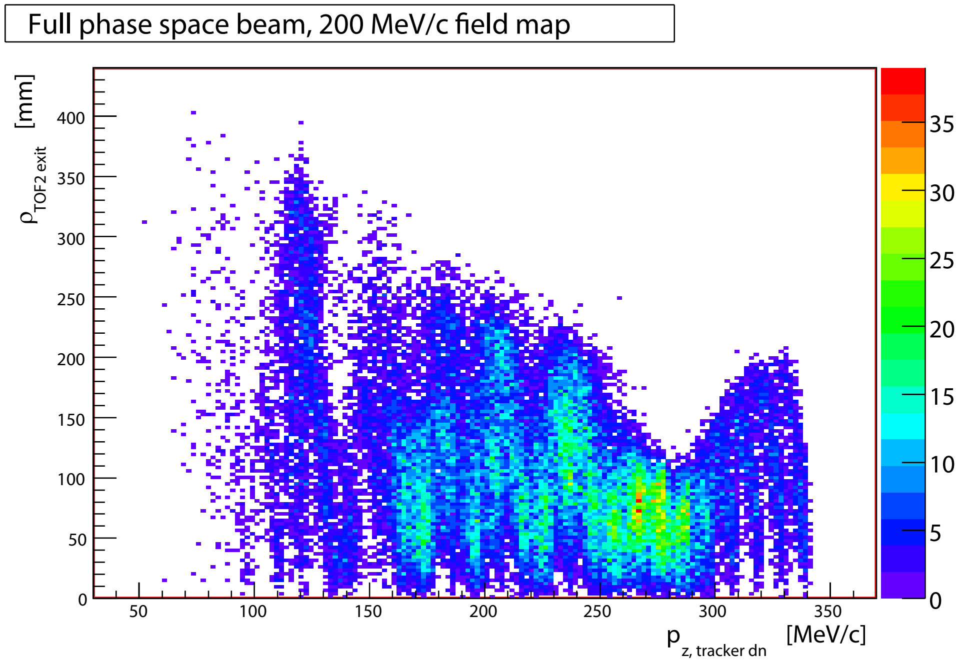

Fig. 10.3: Radial position at TOF2 exit as a function of longitudinal momentum in the downstream spectrometer. Since this setup used a field map optimized for 200 MeV/c muons, there is a resonance at high momentum. At low momentum the maximum radius grows linearly with decreased momentum.

the experiment as possible these radii should be taken as maximum possible values of any beam.

The radial distribution depends strongly on the longitudinal momentum. As figure 10.3 shows, the maximum radius increases linearly with decreasing momentum for low momentum. As figure 10.3 indicates, the maximum radius obtainable depends on at what longitudinal momentum the experimenters no longer consider an event a *good event*[2].

10.2.2 Matched beams

Since the beam used for examining the outer boundaries of the MICE acceptance is far from a realistic beam, it is not meaningful to refer to the scraping as a fractional loss. Instead, matched beams (using the Matcher application) were used with the two field maps that were available[3] for Stage 6. The results are shown in figures 10.4(a) to 10.6(b).

Just like in the case of the full phase space beam, there is a relation between the maximum obtained radius and the longitudinal momentum. See figure 10.7(a) and 10.7(b). For both setups the beams formed an ellipse in $p_z : \rho$-space, but due to the Landau nature of energy loss there are events trailing toward low momentum and high radius. From the

[2] See definition of *good event* in section 9.3.2.

[3] Produced by Holger Witte, RAL.

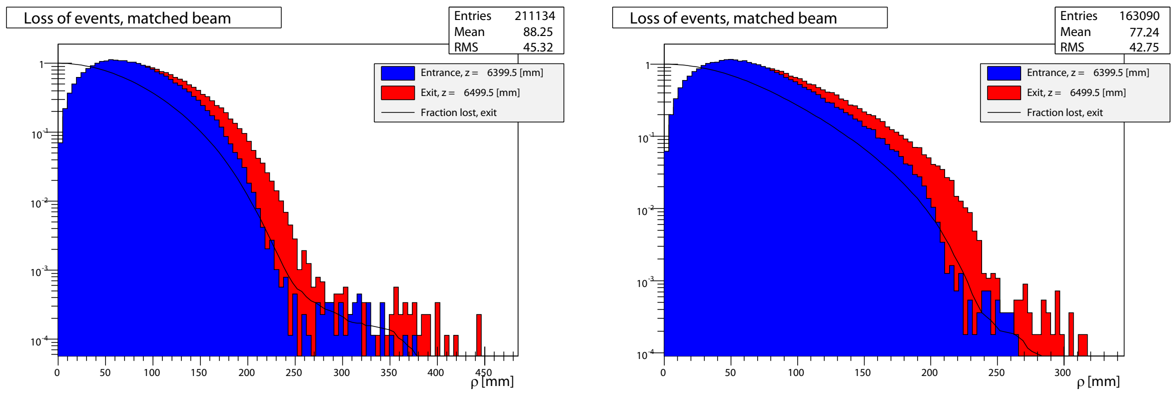

(a) 140 MeV/c (b) 200 MeV/c

Fig. 10.4: Radial position at entrance and exit of the first iron shield for two matched beams. Also plotted is the fraction of the number of muon events which are lost if a cut is made at a certain radius.

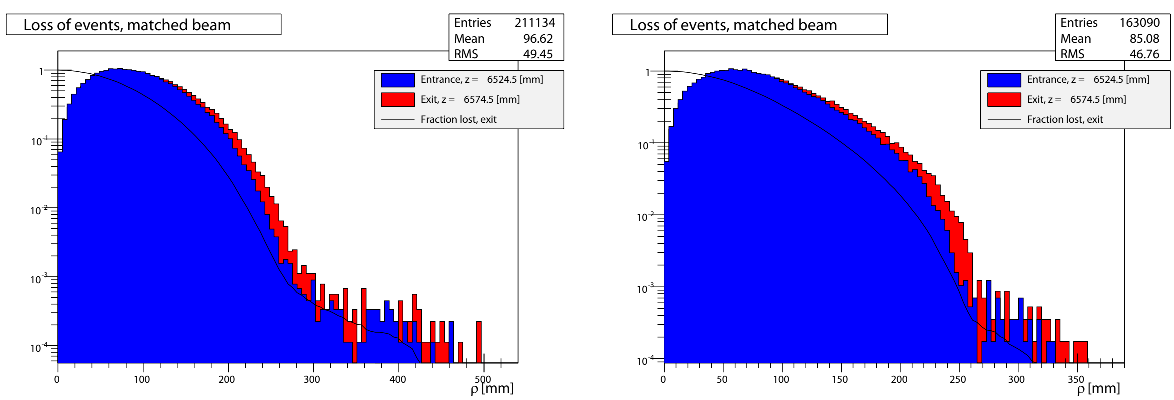

(a) 140 MeV/c (b) 200 MeV/c

Fig. 10.5: Radial position at the entrance and exit of TOF2 for two matched beams. Also plotted is the fraction of the number of muon events which are lost if a cut is made at a certain radius.

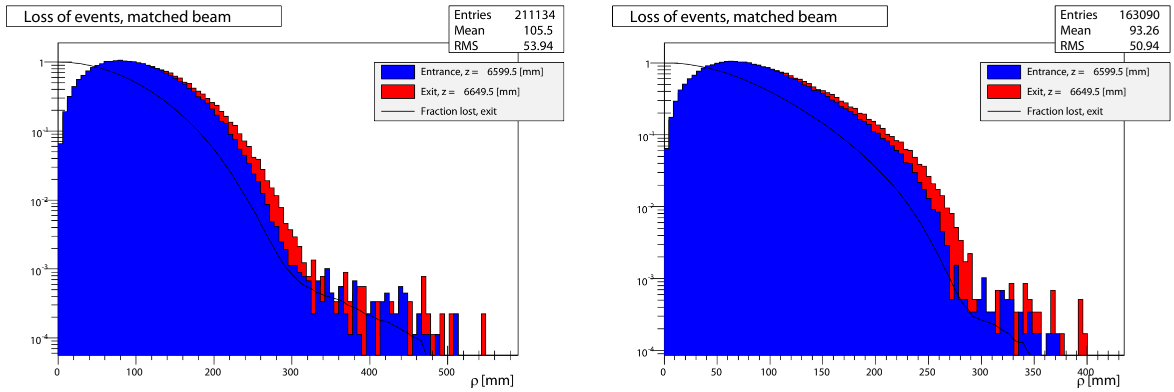

(a) 140 MeV/c (b) 200 MeV/c

Fig. 10.6: Radial position at the entrance and exit of the second iron shield for two matched beams. Also plotted is the fraction of the number of muon events which are lost if a cut is made at a certain radius.

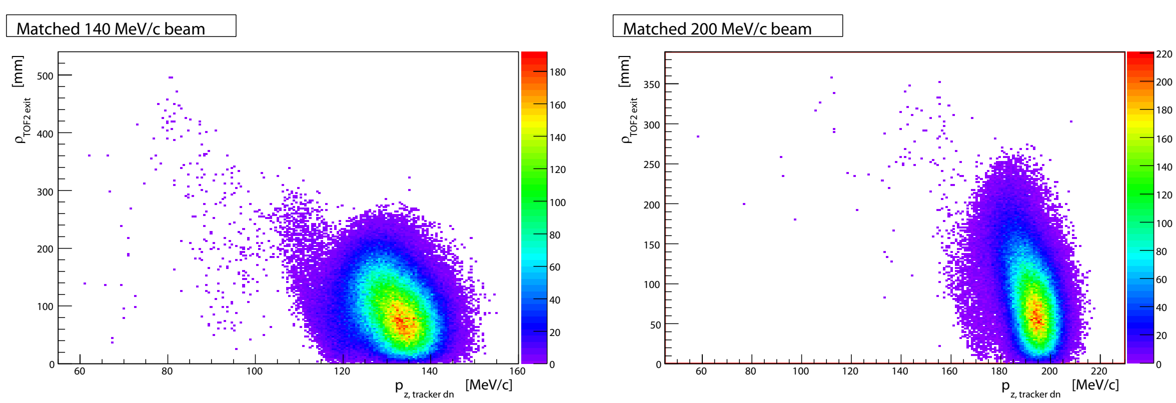

(a) 140 MeV/c (b) 200 MeV/c

Fig. 10.7: Radial position at the exit of TOF2 as a function of the longitudinal momentum in the downstream spectrometer for two matched beams.

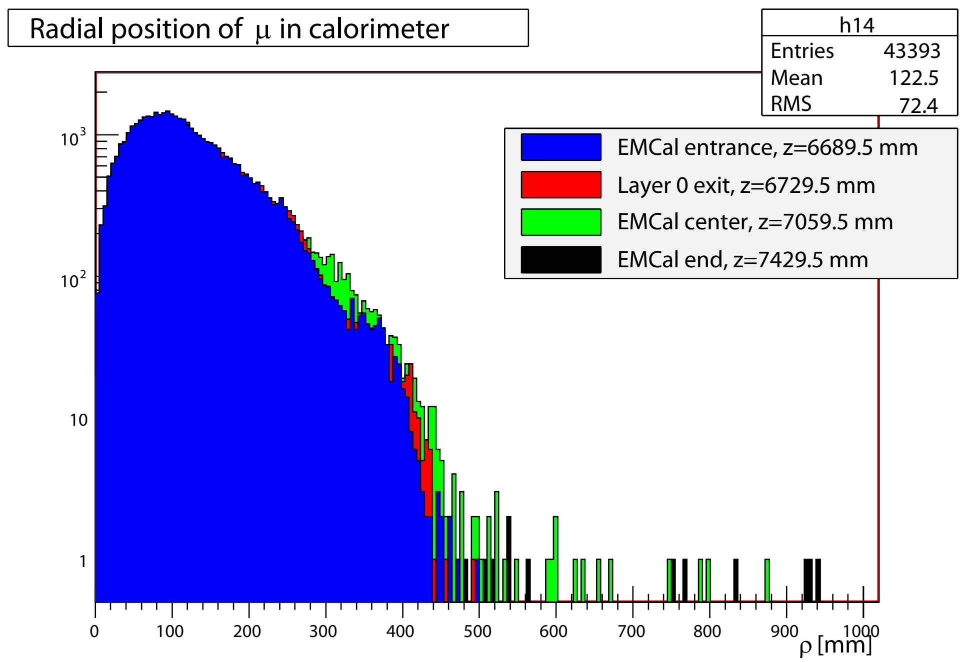

Fig. 10.8: Radial positions at various depths of the calorimeter. Since the iron shields were not physically present in this study, it is likely that muons at very large ρ will be scraped before reaching the calorimeter.

results shown in the figures one can pose the question whether muons in these tails really should be considered good events. If not this would relax the requirements on the sizes of the volumes in the TOF region, since most of the extreme radius events were found in this tail.

10.3 Calorimeter

For the calorimeter the situation was less critical since the active area was already of a realistic size. Originally the size was 120 by 120 cm, but at an early stage it was reduced to 100 by 100 cm. The same full phase space beam as was used in the previous sections was used to evaluate the radial positions at

- the entrance of layer 0
- the boundary between layer 0 and layer 1
- the longitudinal center of the calorimeter
- the exit of layer 10

and the results are shown in figure 10.8.

Since the size of the calorimeter was finite, a muon exiting the one by one meter volume (or missing it completely) would not have its range limited by energy loss other than the minuscule energy loss in air, hence such particles could give a radius much larger than if the calorimeter's transverse size in the simulation was infinite. However, considering the radii of these rare events, it is highly probable that such muons would be first scraped in the iron shields.

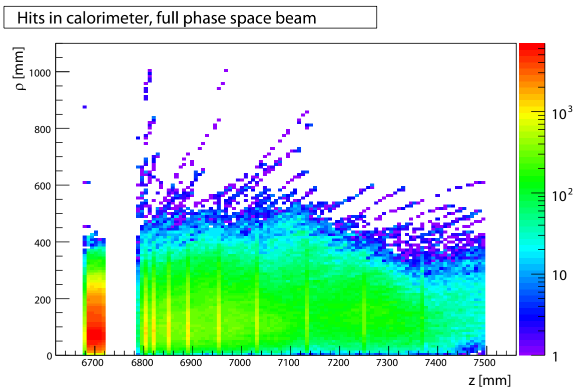

(a) Split

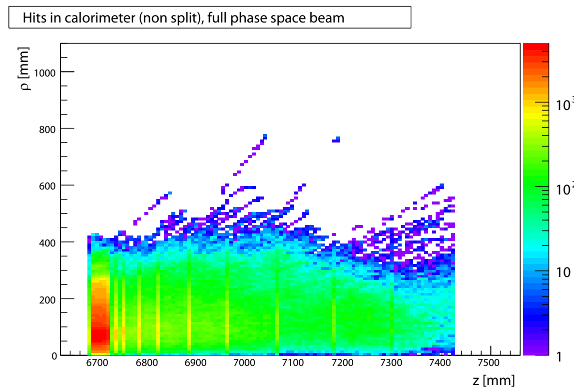

(b) Non split

Fig. 10.9: Plots of spatial positions of muon hits in the calorimeter for split and non-split designs respectively. The beam is the full phase space beam described in section 10.1. The same phenomenon appears using a realistic beam. When a muon traverses a physical boundary, it is forced to take a new step in Geant4, which is why the layer boundaries appear as hot spots.

It was suggested that the calorimeter should be split since an air gap between the preshower layer and the plastic scintillator layers would allow the photomultiplier tubes of the preshower layer to be protected in an analogous way as to those of TOF2. As figures 10.9(a) and 10.9(b) show, however, this would imply that the transverse size of the calorimeter would have to be expanded, which was judged by the detector group not to be in the best interest of the experiment.

10.4 Scraping and emittance

Since particles at large distance from the beam axis normally have a larger single particle emittance, scraping these high amplitude tracks will lead to a bias on the emittance measurement. Since the scraping effectively truncates one of the extremes in the single particle emittance distribution, the bias is more severe than if uniformly distributed particles are lost.

The emittances for the two matched beams were determined in x and y directions at the exit of TOF2, according to the low field approximation in two dimensions

$$\epsilon_x = \frac{1}{m}\sqrt{\sigma_x^2\sigma_{p_x}^2 - \sigma_{xp_x}^2} \tag{10.2}$$

Tab. 10.1: The systematic errors resulting from making a cut on a particular radius ρ at the exit of TOF2. The beams should be symmetrical in x and y; the asymmetry gives a hint on the statistical errors in the study.

p_z	ϵ_x $[\pi mm]$	ϵ_y $[\pi mm]$	ρ $[cm]$	$\Delta\epsilon_x/\epsilon_x$	$\Delta\epsilon_y/\epsilon_y$
140 MeV/c	6.596	6.618	42	$-0.70 \cdot 10^{-3}$	$-0.80 \cdot 10^{-3}$
200 MeV/c	6.923	6.955	30	$-0.63 \cdot 10^{-3}$	$-0.80 \cdot 10^{-3}$

and cuts on the radii were imposed to find the smallest radii where the systematic errors were less than one per mil, in compliance with the MICE design requirements[4]. See table 10.1. This systematic errors were found approximately where the fraction of events lost was no greater than 10^{-4}, an order of magnitude less than the bias itself.

For the cooling measurement, however, the situation is somewhat different. Assuming that the true single particle emittance downstream is identical to the single particle emittance upstream, i.e., no cooling, there is no bias on the cooling measurement even though the emittance measurement is strongly biased by scraping. In another scenario the single particle emittance evolves from a small variance to a large variance, all the while keeping the mean constant. Nor in this case is there any cooling effect, but if the high amplitude particles are scraped, the measured mean single particle emittance will be lower than the true value, and hence there would be an apparent cooling in the apparatus while in reality there is none. Exactly how scraping affects the cooling measurement depends on the magnetic field, the beam and other free parameters and the cooling bias due to scraping is not easily foreseen. A close eye should be kept on this problem.

10.5 Conclusions and decisions

One of the important conclusions from the studies made in this chapter was that the beam envelope at the downstream detectors depends on the longitudinal momentum. Originally the size of TOF2 was meant to be 48 by 48 cm, but at $\rho = 25$ cm one starts losing events below 225 MeV/c. At 30 cm tracks with momentum up to 169 MeV/c are lost and at 35 cm the corresponding threshold is 129 MeV/c. This in addition to the minimum TOF2 radius of 42 cm for the lowest momentum beam in order to stay within emittance bias design specifications, forced a decision to increase the size of TOF2 and associated iron shields.

The matched beams that were studied were both elliptical with tails toward large radius and low momentum. Should the tails be ignored, the radius of TOF2 could be made smaller. This reasoning led to a decision to make the TOF2 60 by 60 cm (full width), the inner radius of the thick iron shield 30 cm and the hole in the thin shield 35 cm. The design was implemented in G4MICE by the author as can be seen in figure 10.10. Practical considerations led to a full width of 92.4 cm for the preshower layer of the calorimeter.

[4] However the detector area is square, so some events are regained by hitting the corners of the detector.

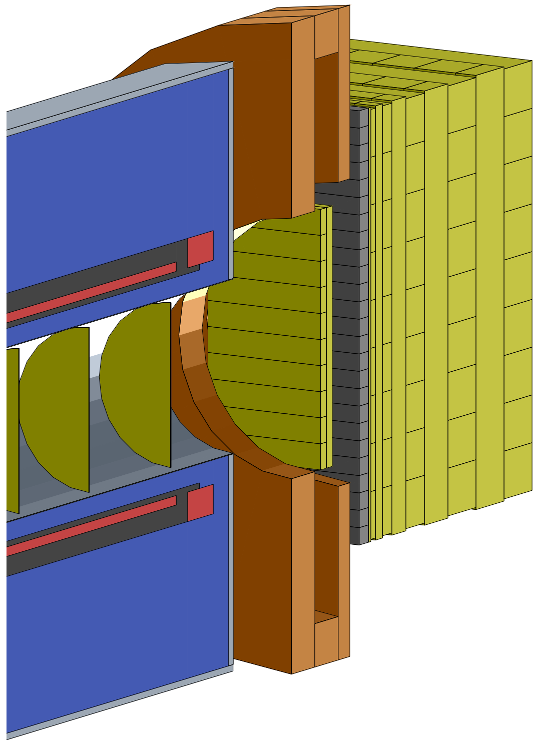

Fig. 10.10: A picture of the downstream region generated in G4MICE, showing a cut view of the iron shield (orange) with the neighboring SciFi, TOF2 and EMCal detectors.

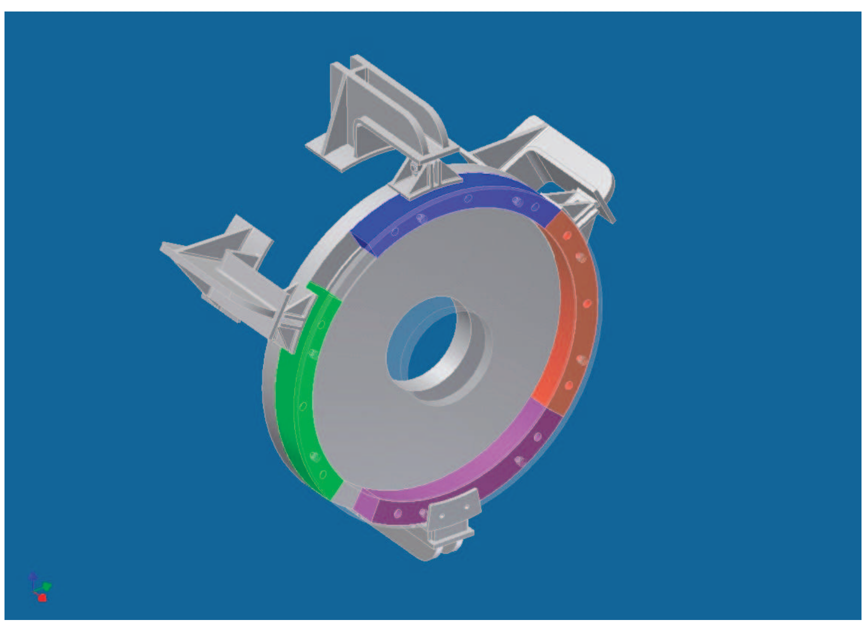

Fig. 10.11: A technical drawing of the iron shield, from the MICE Design Office [56].

11. OUTLOOK: CALORIMETER CONSTRUCTION

Prototype cells for the calorimeter have been built according to the Sandwich design (see section 8.4) and tested in a test beam in 2006. This chapter presents the test beam results and how the calorimeter will evolve from the prototype to a finalized detector in the MICE beamline.

11.1 The BTF test beam

In Summer 2006 a test beam was performed at the BTF at Frascati, Italy, with the objective of testing the electronics and data acquisition developed for use in the MICE experiment. In addition it was a good opportunity to test TOF and calorimeter prototypes. Unfortunately the BTF can only supply electron beams, which limited the usefulness for the electron–muon separation studies presented in this thesis. A series of runs was performed over ten days with a multitude of hardware configurations, and narrow band electron energies of 75, 100, 150, 200, 250, 300 and 350 MeV.

11.1.1 Time of flight prototypes

Three bars of plastic scintillator with the dimensions identical with those of a fully assembled TOF0 were placed in an upstream position. The bars were 45 cm wide, 4 cm high and 2.5 cm thick, and they were separated by 10 and 5 cm respectively, center to center. Different scintillating material were tested, and BC-404 and BC-420 gave resolutions of 46 ps, which meets the MICE design specifications. BC-408 performed worse, with a resolution of approximately 60 ps. The time resolution was noticeably worse for particles hitting the outer edges than for particles hitting in the center between the photo multiplier tubes. This effect is not fully understood and requires further investigation [98].

11.1.2 EMCal layer 0 prototypes

After the TOF bars, there were two modules of the MICE calorimeter layer 0. The second module could be elevated out of the beamline using rails. Each module consisted of three 92.4 cm wide, 4.4 cm high and 4 cm thick cells of the KLOE-light lead and fiber configuration.

The energy was reconstructed using (9.16) and multiplied by an additional factor 2, but since the number of electrons in the 10 ns beam spill is Poisson distributed, cuts had to be performed to select single particle events. The ADC distributions given by the time

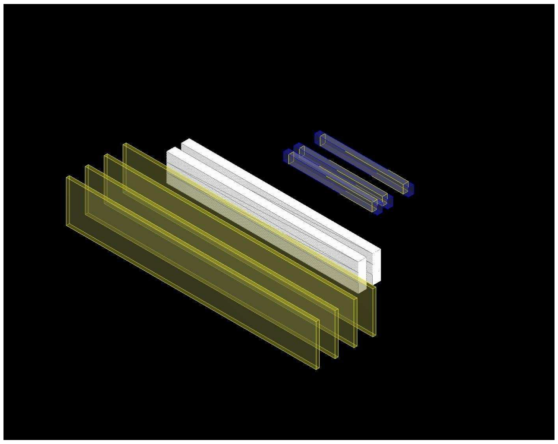

(a) BTF setup

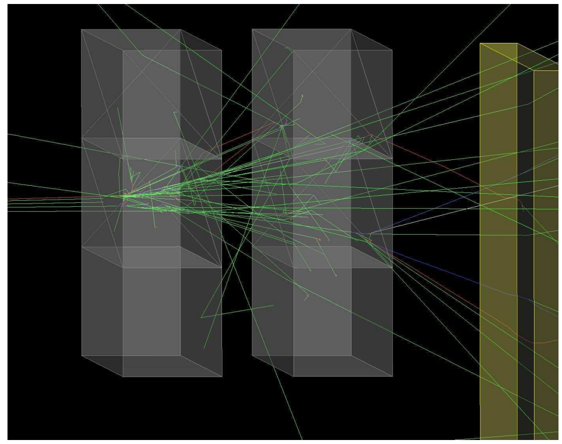

(b) Electron event

Fig. 11.1: The Frascati test beam simulated in G4MICE. (a) The experimental setup. The beam is coming from the upper right corner. (b) An electron hitting the calorimeter prototype, inducing an electromagnetic shower.

of flight modules contained two peaks, corresponding to single or double electron events, and by making a narrow cut around the first peak the single particle signal was cleaned up considerably. Further improvements were made by rejecting events which suffered from overflow in the TDC information of the calorimeter modules, and by rejecting events which were not fully contained in the calorimeter. By looking at the runs when no time of flight modules were placed in front of the calorimeter, it was concluded that the average energy loss in the time of flight modules was 21 MeV, which was subtracted from runs when they were present. The data for the 100 MeV beam gave a relative energy resolution of 23% [99], equivalent to 7.2% at 1 GeV. This should be interpreted as an upper limit due to the additional energy straggling in the preceding TOF layers. The energy resolution corresponds reasonably well with the expected values derived from KLOE data (5% at 1 GeV, according to (8.5)).

Analysis of the test beam data showed that the good linearity between reconstructed and beam energy at low energies worsened at higher energies due to poor shower containment. As figure 11.2 shows, the deviation from linearity occurs around 150 MeV and worsens with increased energy. This should be compared with (8.10), which states that the shower maximum occurs at the back of the preshower layer for electrons at approximately 145 MeV. Hence the G4MICE simulation is in agreement with the experimental data.

In addition, a simulation was performed by Pietro Chimenti using the G4MICE configuration the author of this thesis had prepared for the test beam. However, the digitization was not used and the simulation results thus assumed no smearing due to electronics response. The simulation reproduced the deviation from linearity, and the limited energy resolution of the preshower was concluded to be insufficient for particle identification. In agreement with the work presented in chapter 8, one preshower layer was deemed better than two layers with respect to particle identification [101].

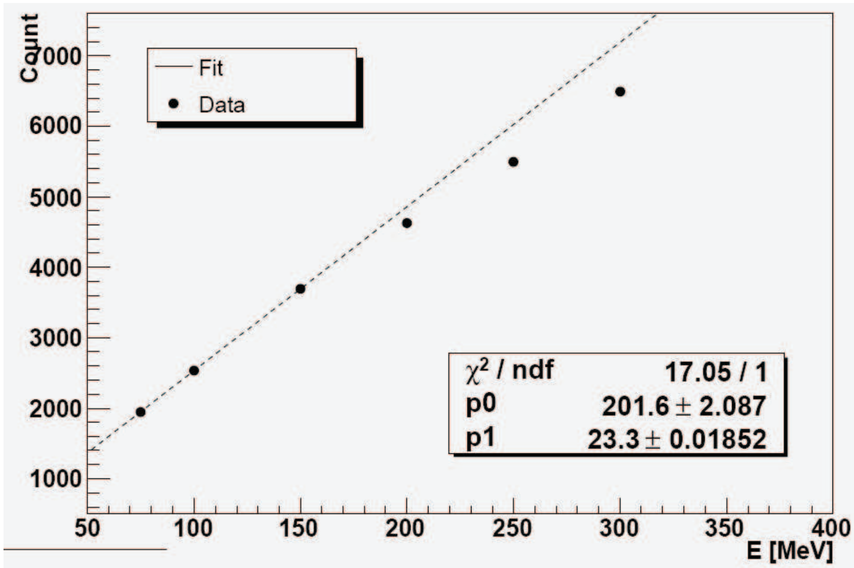

Fig. 11.2: The linearity of the preshower layer [100]. The figure shows the ADC counts measured in the BTF test beam as a function of the electron energy. The straight line is a fit through the low energy points. At $E \gtrsim 150$ MeV the reconstructed energy deviates from the linear dependence due to poor shower containment.

11.1.3 EMCal layers 1-10 prototypes

There were four bars of plastic scintillator placed at the most downstream end, each 160 cm wide, 20 cm high and 1.5 cm thick, which were on loan from the ATLAS experiment. In addition a number of extruded scintillators from Fermilab, 120 cm wide, 7.6 cm high and 4.5 cm thick, were tested. Due to the presence of TOF and preshower modules in front of the plastic scintillators firm conclusions regarding the energy resolution of the different alternatives could not be drawn, but the extruded scintillator alternative appeared a viable and affordable choice.

11.2 The calorimeter assembly

The calorimeter uses the Sandwich design, consisting of a lead–fiber preshower layer followed by a fully active plastic scintillator region, in accordance with the studies performed by the author (chapter 8). The design being manufactured is very similar to the design used in the simulations.

11.2.1 Layer 0

The preshower layer uses the same 0.3 mm grooved lead foils and 1 mm diameter fibers as was used in the simulations. It is separated into 132 mm high modules read out by three photo multipliers per side, thus corresponding to cell heights of 44 mm, whereas the simulation used 40 mm high cells arranged in modules of ten cells per module. However the more important longitudinal thickness, 40 mm, is identical for both the final design and the simulations. The preshower layer consists of seven such modules, hence the active area is square with dimensions $\approx 92.4 \times 92.4$ cm. As shown in chapter 10 this is enough to cover almost all good muons.

Since each cell is read out on both sides, 42 photo multipliers are needed, which have been recovered from the HARP experiment. Two CAEN TDC V1290 modules (64 channels) and eighteen CAEN ADC V1724 modules (144 channels) have already been purchased, but more are likely to be needed.

11.2.2 Layers 1 to 10

The subsequent layers are made of plastic scintillator as in the proposed design. Due to financial considerations however, extruded scintillators with wave length shifting fibers will be used. This changes some of the assumed parameters used in the simulation and digitization of the calorimeter, which should hence be measured and adjusted accordingly before any new simulation study is launched.

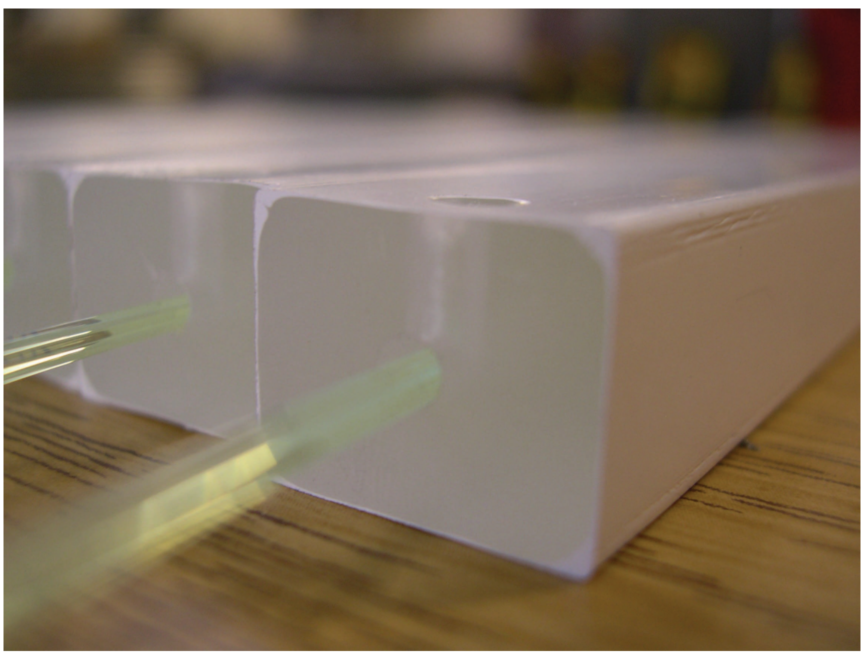

Fig. 11.3: The extruded scintillator used in the calorimeter, with glued wavelength shifting fiber. The bar is 15 mm thick along the beam axis, and 19 mm wide.

The longitudinal segmentation presented in chapter 8 is being used as a baseline, but consideration of practical implications of the extrusion process must be taken into account when finalizing the thicknesses of the layers. It has been suggested to group the horizontal and vertical layers in pairs, and use a fixed thickness of the layers for both directions in such a pair of layers. Layers of variable thickness are constructed by ganging rows of

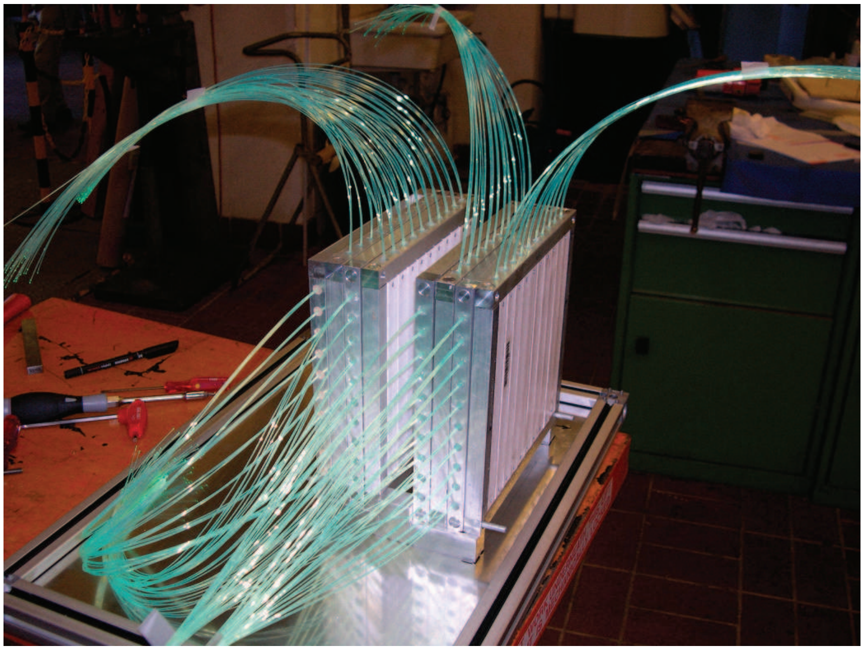

Fig. 11.4: Eight prototype calorimeter modules with extruded scintillators, fibers and casing. Each plane is made of ten bars and covers an active area of 19×19 cm. The fibers are extracted through holes in the aluminum casing and connected to the electronic read out.

the fibers of several extruded scintillator bars with each other at the readout. Each row of scintillator bars is held together by an aluminum frame, thus forming a module. The module is 15 mm thick, but the contact of two neighboring frames adds 0.5 mm of dead space between each module which will be filled with plastic sheets (passive). The default ganging of modules uses 2×1, 2×2, 2×5, 2×8, 2×9 modules [102], thus forming ten layers in total[1]. The total thickness of these ten layers thus obtained is 50 modules, or 775 mm (of which 750 mm is active).

Each extruded scintillator bar is 19 mm wide, and each module is made of 52 bars [102]. This means that the modules have 988×988 mm active area transversally, and the weight of each module including the frame is expected to be between 15 and 20 kg. The total weight of all ten layers is hence between 750 and 1000 kg, which can easily be supported by conventional stands.

Furthermore, for cost reasons, the transversal segmentation should be optimized in order to keep the number of channels to a minimum. Since the transverse segmentation is not vital for the particle identification algorithm, but of importance for pile up effects, the author has suggested that the size of each bar should be related to the expected hit rate. This would hence make the segmentation finer in the center of the calorimeter and more coarse toward the edges of the fiducial volume. Since the fibers of the preshower layer can be arbitrarily grouped before connection to the photo multipliers, its segmentation and

[1] This is identical to the number of layers used in the simulations presented in chapters 8 and 9, but with a few centimeters extra total thickness and slightly different thickness of individual layers.

channel usage could also be considered in the overall picture. However it would make the calorimeter reconstruction more complicated.

Before any final decision is made, simulation studies should be performed to validate the design with respect to cost and particle identification performance. Since this would require a pileup study, G4MICE should introduce a spill generator, with events distributed according to the micro structure of the beam.

11.2.3 Front end electronics

The choice of front end electronics has yet to be made, but three options have been suggested [102]:

1. Photonics PMTs from Geneva University, equipped with FADCs.
2. Hamamatsu PMTs from Trieste with threshold mode electronics.
3. The same Hamamatsu PMTs as above, but with ADCs.

The second option would be the cheapest but it is unclear whether the performance would be sufficient to meet the experimental requirements. Furthermore, INFN has 80 FADCs that might be possible to use for the calorimeter without additional cost to MICE. To reach a decision, a study has been launched using G4MICE with the objective of determining the number of channels needed, the lateral segmentation of the layers and will evaluate the performance of the suggested threshold mode electronics.

11.3 Time schedule

For MICE Stage 1, TOF0 and TOF1 must be installed in order to operate the experiment, while the schedule for the larger TOF2 is less pressing. Since the experimental objective at this stage is to understand the beamline, measuring the beam content with respect to muons and pions is desired. Since the momentum is unknown, the calorimeter must be installed to work in conjunction with the Čerenkov and the time of flight measurement.

The MICE experiment was scheduled to shoot its first beam September 15, 2007, and the full calorimeter was not expected to be constructed and installed on time. The full preshower layer and a number of extruded scintillator bars were not foreseen to be finished on schedule. However a recent delay to the experiment might imply that the calorimeter along with the other detectors which are part of MICE Stage 1 can be installed and calibrated taking cosmic ray data before the first muon beam arrives.

CONCLUSIONS AND SUMMARY

The first chapter was a short summary of the history of neutrino physics, and was written for the general public. It showed how our understanding of the neutrinos has evolved from Pauli's hypothetical ghost particle, which cannot be detected, to the vampire particle, which does not have a mirror image, to the present notion of the neutrinos. The discovery of neutrino mixing and the subsequent conclusion that the neutrinos have masses has fundamentally altered our view of the neutral leptons, and forced particle physicists to extend their theories beyond the Standard Model.

The second chapter started off where the historical introduction ended. This chapter was intended for a reader rather immersed in the field, and reviewed more in detail the evidence of the neutrino mass, and the implications thereof. If the neutrinos have mass, according to our understanding of particles and forces, there must be right handed neutrinos in addition to the observed left handed neutrinos. In the simpleminded extension of the Standard Model these right handed neutrinos should have the same mass as their left handed counterparts. However since no right handed neutrinos have ever been observed, there is obviously something wrong with the Standard Model.

A popular way of explaining the apparent paradox is to assume that the right handed neutrinos have very large mass, too large for detection through conventional experiments. In what is known as the See-Saw model, the extremely light left handed neutrinos are light as a natural consequence of the heavy mass of the right handed neutrinos. For this theory to work, the neutrinos must be Majorana neutrinos, meaning that a neutrino is its own antiparticle. The only known possibility to experimentally determine the Majorana nature of the neutrinos is through neutrinoless double beta decay experiments, where the simultaneous decay of two nuclei are coupled through a Majorana neutrino, thus giving a discrete energy spectrum of the final state electrons. However due to the rare nature of the process, these types of experiments are plagued by significant backgrounds and experimental uncertainties. Assuming that there is a symmetry between leptons and quarks, the neutrino deviation from the "natural" mass scale leads to a predicted mass of the right handed neutrinos which is very close to the Grand Unified Theory energy. Thus neutrino experiments could be an indirect way of exploring the GUT scale experimentally.

Another feature of the neutrino mixing is the possibility of leptonic $\mathcal{CP}$ violation. Since the tiny mass of the neutrino comes into the equations for $\mathcal{CP}$ violation using charged leptons, it can, in practice, only be observed through neutrino oscillations. Leptonic $\mathcal{CP}$ violation is the primary candidate for the observed matter–antimatter asymmetry observed in the Universe, through the so called Leptogenesis. The principle idea is that shortly after the Big Bang the Universe cooled below the GUT energy and produced heavy right handed

Majorana neutrinos, which through leptonic $\mathcal{CP}$ violation created a $\mathcal{CP}$ asymmetry as the neutrinos decayed into lighter particles such as Higgs bosons.

At the end of the second chapter, some theories of neutrino masses and the connection to the Grand Unification Theories were discussed. While the minimal super symmetric extension to the Standard Model is ruled out as a GUT candidate theory due to the presence of neutrino masses and the non-observation of proton decays, SO(10) is still a possibility. An introduction to left right symmetric models with the associated baryon-lepton number conservation is presented as an explanation for the leptonic parity violation, with the predicted appearance of right handed weakly interacting bosons at higher energies. The author presents limits on the masses of these new bosons, with the conclusion that their masses might be within reach of a future collider experiment.

The third chapter presented experiments which, using the processes in chapter five, could solve many of the ambiguities and questions presented in chapter two. Conventional neutrino beams produce neutrinos from pions which in turn are produced in proton interactions with a target. In addition to the desired ν_μ, the beam is irreducibly contaminated with other neutrino flavors and their antiparticles. The highperforming conventional neutrino beam experiment T2K is presented, featuring the off axis near detector ND280. Running off axis by a few degrees makes the energy spread of the neutrinos more narrow, and thus "wrong flavor" neutrinos can more easily be identified and ruled out as background to neutrino oscillation. Should the size of the neutrino mixing angle θ_{13} be large, T2K and NOνA will have the ability to measure it in the immediate future, thus directing the path experimental neutrino physics shall take in the future.

A natural improvement to the conventional neutrino beams is to raise the flux of neutrinos by using high power proton drivers. This type of neutrino beam is called a Super beam, and negates the effect of the reduced neutrino flux with offaxis configurations. Its largest advantage is its improved sensitivity to charge parity violation, but the intrinsic neutrino impurities can never fully be eliminated, thus limiting the usefulness of Super beam experiments.

A second conceptual neutrino beam produces low energy ($\lesssim 1$ GeV) neutrinos from decaying radioactive ions stored in large storage rings with straight sections. This is called a Beta beam, and has the advantage over other neutrino beams in that it has a single, pure, neutrino flavor. This allows detection of neutrino oscillations through the so called golden channel, which is the oscillation $\nu_e \to \nu_\mu$. The detection of a muon in the far detector is simple, and the absence of $\bar{\nu}_\mu$ in the beam means that the detector does not have to be magnetized. This allows the use of megaton Water Čerenkov detectors, which by now are a standard technique for neutrino detection. Such a facility however, cannot be used for detection of $\nu_e \to \nu_\tau$, and is of too low energy to be sensitive to matter effects, limiting its ability to solve degeneracies in the (θ_{13}, δ) plane.

The third candidate neutrino beam concept is the Neutrino Factory, which similarly to the Beta beam uses unstable particles stored in a storage ring for producing a neutrino beam, but instead of ions the Neutrino Factory uses muons. The muons are produced in proton collisions with a mercury jet target, and the pions produced are magnetically collected and drifted through a decay channel, where the muons are produced. The muons have at this stage a very large emittance, which hinders efficient subsequent acceleration. The muon beam is therefore transversally cooled via ionization cooling, using a cooling channel consisting of alternating RF cavities and low Z absorbers. After cooling the muons are accelerated in the subsequent RLA, recirculating linear accelerator, and FFAG, Fixed Field Alternating Gradient accelerator. A novel idea for cooling relies on a helical cooling magnet, which relies on the nonlinearities of the magnetic field effects instead of the stochastic energy loss to break the emittance conservation.

While the most likely detectors for Super beams and Beta beams are huge Water Čerenkov detectors, the Neutrino Factory does not come to its full advantage without a magnetic field due to the intrinsic contamination of charge parity conjugate neutrinos in the beam, which could obscure the neutrino oscillations. One proposed detector for a Neutrino Factory is the Magnetized Iron Neutrino Detector (MIND), which is a sandwich of extruded plastic scintillators and magnetized iron to both provide the necessary target mass and magnetic field of the detector. A similar design is the Totally Active Scintillator Detector (TASD), which does not contain any iron in the fiducial volume but relies on novel techniques for applying an external field to the very large active region. The main advantage of TASD over MIND is that it could also measure the charge of electrons. It is possible that the two designs might reach a consensus and merge their designs in the future, conceivably forming a hybrid detector also incorporating magnetized emulsion cloud chambers for tau lepton tagging.

Another suggested neutrino detector is a huge liquid argon time projection chamber (LArTPC), with a fiducial mass somewhere between 10 and 100 kiloton. Such a device would be sensitive to both $\nu_e \to \nu_\mu$ and $\nu_e \to \nu_\tau$ oscillations, with a low energy threshold comparable to TASD. If the magnetic field is at least one tesla, charge determination of electrons would be possible, thus opening up the $\nu_\mu \to \nu_e$ oscillation channel. The feasibility of the magnetization of the device is however not clear, and the drift length of several meters that the scale of the detector implies could cause serious problems. Since a LArTPC is sensitive to cosmic ray background it cannot operate on the surface but would have to be placed approximately 200 meters underground to have a physics reach comparable with SuperKamiokande, but it does not require the great depths of the Čerenkov detectors.

The chapter ended with a performance comparison of the different neutrino facilities. Should θ_{13} be small, the best facility is always the Neutrino Factory. For larger values of θ_{13} the possibility of using a Beta beam facility opens up, and for even larger values Super beams would have the same sensitivities to charge parity violations and neutrino mass hierarchies as the Neutrino Factories and the Beta beams. If θ_{13} is zero, a Neutrino Factory would thus give the best upper constraints, though very few theories predicts the mixing angle to be zero and that scenario is deemed unlikely.

In order to demonstrate the principle of ionization cooling in practice, the Muon Ionization Cooling Experiment, MICE, is being built at Rutherford Appleton Laboratories in the United Kingdom. Chapter four was an introduction to MICE, while the following chapters of this thesis dealt with specific details of the experiment. The experiment will measure the emittance reduction of a muon beam, using one particle at the time going through a section of a Neutrino Factory cooling channel. The MICE beam produces muons from pions that are momentum selected in a bending magnet and then decay in a solenoid. Muons of approximately 200 MeV/c are selected with a second magnetic bend. The pions themselves are produced by dipping a titanium target into the halo of the ISIS proton beam. The aim is to produce roughly 600 good muon events per ISIS spill.

The beam contains mainly muons with a very small contamination of pions which survived the momentum selection bend. In order to identify these pions, two time of flight detectors, TOF0 and TOF1, are positioned in the beamline. Together with a Čerenkov detector, they can clearly separate pions and muons. The Čerenkov detector uses two aerogels with different refraction index to span the momentum region used in MICE.

Since the experiment will examine the emittance reduction at different initial emittances, a lead diffuser is placed in the beamline. After the diffuser a spectrometer is installed in a four tesla homogeneous field. The base line tracker consists of five planes of scintillating fibers, which provides fine resolution measurements of momentum and position of the muon tracks. An alternative tracker design, with less material in the path of the muons, is based on the time projection principle, using high voltage to drift ionization electrons to a region where the signal is amplified using GEMs and read out by FADCs.

Downstream of the spectrometer the cooling channel begins, which consists of three liquid hydrogen absorbers, interspaced by two linear accelerators consisting of four 201.25 MHz cavities each. The transverse emittance is reduced by stochastic energy loss in the liquid hydrogen through ionization, while the RF cavities replace the lost momentum in the longitudinal direction. A full Neutrino Factory cooling channel would consist of a large number of such cooling sections, but one section is deemed adequate for demonstration of the ionization cooling principle, as the obtained cooling for a minimum ionizing muon will be 10%, which the experiment will measure to a relative precision of 1%, i.e., $(10 \pm 0.1)\%$. The cooling section is initiated and terminated by hydrogen absorbers to prevent electrons from RF induced background to flood the spectrometers. The absorbers are bellow shaped with very thin aluminum windows which provides maximum strength with minimum material in the beamline. An extra set of windows encases the absorbers to ensure vacuum integrity and an extra degree of safety to hydrogen leakage.

After the cooling channel, another solenoid with spectrometer, identical to the upstream spectrometer is placed. This allows the transverse emittance to be measured both upstream and downstream of the cooling channel. In addition a third time of flight detector, TOF2, is placed downstream of the second spectrometer, giving the experiment the ability to measure the time coordinate of each particle, thus longitudinal cooling. The combination of TOF1 and TOF2 information will also be used for estimating the RF phases of the traversing particles, and will be used together with the measured momentum to reject electron contamination in the beam.

At the very end of the experiment the muons are stopped in a calorimeter. The first layer of the calorimeter is four centimeters thick and consists of grooved lead foils and scintillating fibers while the following layers are made of plastic scintillators of a total longitudinal thickness of seventy centimeters. The calorimeter is dedicated to electron–muon separation, but is also useful for pion identification and can provide an independent measurement of the muon momentum by range and energy by amplitude.

The fifth chapter contained descriptions of the most important processes and interactions for the detection and classification methods of the particles of interest for this thesis. Since it is impossible to encompass the full extent of phenomena associated with the processes, due to the complexities introduced by atomic shell structure at low energy et cetera, the focus is on general behavior in the energy range given by the MICE experimental specifications, and on how the models are implemented in Geant4, the main software package used for simulation studies in later chapters.

The section on muon decay kinematics motivated why muons and electrons originating from muon decay fill the same phase space in MICE's operational momenta, and hence why there is a need to identifying individual particles in the beam. At these momenta the main contributing process to the energy loss for muons is ionization, and the differences and similarities between ionization of muons and electrons are explained. As bremsstrahlung is of major importance to the study of RF cavity induced photonic backgrounds, this process and its associated simulation implementation of the model were also presented. Another process whose importance to MICE cannot be overstated is multiple scattering, since the heating term in the ionization cooling mechanism depends directly on multiple scattering and its associated effects. The theoretical models describing the multiple scattering have evolved in recent years, and this is reflected in the evolution of the Geant4 implementation. The MuScat experiment has provided vital data for multiple scattering of muons in liquid hydrogen, and from comparison of its data with simulations it was concluded that any version of Geant older than 4.8.1 does not perform satisfactory at large scattering angles.

The last process discussed in this chapter was electromagnetic showers, which is a potpourri of all of the above mentioned processes. It is normally triggered by hard bremsstrahlung of an electron incident on a dense material, and subsequent interactions create a tree of electrons, positrons and photons. Since the cross section for photons is lower than the cross section of electrons, the photon fraction of the shower rises with longitudinal depth. As the muons have too low energy in MICE to induce electromagnetic showers, this principle is used in the design of the calorimeter to break up electron tracks, before the fully active part of the calorimeter samples the energy of the muons. Since this latter material is transparent to photons, the longitudinal profiles of incident electrons and muons look very different, even though the particles have similar energies.

In order to study various issues in MICE, a software package called G4MICE has been developed, which was described in chapter six. G4MICE has simulation capabilities using the standard particle physics simulation package Geant4. In addition the Digitization application simulates the response of the read out electronics and the conversion of the Geant4 output to data of the same format as the actual experiment will obtain. Another application in G4MICE is the reconstruction of tracks and events which has been successfully used in the tracker test beams. Extensive analysis features are also included in the package, allowing particle identification, emittance calculations and other topics of interests to be thoroughly studied.

The seventh chapter described the three main sources of background to the MICE experiment; pions which survived the second momentum selection bend, positrons from muon decay in flight and electrons from RF induced background. The last of these three is generated when the RF cavities are operated at high fields in the presence of a magnetic field. The effect has been studied experimentally at LabG at Fermilab in the United States with a small 805 MHz cavity. It is presently being studied in the Fermilab MuCool Test Area using a prototype MICE RF cavity. In the near future it will also be tested with a coil providing a field strength which closely resembles the MICE running conditions. Effects of conditioning, polishing and titanium coatings will be studied as possible measures to reduce the emission of electrons.

Simulation studies performed by the author are presented which showed that all electrons are stopped in the liquid hydrogen. However the electrons have a small probability to create photons through bremsstrahlung, and due to the large number of RF induced electrons involved, this forms a substantial background of gamma rays for the spectrometers and time of flight detectors. This background can cause hits or convert back to free electrons through the photoelectric effect or Compton scattering. Due to the energy spectrum of bremsstrahlung photons and the limited length of the linacs, the energy of the RF background is much lower than the muons, which aids in its rejection.

The phasing of the RF cavities infers that the highest energies and highest background rates will be in the downstream direction. Using the spectrum given by the simulations, the scintillating fiber tracker has shown that it can satisfactory deal with the RF induced background, but it has more problems for events in the downstream direction since the particles are travelling parallel to the muon tracks, and it is unknown how the spectrometer can cope with the higher rates given by new MTA measurements.

A model for the emission of electrons and production of photons was presented. It successfully reproduces the very strong dependence on electric field gradient that has been observed in many experiments. At moderate gradients, the number of photons in the detector per electron emitted from the cavities increases fast with increased electric field gradient. At higher gradients, the creation of new emitting sites through breakdown and the activation of pre-existing sites account for most of the observed gradient dependence. The model reproduces the rates measured in the MTA, and is to our knowledge the first model of its kind.

The background created by decaying muons is a serious problem since it will bias the emittance measurement beyond acceptable levels if left unchecked. Simulation studies performed by the author in chapter eight showed that the reduction of positron impurities using only the measured time of flight and momentum is not enough, and a dedicated detector is necessary to deal with the problem. Originally the task of downstream particle identification was assigned to a Čerenkov detector and a calorimeter, but the studies resulted in an improved calorimeter design which rendered the Čerenkov detector redundant.

The original calorimeter design, "KLOE-light" (KL), used four layers of four by four centimeter cells made of grooved lead foils and one millimeter diameter scintillating fibers glued in the grooves in a triangular pattern. The 120 cm long cells were read out at both ends by photomultiplier tubes for improved energy reconstruction and transverse hit point determination. The use of a high Z passive material promotes electromagnetic cascades of incident electrons and is useful for capturing photons of high energy. However a sampling calorimeter such as KL always has a significant part of its energy loss concentrated in the high Z material, and the limited sampling fraction leads to a poor energy resolution.

For MICE the energy of the muons by the time they reach the calorimeter is very low, and particle identification purely based on energy reconstruction is thus impossible. For this reason, and as an attempt to make the detector more affordable, different calorimeter designs using a fully active fiducial volume where considered. The design deemed most profitable uses an initial layer identical to the KL design, but with the following layers consisting of only plastic scintillator. Initially a second layer identical to the preshower layer was intended to be placed at the downstream end of the calorimeter, thus sandwiching the plastic in lead, in order to capture photons from electromagnetic showers generated in the first layer. However the benefit to cost ratio of this extra back end layer was considered too low, hence the last layer was removed from the design. The final design still uses the name Sandwich (SW) design for this reason. The plastic scintillator was segmented longitudinally with respect to the range resolution of the tracks, and much of the discriminating power of the device comes from the longitudinal profile of the energy deposition.

Using the same number of channels and identical electronics, the SW design was proven superior to the KL design for both $e - \mu$ and $\pi - \mu$ separation at all energies applicable to the MICE experiment. The baseline calorimeter design was thus accordingly changed to the Sandwich concept. In addition the high performance of the SW design caused the development on the downstream Čerenkov detector to be abandoned.

The ninth chapter described the methods by which the muons are separated from background events originating from muon decay. By using G4MICE simulations of a muon beam spanning all momenta of interest, relations describing the energy loss, and the change of the polar angle, through volumes between TOF1 and the calorimeter were found. These relations were used to extrapolate the track through a module in the presence of energy loss and magnetic field. Thus given the information recorded by a spectrometer, the expected energy deposition and range in the calorimeter can be computed under the assumption that the particle is a muon. This type of inter-detector variable correlations are expressed as asymmetry, where an asymmetry close to zero indicates that the event is a likely muon signal event.

Since no single particle identification variable could adequately remove sufficient background without also losing too many signal events, the problem had to be solved as a multi dimensional problem. By assigning a signal tag to all good events the signal distribution can be fitted using any conventional fitting method. Due to the multi dimensional nature and the level of nonlinearity of the problem, a naive implementation of maximum likelihood method failed. The Fisher discriminant method, however, performed much better, and the Artificial Neural Network (ANN) method performed excellently. Since Fisher is a linear discriminant and the ANN used in this thesis is a nonlinear extension to the Fisher discriminant method, the difference observed between the methods is a measure of the nonlinearity of the problem. An analysis with Boosted Decision Trees gave comparable results with the Artificial Neural Network, but the latter was chosen for its conventionality.

The performance obtained by the downstream particle identification analysis was satisfactory (safety factor 4.3, where the target impurity was 0.2%) for the lowest momentum and very good for the highest momentum (safety factor 179.1). In addition to larger beam impurities at lower momentum due to the larger decay probability, the short range in the calorimeter limits its performance. With respect to emittance measurement, the bias introduced by positrons at the tracker reference planes was around one part per mille before particle identification, the MICE experimental specification. However since a large amount of the background originates from decays inside or after the last tracker reference plane, this figure is too optimistic. If one instead looks at the emittance at the entrance of TOF2, the intrinsic bias is between three to six times higher than the maximum allowed systematic error. After the particles have been identified, however, the bias can be reduced to acceptable levels, and in the case of high momentum beams, any bias on the emittance measurement introduced by the background will be negligible in comparison with other sources of systematic errors.

To study the measurement of cooling itself, i.e., the emittance reduction measurement, a matched beam of nominal 200 MeV/c momentum was examined using the procedure outlined above. In accordance with the findings regarding the emittance measurements, the cooling was underestimated by approximately 4.5%. Thus downstream particle identification must be performed if the experiment is to achieve the design precision of the cooling measurement. The results showed that the particle identification can reduce the bias to a level (a few per mil) where the tracker imperfections clearly dominate the resolution. Regrettably there were no other suitable magnetic field maps available, so no other beam setting could be studied with a matched beam. The results used the tracker reference planes, which we already concluded give optimistic results.

As discussed in chapter ten, one implication of the extensive simulation studies performed for the MICE background problems was the observation of the transverse size of the beam at different locations along the beamline. Since the field lines diverge at the end of the experiment, muons are pulled to large radius, and many particles miss the TOF2 fiducial volume. While increasing the size of TOF2 is expensive, and putting the detector closer to the spectrometer solenoid impossible since the photomultiplier tubes cannot operate in strong magnetic fields, a hybrid solution was found by shielding the detector from magnetic field by sandwiching it with iron shields, linked together at the outer radius. The author was charged with the task to determine the size of the detector and its shield apertures in its new position. At the same time, an optimal size of the calorimeter was to be found, since it had its position shifted upstream to fill the gap where the downstream Čerenkov detector had resided. It was previously feared that the corners of the cryostat for the spectrometer solenoid would intersect the beam of good muon events, but with updated drawings and corresponding field maps, this effect vanished and no further action had to be taken.

Since a 200 MeV/c beam needed a TOF2 aperture of 30 cm radius in order to reduce the bias on the emittance measurement below one per mil, a sixty by sixty centimeter TOF2 active area was considered a reasonable choice. However for the 140 MeV/c beam setting, the required radius using the same arguments would be forced to 42 cm. However many of the large radius events were found in a tail extending towards low energy. Since the maximum obtainable radius of good muon tracks depends almost linearly on the longitudinal momentum, imposing a cut off at low momentum effectively also works as a radial cut off. From this observation it was decided that the upstream aperture in the TOF2 iron shield should be 60 cm in diameter, TOF2 should be 60×60 cm, and the downstream aperture 70 cm in diameter. The preshower layer of the calorimeter will, for practical reasons, use a 92×92 cm area which simulation results indicate is reasonable, while the baseline for the plastic scintillator layers is one meter square. A suggestion to split the preshower layer from the scintillator layers to accommodate PMT shielding similar to the TOF2 case was ruled out as it would force the size of the plastic layers to be considerably enlarged.

The last chapter is an outlook on the construction of the calorimeter, and a presentation of a test beam which was run in Frascati in 2006. The preshower layer uses the design presented in previous chapters. Extruded plastic scintillator will be used for the fully active layers of the calorimeter. Designs for the mechanical support structure and the collection of the wave length shifting fibers have been devised, and construction of the full calorimeter is proceeding.

The MICE experiment is scheduled to shoot its first beam January 2, 2008, and the full calorimeter is expected to be constructed and installed on time for Stage 3 of the experiment, when systematic errors will be examined.

At the very end of the thesis, an appendix described statistical concepts used throughout the document, such as efficiency and purity. The emittance concept is explained, and motivations for the expected time of flight through the experiment were presented. Some fitting methods used for the particle identification algorithm were introduced in the last appendix.

Final words

MICE will measure the performance of a section of a Neutrino Factory cooling channel to very high precision. This thesis has presented all major sources of systematic errors to these measurements arising from the presence of background or scraping. While each of these effects has the potential to bias the experiment, the work presented in this thesis has shown that they can all be dealt with and their effects can be reduced to acceptable levels through proper instrumentation and a well developed analysis.

Appendix A

DEFINITIONS

A.1 Statistics

Here in follows explanations of some expressions used throughout this thesis.

A.1.1 Probability density functions

A probability density function (pdf) is a function which when integrated gives the cumulative probability distribution. Thus the probability of finding a variable x in a certain interval with the probability density function $a(x)$ is

$$P(x_0 < x < x_1) = \int_{x_0}^{x_1} a(x)dx \tag{A.1}$$

where $a(x)$ is normalized such that

$$P(-\infty < x < \infty) = \int_{-\infty}^{\infty} a(x)dx = 1. \tag{A.2}$$

In practice the bin sizes dz are not infinitesimally thin and a sum over all bins is performed instead of an integration,

$$P(-\infty < x < \infty) \approx \sum_{i=0}^{N} a_i \Delta x \tag{A.3}$$

where the distribution is spread over N bins of width Δx.

Note that for convenience the notation for the p.d.f is chosen such that

$$a(x) \equiv P(X|A) \tag{A.4}$$
$$b(x) \equiv P(X|B) \tag{A.5}$$

where the right hand side is the notation used in most textbooks on statistics.

A.1.2 Likelihood

Let the observations $\mathbf{X}$ have a probability density function $p(\mathbf{X}|\mathbf{T})$, where $\mathbf{T} = (\theta_1, \theta_2)$ is some parameter. Then the likelihood function is

$$L(\mathbf{X}|\mathbf{T}) = \prod_{i=1}^{N} p(X_i|\mathbf{T}). \tag{A.6}$$

Note that the likelihood is not a p.d.f.

A.1.3 Likelihood ratio

If the set of events are such that they can only be exclusive of type A or type B, and the events always belong to one of these two sets, the individual probability distribution functions are mutually exclusive. This property can be used to define the likelihood ratio

$$r_i = \frac{L(X_i|\mathbf{T} \in \nu)}{L(X_i|\mathbf{T} \in \theta)} \tag{A.7}$$

where θ is the total $\mathbf{T}$-space and ν is a subspace of θ. Expressed as the likelihood ratio for the event to belong to A in a region of $\mathbf{X}$,

$$r(x_0 < x < x_1|\mathbf{T} \in A) = \int_{x_0}^{x_1} \frac{a(x)}{a(x) + b(x)} dx. \tag{A.8}$$

In order to make this quantity defined in regions of x where $a(x) + b(x) = 0$ the integration limits x_0 and x_1 were automatically chosen so that $a(x) + b(x)$ equaled a constant nonzero number. This gives variable bin sizes along x while the area under $a(x) + b(x)$ is fixed.

A.1.4 Separation

Given two normalized probability distribution functions $a(x)$ and $b(x)$, the separation s is a measure of the overlap of the two functions. It is defined as

$$s \equiv \int_{-\infty}^{\infty} \frac{(a(x) - b(x))^2\, dx}{a(x) + b(x)} \tag{A.9}$$

where in the case

$$\int_{-\infty}^{\infty} a(x)dx = \int_{-\infty}^{\infty} b(x)dx = 1 \tag{A.10}$$

s is equal to 0 if the two functions are identical and equal to 1 for two distributions without any overlap.

A.1.5 Correlation

Correlation indicates the strength of direct linear relationship of two variables and is the covariance of the two variables divided by the product of their standard deviations. The variance of a variable with the distribution $a(x)$ is

$$\sigma_a^2 = \int_{-\infty}^{\infty} a(x)(x-\mu)^2 dx \tag{A.11}$$

where μ is a known population mean. If the underlying distribution is not known, then the sample variance may be computed as

$$\sigma_a^2 = \sum_{i=1}^{N} \frac{(a_i - \overline{a})^2}{N} = \sum_{i=1}^{N} \frac{a_i^2}{N} - \overline{a}^2 \tag{A.12}$$

where $\overline{a}$ denotes the sample mean.

The covariance of functions a and b is

$$\sigma_{ab} = \sum_{i=1}^{N} \frac{(a_i - \overline{a})(b_i - \overline{b})}{N} = \sum_{i=1}^{N} \frac{a_i b_i}{N} - \overline{a}\overline{b} \tag{A.13}$$

and from this follows

$$\sigma_{aa} = \sigma_a^2. \tag{A.14}$$

Hence, the correlation is written as

$$\rho_{ab} = \frac{\sigma_{ab}}{\sigma_a \sigma_b} = \frac{\sigma_{ab}}{\sqrt{\sigma_{aa}\sigma_{bb}}} \tag{A.15}$$

or

$$\rho_{ab}^2 = \frac{\left(\sum (a_i - \overline{a})(b_i - \overline{b})\right)^2}{\sum (a_i - \overline{a})^2 \sum (b_i - \overline{b})^2} \tag{A.16}$$

$$= \frac{\left(\sum a_i b_i - N\overline{a}\overline{b}\right)^2}{\left(\sum a_i^2 - N\overline{a}^2\right)\left(\sum b_i^2 - N\overline{b}^2\right)} . \tag{A.17}$$

From the equations above it is clear that two uncorrelated distributions will have $\rho^2 = 0$ and two maximally correlated functions will have $\rho^2 = 1$.

A.1.6 Asymmetry

The asymmetry between the probability density functions a and b is defined as

$$d(x) \equiv \frac{a(x) - b(x)}{a(x) + b(x)} \tag{A.18}$$

and is thus an indicator of how different the two functions are at x. The asymmetry always takes a value between -1 and $+1$, with the exception where $a(x) + b(x) = 0$ where the asymmetry is undefined. Given the measured and expected response of detector B, using information from detector A, the asymmetry gives a measure of quality of the assumption that the particle in both detectors is a muon.

A.1.7 Efficiency

The efficiency of event type A is the ratio between selected A type events and total number of A type events. If the distribution of A type events on a variable x is $a(x)$, the efficiency of for the selection $x_0 < x < x_1$ is

$$\epsilon(x_0 < x < x_1) = \frac{\int_{x_0}^{x_1} a(x)dx}{\int_{-\infty}^{\infty} a(x)dx}. \tag{A.19}$$

The distribution function $a(x)$ does not have to be normalized.

A.1.8 Purity

The purity w.r.t. events of type A of a sample is the ratio of A type events and any type of event. The purity of a selection $x_0 < x < x_1$ is calculated as

$$p(x_0 < x < x_1) = \int_{x_0}^{x_1} \frac{n_a(x)}{n_a(x) + n_b(x)} dx \tag{A.20}$$

where $n_b(x)$ is the distribution of events of any type but A, and

$$n_a(x) = N_A a(x) \tag{A.21}$$
$$n_b(x) = N_B b(x) \tag{A.22}$$

where N_A and N_B are the total number of events of corresponding type in the sample. The intrinsic purity is defined as equation (A.20) with the integration limits set to plus and minus infinity.

The same integral, but with the normalized probability density functions $a(x)$ and $b(x)$, gives the probability that the event found in the selection is of type A:

$$P(x_0 < x < x_1) = \int_{x_0}^{x_1} \frac{a(x)}{a(x) + b(x)} dx. \tag{A.23}$$

A.1.9 Relations between purity and efficiency

If the signal efficiency is ϵ_s and N_s and N_b are the total number of signal and background events respectively in the sample, the required background efficiency ϵ_b in order to have a purity p is

$$\epsilon_b = 1 + \epsilon_s \frac{N_s}{N_b} \left(1 - \frac{1}{p}\right). \tag{A.24}$$

This relation is used in this note for evaluation of the particle identification algorithms used by fixing ϵ_s and p by user requirements, while N_s and N_b are taken directly from the sample.

A.2 Emittance

When designing a beamline it is desirable to minimize divergences of the beam such that as few particles as possible are lost due to scraping. If electromagnetic fields are used to control the beam, it is not possible to reduce the size of the beam without increasing the momentum spread and vice versa. In the case of Gaussian distributions of position and momentum, the phase space diagrams form ellipses of constant densities where the position and momentum are more or less correlated, thus tilting the ellipses. Emittance can be understood as the area under such an ellipse, and the conservation of emittance is due to the fact that the area of an ellipse does not change under rotation.

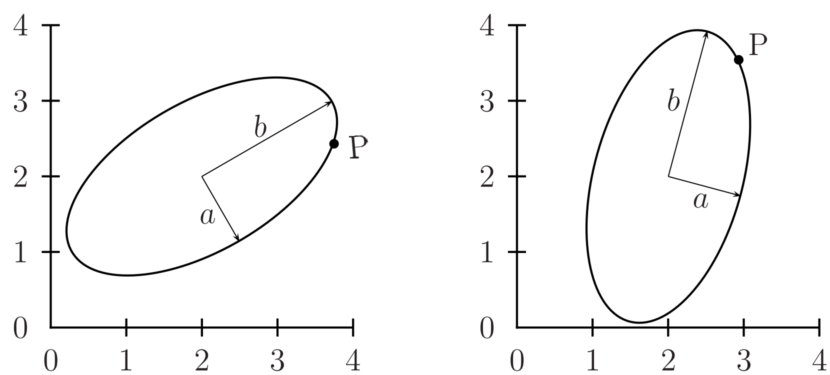

Fig. A.1: Geometrical interpretation of emittance conservation. Suppose the horizontal axis indicates the position and the vertical axis the momentum. The figure on the left is phase rotated to the figure on the right, decreasing the position spread and increasing the momentum spread. The phase rotation of the ellipse conserves the geometrical shape and hence also the area of the ellipse, which is proportional to the beam emittance. A specific particle P will rotate with the bunch, so if it was found on the boundary in the left plot it is still found on the boundary after rotation, hence single particle emittance is also conserved.

The equation for an arbitrary ellipse in the $x-p$-plane is

$$1 = \frac{x^2}{\sigma_x^2} + \frac{p^2}{\sigma_p^2} + \frac{xp}{\sigma_{xp}} \tag{A.25}$$

which using linear algebra notation can be expressed as

$$1 = \mathbf{x}^T \mathbf{V}^{-1} \mathbf{x} \tag{A.26}$$

where $\mathbf{V}$ is a covariance matrix such that $\mathbf{V}_{11} = \sigma_{xx} = \sigma_x^2$. The last step is given by (A.14). Provided that $\mathbf{V}$ is diagonalizable there exists a transformation $\mathbf{D}$ such that

$$\mathbf{V} = \mathbf{D}\hat{\mathbf{v}}\mathbf{D}^{-1} \tag{A.27}$$

where $\hat{\mathbf{v}}$ is a diagonal matrix containing the eigenvalues of $\mathbf{V}$ on the diagonal.[1] If the beam undergoes linear transformations $\mathbf{M}$,such as phase rotation, skews and stretches, $\mathbf{M}$ can be diagonalized in a similar manner, and thus the eigenvalues of n transformations $\mathbf{M}$ is just the eigenvalues of $\mathbf{M}$ to the power of n. Thus, the determinant of $\mathbf{V}$ is unchanged by the linear transformations. Since the area of the ellipse is given by

$$A = \pi\sqrt{|\mathbf{V}|} \tag{A.28}$$

the area of an ellipse is constant under any linear transformation $\mathbf{M}$. $\mathbf{M}$ is often called the *transfer map* [35]. The conservation of area under the ellipse is what makes the concept of emittance useful. In a more rigorous manner the emittance conservation can be proved using Liouvilleś Theorem, which proves that the density in a volume element is constant under a canonical transformation.

A.2.1 Beam emittance

The normalized beam emittance in N dimensions is defined as [35]

$$\epsilon^N \equiv \frac{\sqrt[N]{|\mathbf{V}|}}{m} \tag{A.29}$$

where m is the mass of the particle.[2] In this thesis, this mass is always identical to the mass of a muon. Working in natural units $c = 1$ so the mass term in the denominator cancels the momentum term in the numerator, which gives a remaining unit of length. However due to historical reasons, the emittance is usually expressed in π *mm rad*, a remnant from the geometric analogy (A.28). Whenever the term *transverse emittance* is used throughout this thesis, it is the four dimensional emittance using the dimensions (x, p_x, y, p_y) which is referred to unless the contrary is explicitly stated.

A.2.2 Single particle emittance

The single particle emittance, often called the amplitude of a particle, is defined as [35]

$$\epsilon_i \equiv \epsilon \mathbf{x}_i^T \mathbf{V}^{-1} \mathbf{x}_i \tag{A.30}$$

and describes the position in phase space of particle i, relative to a bunch of particles. The single particle emittance is a conserved quantity under linear transportation, and it forms a contour in phase space along which the particle can move.

[1] These eigenvalues are the square of the half axis of the ellipse (a and b in figure A.1).

[2] For a Gaussian beam, this definition of the emittance coincides with the hypervolume. For non-Gaussian beams, this is not generally true, and some authors prefer to define the emittance as the hypervolume thus making (A.29) invalid.

By explicitly writing out the vector indexes

$$\epsilon_i = \epsilon \sum_j^N \sum_k^N x_j^{(i)} x_k^{(i)} \mathbf{V}_{jk}^{-1} \tag{A.31}$$

where N is the number of dimensions, a relation between the mean single particle emittance and the beam emittance can be found.

$$\langle \epsilon_i \rangle = \epsilon \sum_j^N \sum_k^N \left\langle x_j^{(i)} x_k^{(i)} \right\rangle \mathbf{V}_{jk}^{-1} = \epsilon \sum_j^N \sum_k^N \mathbf{V}_{jk} \mathbf{V}_{jk}^{-1} = \epsilon \sum_j^N \sum_k^N \mathbf{I}_{jk} = N\epsilon. \tag{A.32}$$

Furthermore this demonstrates that the beam emittance is also conserved in the limit of very few particles.

If the phase space distribution of particles is Gaussian, the hyperellipses formed by fixed values of single particle emittance coincide with equiprobable contours of the distribution. The distribution of single particle emittance thus follows a chi-square distribution

$$f(\epsilon_i) = \frac{\frac{1}{2}\left(\frac{\epsilon_i}{2}\right)^{\frac{N}{2}-1} e^{-\frac{\epsilon_i}{2}}}{\Gamma\left(\frac{N}{2}\right)} \tag{A.33}$$

which is illustrated in figure 7.2 for the case $N = 4$. Since this distribution produces long exponential tails, the finite dimensions of an experiment infers scraping and a deviation from the Gaussian approximation in the asymptotic limit.

Appendix B

ADDITIONAL FIGURES

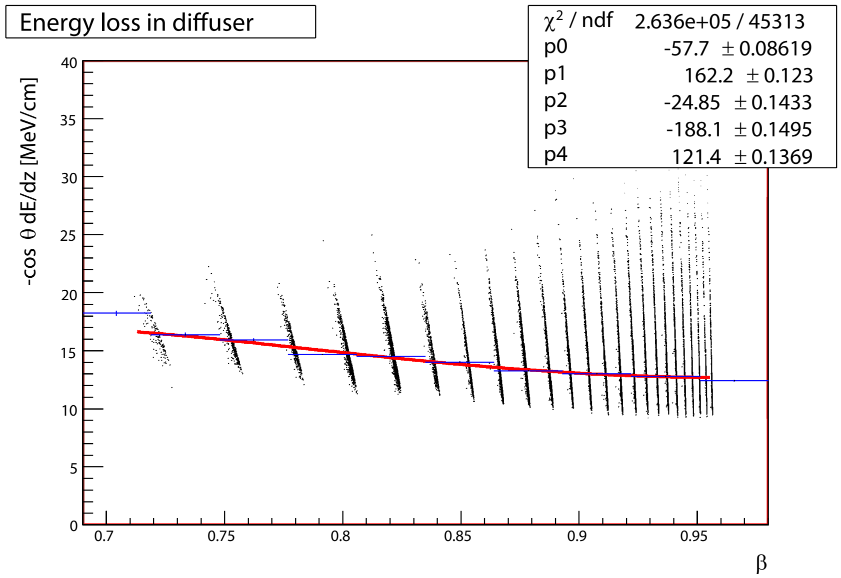

Fig. B.1: Energy loss in the diffuser as a function of the beta in the upstream tracker reference plane. Since the tracker reference plane is downstream of the diffuser, the β and θ are measured after the energy loss.

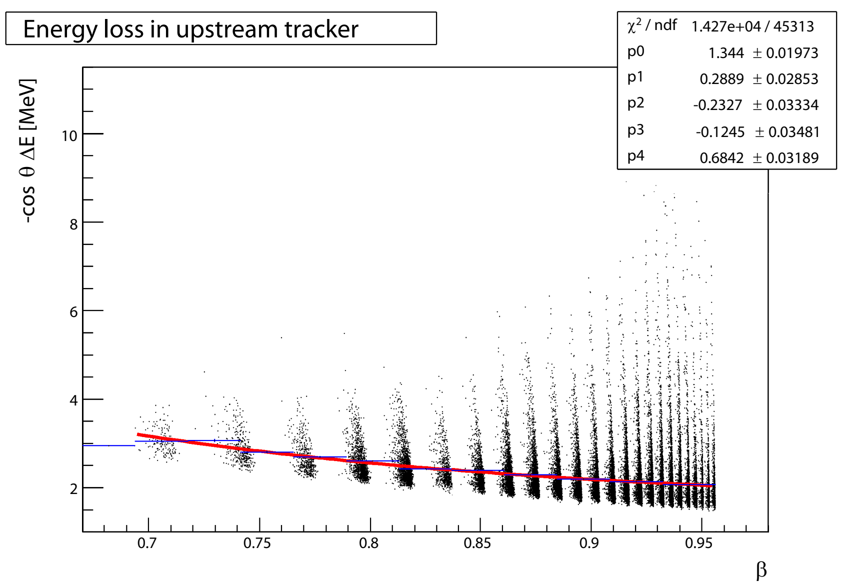

Fig. B.2: The energy loss in upstream tracker as function of β in its tracker reference plane. Since the tracker reference plane is downstream of the area of energy loss, the value on the horizontal axis is the value after the energy loss has occurred.

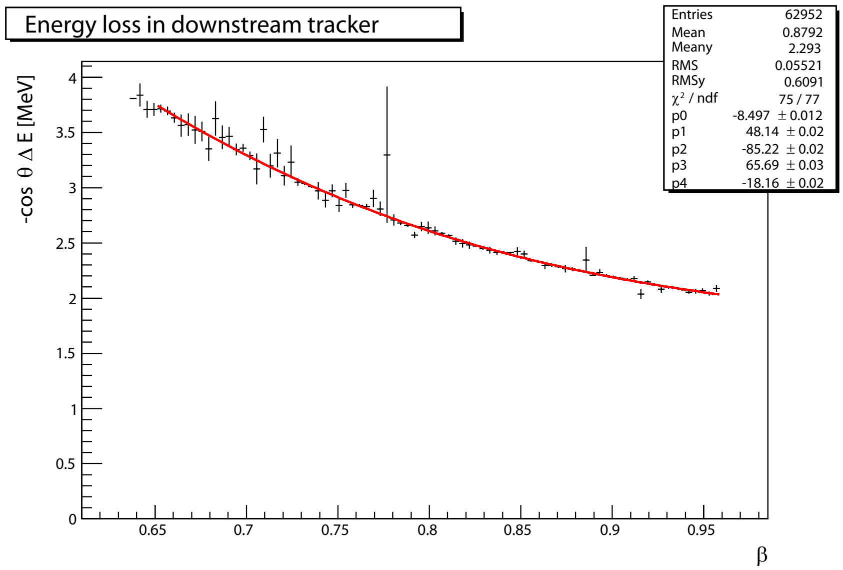

Fig. B.3: The energy loss in downstream tracker as function of β in its tracker reference plane. Since the tracker reference plane is upstream of the area of energy loss, the value on the horizontal axis is the value before the energy loss has occurred.

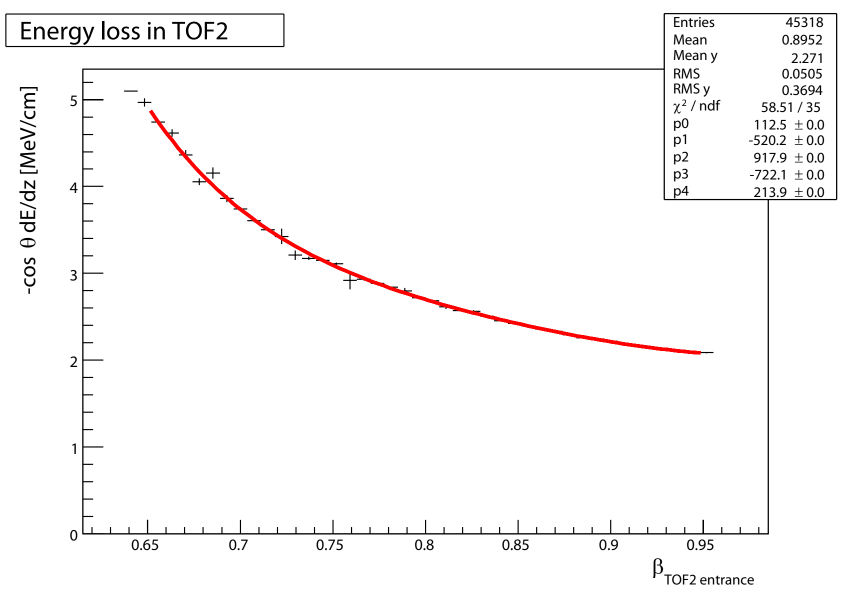

Fig. B.4: The energy loss in TOF2 as function of β at the upstream surface of TOF2.

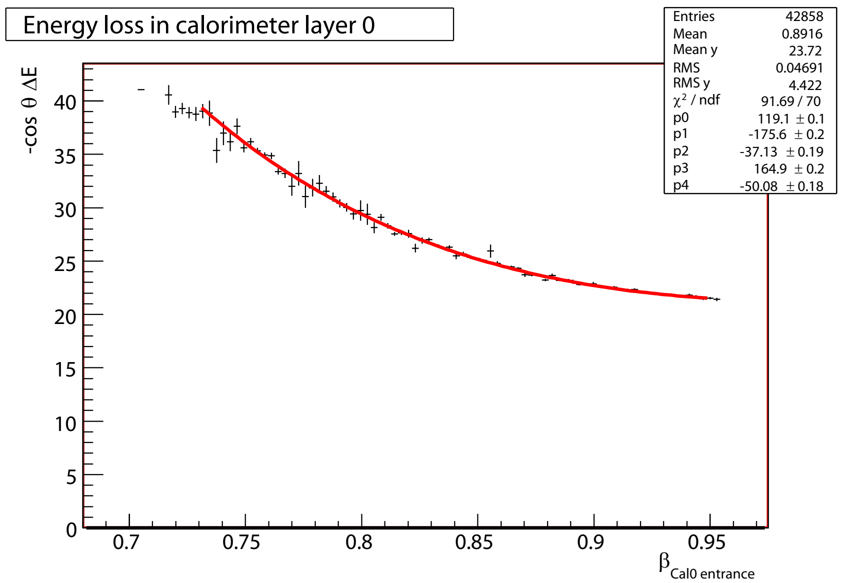

Fig. B.5: The energy loss in the preshower layer of the calorimeter as function of β at the upstream surface of the calorimeter.

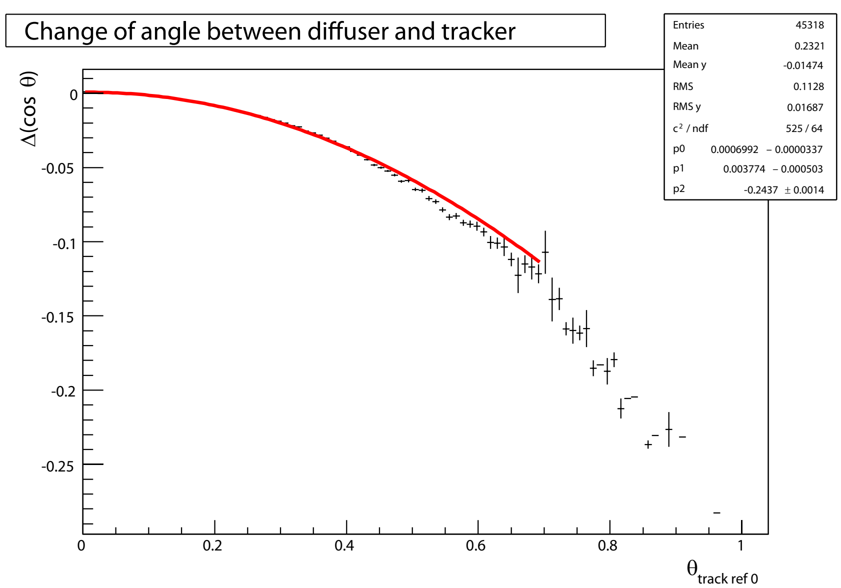

Fig. B.6: The change in angle from the beam axis in between the diffuser and the upstream tracker reference plane. The difference in angle is a combination of multiple scattering in the scintillating fibers and transverse magnetic field effects, though the magnetic field effects dominate.

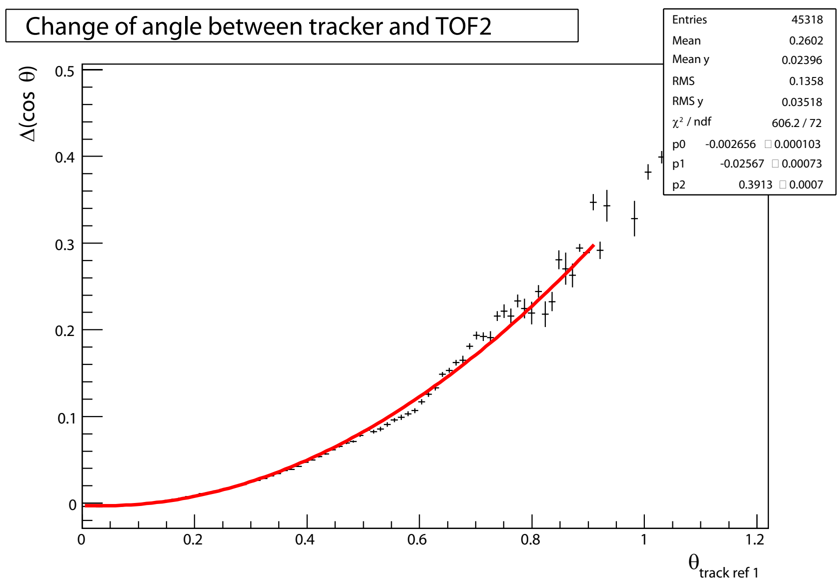

Fig. B.7: The change in angle from the beam axis in between the downstream tracker reference plane and TOF2. The difference in angle is a combination of multiple scattering in the scintillating fibers and transverse magnetic field effects, though the magnetic field effects dominate.

Appendix C

TIME OF FLIGHT PREDICTIONS

The expected time of flight used in chapter 9 uses the longitudinal velocity

$$\beta_z = \frac{p_z}{\sqrt{p^2 + m^2}} \qquad , \; p = |\mathbf{p}| \tag{C.1}$$

where the mass m is and the particle mass and p the momentum. To first order the time of flight is given by

$$t' = \frac{\Delta z}{c(\beta_z^{up} - \beta_z^{down})}(\ln(c\beta_z^{up}) - \ln(c\beta_z^{down})) \tag{C.2}$$

for all regions. This expression follows from the assumption that the velocity changes linearly between the starting and ending positions

$$t' = \int \frac{\mathrm{d}t}{\mathrm{d}x}\mathrm{d}x = \int \frac{\mathrm{d}x}{c\beta_z^{up} + kx} = \left[\frac{\ln c\beta_z^{up} + kx}{k}\right] \tag{C.3}$$

where k is fixed by the boundary conditions. This first approximation must be corrected due to second order effects such as magnetic field effects and multiple scattering.

C.1 Magnetic field

In classical physics

$$F = q(\mathbf{E} + \mathbf{v} \times \mathbf{B}) \tag{C.4}$$

so in the longitudinal direction

$$F_z \sim v_x B_y - v_y B_x \tag{C.5}$$

since there is no electric field in the absorbers. MICE is using magnetic field flips in the absorbers. As shown in figure C.1(a), in the center of the flip, the magnetic field in the longitudinal direction is zero, and the magnetic field has a transverse component which is dependent on

$$\rho = \sqrt{x^2 + y^2} \tag{C.6}$$

almost linearly, such that

$$B_\rho(z = 0) = b\rho \tag{C.7}$$

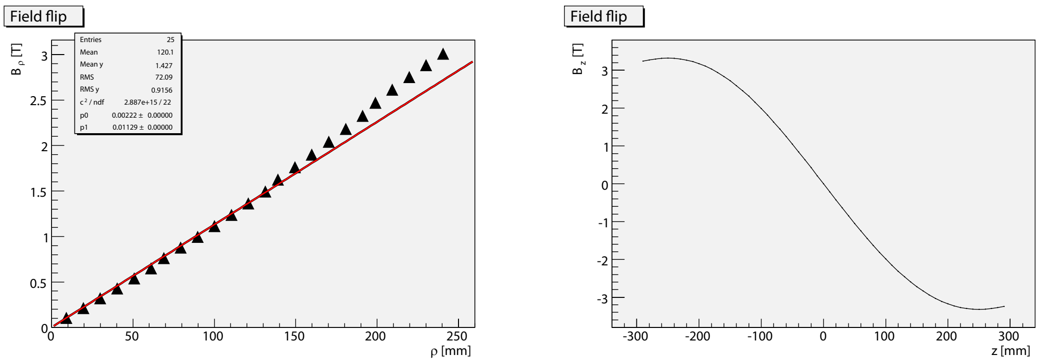

(a) Transversal magnetic field in flip

(b) Longitudinal magnetic field in flip

Fig. C.1: (a): The transverse magnetic field versus the distance from symmetry axis in the center of a MICE SFoFo channel field flip. The triangles indicate the values of the field map used in G4MICE. The red line is a linear approximation of the radial field strength (see equation (C.7)). (b): The longitudinal magnetic field versus the longitudinal position in the center of a MICE SFoFo channel field flip. Values comes directly from G4MICE.

where b is a constant. Assuming a cylindrically symmetric field, trigonometry gives

$$F_z \dot{\sim} b(v_x y - v_y x). \tag{C.8}$$

Recalling that the momentum is related to the force by

$$\frac{\mathrm{d}p}{\mathrm{d}t} = F \tag{C.9}$$

we have arrived at a classical expression for momentum transfer due to the magnetic field:

$$\frac{\mathrm{d}p_z}{\mathrm{d}t} \sim v_x y - v_y x. \tag{C.10}$$

The momentum transfer affects the time of flight in two ways. Most notably it can give a net gain, or loss, of longitudinal momentum while keeping the energy conserved. This will cause a particle to move at different velocities upstream compared to downstream. A second effect is that of a particle which loses p_z and later regains it such that the momentum upstream and downstream of a field flip is identical. Such a particle has a longer time of flight compared to a particle travelling a constant velocity. Since the spectrometers measure the same longitudinal momentum, the spectrometers are blind to this last effect, unless it can be foreseen using equation (C.5). In addition, the field flip shifts the larmor center from the beamline, and since the field direction depends on ρ according to (C.7) the particle is influenced by an inhomogeneous magnetic force as it precesses around the posterior larmor center.

In the discussion that follows the notation

$$\eta \equiv p_x y - p_y x \tag{C.11}$$

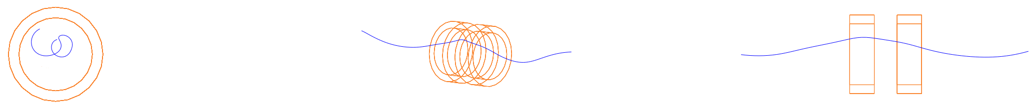

(a) View 0°. (b) View 45°. (c) View 90°.

Fig. C.2: Upstream flip. The larmor center displacement is clearly visible in C.2(a).

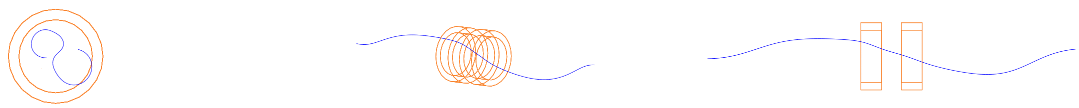

(a) View 0°. (b) View 45°. (c) View 90°.

Fig. C.3: Center flip.

is used for the expected longitudinal Lorentz force[1] in the center of the field flip. The effect of the field flips is illustrated by a randomly chosen visualized event from a 6π mm beam in G4MICE on the front page. Figures C.2 to C.4 show the same track for the each field flip individually and the immediate surrounding area.

Since the expected time of flight already takes the difference in p_z into account through (C.2), the effect of momentum transfer should already have been dealt with unless the momentum changes back and forth between the two measurements. Switching to spherical coordinates for the momentum, and cylindrical coordinates for the position,

$$\begin{cases} p_x &= p\sin\theta\cos\phi \\ p_y &= p\sin\theta\sin\phi \\ p_z &= p\cos\theta \\ x &= \rho\cos\alpha \\ y &= \rho\sin\alpha \\ z &= z \end{cases} \tag{C.12}$$

and defining the angular difference of momentum and position as

$$\beta \equiv \phi - \alpha \tag{C.13}$$

η can be expressed as

$$\begin{aligned} \eta &= \rho p\sin\theta\left(cos\phi\sin\alpha - \sin\phi\cos\alpha\right) \\ &= -\rho p\sin\theta\sin\beta. \end{aligned} \tag{C.14}$$

To summarize, the momentum transfer does two things to a particle:

- It changes the momentum so that $p_{z,in} \neq p_{z,out}$.
- It delays particles even when $p_{z,in} = p_{z,out}$.

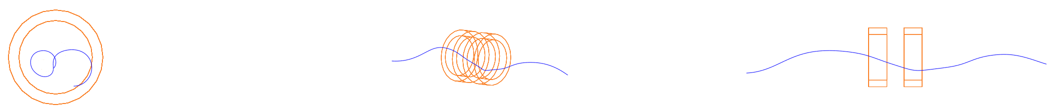

(a) View 0°. (b) View 45°. (c) View 90°.

Fig. C.4: Downstream flip.

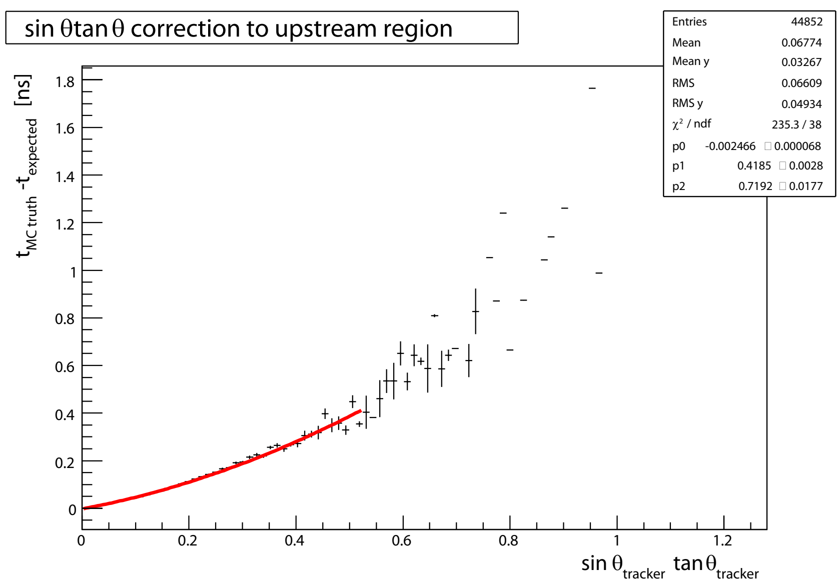

Fig. C.5: The next to leading order correction to the expected time of flight in the cooling channel where the uncorrected time of flight expectation is given by equation (9.15).

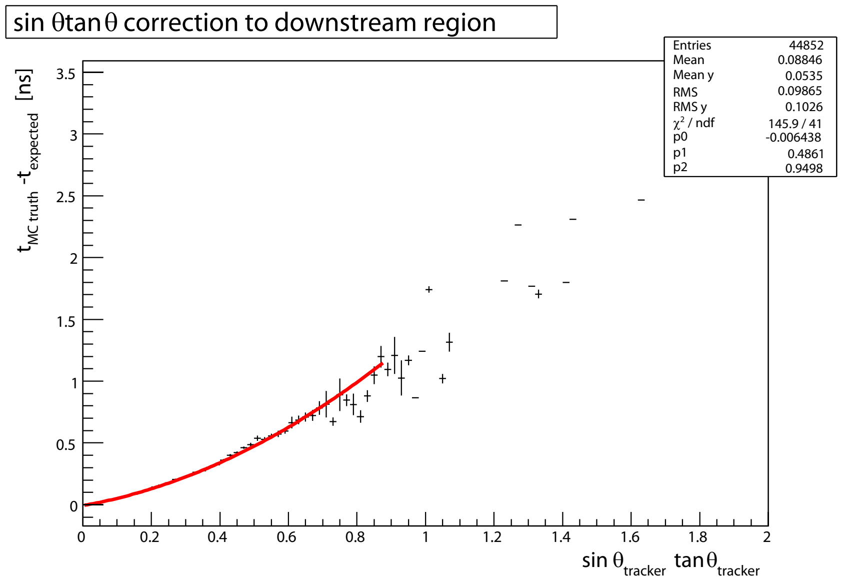

Fig. C.6: The leading order correction to the expected time of flight in the cooling channel where the uncorrected time of flight expectation is given by equation (9.15).

If it was possible to directly extract the beam variables at the flip, η would be a good estimate for the time of flight discrepancy $t - t'$. However, one must predict the beam inside the flip from spectrometer information in order to use equation (C.11). Assuming that the beam grows transversally as it approaches a field flip due to the falling strength of the longitudinal field,

$$\eta \sim \sin\theta \tan\theta \tag{C.15}$$

where $\sin\theta$ comes from equation (C.14), and $\tan\theta$ originates from a simple extrapolation for the distance from the beam axis.

Performing fits based on variables derived from the Lorentz force in this way on a beam with no material in the cooling channel gave the discrepancy between the Monte Carlo truth and expected time of flight

$$\sigma_{t-t'} = \sigma_{\sin\theta\tan\theta} \oplus \sigma_{\Delta\theta} \oplus \sigma_{\rho_{up}} \oplus \sigma_{unknown} \tag{C.16}$$

where

$$\begin{aligned}
\sigma_{\sin\theta\tan\theta} &= 142.0 \text{ ps} && \text{(C.17)}\\
\sigma_{\Delta\theta} &= 42.0 \text{ ps} && \text{(C.18)}\\
\sigma_{\rho_{up}} &= 11.9 \text{ ps} && \text{(C.19)}\\
\sigma_{unknown} &= 14.7 \text{ ps.} && \text{(C.20)}\\
& && \text{(C.21)}
\end{aligned}$$

[1] Electric charge and mass were intentionally left out of the expression.

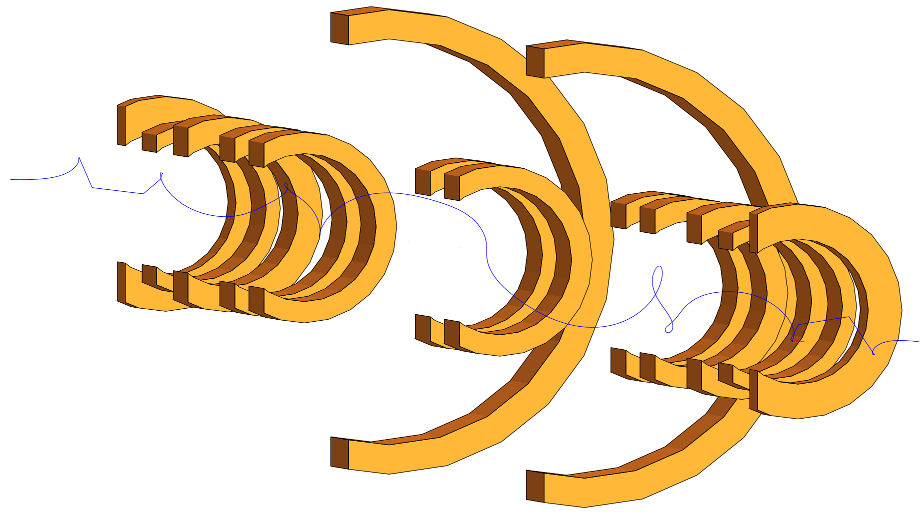

Fig. C.7: A μ^+ from a 6πmm beam going through the MICE cooling channel. In this figure the particle was only under the influence of magnetic field, hence $\frac{\mathrm{d}E}{\mathrm{d}t} = \frac{\mathrm{d}|\mathbf{p}|}{\mathrm{d}t} = 0$. The picture was generated with G4MICE.

It is clear that although the model for the $\sin\theta\tan\theta$ parameterization is based on some very simple assumptions, it is the dominating effect for correcting the time of flight expectation.

C.2 Matter effects

With the effect of magnetic field examined, the effect of energy loss and other matter effects were studied. Regrettably in the simulation, it was not possible to have the correct description of absorbers and their windows and the RF cavity windows included, while using a homogeneous magnetic field. For this reason, the cooling channel material was added together with the flip-field. To bypass possible effects by RF phases, every linac was given a static electric field designed to return the same energy as was lost in an absorber. This was done so that the energy lost in the absorbers would correspond to a minimum ionizing particle.

After the expected time of flight had been calculated using only longitudinal momentum in the spectrometers, the discrepancy was

$$t - t'_{p_z} = 268.7 \pm 145.4 \text{ ps} \tag{C.22}$$

which was fitted using the method established in the previous section of first fitting using Φ, then $\Delta\theta$. Should the magnetically induced momentum transfer and the energy loss fluctuations be uncorrelated, the energy loss would hence introduce

$$\sigma_{\Delta E} = 33.9 \text{ ps} \tag{C.23}$$

error. Note that this is much smaller than the uncertainty given by inhomogeneity of the magnetic field presented in the previous section.

To get a rough estimate of the importance of the energy straggling, it is useful to remember that a 200 MeV/c muon which changes its energy by one MeV gets a time of flight difference of 27.7 ps over six meters, compared to an unperturbed muon. This estimate assumes particles are traveling as straight tracks both before and after the energy loss event. These results are in good agreement when using the spread in energy loss presented in section 6.2.4.

Appendix D

FITTING METHODS

This section contains short descriptions of some of the fitting methods mentioned in the discussion of the particle identification algorithm. The focus is on two of the three best performing methods at the test shown in figure 9.21.

D.1 Fisher discriminants

The Fisher discriminants method is a linear discriminant analysis which determines an axis in the hyperspace spanned by the input variables such that when projecting the output classes (in the scope of this thesis, the *signal* variable) they are separated by as much distance as possible, while events belonging to the same class are clustered in a small region along the axis. In order to find this axis, the correlation matrix of the input variables is used, hence only linear correlations can be accounted for.

The correlation matrix C is decomposed as

$$C_{kl} = W_{kl} + B_{kl} \tag{D.1}$$

where W is the *within class matrix* and B is the *between class matrix*. W describes the dispersion of events relative to the mean of its own class and is given by

$$W_{kl} = \Big\langle x_{s,k} - \langle x_{s,k} \rangle \Big\rangle \Big\langle x_{s,l} - \langle x_{s,l} \rangle \Big\rangle + \Big\langle x_{b,k} - \langle x_{b,k} \rangle \Big\rangle \Big\langle x_{b,l} - \langle x_{b,l} \rangle \Big\rangle \tag{D.2}$$

where and s and b denotes signal and background respectively, while

$$\begin{aligned} B_{kl} = &\ \tfrac{1}{2} \textstyle\sum_{u=s,b} \Big(\langle x_{u,k} \rangle - \langle x_k \rangle \Big) \Big(\langle x_{u,l} \rangle - \langle x_l \rangle \Big) \\ = &\ \tfrac{\langle x_{s,k} \rangle + \langle x_{s,l} \rangle + \langle x_{b,k} \rangle + \langle x_{b,l} \rangle}{2} - \langle x_k \rangle - \langle x_l \rangle \end{aligned} \tag{D.3}$$

describes the dispersion of events relative to the overall mean of the sample $\langle x_k \rangle$ [96]. The Fisher discriminant analysis thus aims to minimize the *within* dispersion while maximizing the *between* separation, which can be quantified as the ratio of the diagonal elements of the matrices.

The Fisher coefficients F_k for n input variables x_k are

$$F_k = \frac{\sqrt{N_s N_b}}{N_s + N_b} \sum_{l=1}^{n} W_{kl}^{-1} \left(\langle x_{s,l} \rangle - \langle x_{b,l} \rangle \right) \tag{D.4}$$

where N_j is the total number of event type j in the sample. The Fisher discriminant y_i for event i is

$$y_i = F_0 + \sum_{k=1}^{n} F_k x_{k,i} \tag{D.5}$$

where F_0 is an offset that centers the mean $\langle y_i \rangle = 0$ [96].

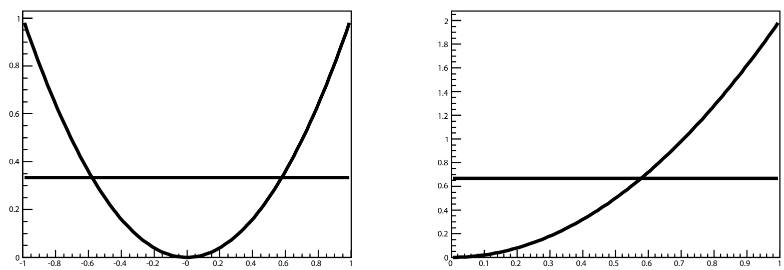

Fig. D.1: Example of variable transformation for the Fisher method. The left figure shows two distributions both with means at zero. The right figure shows the distributions after $x \to |x|$ transformation, separating the two means and thus gaining discriminating power.

Since the Fisher coefficients are zero when the signal and background samples have identical mean values, this method performs best when a prior variable transformation ensures that the distributions are centered in different regions. For example a signal distribution $s(x) = x^2$ and a background distribution $b(x) =$ constant both have a mean of zero over the range $x = [-1, 1]$ and thus hold no discriminating power. Performing the variable transformation $x \to |x|$ makes the Fisher discriminant method useful. This example is illustrated in figure D.1. The asymmetry transformations described in sections 9.3.4 and A.1.6 are examples of how this was performed in practice in this thesis.

D.2 Artificial Neural Networks

The Artificial Neural Networks (ANN), are methods for nonlinear discriminant analysis with a connectivist approach to the computation of the fitted function. Here only Multi Layer Percepteron Artificial Neural Networks, the most common type of ANNs, are discussed.

An Artificial Neural Network can be understood as an expansion of a function using a series of weighted object functions, similar to a Taylor or Fourier expansion. In all ANNs used in this thesis, the object functions are expanded in *sigmoids*,

$$f(x) = \frac{1}{1 + e^{-kx}} \tag{D.6}$$

where k is constant. This expansion is a mapping from input variables x_i stored in what is called the input layer, to the output variables in the output layer. For ANNs dedicated to do particle identification, there is normally only one variable in the output layer, and it is conventionally set to 1 for signal and 0 for background events. Virtually any function can be used for the expansion, but sigmoids are good for fast conversion when fitting block functions such as those used for assigning the particle ID, due to the steep transition between the two flat regions. A sigmoid with $k = 1$ is illustrated in figure D.2(a).

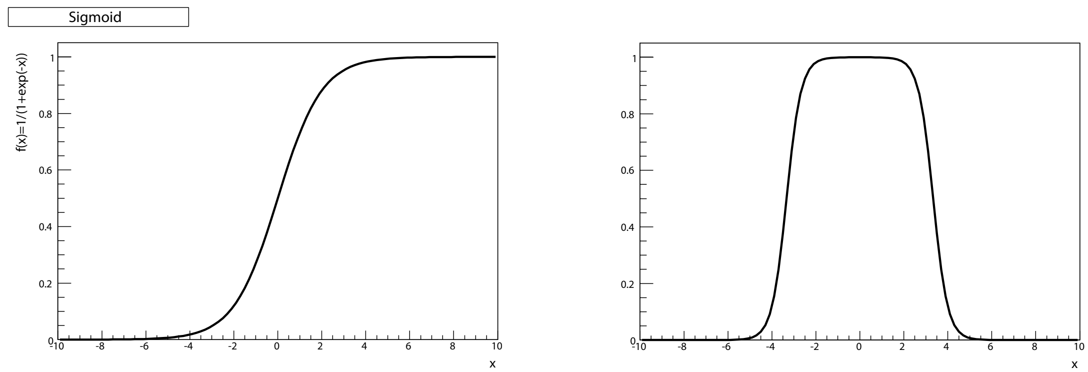

(a) Sigmoid function (b) Two sigmoids

Fig. D.2: (a) A sigmoid function, defined in (D.6). (b) The sum of two sigmoid functions.

Between the input and output layers are one or more *hidden layers*. The number of variables in a hidden layer corresponds to the order of the expansion, and the Weierstrass theorem states that a single hidden layer is enough to approximate any continuous function given an arbitrary size of the hidden layer. The variables in the input, output and hidden layers are often called *neurons* in literature, and the weights for the connections between the neurons are called *synapses*. It is possible in an ANN to use more than one hidden layer, which can be used for achieving the same performance but with a reduced total number of hidden variables. This can give great improvements in time efficiency and robustness of the network. Note that an ANN without a hidden layer is a linear fit in the hyperspace spanned by the input variables, hence it reduces to the Fisher discriminant method.

As an example of a simple fit using an ANN, consider the distribution $g(x) = \sin(x)$ which is fitted using the architecture `1:2:1`, i.e., one input variable x, two hidden variables in a single hidden layer, and one output variable y. The objective is to minimize the quadratic errors

$$E(\mathbf{x}|\mathbf{n},\mathbf{w}) = \frac{1}{2}\sum_i \Big(y(x_i) - g(x_i)\Big)^2 \tag{D.7}$$

such that $y(x) \approx g(x)$, where $\{\mathbf{n},\mathbf{w}\}$ is the set of fitting parameters. This example uses the function

$$y(x_i) = \sum_{j=1}^{2} f_j(x) w_{j,2} + n_3 = \sum_{j=1}^{2} \frac{w_{j,2}}{1 + e^{-(n_j + w_{j,1} x_i)}} + n_3 \tag{D.8}$$

where $w_{j,1}$ denotes the weight (synapse) between the input variable and hidden variable j, and $w_{j,2}$ is the corresponding weight for the output layer side of the hidden layer. In this example the results are seven constants (3 n-type and 4 w-type) which reproduce the true function, but would benefit from expansion in periodic functions instead of sigmoids, or more terms in the expansion, i.e., a larger hidden layer.

The ANNs are usually overly complicated for solving simple problems as the one above, but they really show their usefulness when working on nonlinear problems and where the object function is either unknown or too complicated due to a large number of input variables. For N_h number of hidden variables and N_{in} number of input variables, equation (D.8) generalizes to

$$y_i = \sum_{j=1}^{N_h} \frac{w_{jk,2}}{1 + e^{-\sum_{k=1}^{N_{in}}(n_{jk} + w_{jk,1} x_{k,i})}} + n_{offset} \tag{D.9}$$

for event i. For more than one hidden layer, the additional nesting of neurons and synapses makes an analytic expression such as (D.9) very hard to comprehend.[1] There is however never any need to use the analytic expression explicitly since the text file of weights can be read back in to build the ANN according to its architecture.

During training of the ANN, the errors are computed and backpropagated in an adaptive algorithm. The easiest such algorithm is the steepest descent method, where a training epoch adjusts the weights by a step in the parameter space spanned by the weights in the direction where the error decreases fastest. The step length is proportional to the error and a user defined constant η which controls the step size, and thus the learning rate. After an epoch, the weight parameter space $\mathbf{w}$ is thus [96]

$$\mathbf{w}^{(\rho+1)} = \mathbf{w}^{(\rho)} - \eta \nabla_{\mathbf{w}} E \tag{D.10}$$

where E is given by (D.7). The ANN used in this thesis however, relied on the Broyden-Fletcher-Goldfarb-Shanno (BFGS) method. This is a powerful quasi Newtonian method for minimization which uses an approximative method to calculate the Hessian[2] of the object function. Instead of recalculating a proper Hessian at every step, the approximated Hessian is updated by successive gradient vectors. This combines the advantage of the faster convergence of the Newtonian method compared to the steepest descent method, without the processor consuming calculation and inversion of a proper Hessian[3], which is used in the Newtonian method.

One problem with Artificial Neural Networks is overtraining. Overtraining is the phenomenon where the fitting method starts fitting on individual data points. It happens if too many model parameters are adjusted to too few data points, and thus depends on the fitting method. This can be avoided by increasing the number of events in the sample or by decreasing the number of training epochs. When using ANN, overtraining can be detected by an apparent improvement with increased number of epochs in the training sample, while

[1] The default ANN used in this thesis has 41 neuron weights (n-type) and 391 synapse weights (w-type) plus normalization factors for all input variables.

[2] The Hessian is the Jacobian of second derivatives, and is often called "second derivative matrix" by physicists, or "information matrix" by statisticians. The inverted Hessian, which is used for stepping in the Newtonian method, is often called the "error matrix" by physicists. This notation is hence used in ROOT.

[3] Instead the inverted Hessian is updated directly.

the performance of the test sample worsens. For all implementations used for this thesis, events with odd event number were used for testing and even event numbers were used for training.

Today particle physicists use Artificial Neural Networks mostly for particle identification, but it can be used for any form of fitting and reconstruction. The ANN method is also widely used outside science, for example it is used by economists to predict stock markets, by hospitals to predict occupancy at the urgency receptions, by police departments to detect internal corruption, by technicians to spot problems with aircraft engines etc.

ACKNOWLEDGEMENTS

I would like to express my deepest gratitude to all of those who have helped in making this thesis possible. In particular I would like to thank the following people:

My supervisor Alain Blondel, for giving me the opportunity to work on this project and whose insights in both science as its politics have made me a much better physicist. It has been a pleasure to work with someone who has a genuine interest in particle and accelerator physics, yet never forgets the social aspects, something you have shown well with your excellent barbecue house parties.

Alan Bross, Patrick Janot and Divic Rapin for accepting the invitation to the defense of this thesis with such short notice. And of course for the good grades I received! Of special mention is Professor Bross, who heroically read every page and sent me a full markup version of the text before I had the thesis printed.

Jean-Sebastien Graulich, for your good humor and your understanding and inspiring love for physics. The calorimeter design did not advance as much in years until you came along and turned things around overnight. I find the effort you put in proof reading this thesis astonishing.

The extraordinary secretaries Peggy and Tica, without whom all work in the corridor would come to a quick halt. I cannot thank you enough for all the help with the paperwork and phone calls I received.

Our informatician Yann Meunier, for all the heroic help I have received with everything from printers to computers that were blown to bits. Like you say, bad computer karma generates many interesting errors.

Yağmur Torun, for taking me under your wing and guiding me to my first scientific results and publications. "It builds character", and indeed it does.

Malcolm Ellis, for your lightning speed email responses to all questions I had, no matter how stupid. Also for taking G4MICE to a whole new level, and your good taste of British comedies.

Frederick Orrelana, for helping me through the GRID jungle, without which I would probably still be waiting for my simulation results.

John Cobb, for the useful feedback I received at every analysis and collaboration meeting, and for understanding what I was trying to say, even when I did not fully understand it myself.

Holger Witte, for promptly generating field maps on demand, which I can imagine must have been a true test of patience.

The head of the MICE detector group, Vittorio Paladino, whose interest in my results inspired ever more intense efforts to improve beyond merely sufficient performance.

Jim Norem, for the encouragement and appreciation of the work I performed when trying to make sense of the RF background measurements.

The Moose Boys Kenny Walaron (aka Lord Underpants) and Aron Fish (aka Concrete Boy), whose pole dancing technique and karaoke skills on our world tour through Japan, California and Europe still make me smile.

Chris Rogers, whom with a good sense of humor and a ample dose of patience has taught me most of what I know about emittance and other arcane secrets of accelerator physics.

My office mates Chiara Casella, Vassil Verguilov and Hayk Hakobyan, for suffering through my more talkative moments, for your good ability to stay in touch with real life and for all those rides to Lausanne.

Ingrid Bibollet, the charged bibon, for encouraging me through the thesis when it was all an uphill struggle, for always being there and for having to learn the hard way what it means to be a science widow.

The Bibollet family, for taking me in with open arms and every weekend offering a refuge in the Alps from my science life. And for all the amazing cheese you have put on my plate...

Gianrossano Giannini, for managing to make sense of the group theory mystery, which was making me sleepless, in the course of one bus ride.

My family, for allowing me roam free even though you have no idea of why I am doing this research, and for enduring my long lectures during dinners when I tried to explain why.

Niels van Eldik, Andy Salzburger, Jeroen Stijl, Marleen van Nes and Ed Moyse, for being such great sports both on and off the piste, and for helping me down from the mountain when I made a wee bit too good drop with my snowboard. And for all the beer and whisky too of course.

BIBLIOGRAPHY

[1] W. M. Yao et al. Review of particle physics. *J. Phys.*, G33:1–1232, 2006.

[2] L. Bornschein. Measurements with the KATRIN pre-spectrometer. *Prog. Part. Nucl. Phys.*, 57:49–57, 2006.

[3] M. Fukugita and T. Yanagida. *Physics of Neutrinos and Applications to Astrophysics*. Springer-Verlag Berlin Heidelberg, 2003. 593 p.

[4] B. Kayser. Neutrino Phenomenology. SUSSP61 lecture series, August 2006.

[5] The ISS Physics Working Group. Physics at a future Neutrino Factory and super-beam facility. Technical report, February 2007.

[6] John N. Bahcall, Sarbani Basu, and Aldo M. Serenelli. What Is The Neon Abundance Of The Sun? *Astrophys. J.*, 631:1281–1285, 2005, astro-ph/0502563.

[7] Hiroshi Nunokawa, Stephen J. Parke, and Renata Zukanovich Funchal. What fraction of boron-8 solar neutrinos arrive at the earth as a nu(2) mass eigenstate? *Phys. Rev.*, D74:013006, 2006, hep-ph/0601198.

[8] Y. Ashie et al. Evidence for an oscillatory signature in atmospheric neutrino oscillation. *Phys. Rev. Lett.*, 93:101801, 2004, hep-ex/0404034.

[9] T. Araki et al. Measurement of neutrino oscillation with KamLAND: Evidence of spectral distortion. *Phys. Rev. Lett.*, 94:081801, 2005, hep-ex/0406035.

[10] K. Eguchi et al. First results from KamLAND: Evidence for reactor anti- neutrino disappearance. *Phys. Rev. Lett.*, 90:021802, 2003, hep-ex/0212021.

[11] Abhijit Bandyopadhyay, Sandhya Choubey, Srubabati Goswami, S. T. Petcov, and D. P. Roy. Constraints on neutrino oscillation parameters from the SNO salt phase data. *Phys. Lett.*, B583:134–148, 2004, hep-ph/0309174.

[12] M. Apollonio et al. Initial results from the CHOOZ long baseline reactor neutrino oscillation experiment. *Phys. Lett.*, B420:397–404, 1998, hep-ex/9711002.

[13] F. Ardellier et al. Double Chooz: A search for the neutrino mixing angle theta(13). 2006, hep-ex/0606025.

[14] Antonio Riotto. Theories of baryogenesis. 1998, hep-ph/9807454.

[15] Asan Damanik, Mirza Satriawan, Muslim, and Pramudita Anggraita. Left-Right Symmetry Model with Two Bidoublets and One Doublet Higgs Field for Electroweak Interaction. 0500, arXiv:0705.3999 [hep-ph].

[16] G. Senjanovic and Rabindra N. Mohapatra. Exact Left-Right Symmetry and Spontaneous Violation of Parity. *Phys. Rev.*, D12:1502, 1975.

[17] Rabindra N. Mohapatra and Goran Senjanovic. Neutrino mass and spontaneous parity nonconservation. *Phys. Rev. Lett.*, 44:912, 1980.

[18] J. Schechter and J. W. F. Valle. Neutrinoless double-β decay in $SU(2)\times U(1)$ theories. *Phys. Rev. D*, 25(11):2951–2954, Jun 1982.

[19] M. Doi, T. Kotani, and E. Takasugi. Double beta Decay and Majorana Neutrino. *Prog. Theor. Phys. Suppl.*, 83:1, 1985.

[20] Martin Hirsch, Sergey Kovalenko, and Ivan Schmidt. Extended black box theorem for lepton number and flavor violating processes. *Phys. Lett.*, B642:106–110, 2006, hep-ph/0608207.

[21] H. V. Klapdor-Kleingrothaus, I. V. Krivosheina, A. Dietz, and O. Chkvorets. Search for neutrinoless double beta decay with enriched Ge- 76 in Gran Sasso 1990-2003. *Phys. Lett.*, B586:198–212, 2004, hep-ph/0404088.

[22] D. Autiero et al. The synergy of the golden and silver channels at the Neutrino Factory. *Eur. Phys. J.*, C33:243–260, 2004, hep-ph/0305185.

[23] S. Rigolin. Physics reach of beta-beams and nu-factories: The problem of degeneracies. *Nucl. Phys. Proc. Suppl.*, 155:33–37, 2006, hep-ph/0509366.

[24] Simone S. Gilardoni. Study of particle production and capture for a Neutrino Factory. CERN-THESIS-2004-046.

[25] A. Vacheret. T2K beam line and near detectors. Presented at NuInt07, June 2007.

[26] (ed.) Cornell, J. The EURISOL report: A feasibility study for a European isotope-separation-on-line radioactive ion beam facility. Caen GANIL - (03/12,rec.Mar.04) 1 CD, 622 p.

[27] International Design Study of the Neutrino Factory. Neutrino Factory: specification of baseline for the accelerator complex and detector systems. IDS-NF-Baseline-2007-0.10, Jan 2008.

[28] S. Ozaki, R. Palmer, M. Zisman, and J. Gallardo. Feasibility Study-II of a Muon-Based Neutrino Source. Technical report, BNL-52623, 2001.

[29] M. Zisman. ISS Summary report of Accelerator Working Group - R5. Technical report, Jan 2008. RAL-TR-2007-23.

[30] S. J. Brooks and K. A. Walaron. Computed pion yields from a tantalum rod target: Comparing MARS15 and GEANT4 across proton energies. *Nucl. Phys. Proc. Suppl.*, 155:295–296, 2006.

[31] Silvia Borghi. Hadron production cross section measurement with the HARP large angle detectors. CERN-THESIS-2007-034.

[32] K T McDonald et al. Studies of a Target System for a 4-MW, 24-GeV Proton Beam. Technical Report INTC-P-186. CERN-INTC-2004-016, CERN, Geneva, 2004. revised version submitted on 2004-04-27 15:47:43.

[33] R. Palmer. NuFact05 Cooling Discussion. Presented in Working Group 3, Session 5, June 2005.

[34] S. Berg. Neutrino Factory Storage Ring. NuFact07 Summer School, August 2007.

[35] Chris Rogers. *Beam Dynamics in an Ionisation Cooling Channel*. PhD thesis, Imperial College, London, 2007.

[36] David Neuffer. Principles and Applications of Muon Cooling. *Part. Accel.*, 14:75, 1983.

[37] R. C. Fernow and J. C. Gallardo. Muon transverse ionization cooling: Stochastic approach. *Phys. Rev. E*, 52(1):1039–1042, Jul 1995.

[38] Mohammad M. Alsharoa et al. Recent progress in neutrino factory and muon collider research within the Muon collaboration. *Phys. Rev. ST Accel. Beams*, 6:081001, 2003, hep-ex/0207031.

[39] Robert B. Palmer et al. A Complete Scheme of Ionization Cooling for a Muon Collider. 2007, arXiv:0711.4275 [physics.acc-ph].

[40] (Ed.) Blondel, A. et al. ECFA/CERN studies of a European neutrino factory complex. CERN-2004-002.

[41] A. Bross. Neutrino Factory and Muon Collider R&D in the US. Seminar at RAL, June 2007.

[42] H. Abramowicz, A. Caldwell, R. Galea, and S. Schlenstedt. A muon collider scheme based on frictional cooling. *Nucl. Instrum. Meth.*, A546:356–375, 2005, physics/0410017.

[43] Y. Derbenev and R. P. Johnson. Six-dimensional muon beam cooling using a homogeneous absorber: Concepts, beam dynamics, cooling decrements, and equilibrium emittances in a helical dipole channel. *Phys. Rev. ST Accel. Beams*, 8:041002, 2005.

[44] (Ed.) Autin, B., (Ed.) Blondel, A., and (Ed.) Ellis, John R. Prospective study of muon storage rings at CERN. CERN-99-02.

[45] P. Strolin. Neutrino detectors for super-beams, beta-beams and nu-factories. *Nucl. Phys. Proc. Suppl.*, 149:60–66, 2005.

[46] A. Cervera, F. Dydak, and J. Gomez Cadenas. A large magnetic detector for the neutrino factory. *Nucl. Instrum. Meth.*, A451:123–130, 2000.

[47] A. Cervera et al. Golden measurements at a neutrino factory. *Nucl. Phys.*, B579:17–55, 2000, hep-ph/0002108.

[48] A. Cervera-Villanueva. Review of large magnetic calorimeters for a neutrino factory. *Nucl. Phys. Proc. Suppl.*, 149:201–202, 2005.

[49] A. Cervera. MIND, Magnetised Iron Neutrino Detector. Presented at the Golden07 conference, June 2007.

[50] C. T. Rogers and R. Sandstrom. Simulation of MICE using G4MICE. Prepared for European Particle Accelerator Conference (EPAC 06), Edinburgh, Scotland, 26-30 Jun 2006.

[51] T. Abe et al. Detectors and flux instrumentation for future neutrino facilities. 2007, arXiv:0712.4129 [physics.ins-det].

[52] D. S. Ayres et al. NOvA proposal to build a 30-kiloton off-axis detector to study neutrino oscillations in the Fermilab NuMI beamline. 2004, hep-ex/0503053.

[53] M. Ellis and F. J. P. Soler. Near detector at a neutrino factory. *Nucl. Instrum. Meth.*, A569:127–131, 2006.

[54] The ISS Detector Working Group. Detector summary. Technical report, June 2006.

[55] D. M. Kaplan and K. Long. MICE: The International Muon Ionization Cooling Experiment. 2007, arXiv:0707.1915 [physics.acc-ph].

[56] S. Yang. MICE Design Office. http://www.physics.ox.ac.uk/design/MICE/mice_page.htm, 2007.

[57] P. Soler. Measurement of Particle Production from the MICE Target. Presented at NuFact07, August 2007.

[58] MICE collaboration. MICE Technical Reference Document. http://mice.iit.edu, 2007.

[59] N V Mokhov, S I Striganov, A Van Ginneken, S G Mashnik, A J Sierk, and J Ranft. MARS Code Developments. Technical Report nucl-th/9812038. FERMILAB-PUB-98-379. LA-UR-98-5716, FERMILAB, Batavia, IL, Dec 1998.

[60] R. E. Prael. LAHET calculations for accelerator neutron production. *Astronomische Nachrichten Supplement*, pages 14–19, 1993.

[61] S. Agostinelli et al. GEANT4: A simulation toolkit. *Nucl. Instrum. Meth.*, A506:250–303, 2003.

[62] Kevin Beard et al. G4BeamLine Simulations of Parametric Resonance Ionization Cooling of Muon Beams. *AIP Conf. Proc.*, 821:453–457, 2006.

[63] K. L. Brown and F. C. Iselin. Decay TURTLE (Trace Unlimited Rays Through Lumped Elements): A Computer Program for Simulating Charged Particle Beam Transport Systems, Including Decay Calculations. CERN-74-02.

[64] T.J. Roberts. G4Beamline Analysis of the MICE AUG05 Beamline Design. MICE collaboration meeting, October 2005.

[65] S. Abachi et al. The D0 Detector. *Nucl. Instrum. Meth.*, A338:185–253, 1994.

[66] O. Voloshyn. Reconstruction des traces dans la TPG de l'experiénce MICE. Master's thesis, Université de Genève, October 2005.

[67] V. Ableev et al. TPG, test results. *IEEE Trans. Nucl. Sci.*, 52:2944–2950, 2005.

[68] A. Fish. Tracker Software. MICE collaboration meeting, June 2007.

[69] H. Paul. Gamma absorption coefficient of lead, versus energy.

[70] C. Casella. FAST: A precision measurement of the muon lifetime tau(mu) and G(F). *Nucl. Phys. Proc. Suppl.*, 150:204–207, 2006.

[71] Geant4. *Physics Reference Manual*, May 2007.

[72] W.H. Barkas. Technical Report 10292, UCRL, August 1962.

[73] F. James. Statistical Methods in Experimental Physics. Lecture series, 2007.

[74] S. M. Seltzer and M. J. Berger. Bremsstrahlung spectra from electron interactions with screened atomic nuclei and orbital electrons. *Nuclear Instruments and Methods in Physics Research B*, 12:95–134, August 1985.

[75] H. Olsen and L.C. Maximon. Photon and electron polarization in high-energy bremsstrahlung and pair production with screening. *Physical Review*, 114:887–904, 1959.

[76] M. Ellis. Results from MuScat. In *AIP Conference Proceedings*, volume 896, pages 168–177, March 2007.

[77] J. Baró J. M. Fernández-Varea, R. Mayol and F. Salvat. On the theory and simulation of multiple elastic scattering of electrons. *NIM*, B73:447–473, 1993.

[78] W. W. M. Allison. Calculations of energy loss and multiple scattering (ELMS) in molecular hydrogen. *J. Phys.*, G29:1701–1703, 2003.

[79] R. Brun and F. Rademakers. ROOT: An object oriented data analysis framework. *Nucl. Instrum. Meth.*, A389:81–86, 1997.

[80] R. Veenhof. GARFIELD, recent developments. *Nucl. Instrum. Meth.*, A419:726–730, 1998.

[81] M. Ellis. SciFi Performance. MICE collaboration meeting, February 2005.

[82] T2K. T2K ND280 Techical Design Report. Technical report, November 2006. Internal Document.

[83] J. Norem et al. The Radiation Environment in and near High Gradient RF Cavities. Presented at IEEE Particle Accelerator Conference (PAC2001), Chicago, Illinois, 18-22 Jun 2001.

[84] A. Hassanein et al. Effects of surface damage on RF cavity operation. *Phys. Rev. ST Accel. Beams*, 9:062001, 2006.

[85] I. Kawrakow and D.W.O. Rogers. The EGSnrc Code System: Monte Carlo Simulation of Electron and Photon Transport. NRCC Report PIRS-701, National Research Council of Canada, Sept 2006.

[86] J. Norem et al. Dark current, breakdown, and magnetic field effects in a multicell, 805 MHz cavity. *Phys. Rev. ST Accel. Beams*, 6:072001, 2003.

[87] M. Silari, J. C. Gaborit, L. Ulrici, and S. Agosteo. Radiation produced by the LEP superconducting RF cavities. *Nucl. Instrum. Meth.*, A432:1–13, 1999.

[88] S. E. Harvey et al. Surface analysis of OFE-copper X-band accelerating structures and possible correlation to RF breakdown events. *J. Vac. Sci. Technol. A Vac. Surf. Films*, 22:1326, 2004, physics/0310056.

[89] Steffen Dobert. RF breakdown in high-frequency accelerators. Invited talk at 2004 IEEE Power Modulator Conference and 26th Power Modulator Symposium and 2004 High Voltage Workshop (PMC 2004), San Francisco, California, 23-26 May 2004.

[90] A. Moretti et al. Effects of high solenoidal magnetic fields on rf accelerating cavities. *Phys. Rev. ST Accel. Beams*, 8:072001, 2005.

[91] D. Huang, Al Moretti, and Z Qian. 805 MHz cavity Mo button test data update. Muon Collaboration Friday Meeting, June 2007.

[92] M. Ellis. SciFi Tracker Performance. MICE collaboration meeting, October 2004.

[93] Donald E. Groom, Nikolai V. Mokhov, and Sergei I. Striganov. Muon stopping power and range tables 10-MeV to 100-TeV. *Atom. Data Nucl. Data Tabl.*, 78:183–356, 2001.

[94] F. James. *Statistical Methods in Experimental Physics.* World Scientific Publishing Co. Pte. Ltd., 2006. ISBN 981-256-795-X.

[95] KLOE collaboration. Private discussion, June 2006.

[96] A. Hocker et al. TMVA: Toolkit for multivariate data analysis. 2007, physics/0703039.

[97] C. T. Rogers and M. Ellis. High precision measurement of muon beam emittance reduction in MICE. Prepared for Particle Accelerator Conference (PAC 05), Knoxville, Tennessee, 16-20 May 2005.

[98] M. Bonesini. Some results from BTF testbeam on TOF. MICE collaboration meeting, October 2006.

[99] D. Orestano and A. Cirillo. Analysis of KL tests at BTF. MICE collaboration meeting, October 2006.

[100] A. Cirillo. Collaudo di un Prototipo di Calorimetro a Piombo e Fibre Scintillanti per l´Identificazione di Particelle nell´Esperimento M.I.C.E. Master's thesis, Università degli Studi "Roma Tre", 2006.

[101] P. Chimenti. Progress on BTF test beam simulation. MICE collaboration meeting, October 2006.

[102] P. Chimenti. SW: prototype tests and full detector cost. MICE collaboration meeting, October 2007.

INDEX